جمهورية العراق
وزارة التعليم العالي والبحث العلمي
جامعة بابل
كلية التربية للعلوم الصرفة
قسم الفيزياء

تحضير وخصائص الأغشية الرقيقة لأوكسيد معدني (Bi_2O_3) النانوي المحضرة بتقنية التبخير الحراري لتطبيقات متحسس

اطروحة مقدمة

الى مجلس كلية التربية للعلوم الصرفة جامعة بابل
كجزء من متطلبات نيل درجة الدكتوراه
فلسفة في التربية / الفيزياء

من قبل الطالب

حسنين سعد سهيل عبدالحسين

بكالوريوس تربية فيزياء / جامعة بابل 2007 م
ماجستير تربية فيزياء / جامعة بابل 2019 م

بأشراف

أ. د. علي رزاق عبدالرضا العزاوي

1444هـ **2023 م**

Republic of Iraq
Ministry of Higher Education
& Scientific Research
University of Babylon
College of Education for Pure Sciences
Department of Physics

Synthesis and Characterization of Nano Metal Oxide (Bi_2O_3) Thin Films Prepared by Thermal Evaporation Technique as Sensor Applications

Dissertation

Submitted to the Council of College of Education for Pure Sciences
University of Babylon in Partial Fulfillment of the Requirement for the Degree Doctor of Philosophy in Education / Physics.

by

Hassanein Saad Suhail Abd-Alhussein

B.Sc. in Physics
(University of Babylon, 2007)
M. E. Sc. in Physics
(University of Babylon, 2019)

Supervised by

Prof. Dr. Ali R. Abdulridha Al-Azzawi

2023 A.D **1444 A.H**

الخلاصة

تم تحضير الأغشية الرقيقة النقية من أوكسيد البزموث (Bi_2O_3) والمشوب بـ ZnO بنسب وزنية مختلفة ٪ (0 ، 0.12 ، 0.24 ، 0.36 ، 0.48) بأستخدام تقنية التبخير الحراري تحت ضغط $1x10^{-5}$ mbar. بزمن ترسيب 20 s وبمعدل ترسيب $0.5\ nm.s^{-1}$ ، عند درجة حرارة الغرفة على قواعد زجاجية بسمك 50 ±5 nm وملدنة عند 473 K و 573 K لمدة ساعتين. تمت دراسة الخصائص التركيبية والبصرية لمدى طول موجي nm (200-1100) والخواص الكهربائية للاغشية الرقيقة (DC و AC). تضمنت الخصائص التركيبية حيود الأشعة السينية (XRD) ، وتحويل فورييه للأشعة تحت الحمراء (FT-IR) ، ومجهر القوة الذرية (AFM) ، والمجهر الإلكتروني الماسح (SEM). أظهر حيود الأشعة السينية أن تركيز ZnO-doping يقلل من متوسط حجم البلورة. علاوة على ذلك ، يتم حساب متوسط قيم الإجهاد والخلع باستخدام بيانات XRD.أظهرت نتائج الخصائص التركيبية لطيف FTIR للأغشية الرقيقة أن جميع قمم روابط الامتصاص تبقى في نفس موقع الأطوال الموجية ، أي لم يحدث أي تفاعل كيميائي. أظهرت نتائج الخواص الضوئية للأغشية الرقيقة (Bi_2O_3:ZnO) زيادة في الامتصاصية ، ومعامل الامتصاص ، ومعامل الخمود ، ومعامل الانكسار ، وثوابت العزل الحقيقي والخيالي للأغشية المحضرة ، بينما تناقصت النفاذية وفجوة الطاقة مع زيادة تركيز الجسيمات النانوية (ZnO). تتمتع جميع الاغشية الرقيقة بامتصاص عالي في منطقة الأشعة فوق البنفسجية. أظهرت جميع نتائج الخواص الكهربائية المستمرة للمركبات النانوية أن التوصيل الكهربائي المستمر يزداد مع زيادة تركيز الجسيمات النانوية(ZnO) ودرجات الحرارة ، بينما تقل طاقة التنشيط مع زيادة تركيز الجسيمات النانوية (ZnO). أظهرت نتائج الخصائص الكهربائية المتناوبة للاغشية أن ثابت العزل وفقد العزل الكهربائي للاغشية النانوية يتناقص مع زيادة تردد المجال الكهربائي المسلط ويزداد مع زيادة تركيز الجسيمات النانوية (ZnO). تزداد الموصلية الكهربائية مع زيادة تردد المجال الكهربائي المسلط والنسبة الوزنية للجسيمات النانوية (ZnO). أظهرت نتائج تطبيق الاغشية الرقيقة أن جميع الاغشية لديها حساسية عالية لغاز H_2S وNO_2 . بينما تم الحصول على أقل زمن استجابة وزمن استرداد مع زيادة تراكيز الجسيمات النانوية (ZnO) للأغشية الرقيقة المحضرة.

ABSTRACT

The pure (Bi_2O_3) and ZnO-doped Bi_2O_3 thin films in different weight ratios of (ZnO) (0, 0.12, 0.24, 0.36, and 0.48) wt.% are prepared by thermal evaporation technique under pressure 1×10^{-5} mbar with deposition time 20s and a deposition rate of 0.5 $nm.s^{-1}$, at ambient temperature on 50 ±5 nm thick glass substrates and annealed at 473 K and 573 K for 2 hours. The structural and optical properties of the wavelength's (200-1100) nm and the thin films electrical properties (D.C and A.C) were studied. The structural properties included X-ray diffraction (XRD), Fourier transforms infrared (FT-IR), atomic force microscopy (AFM), and scanning electron microscopy (SEM). X-ray diffraction showed that the ZnO-doping concentration decreases the average crystal size. Furthermore, the average stress and dislocation values are calculated using the XRD data. The results of the structural properties of the FTIR spectrum of the thin films showed that all the peaks of most of the absorption bonds remain in the same location of the wavelengths, i.e., no chemical reaction occurred. The results of the optical properties of (Bi_2O_3:ZnO) thin films showed an increase in absorbance, absorption coefficient, extinction coefficient, refractive index, and real and imaginary dielectric constants of the prepared films, while the transmittance and energy gap decreases with increasing nanoparticle concentration (ZnO). All thin films have high absorbance in the ultraviolet region. All the results of the D.C electrical properties of the thin films showed that the electrical conductivity increases with increasing the concentration of nanoparticles (ZnO) and temperatures, while the activation energy decreases with increasing the concentration of nanoparticles (ZnO). The results of the A.C electrical properties of the thin films showed that the dielectric constant and the dielectric loss of the thin films decrease with the increasing in the frequency of the applied electric field and increase with the increase in the concentration of nanoparticles (ZnO) while the alternating electrical conductivity increases with the increasing in the frequency of the applied electric field and the weight ratios of the nanoparticles (ZnO). The results of applying the thin films showed that all the films have high sensitivity to H_2S and NO_2 gas. While the lowest response time and recovery time were obtained with increasing the concentrations of nanoparticles (ZnO) for the prepared thin films.

بسم الله الرحمن الرحيم

{يَرْفَعِ اللَّهُ الَّذِينَ آمَنُوا مِنكُمْ وَالَّذِينَ أُوتُوا الْعِلْمَ دَرَجَاتٍ وَاللَّهُ بِمَا تَعْمَلُونَ خَبِيرٌ}

صدق الله العلي العظيم

سورة المجادلة : الآية {١١}

Dedication

Thanks go to Allah and at all the whole grace prayer, and peace upon the best creation Mohammad (peace be upon him and his family) and his divine good…

To my father who has given me love and care, and taught me how to face life.

To the spirit of my mother and brother martyr (Fadel) are the source of light in my life.

To my wife and children, the source of love and affection.

To my teachers the lighted candles who are showing us the road of life.

To my close friends

To My country with honour and dignityand Everyone who helped me.

HASSANEIN

Acknowledgments

Praise be to Allah Lord of the world, and best prayers and peace upon his best messenger Mohammed, his pure descendants, and his noble companions.

Then, I would like to express my deep gratitude and appreciation to my supervisor, Dr. Ali R. Abdulridha for his guidance, suggestions, and encouragement throughout the research work, without him, this dissertation would have been impossible.

I would like to thank the staff of the department of physics in college of education for pure sciences in the university of Babylon for their kind attention and assistances.

Finally, I would like to thank all members of my family for their help and encouragement and all who helped me during the preparation of this dissertation.

HASSANEIN

Contents

1.1 General Introduction

Over the past century, nanotechnology has flourished tremendously. Today, numerous fields of study are directly or indirectly related to nanotechnology. In every flow, nanotechnology can be defined as the development, synthesis, characterization, and application of materials and devices by modifying their size and shape at the nanoscale. The prefix nano is also used in product advertising [1]. Nano derives from the Greek term nanos or the Latin word nanus, both of which mean dwarf. It combines the disciplines of Physics, Chemistry, Materials Science, Solid State, and Biosciences. Therefore, more than expertise in a single domain will be required; expertise in Physics, Chemistry, Materials Science, Solid State, and Biosciences is needed [2].

The difference between nanoscience and nanotechnology is that nanoscience gives knowledge about the arrangement of atoms and their basic properties at the nanoscale. In contrast, nanotechnology is the technology used in governing matter at the atomic level to synthesise novel nanomaterials with different characteristics [3].

Nanomaterials are nanotechnology's fundamental and defining components [4]. Nanomaterials are substances with dimensions less than 100 nanometers in at least one dimension. This indicates that their size is significantly smaller than the microscopic size. Nanomaterials are typically between 10^{-9} nanometers in size or billionths of a metre. The physicochemical properties of nanomaterials differ from those of bulk materials, which are inherently dependent on their size and shape. By modifying shape and size at the nanoscale level, nanomaterials produce an unexpectedly distinct character with new properties and capabilities [5]. Depending on their dimensions, nanomaterials may have various structures, such as nanopillars, nanoparticles,

and nanosheets. Zero-dimensional nanomaterials are nanoparticles, one-dimensional nanomaterials are nanorods or nanotubes, and two-dimensional nanomaterials are typically films and layers of the first variety. It is primarily used to classify isolated nanomaterials. When two or more particles interact, their physical properties will alter. These particulates with various constituents are referred to as bulky or 3D nanomaterials [6,7]. As shown in Fig. (1.1), nanostructured materials can be zero-dimensional, one-dimensional, two-dimensional, and three-dimensional.

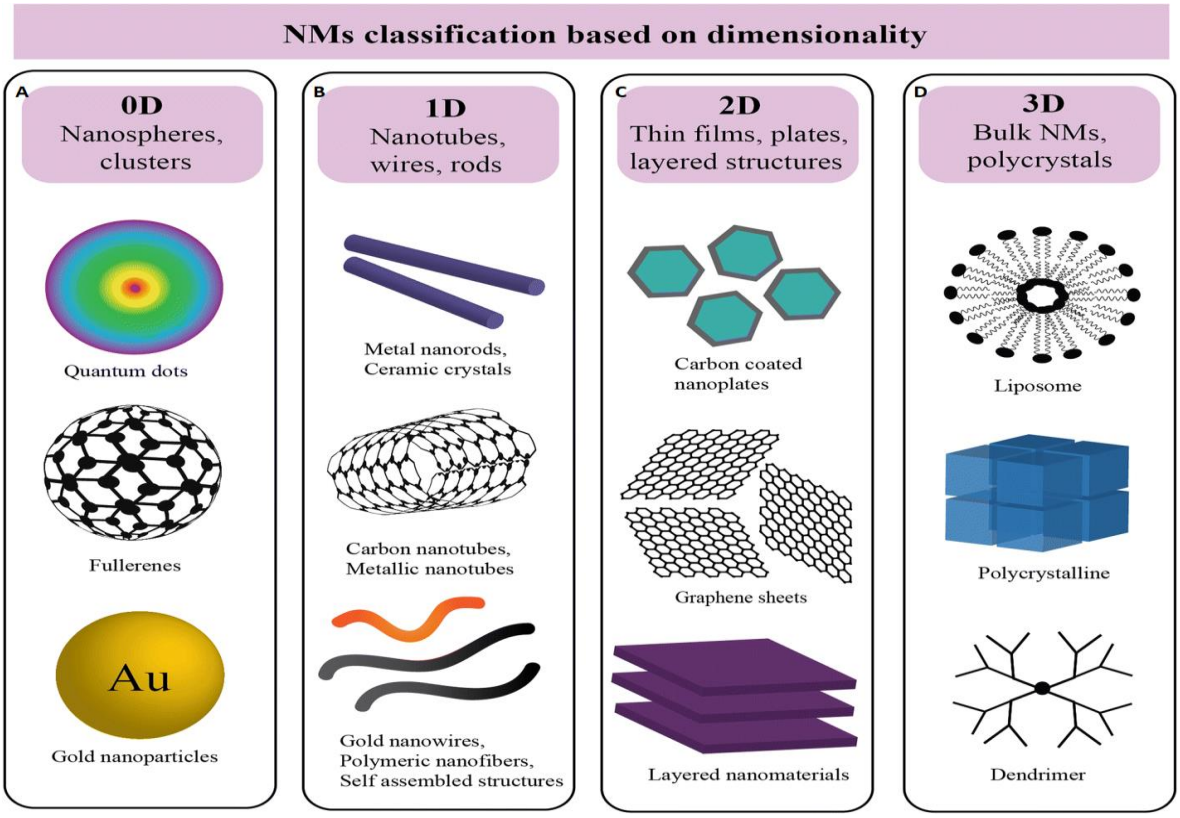

Figure (1.1): Classification of nanomaterials (A) 0D spheres and clusters, (B) 1D nanofibers, wires, and rods, (C) 2D films, plates, and networks, (D) 3D nanomaterial [8]**.**

Population development in recent decades has spurred the rapid expansion of industry and automobile transportation. As a result, toxic and

hazardous chemical species have become pervasive in everyday life and pose a grave threat to human health and the environment [9,10].

Due to the inability to observe, taste, or touch many of these chemical species, invasive species are often the most difficult to observe. For dependable air quality monitoring, gas sensing technology attracts interest in both primary and industrial domains [11].

There are numerous varieties of gas sensors, and their classification criteria vary. Gas sensors can be classified according to the type of sensing material used, the general sensing mechanism of the material, or the type of interaction between the gas sensing material and the gas. Among these categories are semiconductor gas sensors [12,13].

Solid electrolyte gas sensors [14], contact combustion gas sensors, optical gas sensors, quartz vibrator gas sensors and surface acoustic wave gas sensors [15]. Compared to other types of sensors, gas sensors utilizing various metal oxide semiconductors (MOS) as the sensing layers have become the focus of research due to their superior sensitivity, compact size, and low cost [16].

1.2 Nano Metal Oxide

Due to their ability to absorb light, metal oxides have proven extremely useful in numerous applications [17]. Consequently, depositing such nanoparticles of metal oxides onto natural platforms such as glass substrates. Metal and metal oxide nanoparticles have applications in numerous disciplines, such as catalysis, molecular detection, and environmental remediation [18].

Metal oxides have been studied in various applications[19]. Metal oxides derived from the early transition metals displayed extraordinary properties,

including catalytic, electro-optic, electromechanical, ferroelectric, and wave density charging characteristics [20].

These characteristics facilitate their use in numerous chemical reactions, including selective oxidation and dehydration. Due to their unique physicochemical properties, a substantial amount of research has also been devoted to using metal oxides in biomedical applications [21].

Due to their diminutive size, which affects the fundamental properties of any substance, metal oxide nanostructures can manifest distinct physical and chemical characteristics. Nanoparticles, nanowires, nanotubes, and nanoporous structures are among the numerous metal oxide nanoobjects [22].

1.3 Semiconductor Gas Sensors

In recent times, gas sensing, a typical application in intelligent systems, has garnered increasing attention in the industrial and academic spheres. The importance of gas detection technology continues to grow as a result of the numerous and widespread applications it has in the following industries:

1. Industrial production (e.g., methane detection in mines) [23].
2. Automotive industry (e.g., detection of polluting gases from transport (car, bus, etc.) [24].
3. Medical applications (e.g., electronic noses simulating the human sense of smell system)[25].
4. Indoor air quality supervision (e.g., detection of carbon monoxide) [26].
5. Environmental studies (e.g., greenhouse gas monitoring) [27].
6. Toxic fumes are highly hazardous to human health, even when present in incredibly trace amounts, as is common knowledge [28].

Oxides of metals are a fascinating and versatile group of materials because their properties vary from those of metals to those of semiconductors and insulators. Many electronic, chemical, and physical characteristics of metal oxides are extremely delicate and easily altered by slight shifts in their chemical surroundings. Metal oxide thin films have attracted much attention from scientists and engineers as potential electronic substances due to their semiconducting behaviour, structural simplicity, and low cost. The electrical conductivity of semiconductors is known to change depending on the gas or chemical environment surrounding them in the area of gases/chemical sensing.

Gas sensors have broad implications in fields as diverse as environmental monitoring, space exploration, house structure safety, public security, automotive applications, aircraft air conditioning, and sensor networks [29]. Semiconductor oxide- as gas sensors are classified according to the direction of the conductance change due to the exposure to decreasing gases as n-type (conductance heightens, such as In_2O_3, ZnO and SnO_2) or p-type (conductance decreases, such as CuO and NiO). This classification is by the nature of the dominant charge carriers at the surface, that is, electrons or holes [30].

In clarifying the qualities of a working experimental sensor, one must first examine the special characteristics that one might reasonably expect to find in an ideal sensor, typically those which might be, for example:

1. Short response.
2. Selectivity.
3. Sensitivity.
4. Hardness and portability.

Semiconductor gas sensors apply to different applications, including safety apparatus (explosive, leakage, fire, pollution, and poisoning protection), emissions and air quality monitoring, process instrumentation, and measurement technology. For instance, it is possible to detect carbon monoxide (CO), nitrogen oxides (NOx), ammonia (NH3), sulfur gases (H_2S and SO_2), hydrocarbon gases (CxHy), and volatile organic compounds (VOCs). The measurement range depends on the detected gas, ranging from a few production probability limits (ppb) to a percentage. The detection limit varies depending on the specific gas-sensitive material [31].

1.4 Materials Used in This Study

1.4.1 Bismuth Oxide (Bi_2O_3)

Important metallic semiconductor bismuth oxide (Bi_2O_3) is of considerable interest due to its excellent optical and electrical properties, such as a wide band gap, high refractive index, high dielectric permittivity, and good optical conductivity [32]. Bismuth oxides have been investigated for use in numerous disciplines, including fuel cells, sensor technology, and various oxide and ionic conductors [33].

As a component, bismuth oxide is utilized in various catalysts and derivatives. Because face-centred cubic (fcc) Bi_2O_3 has the highest ionic conductivity of all oxide ion conductors, as shown in figure (1.2) compounds based on bismuth oxide (Bi_2O_3) are many superior solid electrolytes than the known stable zirconia [34].

Bismuth-based semiconductors, where Bi_2O_3 is extensively used in solid-state lasers, bioimaging, high refractive index temperature sensors, gas

sensors, optical coatings, glass fabrication, and photoluminescence, have been the subject of a great deal of research in recent years [35].

Bi_2O_3 is nontoxic, easy and cheap to prepare and is well known as a p-type semiconductor with a wide band energy gap that can be varied between 2 and 3.9 eV [36]. As shown in Table (1.1).

In recent years, numerous successful strategies, such as the precipitation method, microwave-assisted synthesis, electrophoresis, and chemical vapour deposition (CVD), have been reported for preparing Bi_2O_3 with various shapes, such as quantum dots, nanoparticles, nanobelts, nanodisks, nanofibers, and thin films [33].

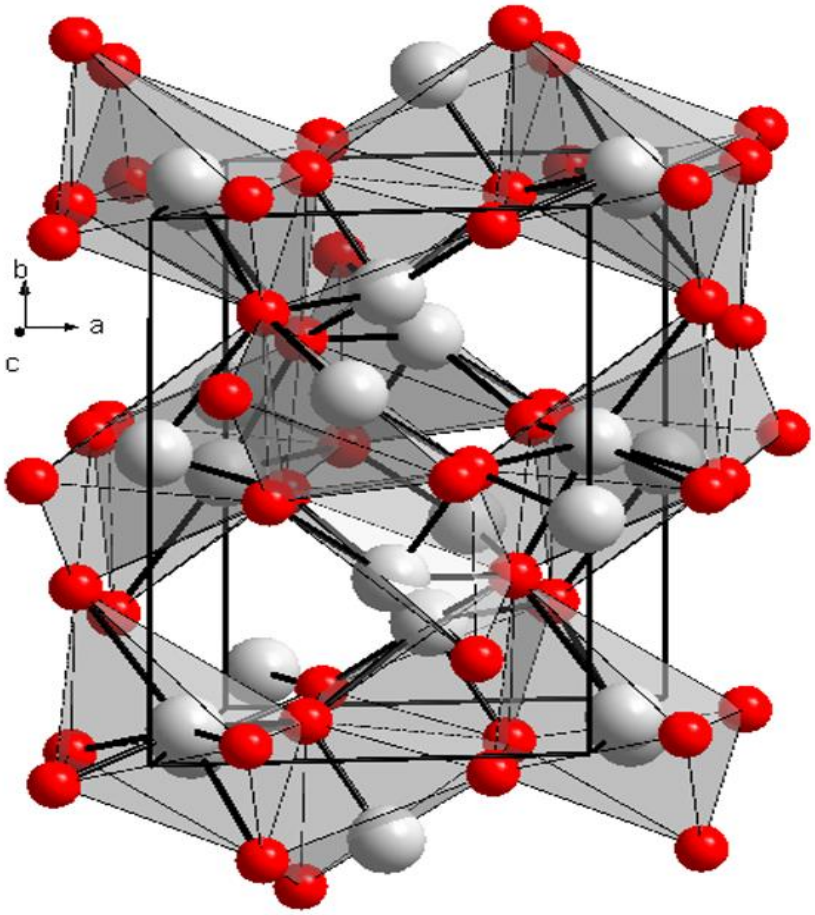

Figure (1.2): Structure of Bi_2O_3 (room temperature phase); red atoms are oxygens and white atoms are Bismuth [37].

Table (1.1): The Physical and Chemical Properties of bismuth Oxide Nanoparticles[38]**.**

Parameters	Bi_2O_3
Density (g/cm^3)	8.9
Molecular mass g / mol	465.96
Appearance	yellow crystals or powder
Solubility in water	Insoluble
Energy gap (eV)	2 and 3.9
Melting point (^oC)	817
Boiling point (^oC)	1890

1.4.2 Zinc Oxide (ZnO)

Zinc oxide has been used in various applications for millennia, and it is now considered a mature engineering material, with annual production approaching half a million tons [39].

Due to its superior optical quality, stability, and piezoelectric properties, among others, ZnO possesses a number of remarkable characteristics. Solar cells, gas sensors, transparent conductive materials, surface acoustic wave devices, and piezoelectric transducers are a few of the many technological fields in which it is extensively employed [40].

Analysis of high-bandgap oxide semiconductors revealed the applicability of ultrathin layers of zinc oxide, ZnO, as shown in figure (1.3), as sensitive layers for detecting specific light wavelengths and molecules. ZnO thin films are one of the most widely used transparent conductive oxides for advanced applications such as window layers in heterojunction solar cells,

thermal mirrors, piezoelectric devices, multilayer photothermal conversion systems, solid gas sensors, etc. ZnO's direct optical energy gap of 3.3 eV, as shown in Table (1.2) can transmit the most valuable solar radiation. In addition, the abundant availability of ZnO in nature reduces its cost, and its acute UV cutoff makes it desirable for many applications [41].

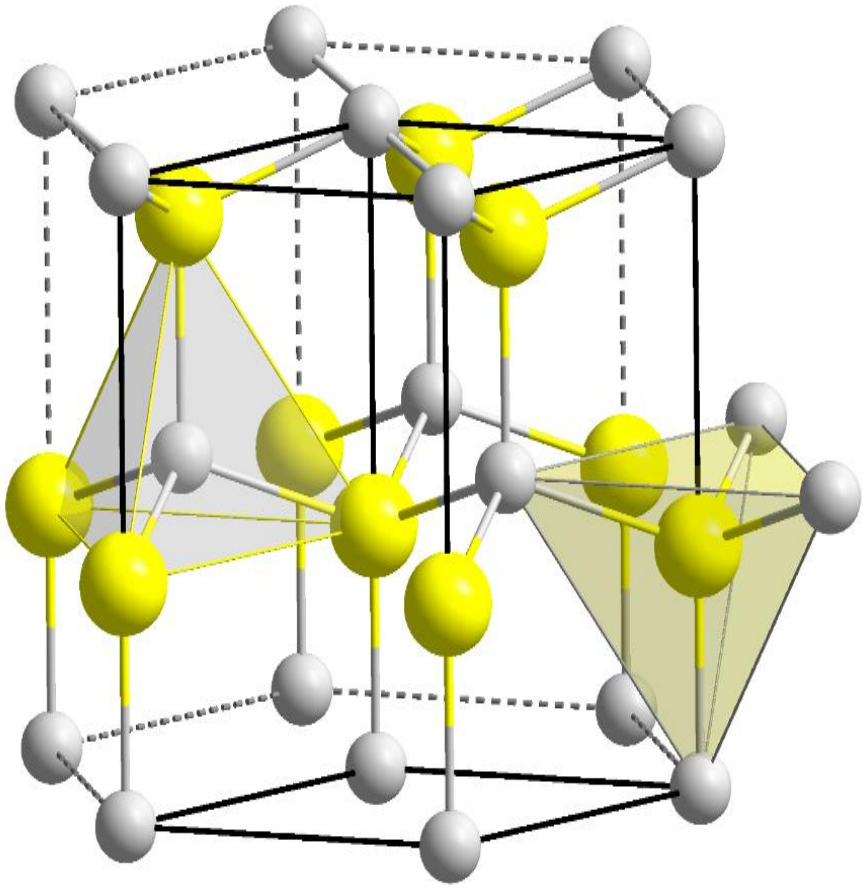

Figure (1.3) : The hexagonal structure of ZnO yellow atoms and white atoms are oxygens [42]**.**

Table (1.2): The Physical and Chemical Properties of Zinc Oxide Nanoparticles[42]**.**

Parameters	ZnO
Density (g/cm^3)	5.606
Molecular mass g / mol	81.408
Appearance	White
Solubility in water	Insoluble
energy gap (eV)	3.3
Melting point (^oC)	975
Boiling point (^oC)	2360

1.5 Literature Survey

Researchers continue to diversify their research studies between completing research and results begun by their predecessors and developing new techniques and methods that enable them to advance scientifically by applying their findings. By developing or discovering new methods to prepare these films (dissolution, evaporation, decomposition, etc.), the number of researchers who prepared films from various materials pure or impregnated with certain elements or by combining two or more materials to obtain films from a substance that increased the mixture of these materials. Following are the names of a few researchers interested in producing ZnO and Bi_2O_3 films:

Fruth, *et al.* in (2006)[37] Studied oxide ion conductors are being more Due to their use in high-value devices like solid oxide fuel cells (SOFC), oxygen sensors, thick ceramic membranes for oxygen separation, and membrane reactors for oxidative catalysis. Bismuth oxides, such as Bi_2O_3, have great potential for such applications due to the dopant in Bi_2O_3 and their impact on the structure and properties of the oxide polymorph forms obtained at high

temperatures. Powder X-ray diffraction, SEM/EDX analysis, and infrared spectroscopy examined Bi_2O_3 molecular changes. Bulk ceramic density, porosity, and electrical activity versus temperature affect structural changes. Antimony and tantalum on bismuth sites expand and stabilize polymorph forms, which may be useful.

Cong, *et al.* in (2007)[43] used the Bi_2O_3 in microwave-sintered ZnO varistors. Compares the Bi_2O_3 vaporization of ZnO varistors sintered by a standard electric furnace. They found that the Bi_2O_3 vaporization in microwave-sintered ZnO varistors is more homogenous from the surface to the inside due to the special thermal gradient inside the samples and that it directly affects the electrical properties of the varistors. Homogenous Bi_2O_3 vaporization creates more typical microstructures, making microwave-sintered samples better electrically.

Khalaf, *et al.* in (2013)[41] investigated the 40 nm zinc oxide thin films on glass plates. Electrode assembly design makes preparing nanocrystalline thin films with minimum grain size easier. Dissected layer morphology and optical properties. X-ray, optical, and atomic force microscopes revealed molecular details and microstructure. (AFM). Plasma-deposited ZnO films have consistent preferential growth of nanocrystalline film and hexagonal-type structure with good crystallinity and no amorphous or other crystalline compounds. Atomic force microscopes measured the smallest and average crystallite size. The optical microscopy found spherical ZnO nanoparticles forming a homogenous spatial film on the substrate without discontinuities. Plasma-deposited ZnO films have (3.1-3.3eV) energy gaps. This work also investigates gas sensing using a homemade gas sensor unit and ZnO **Kalyamwar, *et al.* in (2012)**[44] examined the ZnO nanostructure Thick Films as room-temperature H_2S gas sensors. On a glass substrate, ZnO nanostructures were made by hydrothermal

method and sonication for 30,60, 90, and 120 min. Gas sensing features of synthesized ZnO nanostructures were examined. This method can synthesize ZnO nanostructures for semiconductor gas sensors that can sense poisonous gases like H_2S at room temperature.

Liu, *et al.* in (2013)[45] prepared the electrostatically deposited bismuth (Bi) films by regulating thermal oxidation reaction slope rate and temperature. Surface morphology showed that tens of 25-nm-thick 2D nanoplates form flower-like structures in 3D Bi_2O_3 hierarchy structures. 2D nanosheets are well-crystallized β-Bi_2O_3. The 3D Bi_2O_3 hierarchical structures also emit a robust, broadband photoluminescence signal from 500 to 900 nm, peaking at 759 nm. These novel architectures will likely be used in nanoscale sensors, optics, and electronics.

Mielcarek, *et al.* in(2013)[46] ZnO–Bi_2O_3 binary systems and varistors were examined under biasing electric field and temperature. 50 μA DC at 115 1C aged both samples for 22 h. DC biased TSDC spectrum peaks and varistor voltage dips. Ceramic Bi_2O_3 formed TSDC. 0.01–0.17 eV thermally generated responses. The TSDC current deteriorated at high temperatures when the Bi-rich inter-granular phase produced agglomerates and the Bi_2O_3 was faulty. Amorphous, well-crystallized, and α-Bi_2O_3 had no high-temperature TSDC maximums. The varistor voltage returned to DC bias at normal temperature. Switching the bias from positive to negative dropped the varistor voltage continuously.

Li. *et al.* in (2015)[47] manufactured the ZnO–Bi_2O_3 based polycrystalline varistors as the rapid applications of gapless surge protectors replaced standard gapped SiC designs. These varistors have good symmetric nonlinear current–voltage (I–V) characteristics due to the back-to-back electrical potential barriers formed between successive ZnO grains during step-wise processing cycles. The

degradation and failure processes of electrical potential barriers for acceptable protective characteristics were understood through microstructures, defect structures, and processing parameters. Discussed are varistors' processing factors.

Teimoori, *et al.* in (2015)[48] investigated the Dependence of H_2 Gas Sensitivity of ZnO Thin as a function of film thickness. ZnO thin films of different thicknesses (100, 150 and 200 nm) were deposited using e-beam evaporation technique on SiO_2/Si substrates. Their results showed that the best sensitivity was attributed to the ZnO film of 100 nm thickness at the operating temperature of 400 °C while an increase in film thickness and operating temperature caused the reducing of H_2 gas sensitivity of the samples.

Liu, *et al.* in (2016)[49] reported the ZnO was first made by 95^0C direct deposition with polyethylene glycol surfactant. (PEG-6000). X-ray diffraction, Fourier transform infrared, transmission electron, energy dispersive, and electron microscopy have been used to analyze composite samples. ZnO nanoparticles had a wurtzite hexagonal crystal structure and were nearly spherical, varying from 15 to 28 nm. Additionally, BiO fully covered ZnO nanoparticles. Sol-gel ZnO/Bi_2O_3 nanoparticles (1 mol% Bi_2O_3).

Ahila, *et al.* in(2016)[50] measured the influence of different thicknesses (250,350, and 450 ±20 nm) on the structural and optical properties of thin films of (Bi_2O_3) deposited on glass substrates using thermal evaporation technique under vacuum, (XRD) is used to characterize the structural properties, the results indicate that all films prepared have a polycrystalline structure with preferentially oriented in the [201] with tetragonal structure, These films have high absorption coefficients ($\alpha > 10^4$ cm^{-1}) and direct energy gaps that grow with film thickness, according to optical analyses. Optical observations found that the absorption coefficient, refractive index, extinction coefficient, and

dielectric constants (real and imaginary) are. The film layer affects optical conductivity for wavelengths 300–1100 nm.

Sajjad, *et al.* in (2018)[51] formed the impact of copper doping on ZnO nanoparticles' optical band gap and photoluminescence (PL). To attain the goals, the prepared samples' crystal structure and morphology were identified and confirmed using XRD and SEM tests. From XRD data, the average grain size for pure ZnO was 24.62 nm, which dropped to 18.95 nm for the 5 wt% Cu-doped samples and then increased to 37.80 nm for the 7 wt% Cu-doped samples. From diffuse reflectance spectroscopy (DRS) spectra, the optical band gap of pure and Cu-doped ZnO nanoparticles decreased from 3.13 eV to 2.94 eV as Cu increased to 7 wt%. In the photoluminescence study, the PL technique boosted the visible spectrum. Further analysis was done with FT-IR and EDX tests.

Alharbi, Qasrawi, in(2019)[52] reported the structural, optical, and dielectric features of 200 nm thick Bi_2O_3 thin films deposited on an amorphous germanium substrate. Ge and Bi_2O_3 thin films are made by steam evaporation at 10^{-5} mbar. Heterogeneous Ge/Bi_2O_3 interferences have conduction and valence bands of 0.81 and 1.38 eV, respectively. When using a germanium substrate, flour frequency bands were extended from 5.21–11.0 GHz to 2.59–12.80 GHz, and the drift motion rose by about one order of magnitude. Visible light transmission is explained by heterojunction optical propertie.

Kumari, *et al.* in (2019)[53] formed the ZnO–Bi_2O_3 polycrystalline varistors as technologically important with the fast applications of gapless surge protectors replacing gapped SiC designs. During step-wise processing cycles, back-to-back electrical potential barriers between successive ZnO grains give these varistors superb symmetric nonlinear current–voltage characteristics. Microstructures, defect structures, and processing parameters helped explain

electrical potential barrier degradation and failure processes for acceptable protective characteristics. Varistors' processing variables affect efficiency.

Meng, *et al.* in(2019)[54] synthesized the bismuth oxide films on quartz surfaces using a bismuth metal target. and found Bi3+ ions. XRD and Raman scattering described film structure. The room-temperature film was amorphous. Polycrystalline structure formed above 300 °C. Measurements of transmittance examined film optical qualities. The Tauc plot estimated the optical band gap, which redshifted with substrate temperature, making it a possible visible light photocatalytic material.

Nayef, Kamel, in(2020)[55] investigated the preparation and characterization of Bi_2O_3 nanoparticles (Bi_2O_3NPs) by laser ablation in. X-ray diffraction (XRD) investigation is appeared broad diffraction peak when the size of the crystal becomes inside nanometer. Scanning electron Microscopy (SEM) study results for porous silicon (PS) found sponge like structure and Bi_2O_3NPs nanoparticles appear as bright spots. Observed the reflectivity of Bi_2O_3NPs on PS is less than Si bulk and PS, however. From Raman result show peaks at 81cm−1 and 303cm−1, are the specific bands of α-Bi_2O_3. The band at 303 cm−1. Finally, the variation of operation temperature of NO_2 gas sensors which fabricated from the prepared samples on sensor sensitivity, response time and recover time have been studied, and the maximum sensitivity was about 71% for Bi_2O_3 NPs.

Aus, in(2021)[56] reported the ultrafine bismuth Bi_2O_3 thin films synthesized by physical vapor deposition (PVD) for their morphological, topographical, structural, and optical features. SEM and AFM found that the synthesized thin films have a uniform nano-island structure with an average grain size of 70 nm and a root mean square (RMS) roughness of 2.68 nm. XRD showed bismuth oxide films have polycrystalline monoclinic structures. The films have a narrow

bandgap of 1.95 eV, and the Wemple-DiDomenico model calculated the single-oscillator energy and dispersion energy to be 4.01 and 23.26 eV, respectively.

Wang, *et al.* in(2021)[57] prepared the Gas sensors on metal oxide semiconductors are popular for sensing volatile organic chemicals due to their low cost, ease of fabrication, and stability. Here, we rationally design ethanol gas sensors based on p-Bi_2O_3 and n-ZnO heterostructure with clear interfaces, which have an excellent response of 21.6 towards 100 ppm ethanol, wide concentration detection ranges from 1 to 500 ppm, working temperature as low as 175 °C, short response time of 7 s, and recovery time of 8 s at 100 ppm ethanol. The Bi_2O_3/ZnO sensor also has higher selectivity for ethanol than other organic volatile gases.

Ahmed, *et al.* in(2021)[58] synthesized the thermally evaporated ZnO thin films on unheated glass surfaces. XRD found amorphous ZnO films before heating. The films' diffraction patterns found irregular mixed Tetragonal α-ZnO compounds and Orthorhombic ß-ZnO compounds. AFM found ZnO films have a wide homogeneous surface. XRD data are less than AFM data and rise for all thicknesses with annealing temperature. Optical properties found that transmittance declines with annealing temperature for all thicknesses.

Dhahri, *et al.* in(2022)[59] formed the pure ZnO and ZnO–Bi_2O_3 nanocomposites with 5 and 10 wt% Bi_2O_3. Modeling actual transmittance and reflectance UV–Vis spectra determined optical qualities like refractive index (n), extinction coefficient (k), bandgap (Eg), Urbach energies, and band structure. The band gap and Urbach energies for pure ZnO (3.758 eV) rise with Bi_2O_3 doping in ZnO–Bi_2O_3 hybrid films. X-ray diffraction and SEM examined these nanocomposite films' structural and physical features. Pure ZnO and nanocomposites with Bi_2O_3 have crystalline domains with wurtzite hexagonal structures. As Bi_2O_3 doping rises, crystallite size reduces. SEM-based.

1.6 The Aim of the Study

1- Fabrication of (Bi_2O_3:ZnO) gas sensor for detection of NO_2 and H_2S gases.

2- Obtaining the best sensitivity, response time and recovery time for gas (H_2S and NO_2) for the prepared thin films (Bi_2O_3:ZnO).

2.1 Introduction

This chapter explains the theoretical component, which includes a description of the scientific justifications, physical concepts, relationships, and laws used to understand the findings.

2.2 Thermal Evaporation

In a convection evaporator, the substance is melted by an electric resistance heater, and the vapour pressure is increases to a helpful level for the process. In a high vacuum, vapor can reach the substrate without interacting with or scattering against other gas-phase elements in the chamber. In the vacuum chamber, the absorption of impurities from the residual gas is kept to a minimum. Both of these goals are accomplished by reducing the amount of residual gas in the vacuum chamber [60]. The most straightforward method for transferring a substance onto a substrate is known as thermal evaporation under pressure ($1x10^{-5}$) mbar and given excellent purity of films. Figure (2.1) explains the configuration of a basic coating system [61].

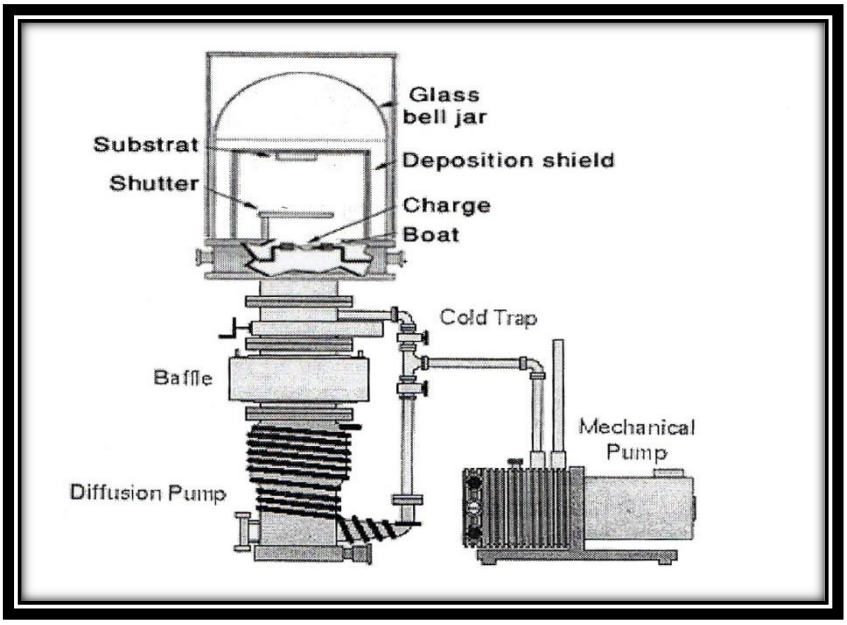

Figure (2.1): Configuration of a basic coating system [61].

2.3 Structural and Morphological Properties

2.3.1 The x-ray diffraction (XRD)

X-ray diffraction is a crucial experimental technique for determining lattice parameters, the preferred orientation for crystallographic identification of unknown materials, defects and tensions, and the average crystal size [62].

When a monochromatic X-ray diffraction beam is directed at a crystal sample, constructive diffractions (also known as interference) from parallel planes of atoms with inter-planar separation d_{hkl} will occur according to Bragg's law, as shown in the figure (2.2). This is demonstrated by the equation [63]:

$$2d_{hkl} sin\,\theta = \lambda \qquad (2.1)$$

where: $d_{hkl} = \frac{d}{n}$ θ: is Bragg diffraction angle (degree), and λ: is the incident X-ray beam's wavelength (Å).

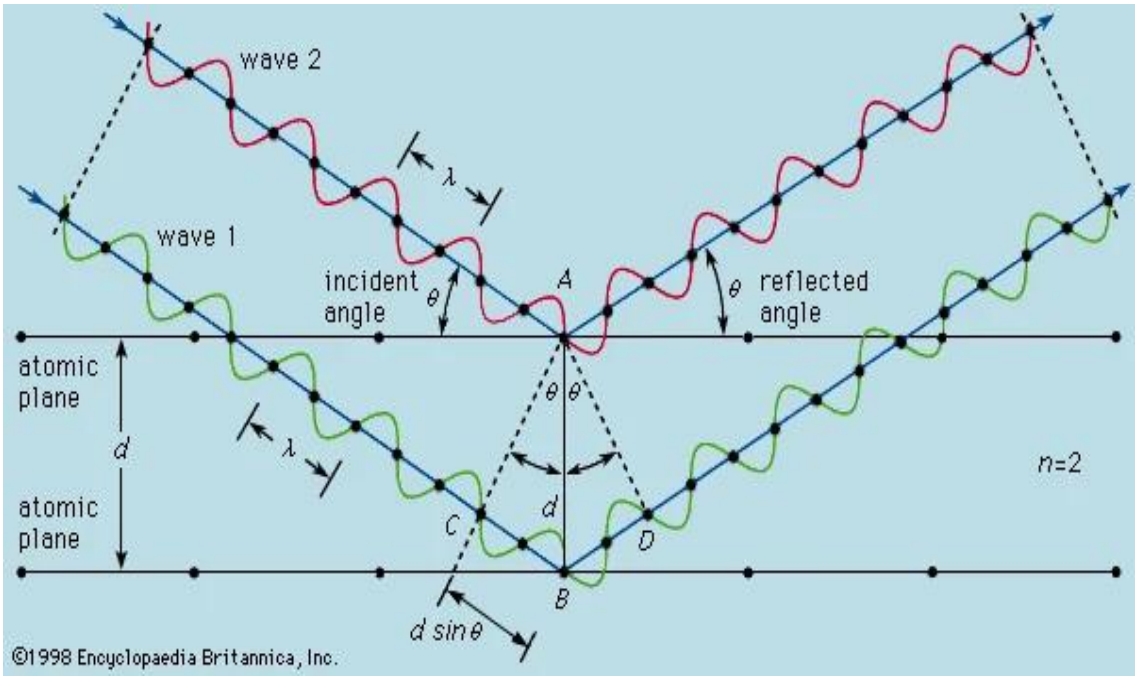

Figure (2.2): Bragg's Diffraction [64].

2.3.2 Parameters calculation

Calculating the different properties used in the study of thin films requires extensive use of X-ray diffraction.

A. Number of layers (N_l)

Based on the percolation hypothesis, we can determine the relationship between sheet thickness (t), the number of crystalline layers (N_l), and D is the dimension of the crystallite in nanometers [65–67]:

$$N = \frac{t}{D^3} \qquad (2.2)$$

B. Crystallite size (D)

Average film crystallite size are estimated by the Scherrer's formula [68,69]:

$$D = \frac{K\,\lambda}{\beta \cos\theta} \qquad (2.3)$$

Where k is a constant (0.94 for spherical particles), λ is the wavelength of the x-ray radiation (Cu-K = 0.154 nm), β is the full breadth at half maximum (FWHM) of the intense and wide peaks

C. Micro strains (ε)

During the growth of thin films, strains are measured and enhanced by stretching or compression of the lattice to maintain a constant c-lattice deviation. Therefore, the strain broadening is due to varying atomic displacements relative to their reference lattice position. This strain can be computed using the given equation [70,71]:

$$\varepsilon = \frac{\beta}{4 \tan\theta} \qquad (2.4)$$

C. Dislocation density (δ)

The dislocation density of a crystal is the number of dislocation lines per unit surface. The dislocation density (δ) can be approximated using the following expression based on Williamson and Smallman's formula [72,73]:

$$\delta = \frac{1}{D^2} \qquad (2.5)$$

2.3.3 Atomic force microscope (AFM)

In 1986, Quate, Gerber, and Binnig were the ones who first developed the atomic force microscope. Its application of it is contingent on the surface characteristics as well as the toughness of the material.

Figure (2.3) depicts the AFM block diagram. The AFM comprises a microscale cantilever with a pointed tip (probe) used to survey the surface of the specimen. The cantilever is typically composed of silicon (Si) or silicon nitride (Si3N4) and has a tip radius of curvature in the nanometer range. AFM traverses a ceramic or semiconductor tip like a phonograph needle over a surface. When the point is brought close to a sample surface, Van der Waals forces between the tip and sample cause the cantilever to deflect. A laser that reflects an oblique angle from the cantilever's very end measures the deflection's magnitude [74].

The resolution of the surface's topography, which is comprised of hills and valleys, is provided by a representation of laser deflection versus tip location on the sample surface. The atomic force microscope (AFM) can be used with the point contacting the material (known as the contact mode), or it can stroke across the surface like a cane used by a blind person (known as the tapping mode) [75].

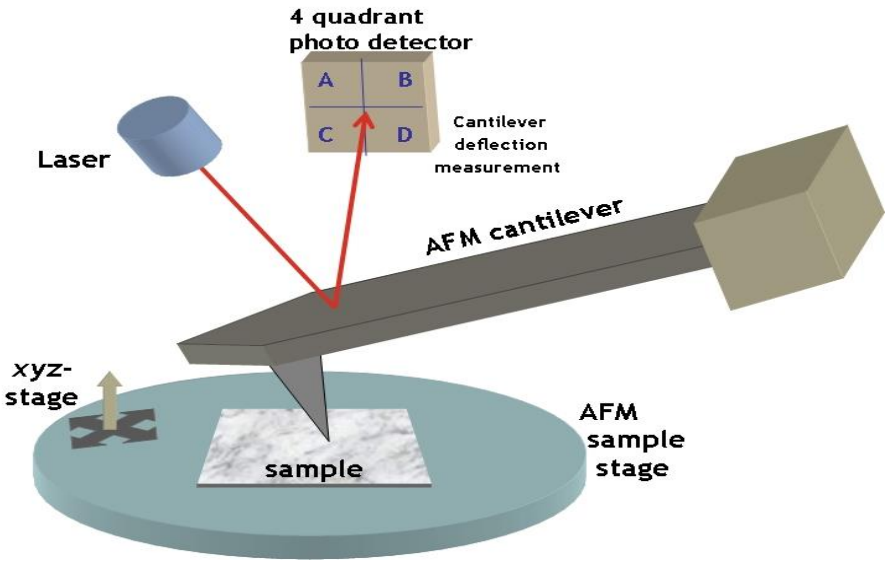

***Figure (2.3): Block diagram of atomic force microscope** [76].*

2.3.4 Scanning electron microscopy (SEM)

The scanning electron microscope, also known as an SEM, is one of the most adaptable instruments that can be used to investigate and analyze the microstructure morphology and chemical composition characterizations of different materials. To comprehend the fundamentals of electron microscopy, it is essential to have a solid foundation in light optics and its underlying principles [77]. The resolution of the unaided eye is approximately ~ 0.1 mm, corresponding to a visual angle resolution of approximately 1/60. (At the optimum viewing distance of 25 cm). By magnifying the visual angle with an optical lens, the resolution limit of optical microscopy is ~ 2,000 Å Light microscopy has been and remains vital to scientific research. Numerous experiments since the 1890s have demonstrated that the magnetic field can deflect electrons [78].

Over the last 80 years, the imaging technique known as electron microscopy has proven to be a game-changer for the fields of science and engineering. This technique has made it possible to study nanoparticles and determine the specific characteristics of these materials. The capability of electron microscopes to image objects that are submicron in size, all the way down to individual atomic locations, has resulted in the development of completely new nanotechnologies. It has also made it possible for extraordinary advancements to be made through the nanoengineering of macro-sized components. To facilitate the development of a wide variety of commonplace items, including mobile phones, televisions with plasma screens, and the materials utilized aeroplanes, widespread use of electron microscopes is required [79].

The scanning electron microscopy (SEM) technique involves focusing a small probe of electrons with energies generally up to 40 keV on a specimen while scanning the specimen along a pattern of parallel lines. The collision of the incoming electrons with the sample surface causes various

signals to be produced, which can then be compiled into a picture or used to analyze the sample surface, as shown in Figure (2.4). These are primarily secondary electrons, which have energies of a few tens of eV, high-energy electrons that have been backscattered from the original stream, and characteristic X-rays [80]. This portion discusses the most significant steps that have been taken to enable the use of such complex physical interaction in a practical tool, thereby transforming the SEM into the powerful instrument that it is today in life science and materials science [81].

There is a maximum magnification beyond which fine features in a picture will no longer be discernible. This is because the imaging method and the human sight have resolution constraints. The focusing power of a establishes the utmost practical magnification beyond which no further details are disclosed [82].

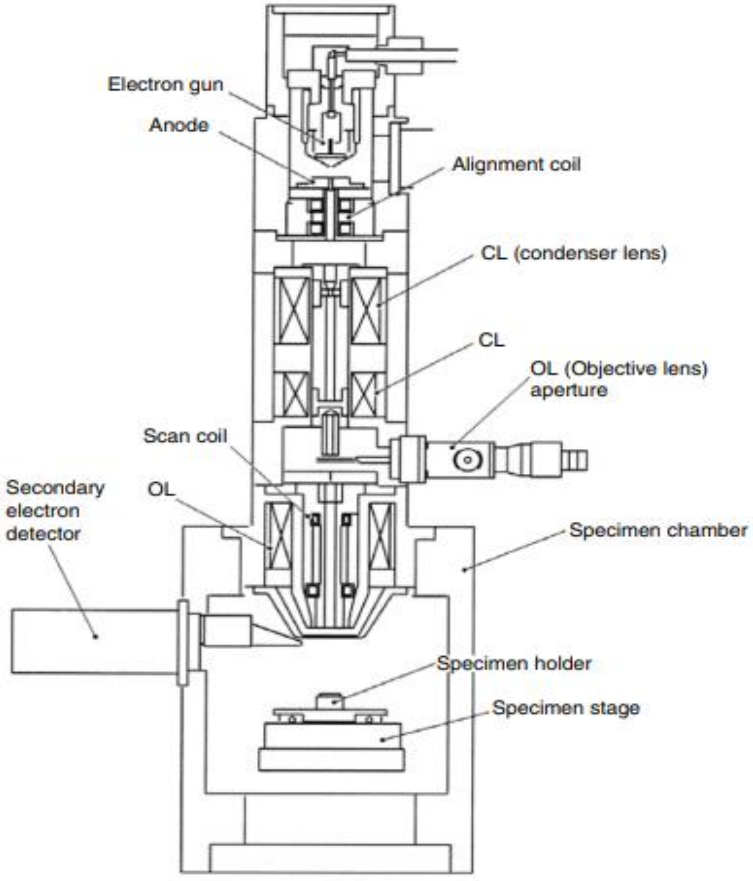

Figure (2.4): SEM device diagram [77]**.**

2.4 Optical Properties

The study of optical properties of nanomaterials aims to increase our knowledge of the quality of the internal structure of nanomaterials, as well as broaden the horizon of possible fields of application.

Spectroscopic techniques, such as UV-Visible and photoluminescence spectroscopy, which reveal information about nanoparticles' electronic structure, are frequently used to characterize optical characteristics. Related optical approaches, such as Raman and near-infrared spectroscopy (NIR), provide information about the crystal structure, including phonon or oscillating frequencies and crystal phases [83].

Optical properties represent one of the main factors in its results, which were based on a lot of analyses about nature of the atomic structure of the material or the effect of the absorption material for photons of light in the incidence of the transfer of electronic within the installation packs and thus shows the installation of power packs as well as the energy gap whether directly or indirectly[84]. That is provided with information about the nature of the change constants visual such as absorption coefficient, coefficient of refraction, extinction coefficient and others [85]. The optical characteristics of nanosized materials go through significant shifts as a consequence of the changes in electronic properties that occur with size [4].

Because energy is connected to wavelength, this indicates that the optical characteristics of the particle can be precisely adjusted depending on its size. If particles are made small enough, quantum effects will come into play. These effects restrict the energies at which electrons and holes can exist in the particles. Consequently, particles can be made to produce or absorb particular wavelengths of light simply by manipulating their size. This can be done in a variety of ways [86].

2.4.1Transmittance, Reflectance, Absorbance and Scattering

Figure (2.5) depicts an object (the sample) irradiated with light at a given incidence angle. The incoming light must penetrate the object's surface to interact with most of the sample's constituent material. For the optical behavior of the entire system, it is evident that the optical properties of surfaces and interfaces will be of utmost importance. After interacting with the sample, light may exit in multiple directions. From a phenomenological standpoint, light may either be [87]:

(a) specularly reflected from the sample,

(b) transmitted through the sample (in a well -defined direction),

(c) absorbed at the sample surfaces or in its volume,

(d) diffusely scattered at the sample surfaces or in its volume,

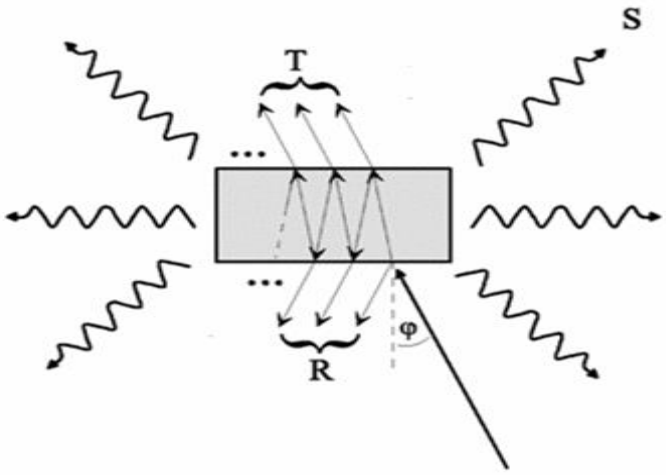

Figure (2.5): shown the definitions of T,R and S. ϕ is the incidence angle [87]**.**

2.4.2 Absorbance (A)

Absorbance can be defined as the ratio between absorbed light intensity (I_A) by material and the incident intensity of light (I_o) following equation [88]:

$$A = \frac{I_A}{I_o} \qquad (2.6)$$

2.4.3 Transmittance (T)

Transmittance (T) is given by reference to the intensity of the rays transmitting from the surface (I_T) to the intensity of the rays incident (I_o) on it, and can be calculated by [89]:

$$T = \frac{I_T}{I_o} \quad (2.7)$$

The electrical transitions can be roughly divided into two categories, which are as follows:

1- Direct transition

This transition happens in semiconductors when the bottom of the conduction band (C.B.) is exactly over the top of the valence band (V.B.), which means they have the same value of wave vector i.e. ΔK=0, in this state the absorption appeared when $h\upsilon=Eg_{opt}$ This transition type required the Law's conservation in energy and momentum. These direct transitions have two types [90]:

a. Direct allowed transition

This transition presents between the top points in the (V.B.) to the bottom point in the (C.B.), as shown in Figure (2.6, A).

b. Directly forbidden transitions

This transition happens between near top points of (V.B.) and bottom points of (C.B.), as shown in Figure (2.6, B). The absorption coefficient for this transitions type given in equation (2.8) [91]:

$$\alpha h\upsilon=B(h\upsilon - E_{g\ opt})^r \quad (2.8)$$

where: B is constant depending on the type of material, υ is the frequency of the incident photon and r is exponential constant, where its value depends on the type of transition, r =1/2 for the allowed direct transition, and r =3/2 for the forbidden direct transition.

2- Indirect transitions

In these transition types, the bottom of (C.B.) is not over the top of (V.B.), in the curve (E-K), the electron transits from (V.B.) to (C.B.) not

perpendicularly where the value of the wave vector of the electron is not equal before and after the transition of the electron. ($\Delta K \neq 0$), this transition type happens with help of the particle is called Phonon, for the conservation of the energy and momentum law. There are two types of indirect transitions, they are [91]:

a. Allowed indirect transitions

These transitions occurred between the top of (V.B.) and the bottom of (C.B.) that is found in a different region of (K-space), as shown in Figure (2.6, C).

b. Forbidden indirect transitions

These transitions exhibited between near points in the top of (V.B.) and near points in the bottom of (C.B.), as shown in Figure (2.6, D). The absorption coefficient for transition with a phonon absorption is given in equation (2.9) [92]:

$$\alpha h\upsilon = B(h\upsilon - Eg\ opt \pm Eph)^r \qquad (2.9)$$

Where, Eph. means the energy of phonon, (-) when phonon absorption and (+) means when phonon mission, r means the exponential constant; its value depends on the type of transition, r=2 for the allowed indirect transition, meanwhile r=3 for the forbidden indirect transition.

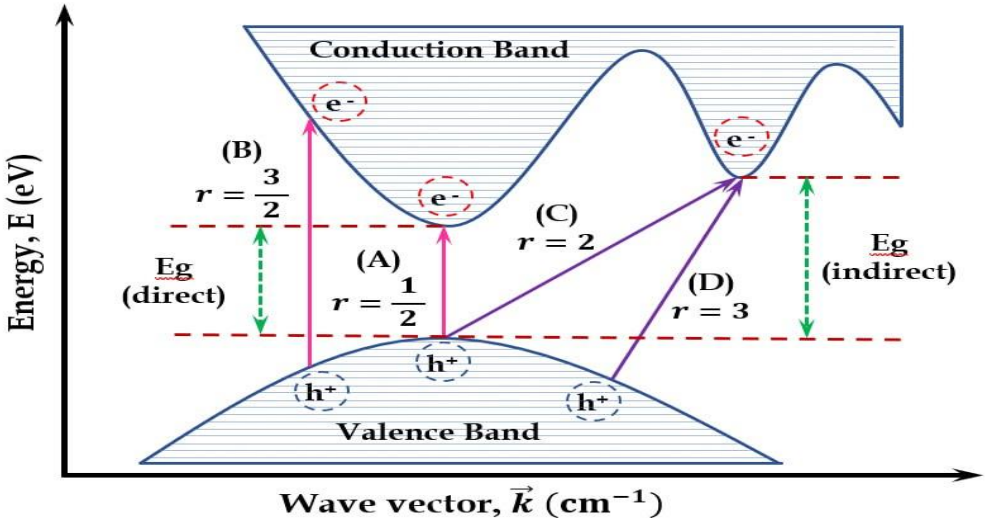

Figure (2.6): The Electronic Transitions Types [92]**.**

(A) Allowed Direct Transition (C) Allowed Indirect Transition

(B) Forbidden Direct Transition (D) Forbidden Indirect Transition

2.4.4 Reflectance (R_r)

It can be calculated using the ratio of the intensity of the rays reflected by the film (I_R) to the intensity of the rays impacted on the film (Io):

$$R_r = \frac{I_R}{I_o} \quad (2.10)$$

and reflectivity can be obtained from absorption and transmission spectrum in accordance to the law of conservation of energy as relation [93].

$$R + T + A = 1 \quad (2.11)$$

2.4.5 Optical constants

A. Absorption coefficient (α)

The absorption coefficient is defined as the ratio of the decrease in the energy flux of incident radiation relative to the distance unit in the direction of incident wave diffusion. Absorption coefficient (α) is dependent on incident photon energy (hυ), material properties, where electronic transitions type (n) or (p) and forbidden energy gap, photon energy yields the following equation [94]:

$$E = h\upsilon \quad (2.12)$$

When the energy of a photon is lower than the prohibited energy gap, that photon will be allowed to pass through, and the expression for transmittance looks like this:

$$T = (1 - R)^2 . e^{-\alpha t} \quad (2.13)$$

If the intensity of the incident ray (Io) is known, the intensity of the transmittance ray (I) can be calculated using the beer Lambert law [87]:

$$I = I_o \exp(-\alpha t) \quad (2.14)$$

the absorption coefficient is measured by cm^{-1}.

$$\alpha t = 2.303 \, log \, {}^{I}/_{I_o} \quad (2.15)$$

Where the amount of log (I/Io) represents the absorbance (A).

The absorption coefficient can be calculated using the following equation [95]:

$$\alpha = 2.303\ (\frac{A}{t}) \quad (2.16)$$

B. Refractive index (n)

It is the ratio between how fast light travels in space versus how fast it travels through a given material. The indicator indicates how much an object is influenced by electromagnetic radiation. There are two components to the refraction index, real and imaginary. The following equation describes it well [96]:

$$n = c/\mathrm{v} \quad (2.17)$$

Where (n) is the coefficient of refraction., (c) is the speed of light in a vacuum, and.(v) is the speed of light in a material medium.

The refractive index can also be expressed in the following equation [97]:

$$n = \frac{1+\sqrt{R}}{1-\sqrt{R}} \quad (2.18)$$

C. Extinction coefficient (k_o)

The accompanying expression shows that the extinction coefficient is the imaginary portion of the complex refractive index (N) [98]:

$$N = n - ik \quad (2.19)$$

Where: n: the real part of refractive index

N: The index of refractivity is complicated and varies depending on the sort of substance. Using the following calculation, one can determine the extinction coefficient of a given substance [99,100]:

$$\mathrm{k_o} = \alpha\lambda/4\pi \quad (2.20)$$

Where λ: is the wavelength of incident photon rays.

D. Dielectric constant (ε)

At optical frequencies, represented by light waves, the electronic polarity is predominant above other surviving kinds of polarization. This is because the dielectric constant symbolizes the ability of matter for polarization, and the matter can respond to different frequencies in a complicated fashion. The following calculation can be used to determine the dielectric constant's real and imaginary values [101]:

$$\varepsilon = \varepsilon_r - i\varepsilon_i \quad (2.21)$$

Where (ε) is the complex dielectric constant and (ε_r, ε_i) are the real and imaginary parts of the dielectric constant, respectively.

It is possible to determine the dielectric constant by using the refractive index. The expression expresses the relationship that exists between the complex value of the dielectric constant and the complex value of the refractive index (N):

$$\varepsilon = N^2 \quad (2.22)$$

It is possible to derive the real and imaginary complex dielectric constants from equation (2.22) and represent them using the corresponding equations [102]:

$$\varepsilon_r = n^2 - k_0^2 \quad (2.23)$$

$$\varepsilon_i = 2nk_0 \quad (2.24)$$

E. Optical conductivity

The optical conductivity (σ_{op}) has been determined from the following equation [101]:

$$\sigma_{op} = \alpha nc/4\pi \quad (2.25)$$

Where c is the velocity of light and α is the absorption coefficient.

2.5 The Electrical Properties

The movement of charged units, also known as charge carriers susceptible to the impact of potential difference, makes up the phenomenon of electricity. In the solid state, these entities are the electrons of the matter, while in the liquid and vapour states, they are the ions of the matter. Even at low temperatures, it has been known for more than four decades that the electrical conductivity of semiconducting metal oxides varies with the composition of the ambient gas atmosphere. Initially, the fundamentals of electrical conductivity and gas-atmosphere interactions were investigated. The initial measurements included sintered bodies and solitary crystals. Considering the results for additional metal oxides [103].

Materials are classified according to its electrical conductivity to:

1-Insulators: its conductivity ranges from 10^{-13}–10^{-6} (ohm .cm) $^{-1}$.

2-Semiconductors: its conductivity ranges from 10^{-6}– 10^{5} (ohm.cm)$^{-1}$.

3-Conductors (metals): its conductivity is more than 10^{6} (ohm .cm) $^{-1}$.

4-Superconductive matters: its conductivity is 10^{20} (ohm .cm)$^{-1}$.

The range of materials and their electrical conductivity are illustrated in Figure (2.7).

Knowledge of atomic energy levels and electronic distribution in these levels is crucial for comprehending the material's electrical characteristics and the process of electrical conductivity [104].

Electrons are located throughout an atom at various energy levels; those closest to the nucleus have stronger connections to the atom. On the other hand, the further electrons are from the nucleus, the weaker the connections are between the electrons and the nucleus. Consequently, electrons that inhabit the orbital that is the farthest away from the nucleus are the ones that have the weakest connection to the nucleus. These electrons, which have many different amounts of energy and are known as valence electrons, are distributed throughout the atom [105].

Significant developments have taken place in optoelectronics technology, with developments in ceramic materials paralleling developments in electronics. Electrically conductive transparent films are particularly attractive because of the growing interest in light interactions with electricity and electronically active materials. This interest makes the study of these interactions increasingly important. In order to meet the stringent requirements imposed by technology, a large number of innovative materials and production methods have been developed. The increasing complexity of applications brings a greater emphasis on the necessary level of image quality. These materials have a wide range of potential applications, including liquid crystal displays, transparent electrodes for solar cells, and photodetectors, to name a few. The simultaneous occurrence of high optical

transparency (>90%) in the visible region, together with electronic conductivity, requires the creation of electron decay in wide-gap (>3 eV) oxides through the incorporation of suitable heterogeneous materials or impurities [106].

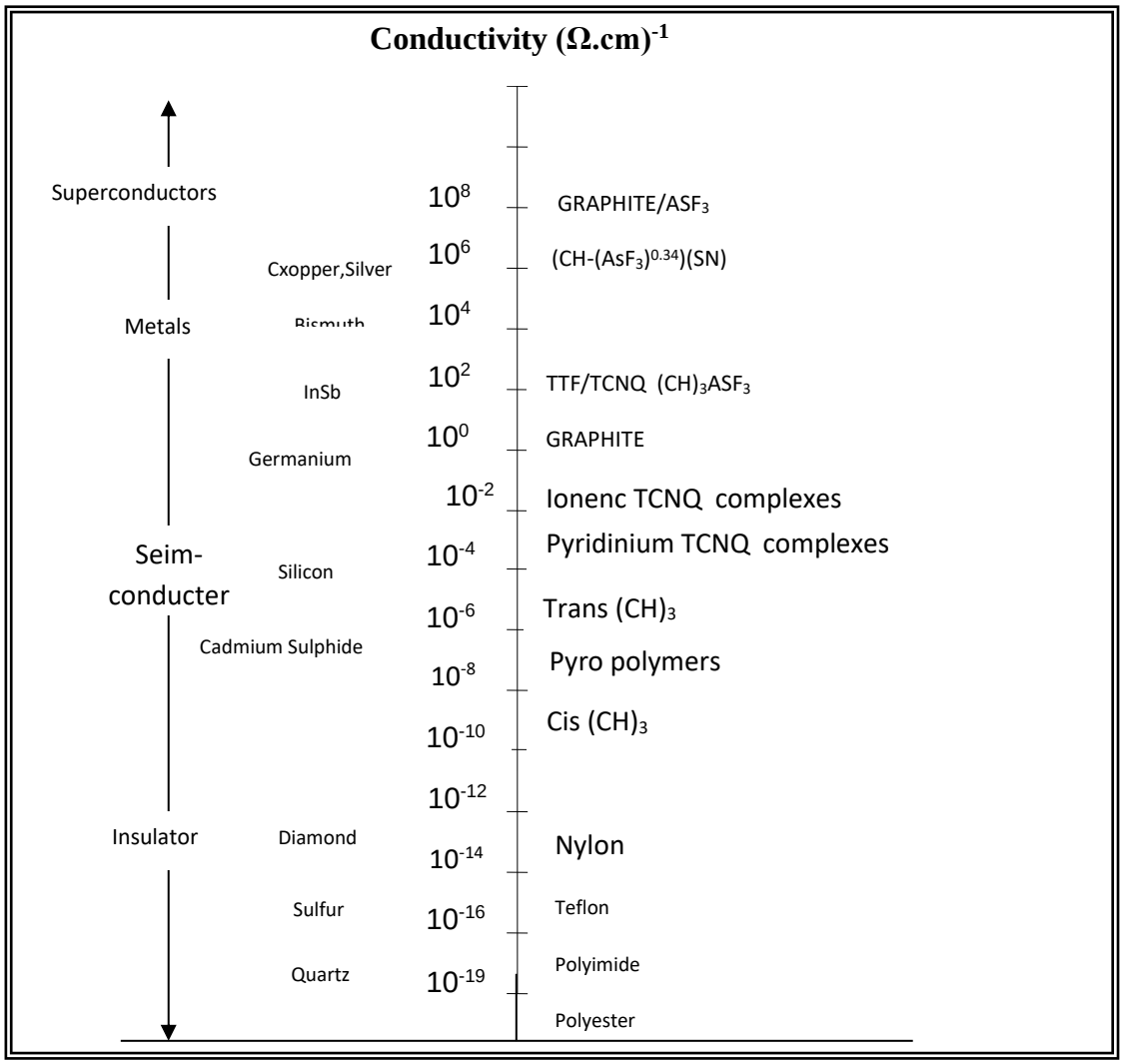

Figure (2.7) :The conductivity of material [105]**.**

2.5.1 Electrical conductivity

The movement of electrical charge from one position in a material to another in response to the action of an external electric field is the process that is referred to as electrical conductivity. Two primary elements determine it: the first is the concentration of charge carriers, denoted by (n), and the second is the responsiveness kinetic of carriers, denoted by (μ) [107].

2.5.2 The D.C electrical conductivity

Materials can be classified according to their conductivity into conductive, semiconducting, and insulating. The conductivity of semiconductors is approximately (10^{-6}-10^{5}) $(ohm.cm)^{-1}$, and the electrical conductivity of semiconductors depends on a stream of electrons going to the positive electrode, accompanied by a flow of holes (positively charged) through the atomic structure of the material heading to negative pole.

The area electrical resistance R_A of a normal body having a section of constant area (A) of length (L), can be calculated using the relation [108]:

$$R_{\mathrm{A}} = \rho_{\mathrm{A}} \frac{L}{b\ t} \qquad (2.26)$$

Where ρ_A represents area resistivity of the substance, which can vary from one to another, the area resistivity is equivalent to the inverse of the bulk conductivity. What this indicates is that the volume conductivity is [109]:

$$\sigma_{\mathrm{A}} = \frac{1}{\rho_A} = \frac{1}{R_{\mathrm{A}}}\ \frac{L}{b\ t} \qquad (2.27)$$

R_A: is the resistance of the thin film, (b) the width of electrodes, (L) the distance between two electrodes, and (t) the sample of thickness.

According to the relation, the conductivity experiences a rise that is exponentially related to the increase in temperature [110]:

$$\sigma = \sigma_{\circ} \exp\left(-\frac{E_{act}}{K_B T}\right) \qquad (2.28)$$

Where σ is electrical conductivity at T temperature, σ_0 is electrical conductivity at absolute zero of temperature, k_B is Boltzmann constant and E_{act} is activation energy.

2.5.3 The electrical polarization

When an electrical field is applied to a capacitor's terminals, consisting of an electrical insulator between its plates, a local displacement occurs for the centres of positive and negative charges. This results in the

generation of induced electrical dipole moments, resulting in an electrical polarity process. The value of this process is equal to the sum of the moments of all dipoles present in the sample unit volume [111]:

$$\mu_i = \alpha E_i^- \quad (2.29)$$

where μ_i is electrical dipole moment, α is polarity of an atom or a molecule and E_i^- is internal field of a molecule, proportional to the external field. Hence, the total dipole moment(P) for a unit volume is [112].

$$P = N_\circ \mu_i \quad (2.30)$$

where, $N_\circ$ is the number of molecules for a unit of volume.

Electrical polarization occurs in all insulators because of impurities, atoms, molecules and ions which have either negative or positive charges [113].

The electrical polarization occurs as a result of the effect of an electrical field which can be expressed in the following equation [113]:

$$P = D - \varepsilon_\circ E \quad (2.31)$$

where D is the electrical displacement, E is electrical field intensity and $\varepsilon_\circ$ is permittivity of free space or vacuum permittivity (8.85×10^{-12} F/m)

$$D = P + \varepsilon_\circ E = \varepsilon_\circ \varepsilon' E \quad (2.32)$$

As

$$\because \varepsilon' = \frac{D}{\varepsilon_\circ E} \quad (2.33)$$

Then,

$$\varepsilon' = 1 + \frac{P}{\varepsilon_\circ E} \quad (2.34)$$

where $\bar{\varepsilon}$ .is the dielectric constant.

The Clausius Mossotti equation illustrates the relationship between a volume unit's relative dielectric constant and its polarizability [114]:

$$\frac{N_\circ \alpha}{3\,\varepsilon_\circ} = \frac{\varepsilon - 1}{\varepsilon + 2} \quad (2.35)$$

2.5.4 Types of polarization

Polarization can be divided in to four types:

1.Electronic polarization (P_e)

The presence of an exterior electrical field causes a disturbance in the distribution of the charge, leading to this phenomenon. A detachment occurs between the positively charged nucleus and the negatively charged middle of the particle [115].

Induced dipoles are produced whenever a positively charged nucleus is present in an element. Electronic polarization can be found in every molecule and within every dielectric despite other kinds of polarization. This particular form of segmentation takes place over an extremely short time. It is operational at most frequencies but drops off working at extremely high frequencies (≈10-15 s), as shown in Figure (2-8 a). Its temperature is sensitive and operates at most frequencies. optical polarization refers to this form of polarization quite frequently [116,117].

2. Ionic polarization (P_i)

As shown in Figure (2-8 b), When an external field is introduced to an ionic lattice, the positive ions move in the direction of the field. On the other hand, the displacement of the negative ions takes place in the opposing direction, which results in a dipole moment for the complete body. The ionic polarization is only slightly affected by temperature, and the primary factor determining it is the interface's composition, which is the location where ions can congregate [117,118].

3.Rotational or orientation polarization (P_d)

Permanent dipoles tend to be directed by the electric field. The thermal motion of the molecules counteracts the rotation, as shown in Figure (2-8 c). Consequently, the orientation polarization is very sensitive

to the frequency of the applied electric field and the temperature. It takes place at low frequencies [117,119].

4.Space charge or interfacial polarization (P_0)

There is typically an interfacial polarization present in heterogeneous materials. The charge concentration at the structural interface causes this polarization. An electric field can initiate the movement of charge carriers such as free electrons, ions, vacancies, and other charge carriers [120,121].

It takes place when a matter possesses impurities, a vacuum, or a structural defect, which results in the concentration of opposing charge on the terminals of the impurity, as demonstrated in Figure. (2-8 d). This entails the production of dipoles within the atom, particle, or section of the material in question. This particular kind of polarization is determined by the level of consistency in the matter and the rate at which it is free from impurities. It takes place almost entirely in radio waves, but depending on the defect that produces the polarization, it can also stretch to frequencies audio below [121].

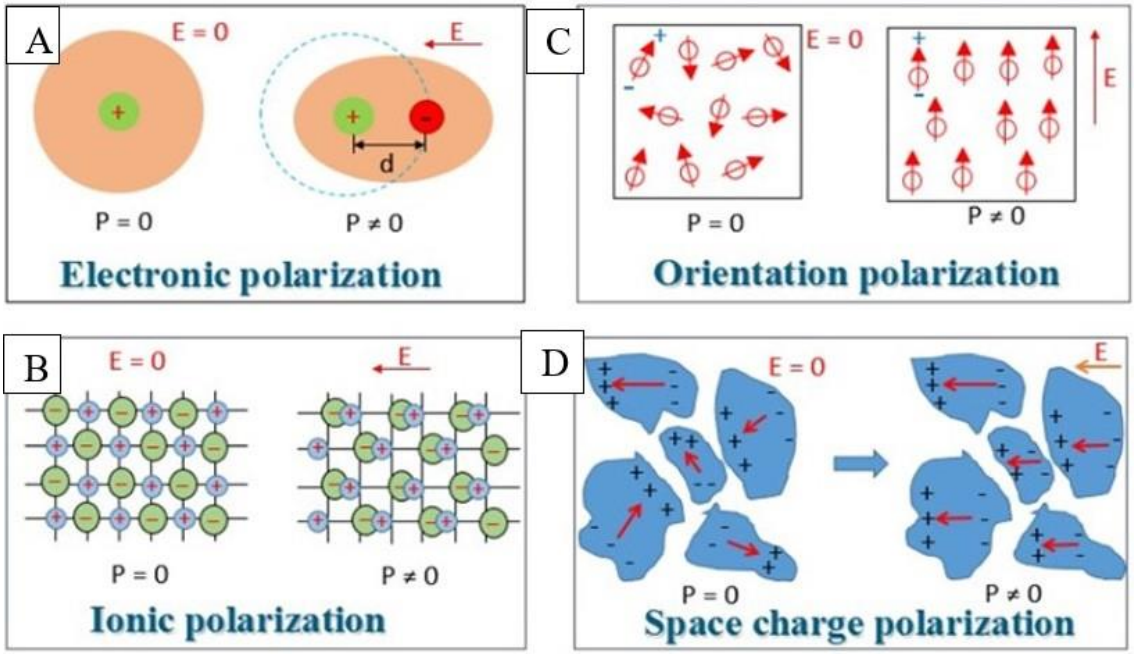

Figure (2-8):A schematic representation of different types of polarization [122]***.***

A. Electrical polarization, B. Ionic polarization, C. Orientation polarization, D. Space charge polarization

2.5.5 The A.C electrical conductivity

Investigating the electrical conductivity and the magnetic characteristics (initial permeability) of the transition metal oxides is of utmost significance in scientific research and this field's implementations [123,124].

The application of nanomaterials is attracting increasing attention from various academic disciplines. As a consequence of this, these materials have been the focus of a great number of studies in the past all over the world due to the significance of their fundamental physical and technological properties and, more recently, for the potential applications that these materials could have, such as sensors and solid-state lasers. Materials, piezoelectric materials, magnetic materials, lustre materials, ceramic materials, catalytic materials, adsorption materials, and ionic conduction materials [125].

The dielectric constant is defined as the ratio of the capacitance of a capacitor with an insulator substance between its conducting plates to the capacity of a capacitor of the same size with a vacuum between its plates [126].

$$I = jwcv \qquad (2.36)$$

where w represents the angular frequency of the applied field (w = 2πf), j represents a fictitious integer, and Vm represents the voltage maximum.

This highlights the fact that the electric current is the total of the conduction current Ip, which is in the same phase as V, and the alternating current Iq, which has a phase difference of π /2, that is [127]:

$$I = I_p + jI_q \qquad (2.37)$$

the capacity of a capacitor constructed of two parallel plates is given by the equation [128]:

$$c = \varepsilon_{\circ} \frac{A}{d} \qquad (2.38)$$

by substituting equation (2.38) in (2.36), get:

$$I = jw\varepsilon\varepsilon_{\circ}\frac{VA}{d} \quad (2.39)$$

The permittivity (ε) must be a complex quantity. It consists of real and imaginary parts, so that the electric current be a complex quantity [129]:

$$\varepsilon = \varepsilon' - j\varepsilon'' \quad (2.40)$$

where ε'' is the dielectric loss so, get:

$$I = jw\varepsilon_{\circ}\frac{A}{d}(\varepsilon' - j\varepsilon'')\mathrm{v} \quad (2.41)$$

by comparing equation (2.40) with (2.39), then:

$$I_p = w\varepsilon''\varepsilon_{\circ}\frac{A}{d}\mathrm{v} \quad (2.42)$$

$$I_q = w\varepsilon'\varepsilon_{\circ}\frac{A}{d}\mathrm{v} \quad (2.43)$$

that the loss factor (tanδ) is given by the following equation:

$$\tan\delta = \frac{I_p}{I_q} = \frac{\varepsilon''}{\varepsilon'} \quad (2.44)$$

This is the amount of electrical energy lost and then transformed into heat energy by the substance. When it comes to electrical applications, a good understanding of calculating the power factor is essential. The development of heat in the substance at high frequencies as a consequence of an excessive power factor could lead to an electrical breakdown [105].

At low frequencies, (c) can be considered a parallel connection between a perfect capacitor and a resistor Rp. So:

$$I = I_p + jI_q = \frac{\mathrm{v}}{R_p} + jwc_pV \quad (2.45)$$

hence, get the impedance:

$$\frac{1}{Z} = \frac{1}{R_p} + jwc_p \quad (2.46)$$

from equations (2.41), (2.42), and (2.46), one can write:

$$R_p = \frac{d}{w\varepsilon''A\varepsilon_{\circ}} \quad (2.47)$$

$$\varepsilon'' = \frac{1}{wR_pC_{\circ}} \quad (2.48)$$

$$\mathrm{C}_p = \varepsilon'\varepsilon_{\circ}\frac{A}{d} \quad (2.49)$$

$$\varepsilon' = \frac{C_p}{C_\circ} \quad (2.50)$$

The presence of alternating voltage as a function of alternating. conductivity is a representation of the energy that is lost in the substance [105]:

$$\sigma_{a.c} = w\varepsilon''\varepsilon_\circ \quad (2.51)$$

$\sigma_{a.c}$ is a measurement of the temperature generated in the substance as a result of the movement of the dipoles in their locations (or the vibration of the charges) as a direct result of the alternating field [128].

2.6 Gas Sensors

The rapid development of industry and vehicle transportation in recent decades due to a growing human population has increaseing the number of toxic gases in the atmosphere. Air pollution damages the brain by impairing cognitive ability, resulting in difficulties with decision-making and daily tasks [130]. Identifying and surveilling combustible, toxic, and exhaust fumes are crucial for energy conservation and preserving the natural environment [131]. In addition, the World Health Organization reports that contaminated air is directly responsible for the deaths of millions of people each year. In light of these facts, monitoring air quality has received significant attention in recent years, intending to save both people and the environment. A gas monitor is one of the most important pieces of electrical equipment for identifying potentially dangerous inorganic compounds [9].

One of the groups of gas sensors presently receiving the most research attention is the semiconducting metal oxide gas sensor group. Due to their cheap cost and versatility in manufacturing, the ease with which they can be utilized, and the large number of gases that can be detected and potential application fields, they have garnered much interest in gas detection under atmospheric conditions and circumstances [132]. In addition to monitoring the change in conductivity of gas-sensing material, this reaction can be detected by measuring the change in capacitance, work function, mass, optical characteristics, or reaction energy (NO_2, NO, NH_3, H_2S, CO_2,

etc.) [133]. and organic (methane, triethylamine, benzene, etc.) gases [134]. Moreover, the gas sensor has also shown its immense presence in various applications such as industry and agriculture processing, aerospace, military, and medical diagnosis [135].

Due to their cheap production cost, ease of miniaturization, and compatibility with existing integrated circuit technology, sensors built on semiconductors have tremendous potential in the sensing industry [136,137].

This thesis will focus primarily on semiconducting metal oxide gas sensors and provide a brief overview of metal oxide gas sensors in general.

The samples were evaluated as H_2S and NO_2 gas sensors at varying operational temperatures. The sensitivity factor (S) was computed using the following formula [138,139]:

$$S = \frac{R_{on} - R_{off}}{R_{on}} \times 100\% \qquad (2.52)$$

R_{on} and R_{off} represent the film's electrical resistance in air and gas, respectively.

Response time is calculated and recovery time curves with extreme operating temperature 200°C to 300°C, determined by the equations [140,141].

$$Response\ time = \left| t_{gas\ (on)} - t_{gas\ (off)} \right| \times 0.9 \qquad (2.53)$$

$$Recover\ time = \left| t_{gas\ (off)} - t_{gas\ (recover)} \right| \times 0.9 \qquad (2.54)$$

3.1 Introduction

This chapter focuses on the experimental details that were used in the fabrication and screening of thin films made of pure (Bi_2O_3) and ZnO-doped Bi_2O_3 thin films, different doping ratios of ZnO (0.12, 0.24, 0.36, and 0.48) wt.% on glass substrates using the thermal evaporation technique. Investigation of structural and morphological features by X-ray diffraction (XRD), atomic force microscopy (AFM), and scanning electron microscopy (SEM), respectively, are the techniques that are used to prepare and test the structure of thin films. Grain size determination is also described as one of the techniques. Optical measurements of thin films such as (transmittance (T), absorbance (A), absorption coefficient (α), optical energy gap (E_g), refractive index (n), extinction coefficient (k_o), and dielectric constants (ε_r and ε_i). The electrical properties of DC and AC thin films were also investigated by measuring the electrical conductivity, energizing energy, dielectric constant and dielectric loss. Thin films have a schematic diagram illustrating the experimental work, as shown in figure (3.1). The application of the gas sensor has also been studied.

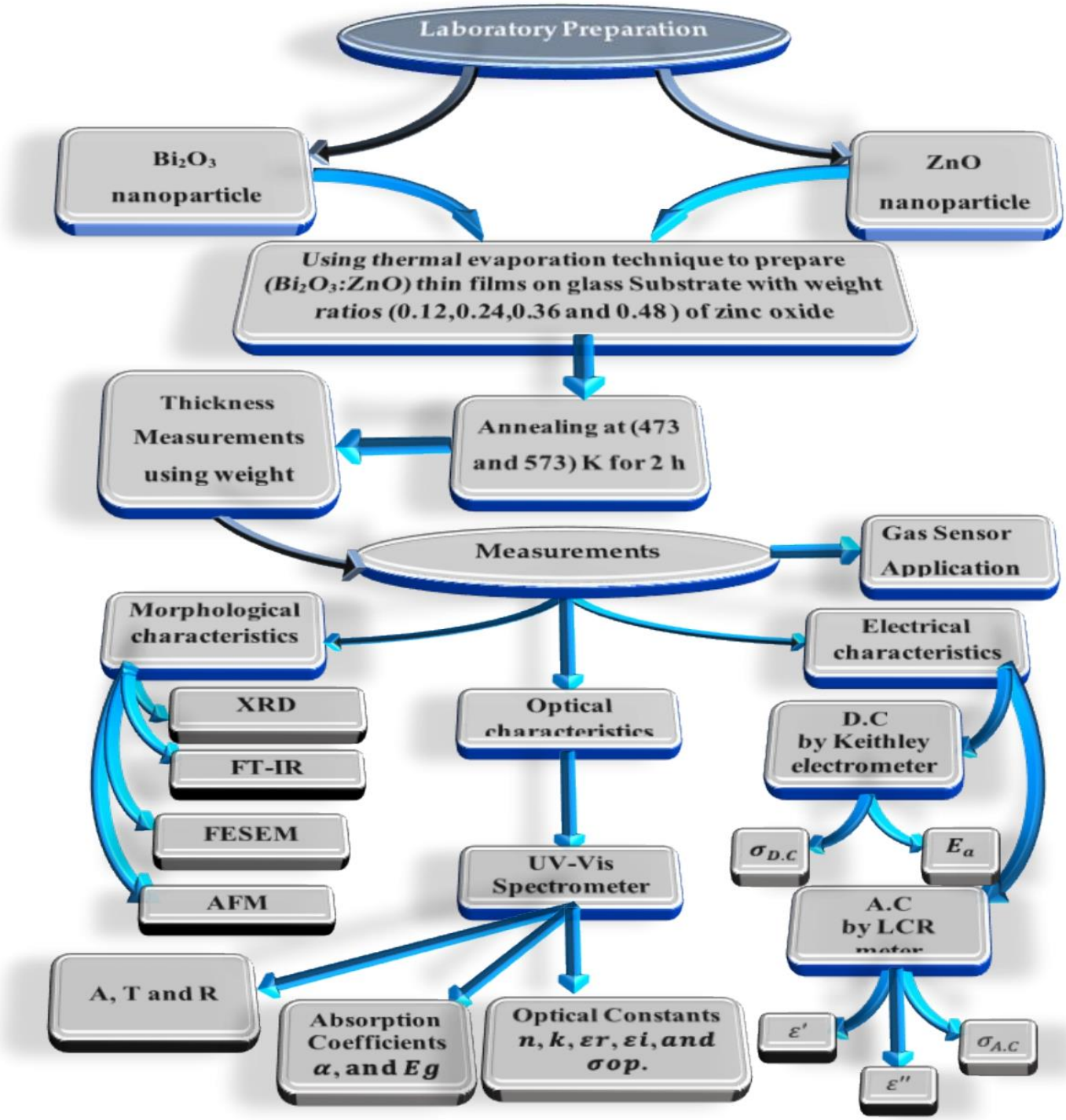

Figure (3.1): Schematic diagram of experimental work.

3.2 Nanomaterial Used

The utilized materials in this study are:

3.2.1 Matrix material

- **Bismuth Oxide (Bi_2O_3) Nanoparticles**

It was obtained as powder form and could be obtained from (Hongwu New Material China) company, with radius (20 - 30) nm and high purity (99.5 %).

3.2.2 Additive material

- **Zinc Oxide Nanoparticles**

It was obtained as powder form and could be obtained from (**Sky Spring Nanomaterials** USA) company, with radius (10 - 30) nm and high purity (99.8%)

3.3 Substrate Preparation

Use of glass substrates to deposit thin films by thermal evaporation. Glass slides each of (2.54 x 7.62) cm^2 and an area of (2 x 2.54) cm^2 were used as 0.1-0.12 cm thick substrates. Following are the procedures that were carried out on these glass slides:

1- Alcohol was used to clean the substrates.
2- The substrates were cleaned ultrasonically for fifteen minutes after being submerged in a clean beaker containing distilled water.
3- In the final step, the glass substrates were dried using an air jet and then rubbed down with some soft paper in preparation for the deposition procedure.

3.4 Evaporation Boat

The most commonly used materials for fumigation boat are metals with a high melting point, such as tungsten (W) (MP = 3370 °C), and molybdenum (Mo) (MP = 2622 °C). In this work, a tungsten vaporization boat was used to vaporize (Bi_2O_3: ZnO), as shown in figure (3.2).

Figure (3.2): Evaporation Boat.

3.5 The Coating Unit

The vacuum unit system is:

1- Edwards Auto 306.

2- In order to heat evaporates, tungsten or molybdenum filaments are used.

3- Ultimate chamber pressure $1x10^{-5}$mbar.

4- Typical filament currents are 100-200 A.

5- Exposes substrate to visible or IR radiation.

6- The maximum thickness of the deposition that can be obtained is 1.5 micrometres.

The main constructions of the typical vacuum coating unit , as shown in figure (3.3).

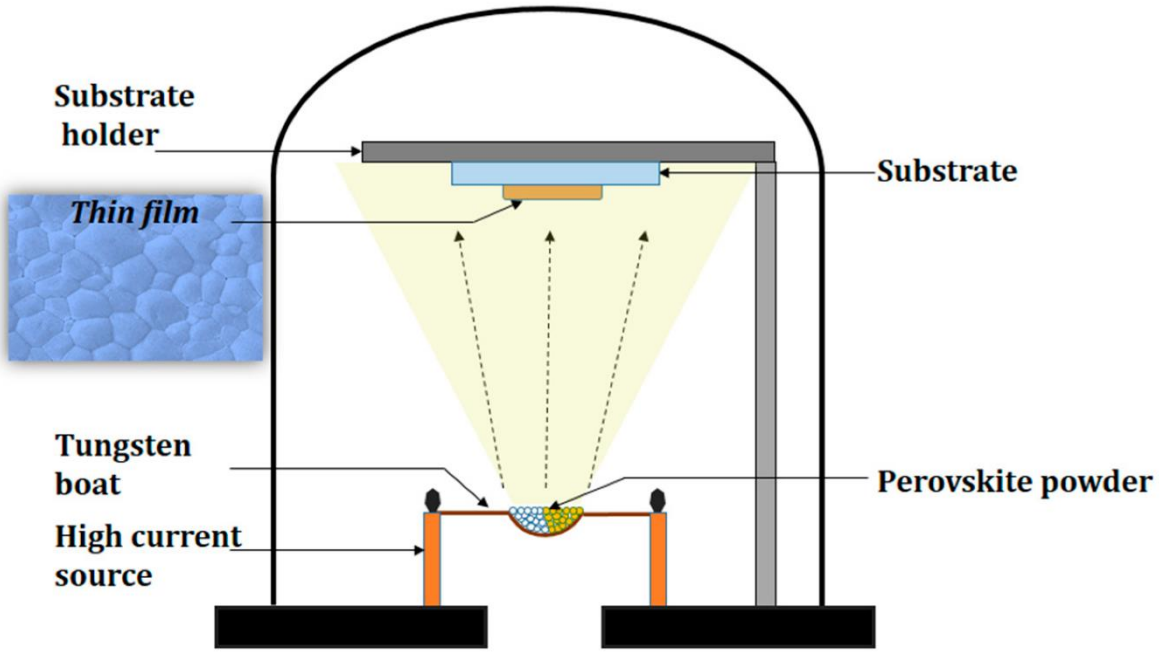

Figure (3.3): Thermal evaporation system.

3.6 Thin Film Growth

The thin films of (Bi_2O_3:ZnO) were obtained. With different weights of (Bi_2O_3:ZnO) according to Table (3-1), The thin films were created using a thermal evaporation method heated by electrical resistance. This method involves sending an electrical current through the boat to generate steam that follows straight paths to the substrate. Generally speaking, there are three steps in any vacuum deposition process, namely creating an evaporator from the source material, transferring the evaporator from the source to the substrate and condensing the evaporator to the substrate to form a precipitated film, as in figure (3.4). In this work, evaporation processes were performed at room temperature (RT). The pressure during evaporation was approximated to 10^{-5} mbar at a sedimentation rate of 0.5 nm. s^{-1}. A constant 15 cm distance between the substrate and the source was maintained.

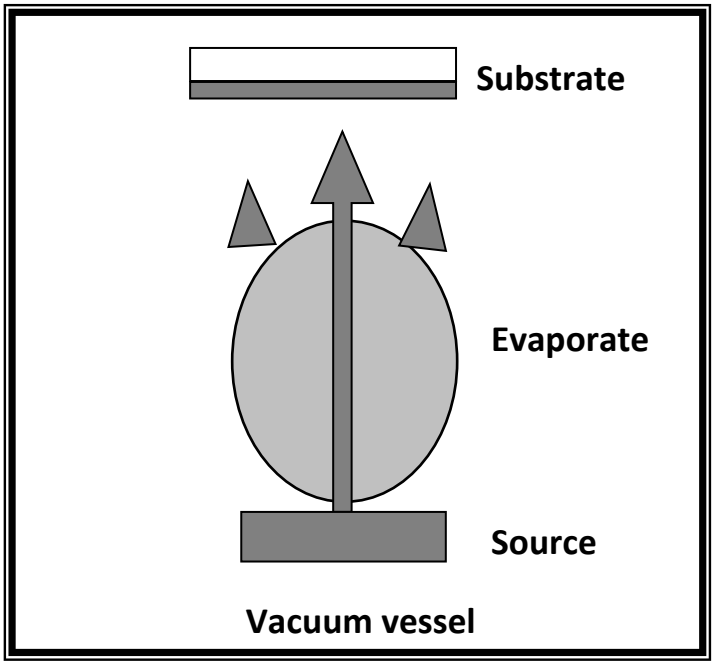

Figure (3.4): Basic steps deposition processes.

Table (3.1): Weight (g) for (Bi_2O_3:ZnO) nanoparticles.

Bi_2O_3 wt	ZnO wt
0.01	0
0.0088	0.0012
0.0076	0.0024
0.0064	0.0036
0.0052	0.0048

3.7 Films Thickness Measurement

One of the most crucial characteristics of a thin films is its thickness. Thin films thickness can be evaluated using a number of different techniques. This study used the optical measurement and weight technique to determine the film thickness.

3.7.1 Optical measurement method

We acquired measurements of the film's thickness using an optical interferometer method. This technique uses the interference that results from the light beam reflecting off the substrate's bottom and the thin layer's surface. We used a He-Ne laser with a wavelength of 632 nm, and the thickness was calculated based on the disparity between the optical path lengths of the two reflections.

3.7.2 The weight method

Thickness of the thin films has been calculated according to the following equation [142]:

$$t = \frac{m}{2\pi\rho R^2} \qquad (3\text{-}1)$$

where:

t: a measure of the thickness of the thin films (nm).

m: mass in (g)

ρ: is the density of material (g/cm^3).

R: is the distance between the substrate and the boat (cm).

This method gives an approximate thickness because not all the material is deposited on the substrate but some of the material lost or fleeing on the sides of the heater.

3.8 Structural and Morphological Measurements

3.8.1 X-ray diffraction (XRD)

The main purpose of these measurements is to investigate the type of the structure of the prepared thin films. This experimental technique has long been used to determine the overall structure of bulk solids, including lattice constants, identification of unknown materials, orientation of single crystals, orientation of polycrystals, defects, stresses, etc. X-ray diffraction using

SHIMADZU X-ray diffracts meter system (XRD-6000) which records the intensity as a function of Bragg's angle, as shown in figure (3.6). Samples were tested in Iran/Tehran. The conditions of the system were: as shown in figure (3.5).

Source CuKα with radiation of wavelength λ = 1.5406 Å.

Target: Cu

Current = 30 mA.

Voltage = 40 kV.

Scanning speed = 0.25 deg/min

the X-ray scans are performed between 2θ values of 10° and 80°.

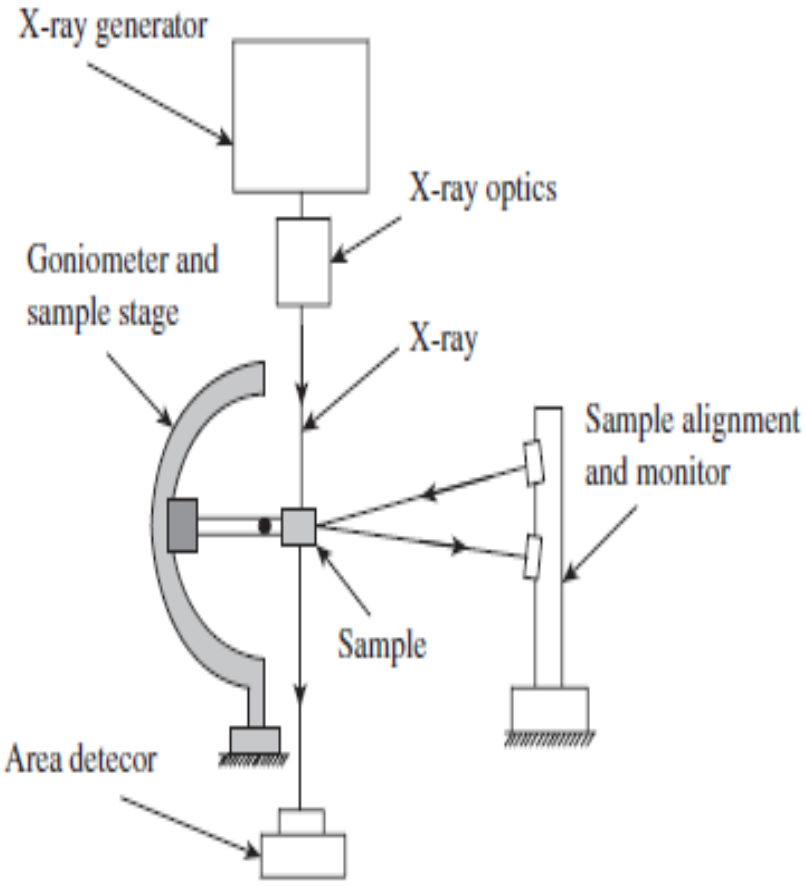

Figure (3.5): The system of XRD.

3.8.2 Fourier transformation-infrared spectroscopy (FTIR)

FTIR spectra were recorded by (Bruker Corporation, German origin, type vertex-70), as shown in figure (3.6). FTIR was carried out at Baghdad University/College of Science/Department of Chemistry. In this study, the range of the studied wave number is (400-4000) cm^{-1}.

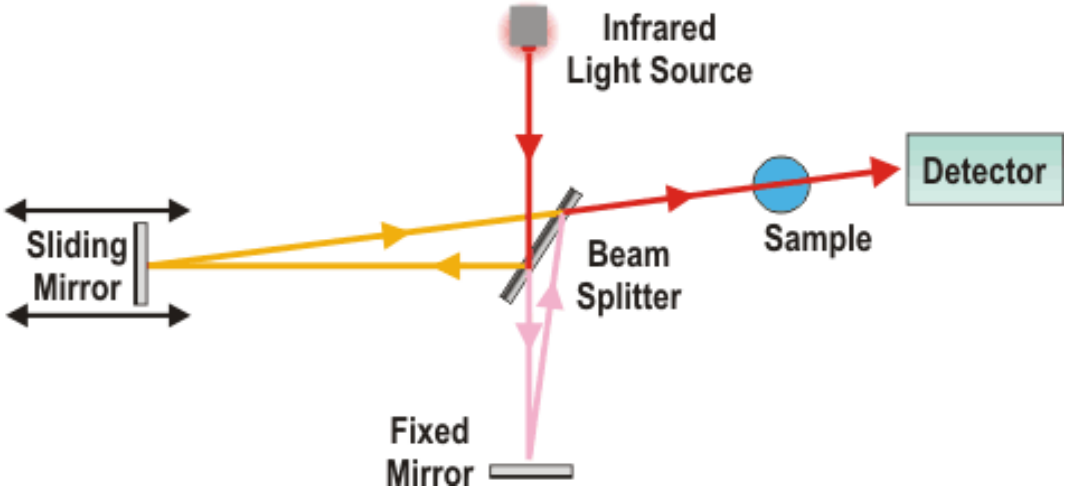

Figure (3.6): Fourier transform infrared spectroscopy

3.8.3 Atomic Force Microscope (AFM)

This instrument is used to take a look on surfaces on a molecular level. It observes the surface roughness and topography of deposited thin films. This device determines the size and other characteristics of the synthesized nanoparticles, an atomic force microscope (AFM) is used, as shown in figure (3.7). The most important part of an atomic force microscope is the tip with its nanoscale radius of curvature. The tip is attached to a micron scale cantilever which reacts to the Van der Waals interaction and other forces between the tip and sample, Samples were tested in University of Babylon/College of Education for Pure Sciences/Department of Physics.

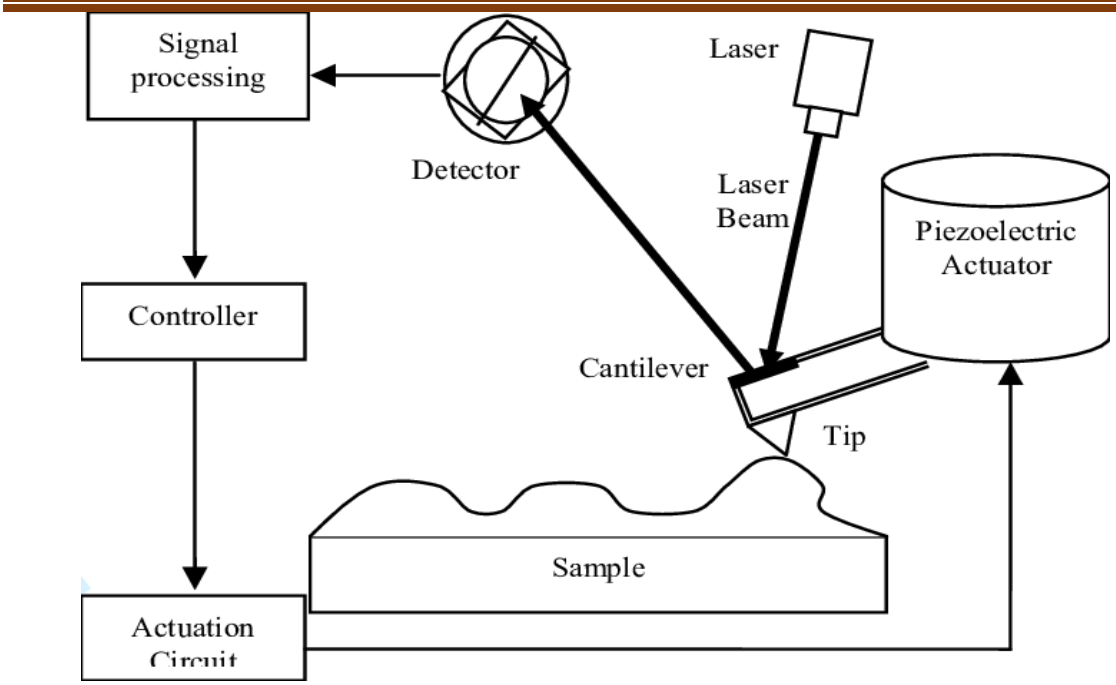

Figure (3.7) The system of AFM.

3.8.4 Scanning electron microscopy (SEM)

A scanning electron microscope (SEM) is an electron microscope that images the surface of a sample by scanning it with a high-energy beam of electrons in a point scanning pattern. SEM test samples must be electrically conductive, at least on the surface, and electrically grounded to prevent the buildup of electrostatic charges on the surface. A small fraction (2 x 2) cm of the sample was taken for examination by SEM, in this work a low vacuum scanning electron microscope was used, as shown in figure (3.8). The surface morphology of the (Bi_2O_3:ZnO) thin films was observed using (Bruker Nano GmbH, company, German original, type vertex 5600 LV SEM) Iran/Tehran.

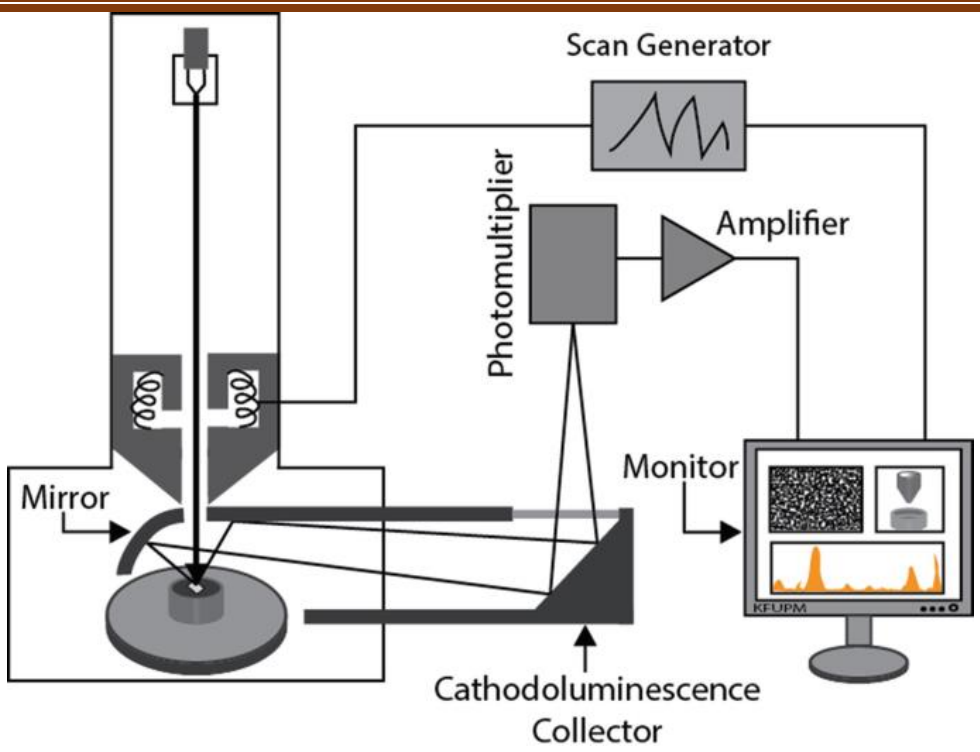

Figure (3.8): Diagram for system of SEM device.

3.9 Optical Properties Measurements

The optical measurements of the Bi_2O_3:ZnO thin films were recorded in the wavelength range (200–1100) nm using a dual-beam spectrophotometer (Shimadzu, UV-1800 A0, Japan), as shown in figure (3.9). The absorption spectrum is recorded at room temperature. A computer program (UV Probe software) was used to obtain the optical constants, absorbance, transmittance, absorption coefficient, extinction coefficient, refractive index, optical conductivity, and dielectric constant (real and imaginary parts), allowing direct allowed and forbidden transmission and energy gap, Samples were tested in University of Babylon/College of Education for Pure Sciences/Department of Physics.

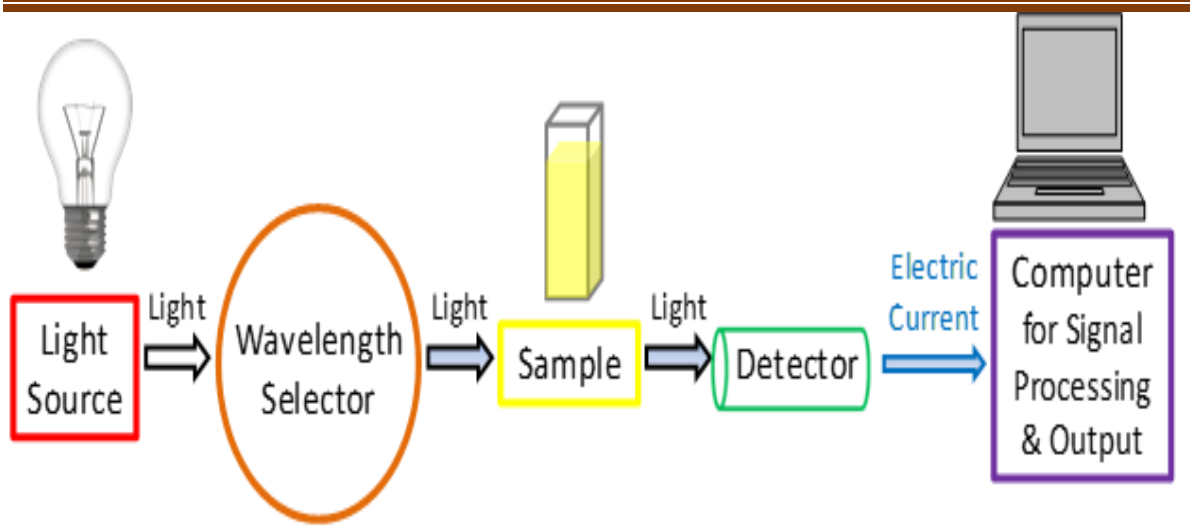

Figure (3.9): UV photographic of spectrophotometer.

3.10 Measurement of A.C. Electrical Conductivity

The electrical conductivity in alternating current was measured with a type LCR meter (**HIOKI 3532-50 LCR Hi TESTER (Japan)**). The sample was taken and connected to the two electrodes of the device at different frequencies (100Hz-5MHz) at room temperature, as shown in figure (3.10). The amplitude and dispersion factor were recorded for all samples. The dielectric constant, dielectric loss and conductivity were calculated from these data, Samples were tested in University of Babylon/College of Education for Pure Sciences/Department of Physics.

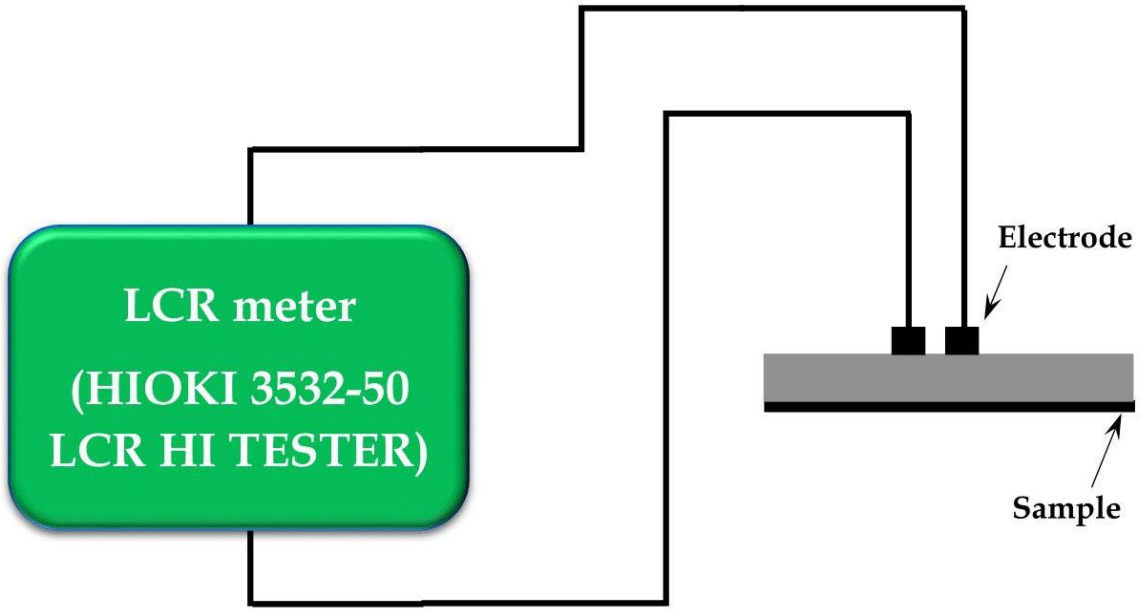

Figure (3.10): LCR Hi TESTER device

3.11 Measurement of D.C. Electrical Conductivity

The electrical conductivity of DC is calculated by measuring the electrical resistance of DC at temperatures between (30-150) degrees Celsius. The sample was placed in the oven and the electrical resistance was recorded, as shown in figure (3.11). The resulting data were taken from a Keithley electrometer (type 2400 source) for different temperatures at the University of Babylon / College of Education for Pure Sciences / Department of Physics.

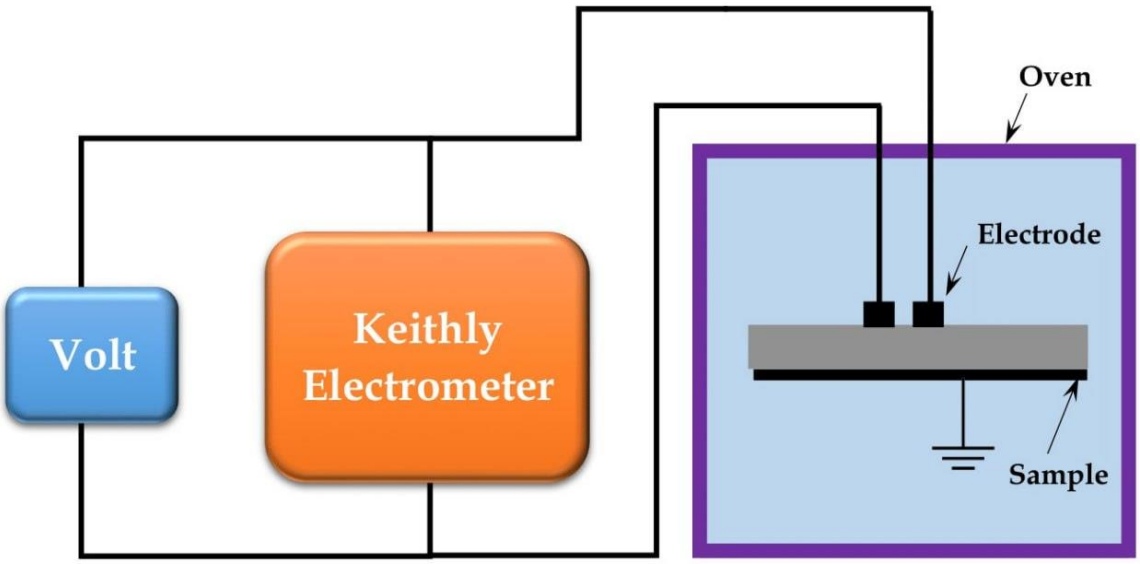

Figure (3.11): Diagram for system of D.C electrical measurement system.

3.12 Gas Sensors Application Measurements

A suitable setup is constructed to determine the sensitivity parameter of the fabricated (H_2S and NO_2) gas sensor detector. This determination focuses primarily on the detector's response time and recovery time. Figure (3.12) depicts the gas sensor testing system, which includes the following components: a cylindrical test chamber made of stainless steel, measuring 30 centimetres in circumference and 35 centimetres in height. The chamber has an effective capacity of 6594 cc. It is equipped with an inlet that lets the gas being tested flow into it and an air admittance valve that lets atmospheric air flow back in after the chamber has been evacuated. The electrical connections that need to be made to the heater, thermocouple, and sensor electrodes can be made thanks to a multi-pin feedthrough at the bottom of the container. Inside the chamber is where you will find the heater, comprised of a thermocouple and a heated plate. Its purpose is to maintain a consistent operating temperature for the sensor. APC-interfaced digital multimeter of type UNI-T UT81B, and Laptop PC, is used to register the variation of the sensor current. The mixing gas is fed by zero

air and test gas through a flow meter and needle valve arrangement. The mixing gas is feeding through a tube over the sensor inside the test chamber to give the real sensitivity. The samples were examined at the University of Baghdad / College of Science / Department of Physics.

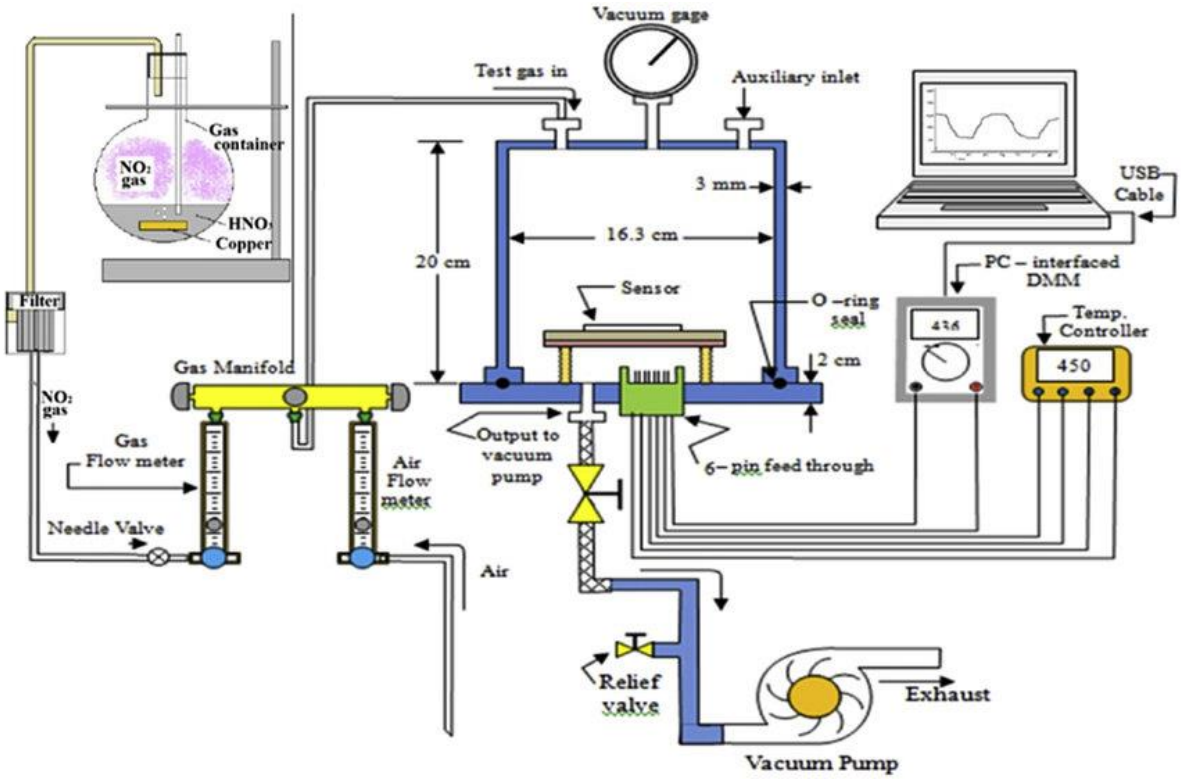

Figure (3.12): A photo of gas sensor testing system

4.1 Introduction

This chapter presents the results and discussion of the structural, morphological, optical and electrical properties of pure Bi_2O_3 and ZnO-doped Bi_2O_3 with different ZnO ratios and the effect of annealing on the prepared thin films. On the other hand, this chapter includes the results and their discussion of the effect of temperature difference on the electrical conductivity of DC and AC electrical measurements of (Bi_2O_3:ZnO) thin film. This chapter also studies thin films as gas sensors.

4.2 Structural and Morphological Properties

4.2.1 X– ray diffraction analysis

The XRD spectra of pure and ZnO-doped Bi_2O_3 thin film with different ratios of ZnO (0.12, 0.24, 0.36 and 0.48) wt.% prepared by thermal evaporation technique at RT under pressure up to 1×10^{-5} mbar with rate of deposition 0.5 nm. sec^{-1} was annealed at (473 and 573) K temperatures for 2 hours and thicknesses of 50 ±5 nm. Peaks of XRD were recorded between 10^o - 80^o.

The XRD pattern for pure and ZnO-doped Bi_2O_3 thin films is shown in figures (4.1), (4.2). One peak attributed to diffraction from the surface $(\bar{1}21)$ was observed in most cases of XRD spectra for the sample deposited at room temperature, which corresponds to the position $2\Theta = 27.45^o$ for pure Bi_2O_3 at a temperature 473 K, which is in good agreement with the standard value 27.41^o at a temperature 573 K, taken from the Joint Committee of Powder Diffraction Standard (JCPDS) card file data (79-2205) [143].

The presence of a diffraction peak of (001), which corresponds to the position $2\Theta = 31.72^o$ for pure ZnO, which is in good agreement with the standard value of 31.77^o, respectively taken from the Joint Commission on Powder Diffraction Standard (JCPDS) Card File Data (36-1451) [144]. This indicates that the pure Bi_2O_3 doped with ZnO films prepared by

thermal evaporation technique shows a hexagonal wurtzite-type crystal structure, and this behavior is from increasing the degree of crystallinity of the films. The test results were tabulated in Tables (4.1),(4.2) and (4.3). The results were in agreement with the research [145]. The intensity of the $(\bar{1}21)$ peak decreases with the increasing in the ZnO ratio.

The presence of a diffraction peak of $(\bar{1}21)$ indicates that films have a $(\bar{1}21)$ preferred orientation at a temperature of 473 K and 573 K, which corresponds to the position $2\Theta = 27.45$ and $2\Theta = 27.41$ for pure Bi_2O_3, that is only a $(\bar{1}21)$ diffraction peak is detected in the films. This indicates that pure Bi_2O_3 and doped with ZnO films prepared by thermal evaporation technique show a good (a,b and c) axis orientation to the substrate with a monoclinic wurtzite-type crystal structure and this behavior of the increases degree of crystallinity of films. The results are in good agreement with the researche [146,147].

Generally, it can be noticed from such figures that the distinct diffraction peaks decreases with increasing annealing temperatures, which leads to an increasing in the crystallite size, as evaluated in Tables (4.1) and (4.2). Additionally, the values of dislocation density (δ), microstrain (ε) and number of layers (N) of (Bi_2O_3:ZnO) films follow the change that has accompanied the crystallite size under the influence of annealing temperatures and thicknesses, which is summarized in Table (4.3).

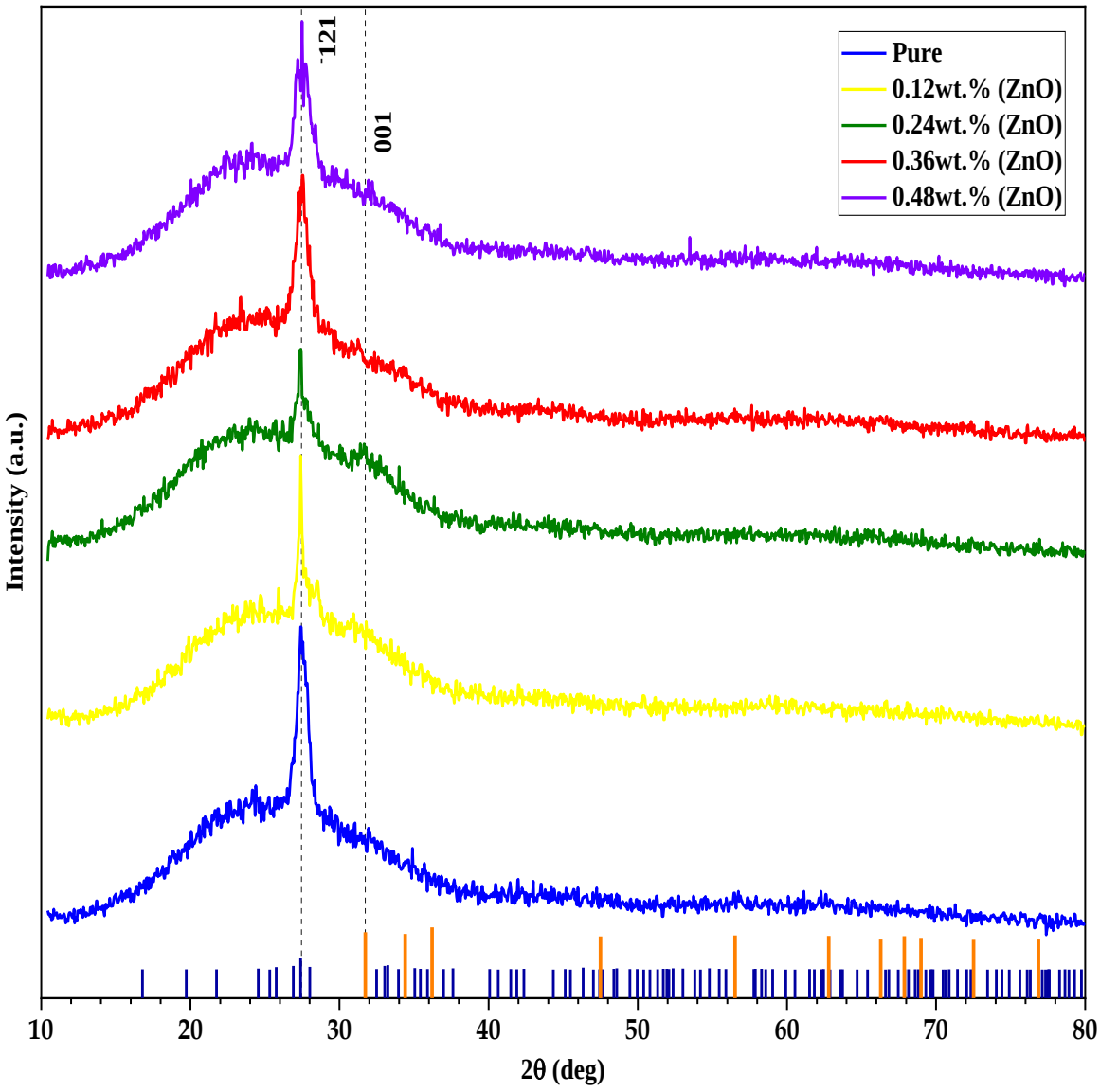

Figure (4.1): The XRD spectrum of Bi_2O_3 and (Bi_2O_3:ZnO) thin films at temperature 473K.

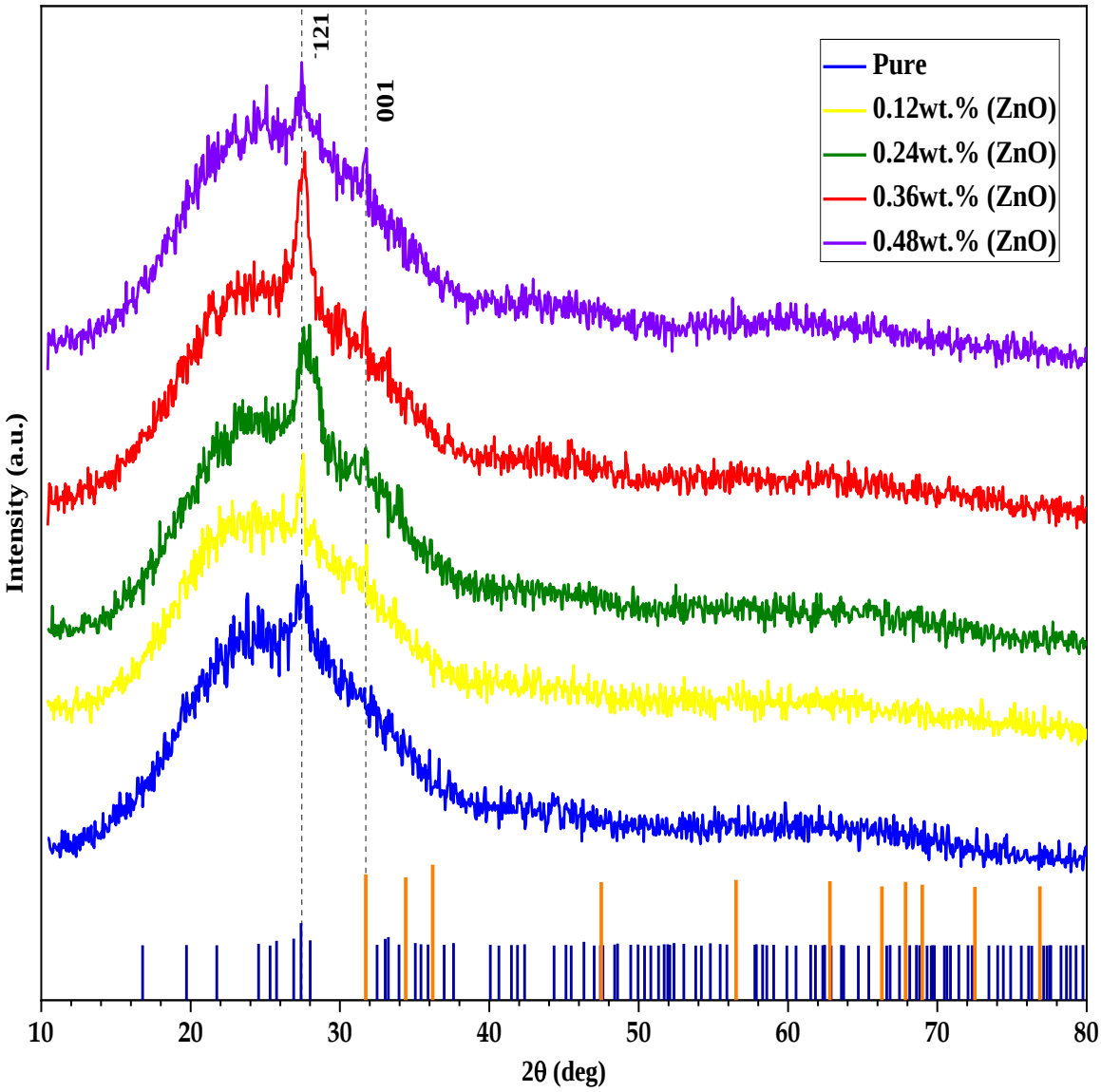

Figure (4.2): The XRD spectrum of Bi_2O_3 and (Bi_2O_3:ZnO) thin films at temperature 573K.

Table (4.1): The obtained result of the XRD for (Bi_2O_3:ZnO) thin films at an annealing temperature of 473K.

T(K)	Sample No.	hkl	$2\theta^0$	d-spacing (A^0)	β^0	D (nm)
473 K	Pure (Bi_2O_3)	$(\bar{1}21)$	27.41323	3.25358	0.492	17.34853
	0.12 wt.% ZnO	$(\bar{1}21)$	27.54140	3.23605	0.960	8.89355
	0.24 wt.% ZnO	$(\bar{1}21)$	27.41140	3.25379	0.984	8.67423
	0.36 wt.% ZnO	$(\bar{1}21)$	27.52922	3.23745	0.840	10.16380
	0.48 wt.% ZnO	$(\bar{1}21)$	27.40939	3.25403	0.984	8.67419
	0.12 wt.% ZnO	(001)	31.63651	2.77130	0.154	56.14697
	0.24 wt.% ZnO	(001)	31.65120	2.78291	0.128	67.37881
	0.36 wt.% ZnO	(001)	31.74012	2.78031	0.154	56.16138
	0.48 wt.% ZnO	(001)	31.78714	2.78419	0.307	28.08397

Table (4.2): The obtained result of the XRD for (Bi_2O_3:ZnO) thin films at an annealing temperature of 573K.

T(K)	Sample No.	hkl	$2\theta^0$	d-spacing (A^0)	β^0	D (nm)
573 K	Pure (Bi_2O_3)	(-121)	27.45902	3.24557	0.960	8.89199
	0.12% ZnO	(-121)	27.54140	3.23605	0.960	8.89355
	0.24%(Bi_2O_3:ZnO)	(-121)	27.61877	3.22716	0.960	8.89503
	0.36%(Bi_2O_3:ZnO)	(-121)	27.66274	3.22213	0.840	10.16670
	0.48%(Bi_2O_3:ZnO)	(-121)	27.64635	3.22400	1.920	4.44778
	0.12%(Bi_2O_3:ZnO)	(001)	31.63651	2.77130	0.154	56.14697
	0.24%(Bi_2O_3:ZnO)	(001)	31.65120	2.78291	0.128	67.37881
	0.36%(Bi_2O_3:ZnO)	(001)	31.74012	2.78031	0.154	56.16138
	0.48%(Bi_2O_3:ZnO)	(001)	31.78714	2.78419	0.307	28.08397

Table (4.3): Values of number of layers, dislocation density and micro strain of (Bi_2O_3:ZnO) thin films an annealing temperature of 473K and 573K.

(T) K	Sample No.	Number of layers	Dislocation density	Micro strains
		$N_l \times 10^8$ (m^{-2})	δ (m^{-2})	Ɛ
473 K	Pure (Bi_2O_3)	0.000958	0.003323	0.008802
	0.12 wt.% ZnO	0.007108	0.012643	0.017091
	0.24 wt.% ZnO	0.007661	0.013290	0.017605
	0.36 wt.% ZnO	0.004762	0.009680	0.014962
	0.48 wt.% ZnO	0.007661	0.013291	0.017606
573 K	Pure (Bi_2O_3)	0.007112	0.012647	0.017145
	0.12 wt.% ZnO	0.007108	0.012643	0.017091
	0.24 wt.% ZnO	0.007104	0.012639	0.017042
	0.36 wt.% ZnO	0.004758	0.009675	0.014887
	0.48 wt.% ZnO	0.056825	0.050549	0.034048

4.2.2 Fourier transforms infrared analysis (FTIR)

The FTIR spectra of (Bi_2O_3:ZnO) thin film at room temperature in the range (400-4000) cm^{-1} with the various ratios of (ZnO) nanoparticles are shown in figures (4.3) and (4.4). Bands of vibrational stretching and bending were observed in the spectra, characteristic of the functional groups produced in thin films. The band at 3421.48 cm^{-1} is identified as the stretching vibration of the hydroxyl group (O - H), which is common in oxide glasses because water is trapped during manufacturing. The absorption bands of the O–Bi and O–Zn asymmetrical stretching vibrations at about 1126.35 cm^{-1} and 1421.44cm^{-1} and 1575.73cm^{-1} can be noticed as the Bi_2O_3 loading in the thin film increases specifically, as shown in the table (4.4), Overlapping stretching vibrations of Bi–O bonds of BiO_6

coordination octahedra and Zn–O bonds account for the bands in the area from 649.97 cm^{-1} into 923.84 cm^{-1} [146].

1- The higher the layer density, the more atoms and ions there are in the light path, which raises the absorption peaks before and after adding (ZnO).
2- The result FTIR shows, the slight change in the intensity of some absorption bands, these elements also cause visible changes in the spectral features of the samples. These slight banding changes are likely related to defects caused by the change transfer interaction between the individual particles of the nanomaterials. Through the bonding sites, it was also found that there was no chemical interaction between the prepared materials.

These results are similar to the results that are reported by the previous researchers [147].

Table (4.4): Patterns of Molecular Vibrations of (Bi_2O_3:ZnO) thin films an annealing temperature of 473K and 573K.

Vibrational	**Wave Number (cm^{-1})**	**Function Groups**
Hydroxy group, H-bonded OH stretch (broad)	3421	O – H
Carboylic acid or Keton stretch	1126.35	O – Bi O –Zn
Alkenyl stretch	1421.44	O – Bi O –Zn
Aromatic ring stretch	1575.73	O – Bi O –Zn
Epoxy and oxirane rings stretch	923.84	O – Bi O –Zn
Aromatic out-of-plane bend (several)	649.97	O – Bi O –Zn

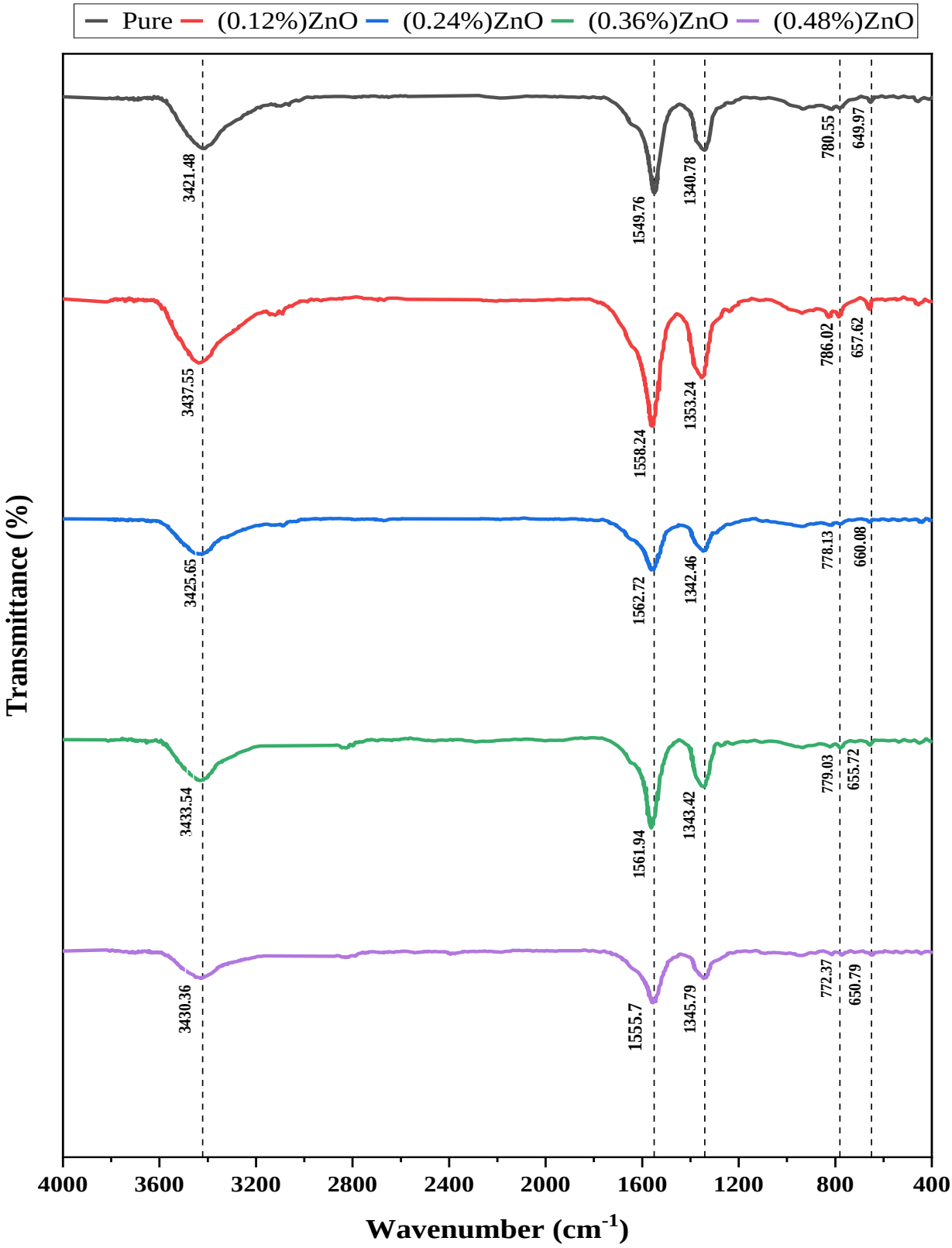

Figure (4.3): FTIR spectra of Bi_2O_3-based optical limiting filters ZnO NPs at 473K.

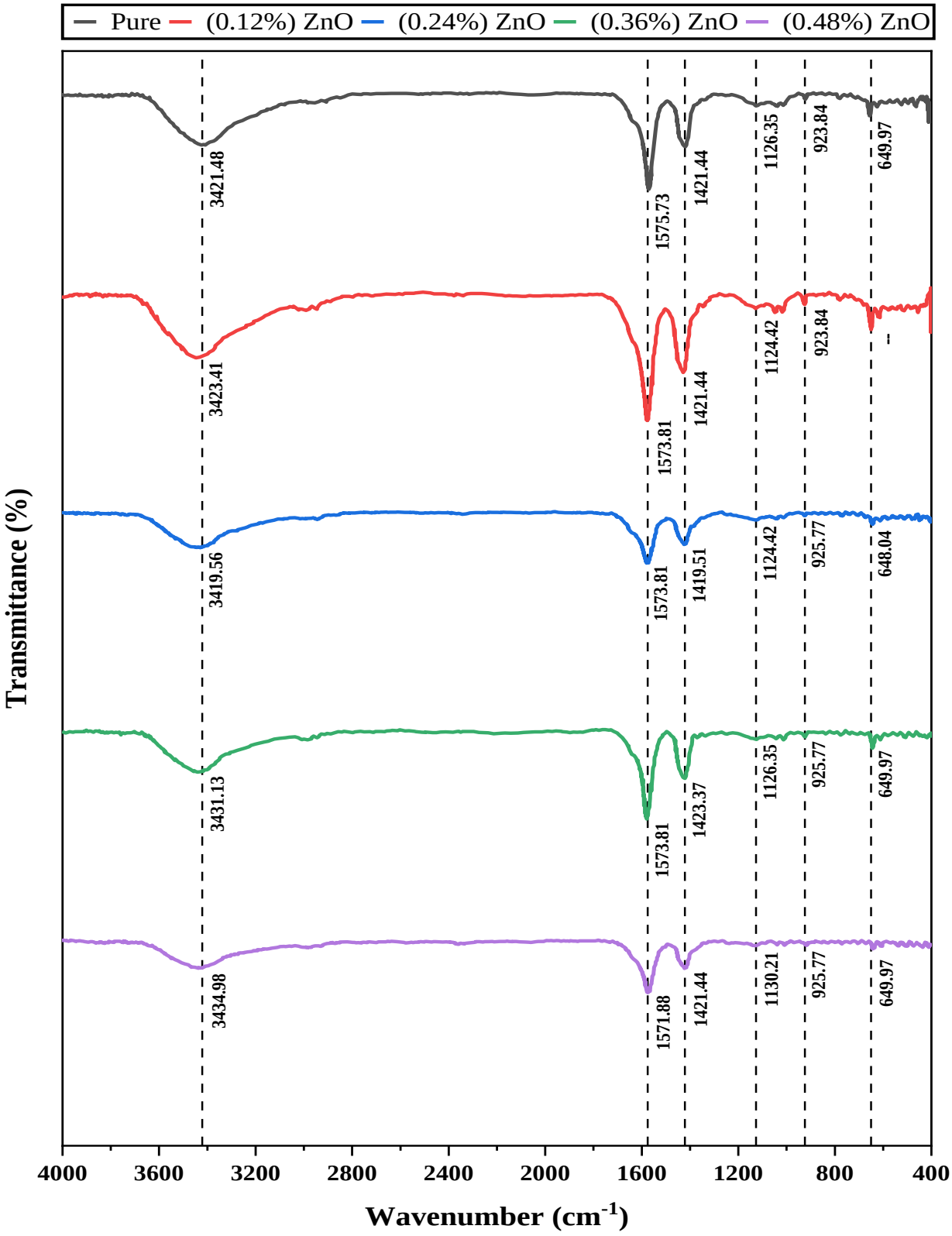

Figure (4.4): FTIR spectra of Bi_2O_3-based optical limiting filters ZnO NPs at 573K.

4.2.3 Atomic force microscope (AFM)

Studying microscopic examination to research the surfaces of thin films materials that have been deposited. The atomic force microscope (AFM) is an important piece of equipment for producing an illustrative picture of the distribution of the particle size of the crystal on the surface, as well as for calculating the thickness of the film, roughness, and grain size. It is possible to investigate, with the help of AFM, how various parameters such as thickness, temperature, preparation technique, and so on affect the qualities of the film material that is deposited [56].

The surface morphology of the (Bi_2O_3:ZnO) thin films was studied by pressing in the AFM mode as a function of annealing temperatures. Typical 2D and 3D thickness and schematic diagram of the distribution of growth grain clusters on the surfaces of deposited (Bi_2O_3:ZnO) thin films with a thickness of (50 ±5) nm, as shown in Figures (4.5), (4.6), (4.7), (4.8) and (4.9) at an annealing temperature of 473 K, as for figures (4.10), (4.11), (4.12), (4.13) and (4.14) the annealing temperature is 573 K. The white areas in the figures above represent the formation of agglomerated granules one above the other. Neighboring grains aggregate to form large clusters for these regions. Therefore, the granules in the white areas are larger in size compared to the others. From these observations, the film growth mechanism is believed to consist of the first layer and then islet-type growth [58].

The images of all the (Bi_2O_3:ZnO) thin films show a uniform granular surface topographic, and it could find the grains are uniform distribution over the glass substrates without any cracks. The roughness and root mean square RMS (it represents total highs surface and lows squared divided by the sum of the number all under the square root, which describes the surface roughness rate higher) values of films are increases with increasing annealing temperature at different values 473 and 573 K

within the same thickness. The increase of root means square increases crystalline growth in the vertical direction more than horizontal direction [150]. The film crystallites become larger, and consequently, the surface roughness and surface thickness are larger [151]. The surface thickness rate value represents the thickness of the film surface roughness, which accounts for the highest crystalline granular tops on the surface. The test results were tabulated in Table (4.5). These results are consistent with previous studies that showed increased roughness and RMS with increasing annealing time [150].

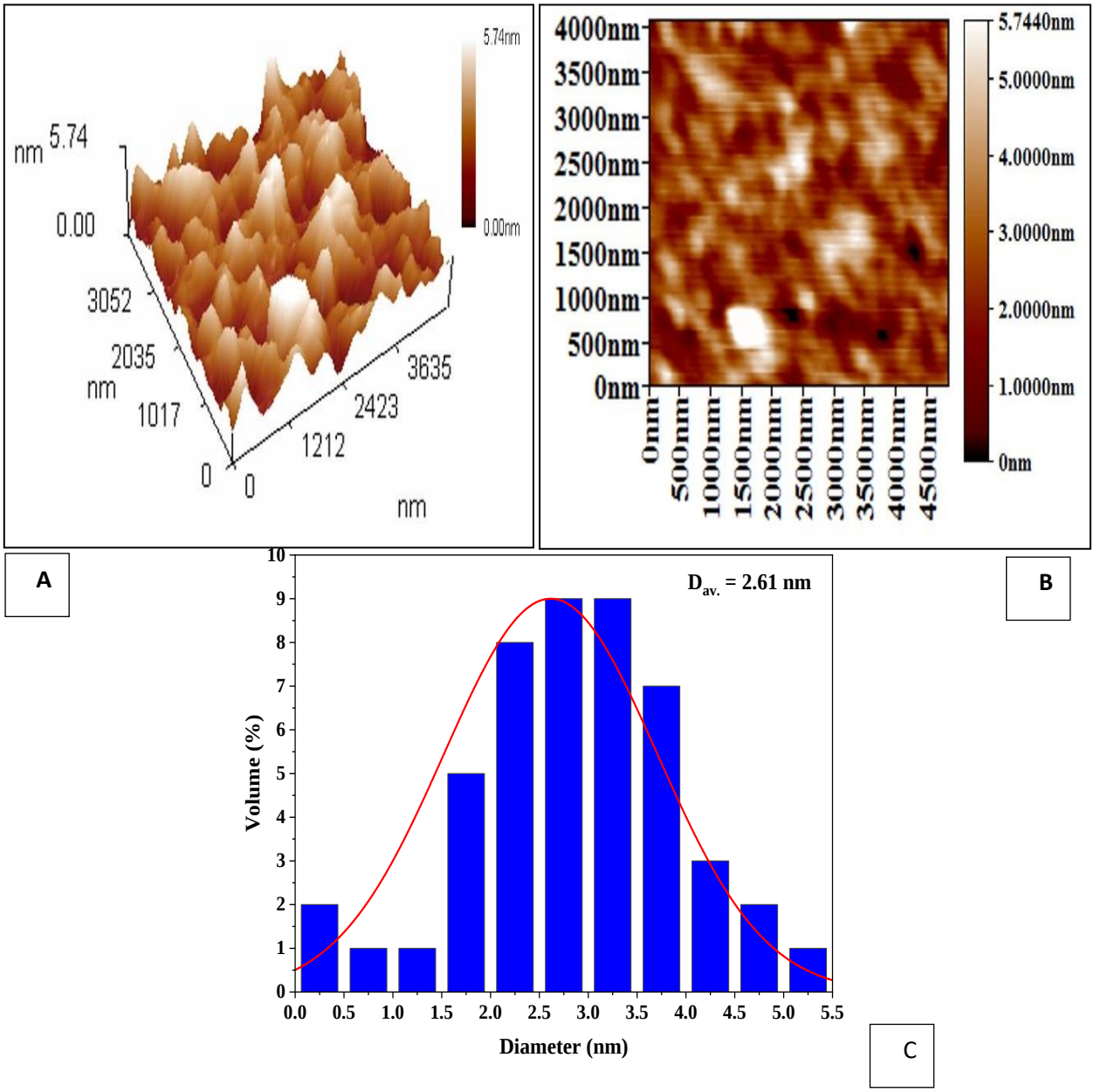

Figure (4.5): AFM surface morphology of Bi_2O_3 thin films pure a) 3-D, b) 2-D, and c) granularity distribution at 473 K.

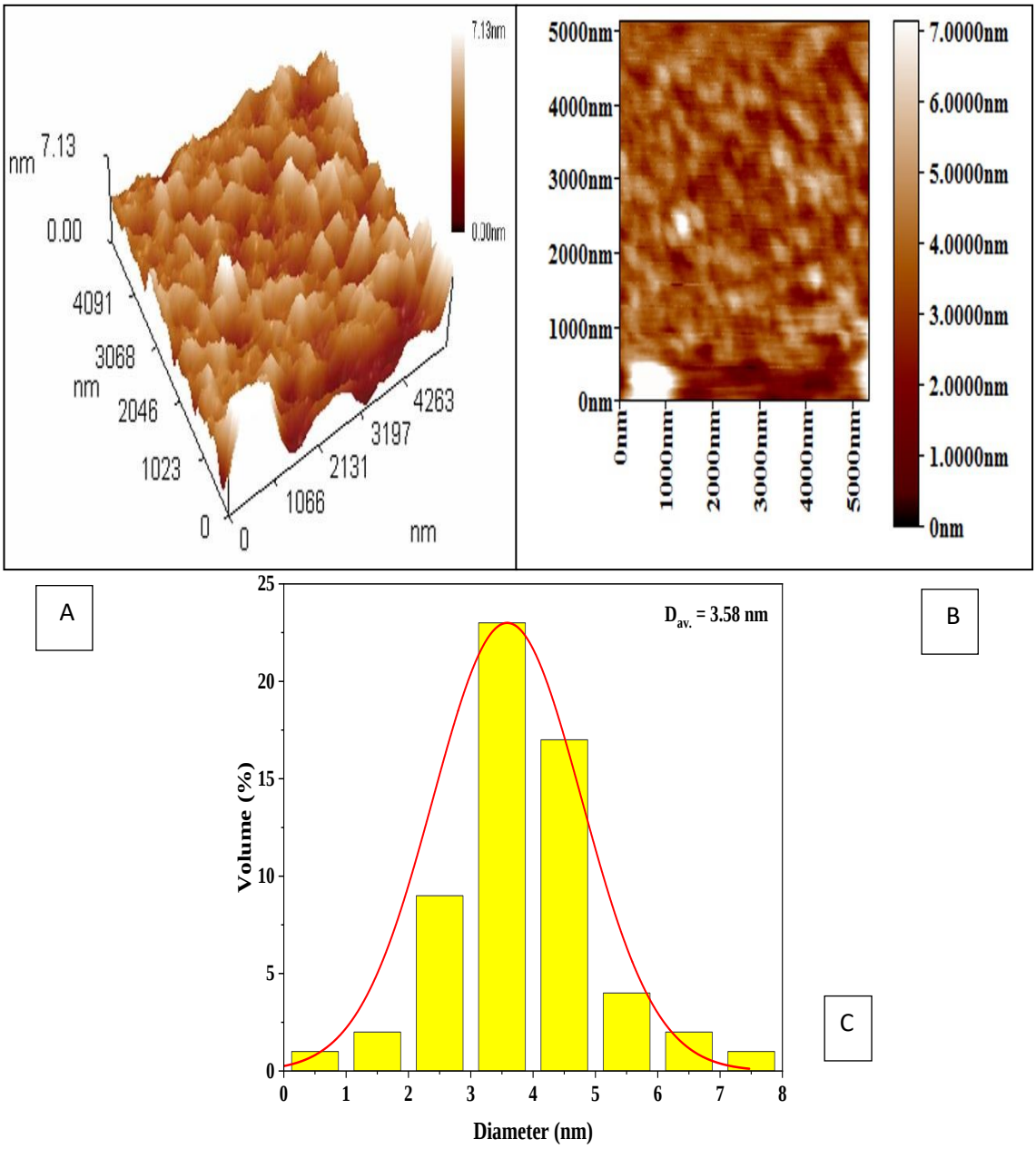

Figure (4.6): AFM surface morphology of (Bi_2O_3:ZnO) thin film for a concentration of 0.12 wt.% (ZnO) NPs a) 3-D, b) 2-D, and c) granularity distribution at 473 K.

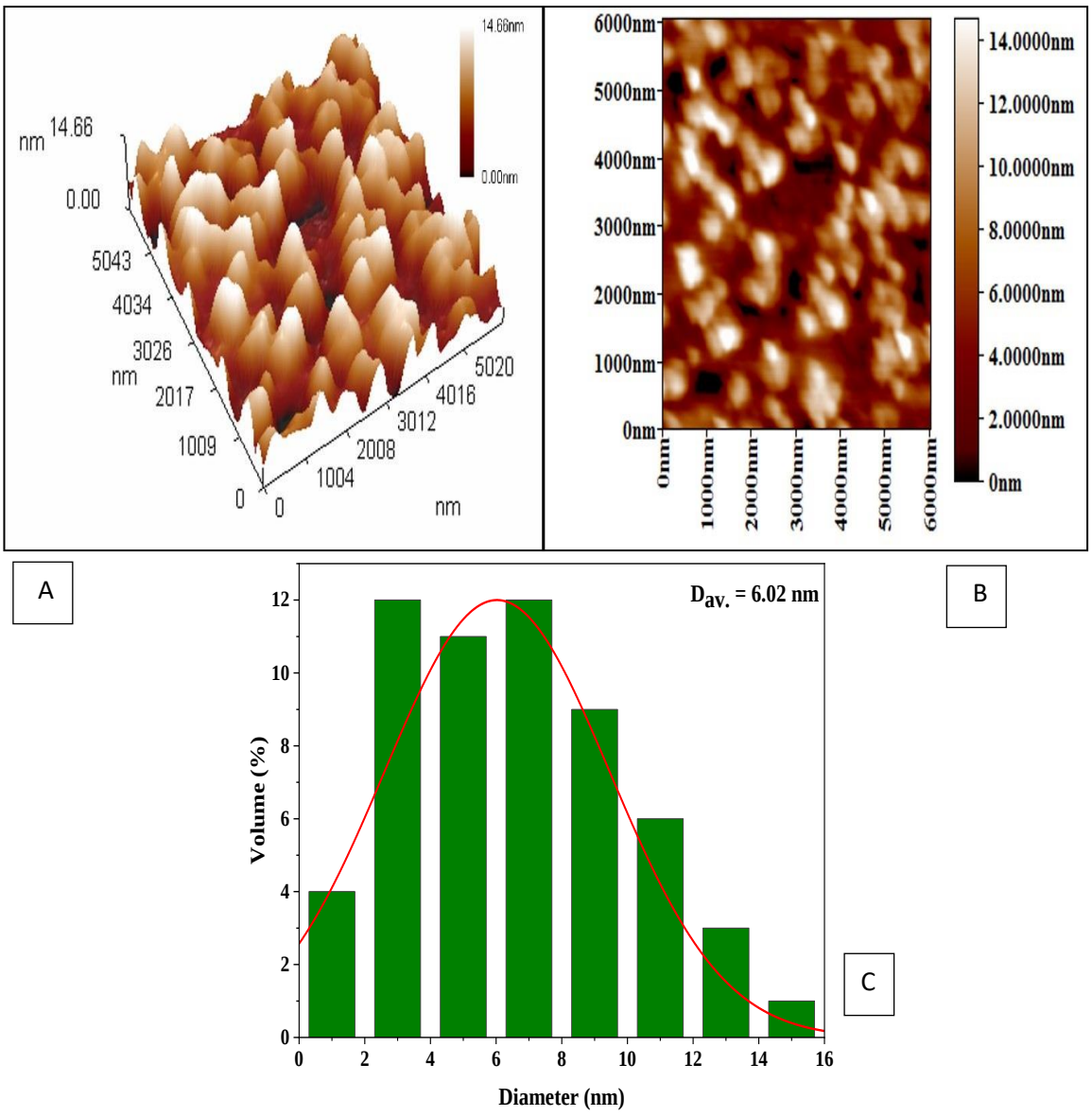

Figure (4.7): AFM surface morphology of (Bi_2O_3:ZnO) thin film for a concentration of 0.24 wt.% (ZnO) NPs a) 3-D, b) 2-D, and c) granularity distribution at 473 K.

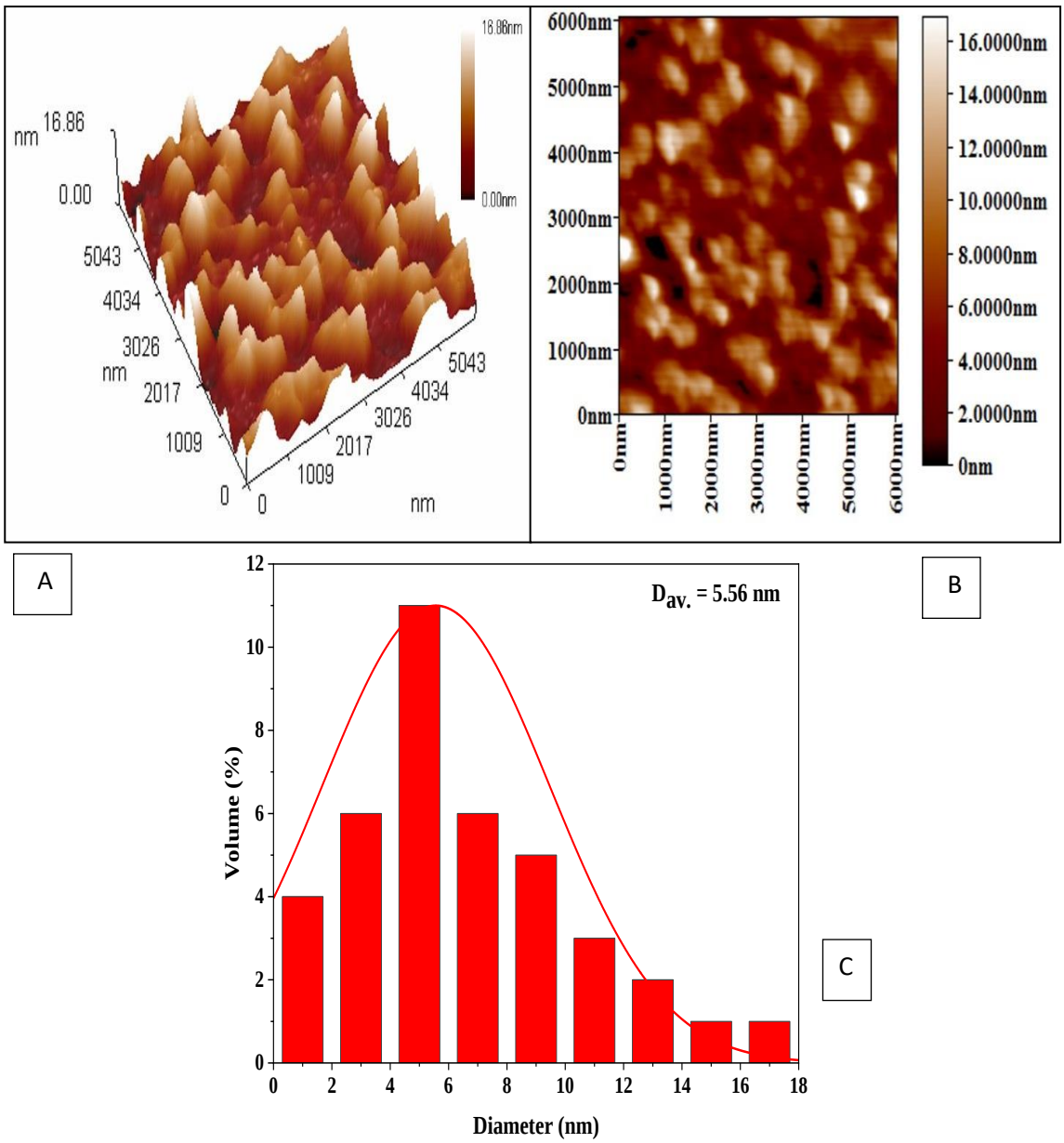

Figure (4.8): AFM surface morphology of (Bi_2O_3:ZnO) thin film for a concentration of 0.36 wt.% (ZnO) NPs a) 3-D, b) 2-D, and c) granularity distribution at 473 K.

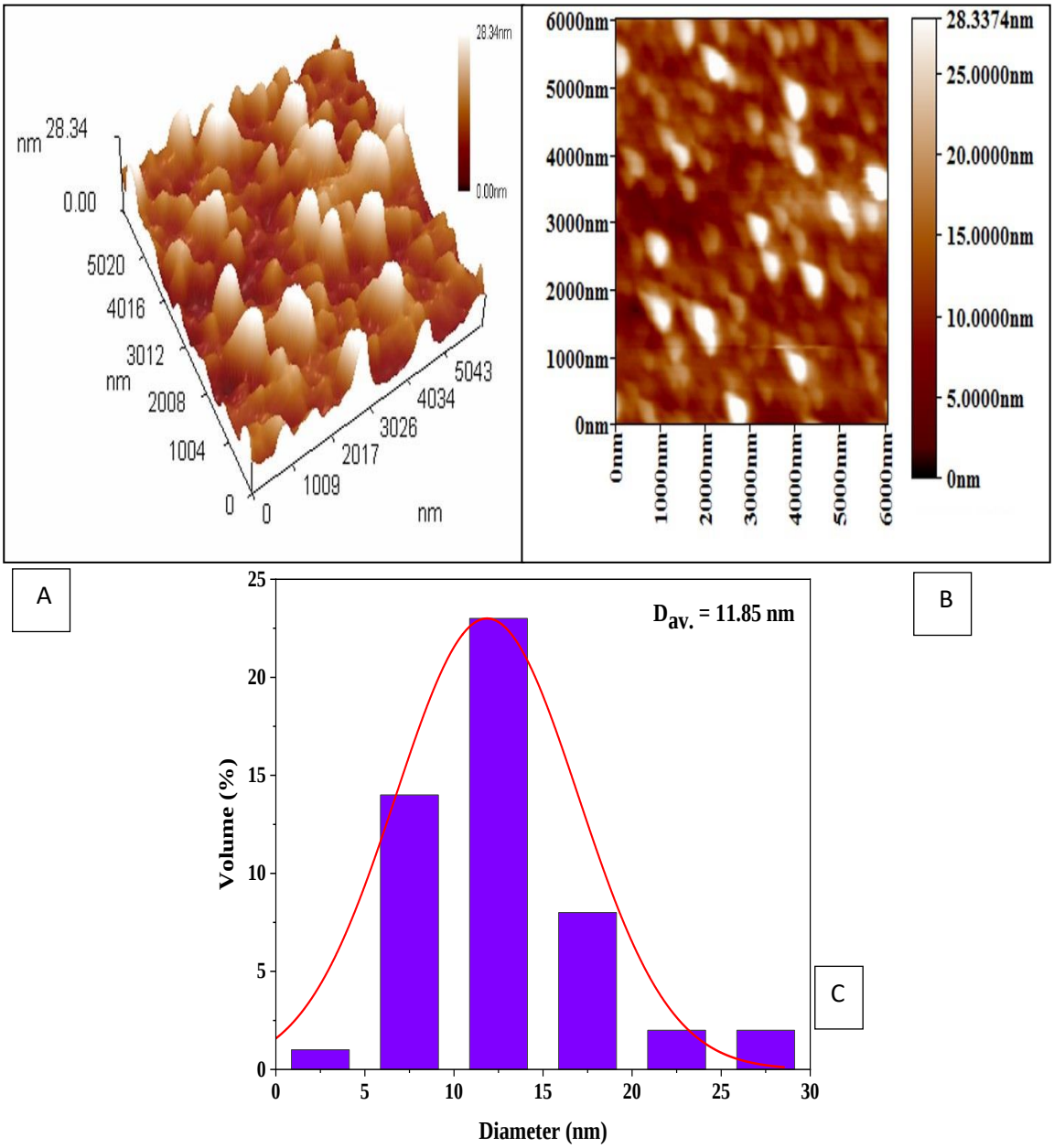

Figure (4.9): AFM surface morphology of (Bi_2O_3:ZnO) thin film for a concentration of 0.48 wt.% (ZnO) NPs a) 3-D, b) 2-D, and c) granularity distribution at 473 K.

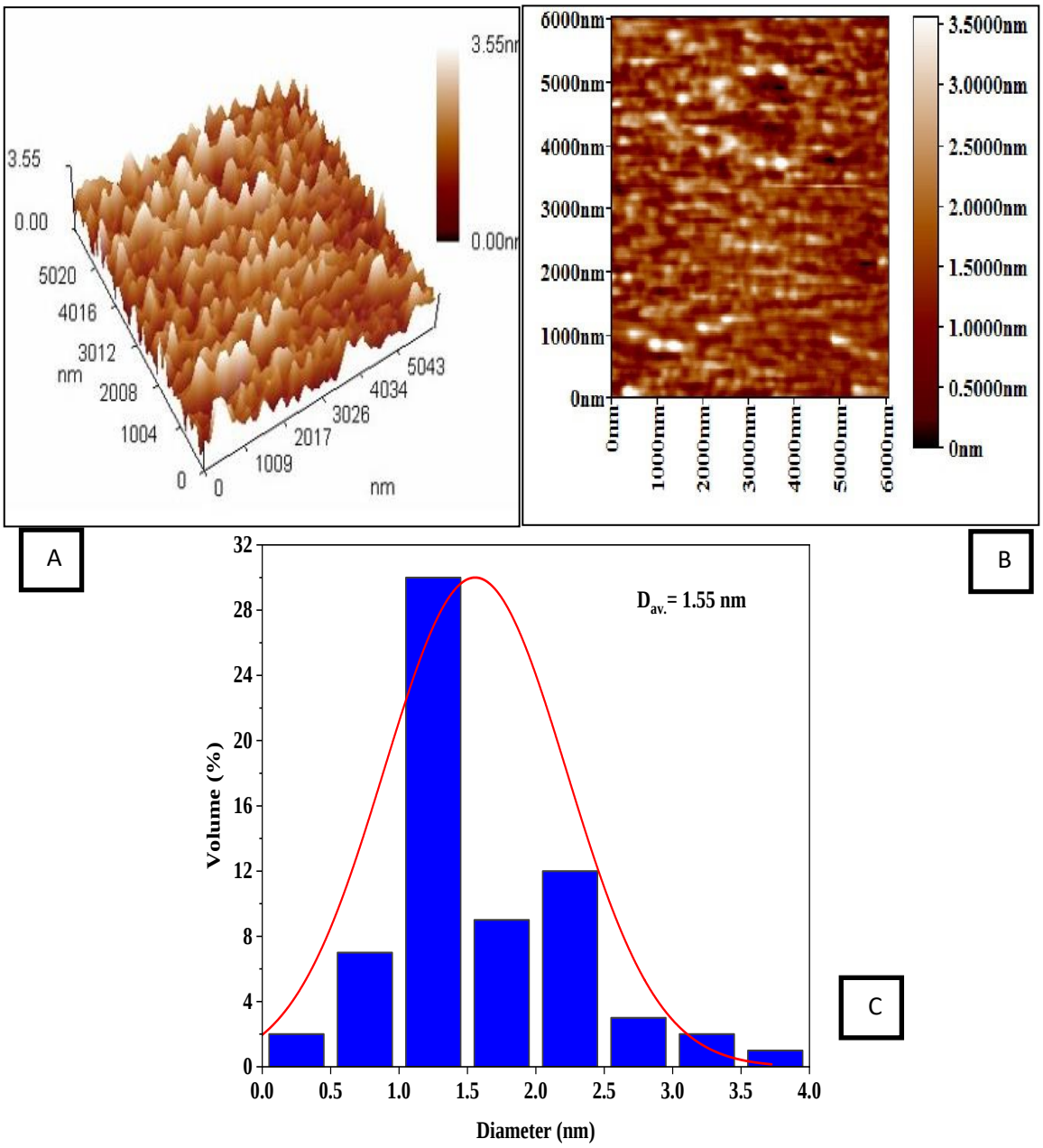

Figure (4.10): AFM surface morphology of Bi_2O_3 thin films pure a) 3-D, b) 2-D, and c) granularity distribution at 573 K.

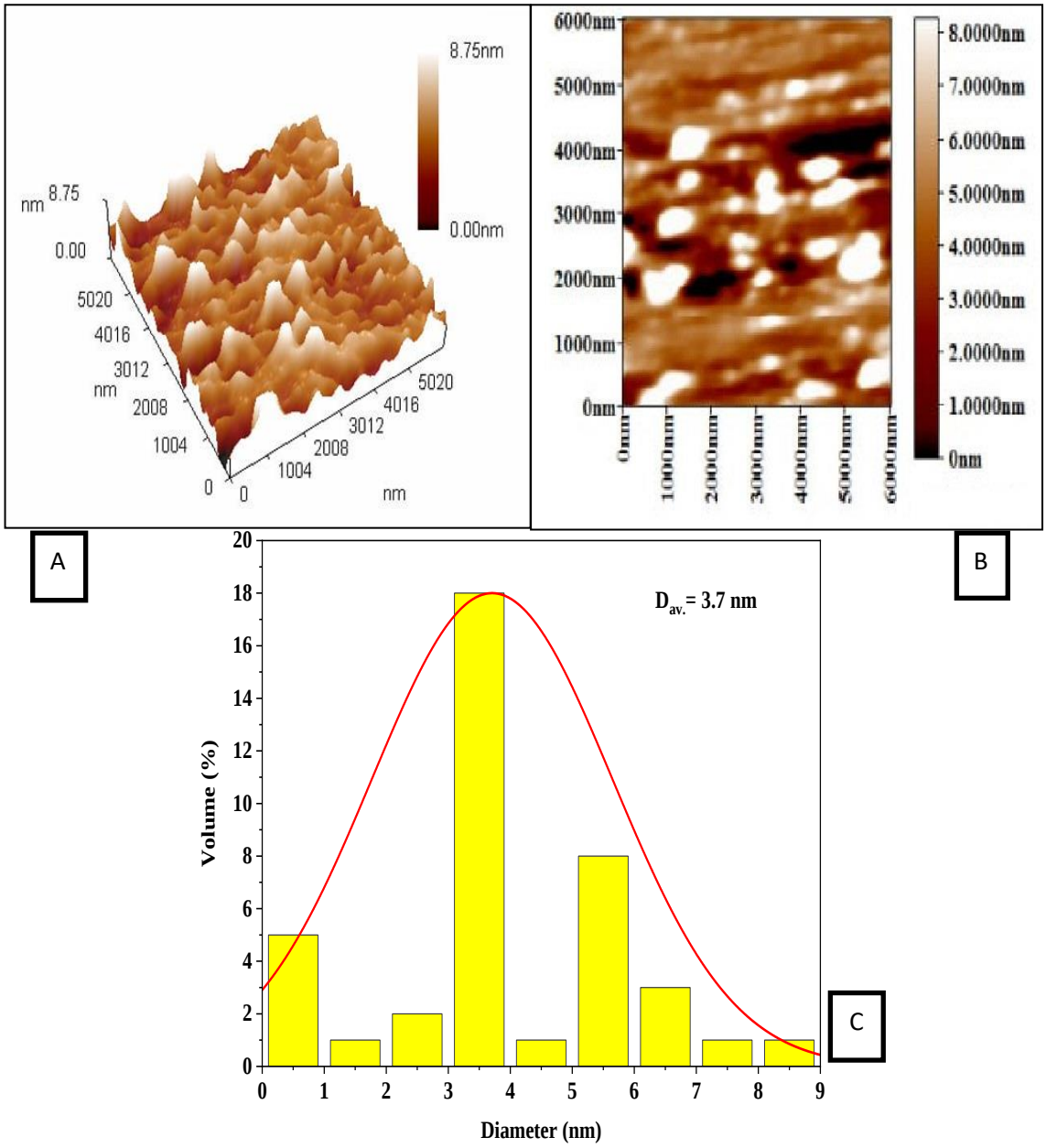

Figure (4.11): AFM surface morphology of (Bi_2O_3:ZnO) thin film for a concentration of 0.12 wt.% (ZnO) NPs a) 3-D, b) 2-D, and c) granularity distribution at 573 K.

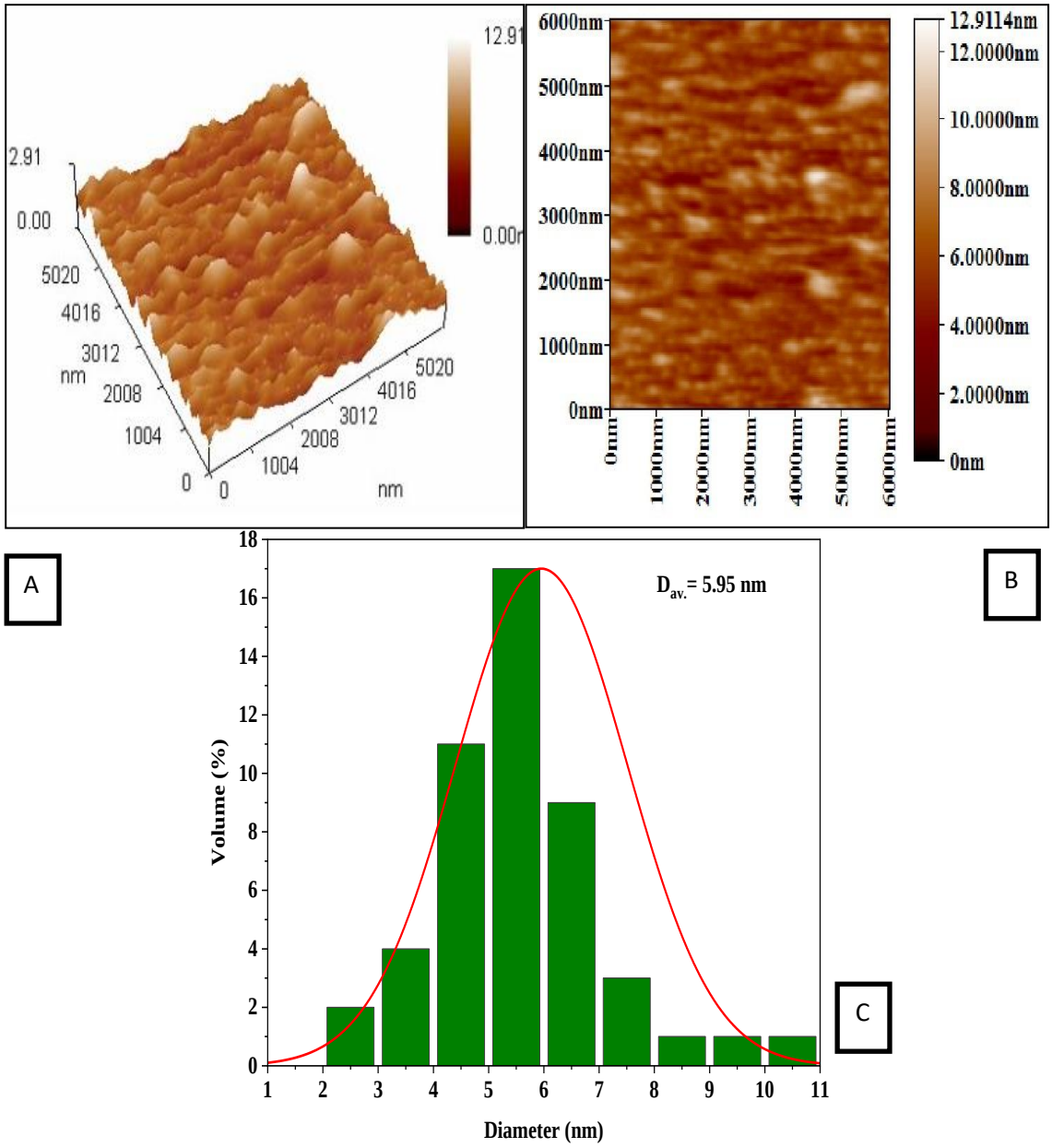

Figure (4.12): AFM surface morphology of (Bi_2O_3:ZnO) thin film for a concentration of 0.24 wt.% (ZnO) NPs a) 3-D, b) 2-D, and c) granularity distribution at 573 K.

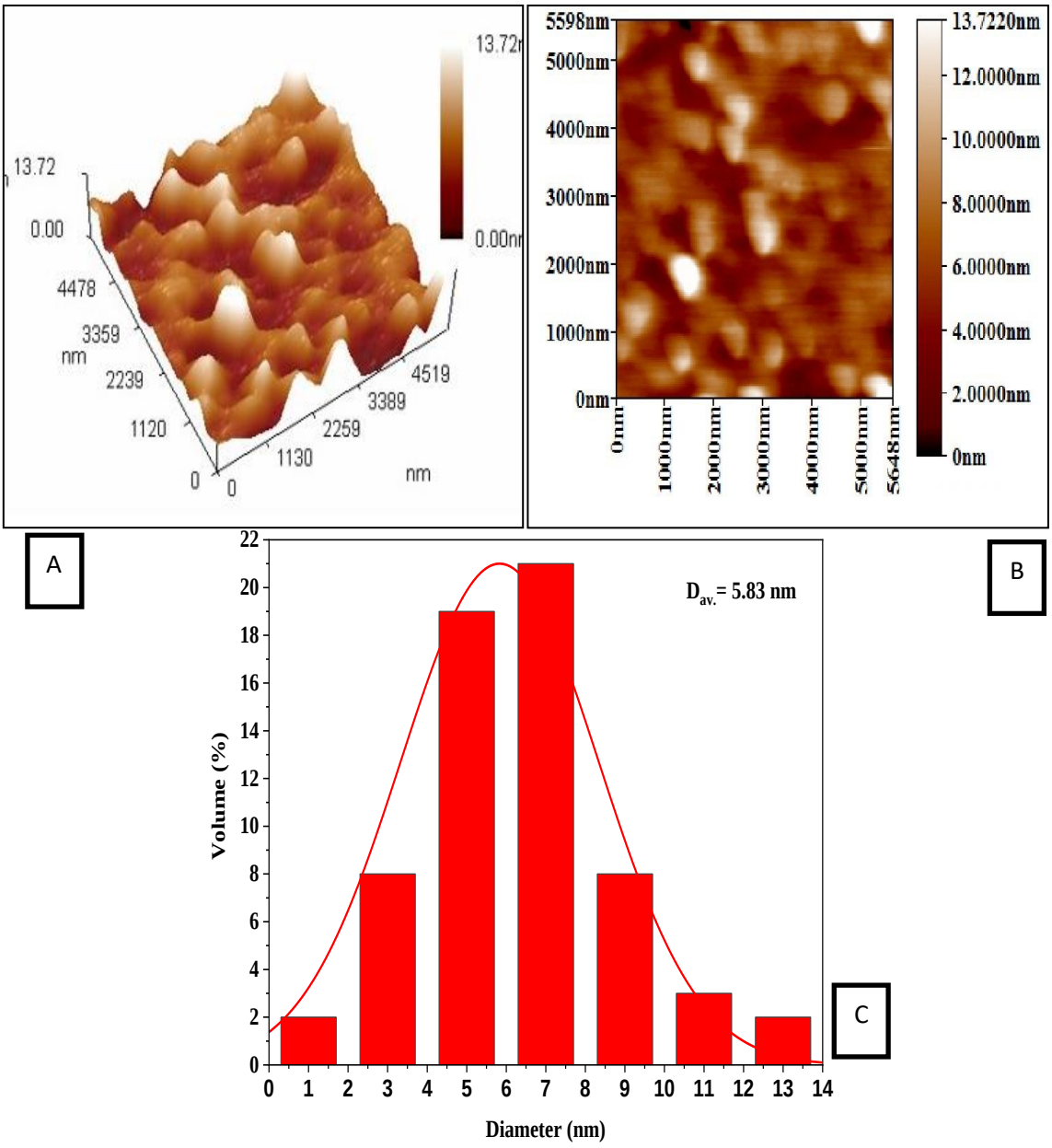

Figure (4.13): AFM surface morphology of (Bi_2O_3:ZnO) thin film for a concentration of 0.36 wt.% (ZnO) NPs a) 3-D, b) 2-D, and c) granularity distribution at 573 K.

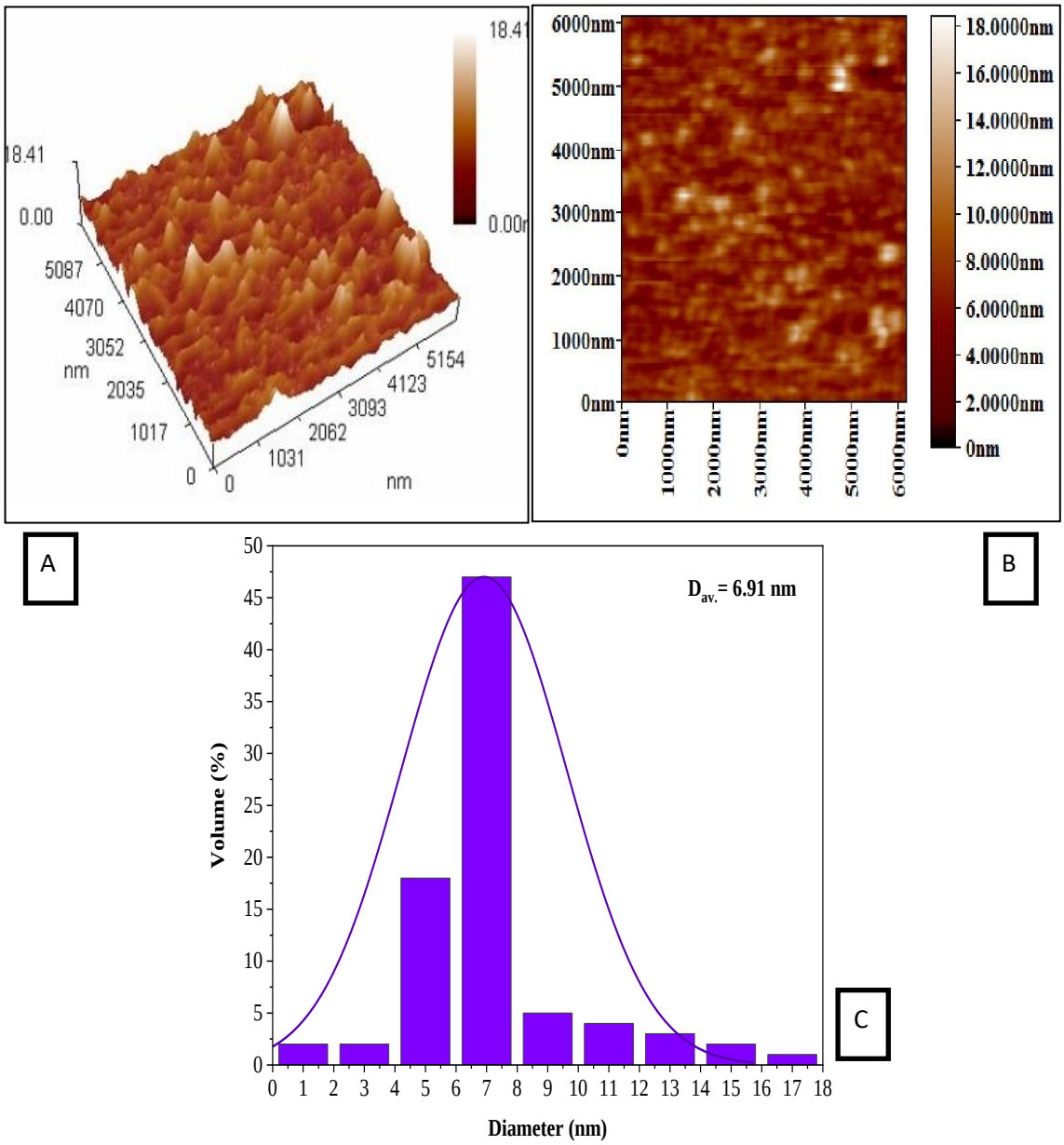

Figure (4.14): AFM surface morphology of (Bi_2O_3:ZnO) thin film for a concentration of 0.48 wt.% (ZnO) NPs a) 3-D, b) 2-D, and c) granularity distribution at 573 K.

Table (4.5): morphological characteristics for (Bi_2O_3:ZnO) thin films at an annealing temperature of 473K and 573K.

(T) K	Sample No.	Root mean square Sq (nm)	Roughness Sa (nm)	Ten-point heigh Sz (nm)	Average Diameter (nm)
473 K	Pure (Bi_2O_3)	1.04	0.814	5.6	1.329
	0.12 wt.% ZnO	1.03	0.776	6.85	1.177
	0.24 wt.% ZnO	3.5	2.94	14.2	5.293
	0.36 wt.% ZnO	3.72	2.72	16.2	5.691
	0.48 wt.% ZnO	5.12	3.83	25.7	6.757
573 K	Pure (Bi_2O_3)	0.571	0.442	3.55	0.835
	0.12 wt.% ZnO	0.726	0.566	8.75	1.14
	0.24 wt.% ZnO	1.09	0.841	12.91	1.637
	0.36 wt.% ZnO	1.78	1.33	13.72	2.736
	0.48 wt.% ZnO	2.22	1.7	18.41	2.758

4.2.4 Scanning electron microscopy (SEM)

Using a scanning electron microscope, Figures (4.15) and (4.16) exhibits photograph of Nanoparticles in the studied thin films (SEM). The formation of nanoparticle clusters at lower chemical concentrations can account for these observations. Due to the nanoparticles, Bi_2O_3 can facilitate the construction of a network when there is a more significant contact of ZnO nanoparticles. This increases the number of charge carriers [152,153].

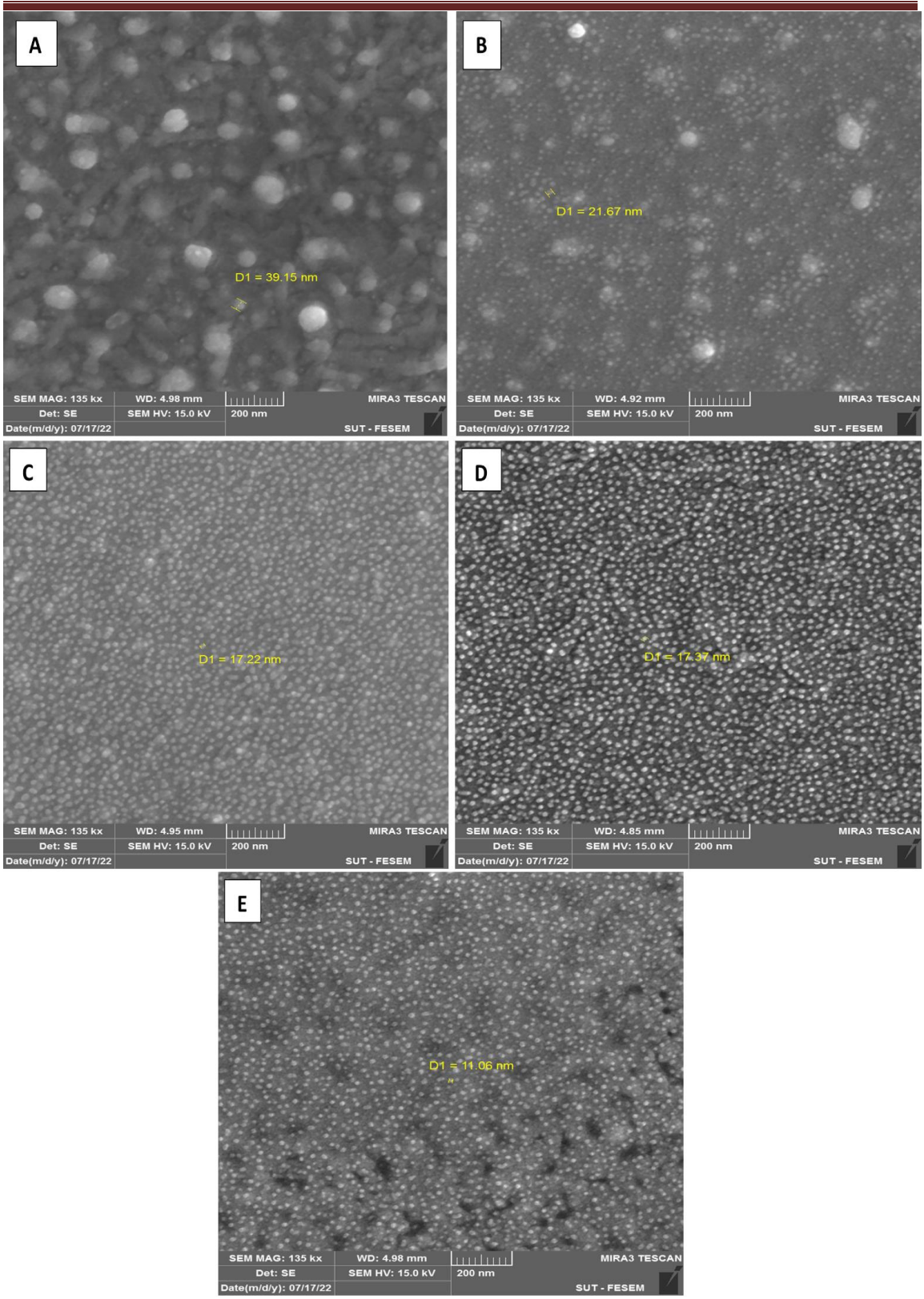

Figure (4.15): SEM images of (Bi_2O_3:ZnO) thin film: A) pure B) 0.12 wt.% (ZnO) NPs, C) 0.24 wt.% (ZnO) NPs, D) 0.36 wt.% (ZnO) NPs and E) 0.48 wt.% (ZnO) NPs at 473 K.

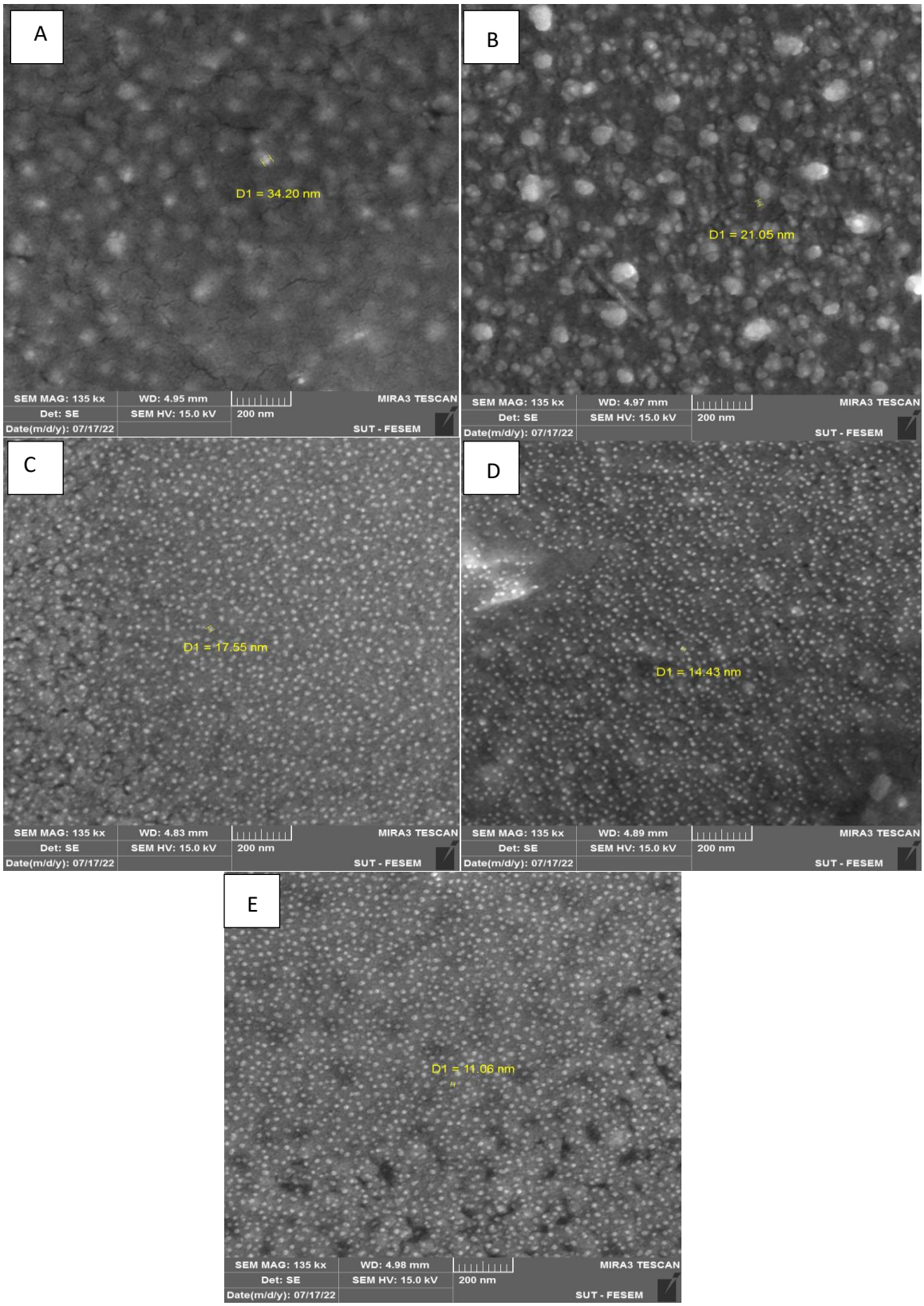

Figure (4.16): SEM images of (Bi_2O_3:ZnO) thin film: A) pure B) 0.12 wt.% (ZnO) NPs, C) 0.24 wt.% (ZnO) NPs, D) 0.36 wt.% (ZnO) NPs and E) 0.48 wt.% (ZnO) NPs at 573 K.

4.3 The Optical Properties

The study of the optical properties of (Bi_2O_3:ZnO) thin films prepared by thermal evaporation technique under the pressure of 1×10^{-5} mbar with a rate of deposition (0.5) nm. s^{-1}, which is annealed at 473 and 573 K temperature for 2 hr and thicknesses consistently 50 ±5 nm, are carried out at normal incidence in the spectral range from 200 to 1100 nm using Shimadzu model UV-1800 OA (JAPAN)double-beam spectrophotometer. It is useful in the task of determining optical properties, such as transmittance (T), reflectance(R), absorption coefficient (α), optical energy gap (Eg), refractive index (n), extinction coefficient (k_o), real and imaginary dielectric constant (ε_r, ε_i) by analyzing absorbance spectrum.

4.3.1 Absorbance (A)

The absorbance (A) is calculated by using equation (2.6). The absorbance of (Bi_2O_3:ZnO) thin film with varied concentrations of ZnO for wavelength ranging between (200-1100) nm was recorded at room temperature. Figures (4.17) and (4.18) display the variation of optical absorbance with wavelength for the (Bi_2O_3:ZnO) thin film. From these figures, it can be noted that the spectra reveal that all these films show more absorbance in the ultraviolet region. All thin films show low absorbance in the visible region. This behavior can be explained as follows: at high wavelength, the incident photons do not have enough energy to interact with atoms, and thus the photon will be transmitted. When the wavelength decreases (at the neighborhood of the fundamental absorption edge), the interaction between incident photon and material will occur, and the photon will be absorbance. The absorbance increases with the increasing weight percentages of the nanomaterials. This is due to absorb the incident light by free electrons [149]. These results are similar to those of the other researchers [154].

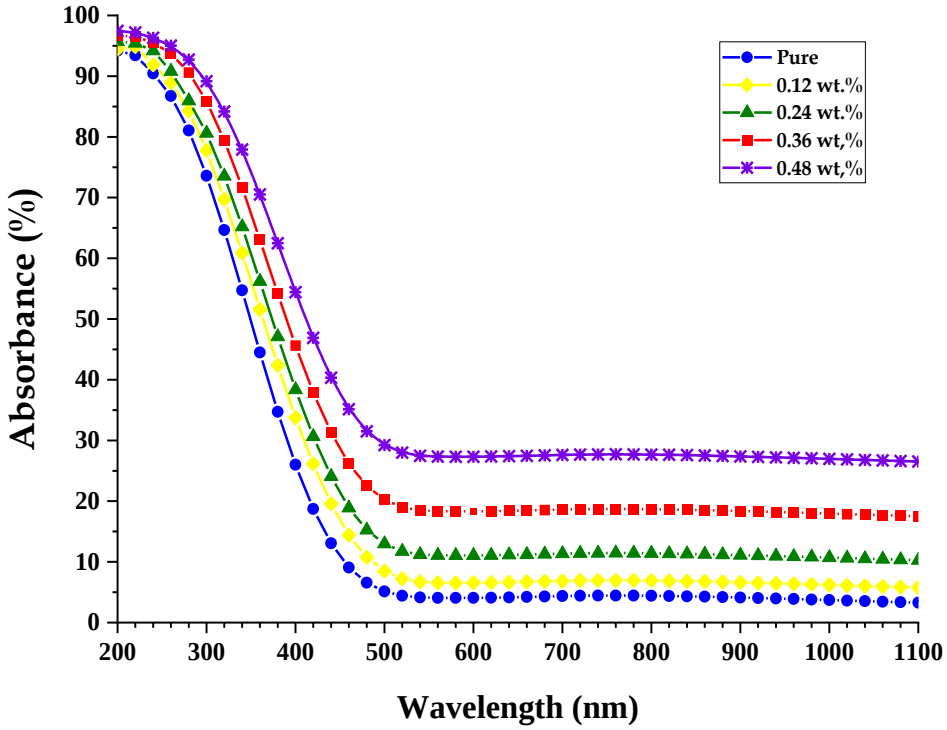

Figure (4.17): The absorbance as function of wavelength for (Bi_2O_3:ZnO) thin films at 473 K.

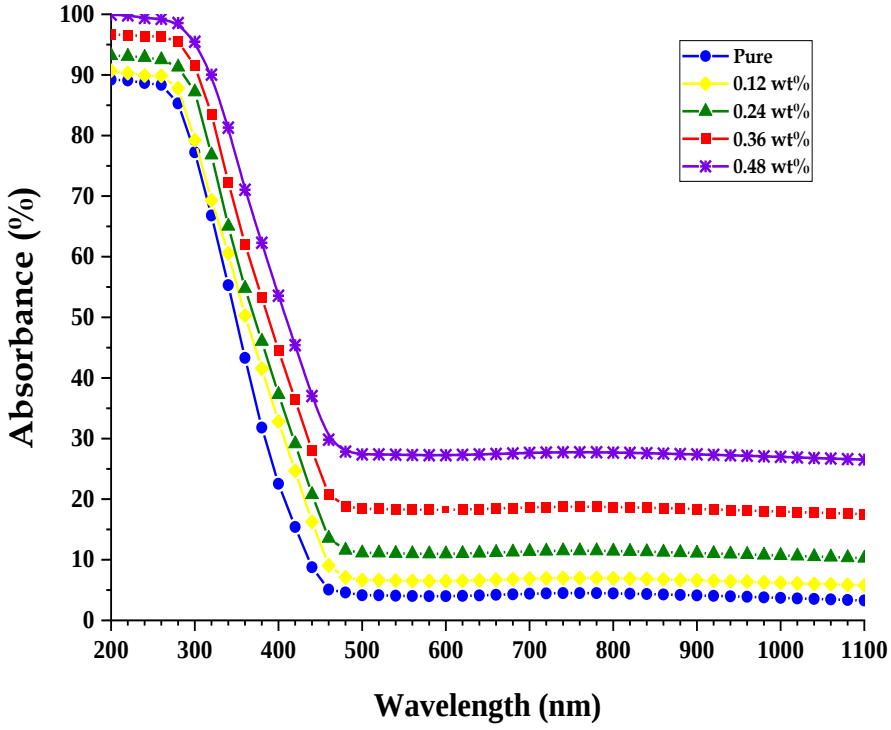

Figure (4.18): The absorbance as function of wavelength for (Bi_2O_3:ZnO) thin films at 573 K.

4.3.2 Transmittance (T)

The transmittance (T) is calculated by using equation (2.7). Figures (4.19) and (4.20) show the transmittance (T) as a function of wavelength for (Bi_2O_3:ZnO) thin films. The figures indicate that the transmittance for all samples is increases with the increasing of wavelength. It is clearly noticed that the pure film has high transmittance because electrons are linked to atoms strong by covalent bonds, consequently free electrons at that time can not the break linkage, hence movement it need to photon with high energy but when adding different rate of ZnO nanoparticles, the average transmittance of the films reduces slightly due to contain electrons in it outer orbits can be absorb the energy of the incident photon and travel to higher energy levels. The traveled electron to higher levels have occupied vacant positions of energy bands, so that this process is not accompanied by the emission of radiation ,where the incident light is absorbed by the substance. This behavior agrees with [59,155].

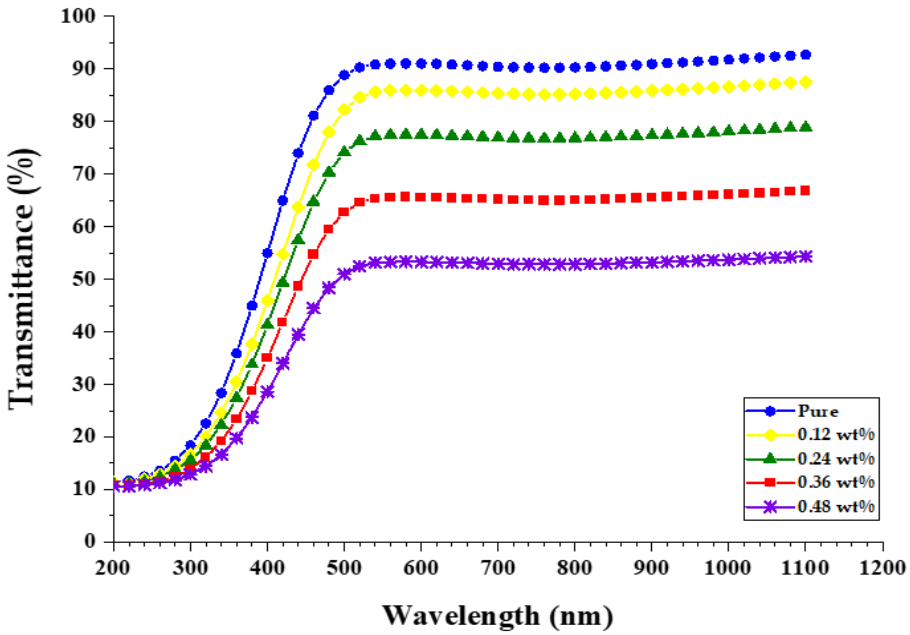

figure (4.19): The transmittance spectrum of pure Bi_2O_3 sample and doped with ZnO NPs at 473 K.

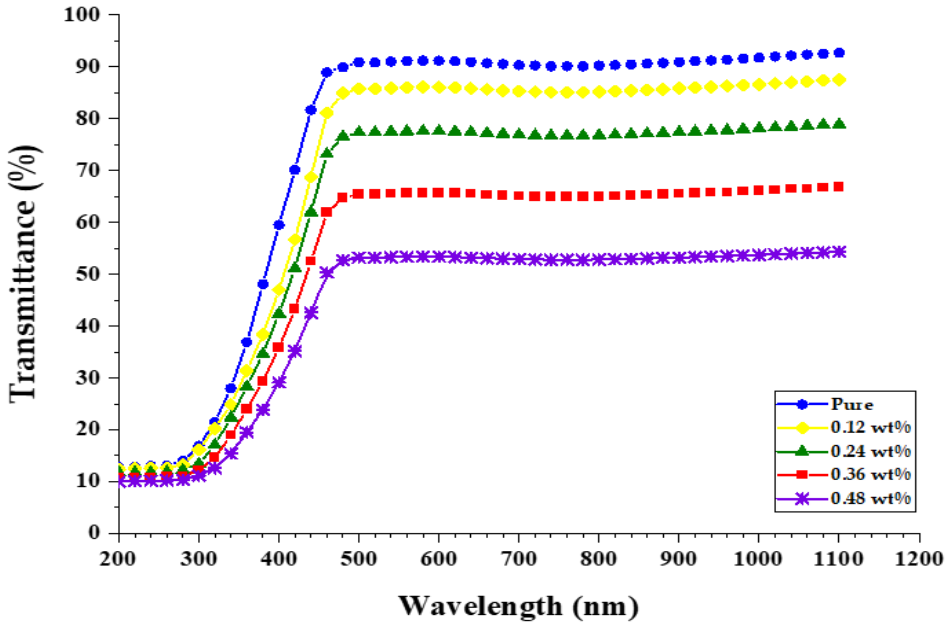

Figure (4.20): The transmittance spectrum of pure Bi_2O_3 sample and doped with ZnO NPs at 573 K.

4.3.3 Reflectance (R)

The change in the ratio between the intensity of reflection of the reflected beam to the amount of incident radiation. The reflectivity was calculated depending on the spectral absorbance and the transmittance by the energy conservation law and according to equation (2.11).

Figures (4.21) and (4.22) show the change in reflectivity as a function of the wavelength of the (Bi_2O_3:ZnO) nanostructured thin films. To note that the reflectivity gradually increases to a maximum value at certain wavelengths, and then decreases with the increasing in wavelength we note that it is in a curved shape, and we explain that the absorption is small at those wavelengths, and this is due to the increasing in reflectance from the surface of the film. Since the reflectivity depends on the surface roughness, we observe a difference in the value of the highest peak positions as a result of different structural properties, as the reflectivity of the film generally increases with the doping ratio.

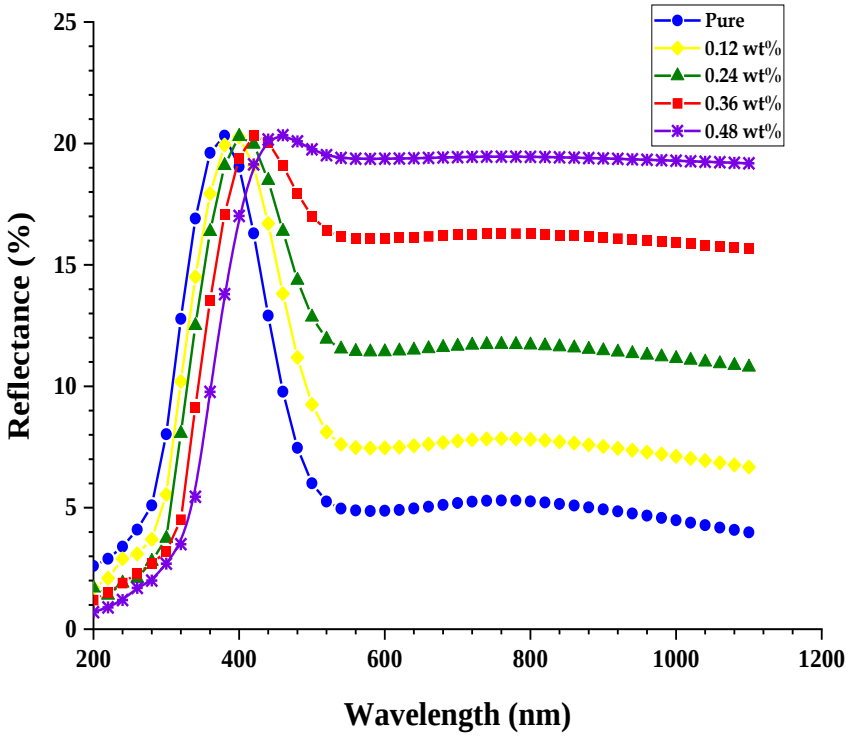

Figure (4.21): The reflectance spectrum of pure Bi_2O_3 sample and doped with ZnO NPs at 473 K.

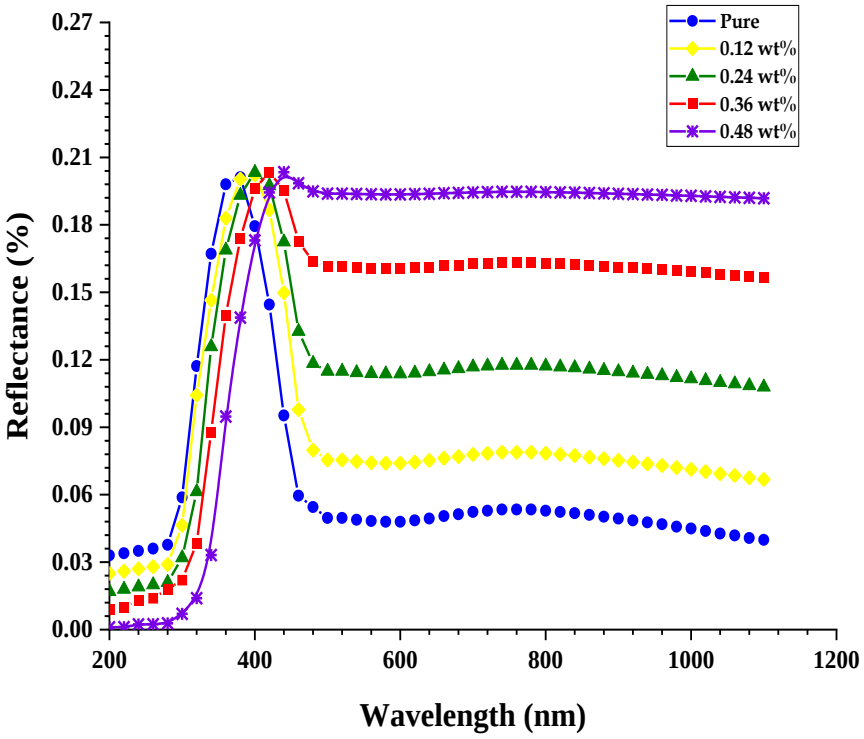

Figure (4.22): The reflectance spectrum of pure Bi_2O_3 sample and doped with ZnO NPs at 573 K.

4.3.4 Absorption coefficient (α)

The absorption coefficient α is calculated by using equation (2.16). Figures (4.23) and (4.24) show the absorption coefficient α as a function of photon energy Absorption coefficient is plotted against photon energy for thin films (Bi_2O_3:ZnO). It can be seen that the absorption coefficient is the smallest at high wavelength and low energy. This means that the possibility of electron transition is little because the energy of the incident photon is not sufficient to transition the electron from the valence band to the conduction band in a semiconductor material [156].

At high energies, absorption is good, which is a good sign of a high probability of electron transformations. As a direct result, the energy of the incoming photon is sufficient to coerce one electron to move from the valence band to the conduction band in the energy spectrum. During the incident, the energy of the observed photon was higher than the allowed energy gap [157].

Direct electron transfer occurs when the absorption coefficient is large ($\alpha > 10^4$) cm^{-1} at high energies. The electron and photons are conserved as they travel through the transition. While at low energies, values of absorption coefficient ($\alpha < 10^4$) cm^{-1} are likely to occur, which leads to the indirect transition of electrons, and the phonon helps to maintain electronic momentum. The thin-film absorbance coefficient (Bi_2O_3:ZnO) is greater than 10^4 cm^{-1}, just one of the many findings. This demonstrates that electron transfers straightforwardly take place. The findings of this research are comparable to those of the other researchers [59].

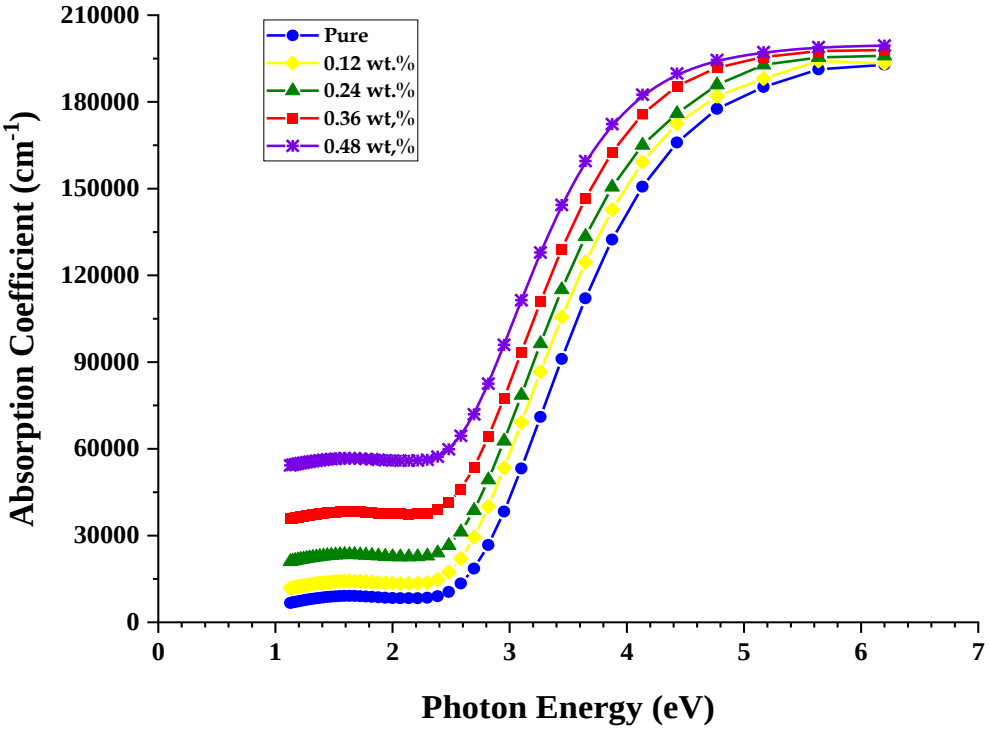

Figure (4.23): The absorption coefficient α of pure Bi_2O_3 sample and doped with ZnO NPs as a function of photon energy hv at 473 K.

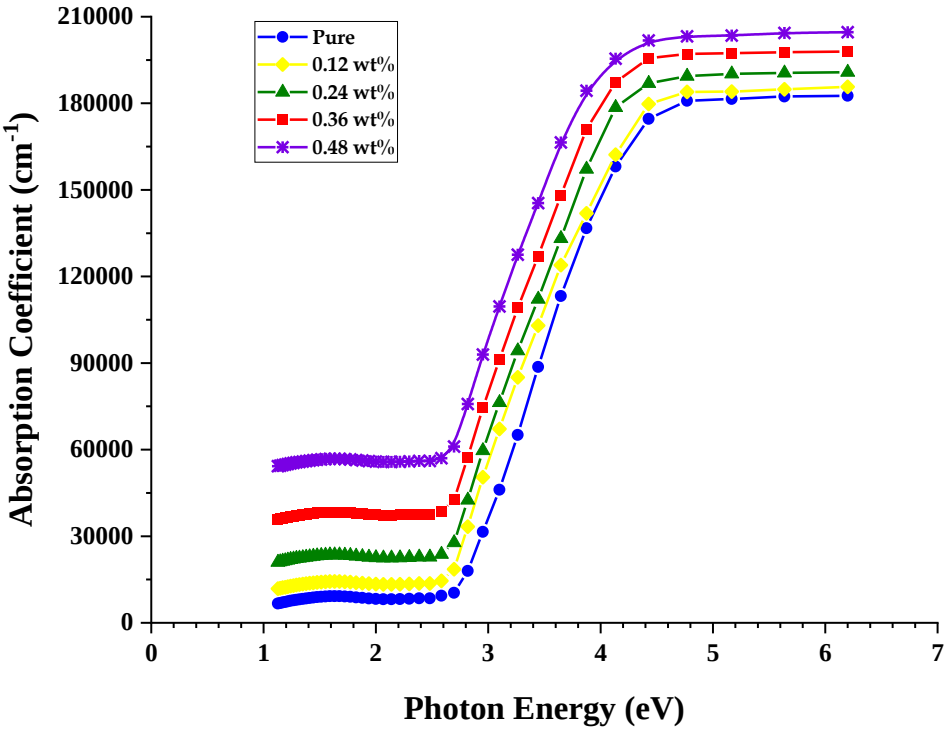

Figure (4.24): The absorption coefficient α of pure Bi_2O_3 sample and doped with ZnO NPs as a function of photon energy hv at 573 K.

4.3.5 Energy gaps of the (allowed and forbidden) direct transition

It has been determined how much of a difference there is between the allowed and forbidden direct transition band energy gaps by using equation (2.9). Calculating the allowed direct transition band energy gap takes place when the value of r = 1/2; however, when the value of r = 3/2, the calculation of the forbidden direct transition band energy gap takes place.

Figures (4.25) and (4.26) show the Absorption edge $(\alpha hv)^2$ for (Bi_2O_3:ZnO) thin film as a function of photon energy, where the energy gap for the allowed direct transition is calculated by drawing a straight line from the upper portion of the curve toward the (x) axis at the value $(\alpha hv)^2 = 0$ [158].

The obtained values are listed in Tables (4.6) and (4.7). The energy gap values drop as the percentage of Zinc oxide nanoparticles in the mixture increases. As the percentage of Zinc oxide nanoparticles in the sample increases, site levels are created in the forbidden energy gap, allowing electrons to move from the valence band to the local levels and then to the conduction band.

This decrease in energy gap explains why electrons are transferred from the valence band of (Bi_2O_3:ZnO) to conduction band electrons [159].

Calculating the forbidden transition of the direct energy gap follows the same steps as those used to determine the allowed transition of the direct energy gap for the (Bi_2O_3:ZnO) thin films, as can be seen in tables (4.6) and (4.7). The prohibited transition of the direct energy gap for the (Bi_2O_3:ZnO) thin films can be seen in Figures (4.27) and (4.28).

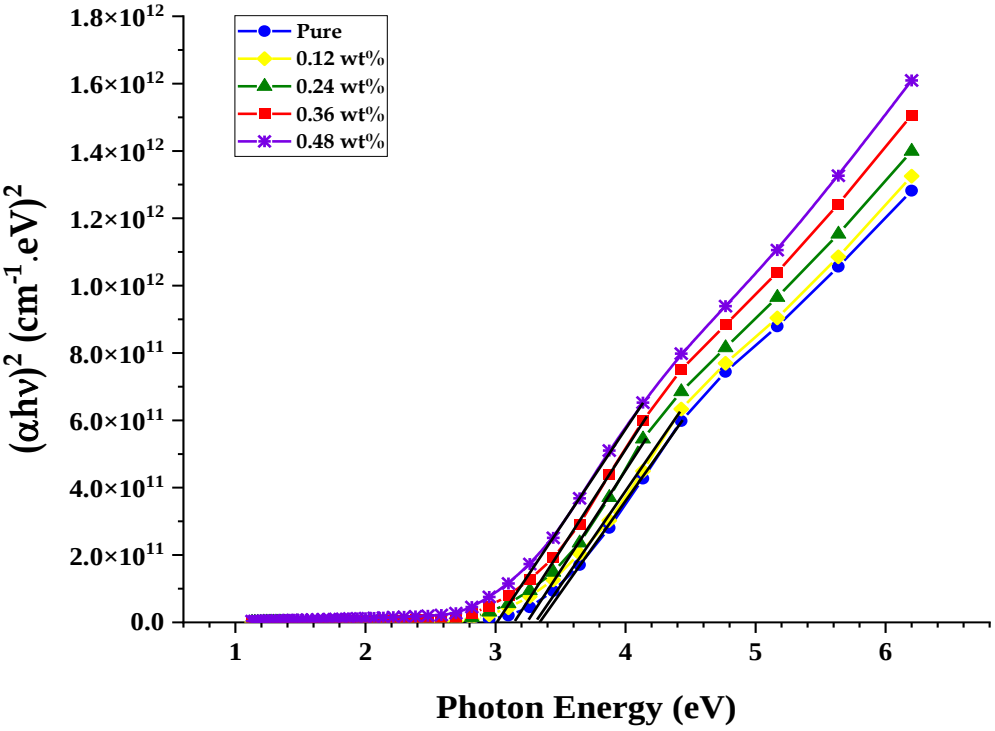

Figure (4.25): Plot of $(ahv)^2$ of pure Bi_2O_3 sample and doped with ZnO NPs as against photon energy hv at 473 K.

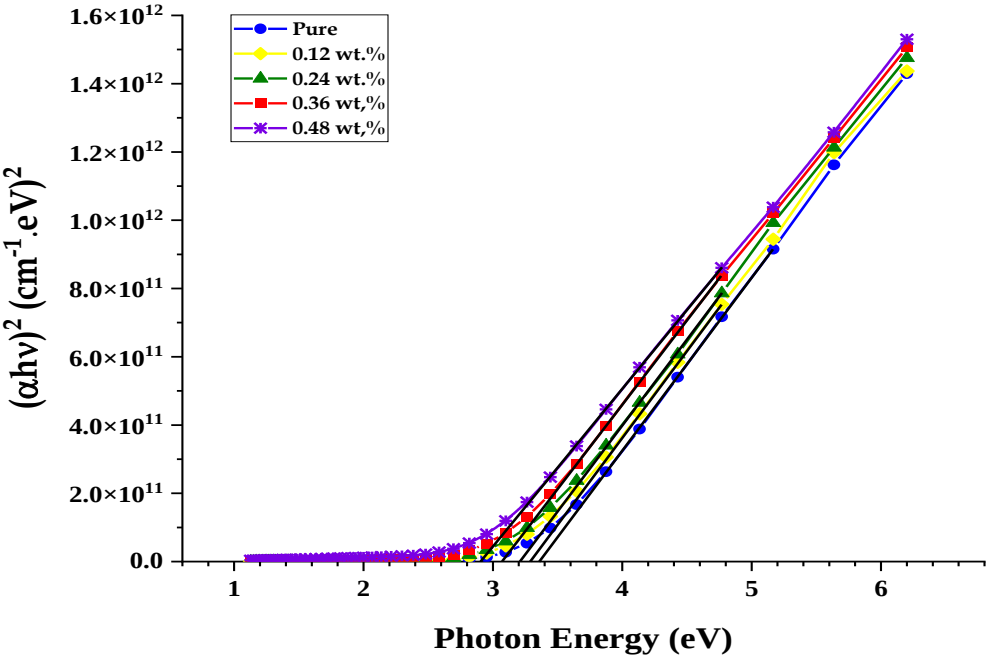

Figure (4.26): Plot of $(ahv)^2$ of pure Bi_2O_3 sample and doped with ZnO NPs as against photon energy hv at 573 K.

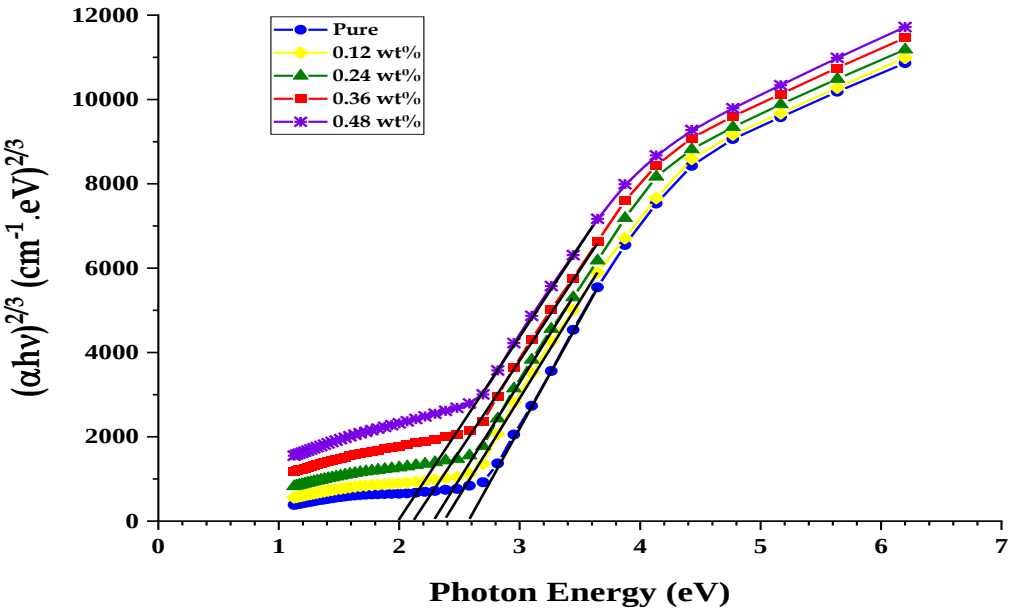

Figure (4.27): Plot of $(ahv)^{2/3}$ of pure Bi_2O_3 sample and doped with ZnO NPs as against photon energy hv at 473 K.

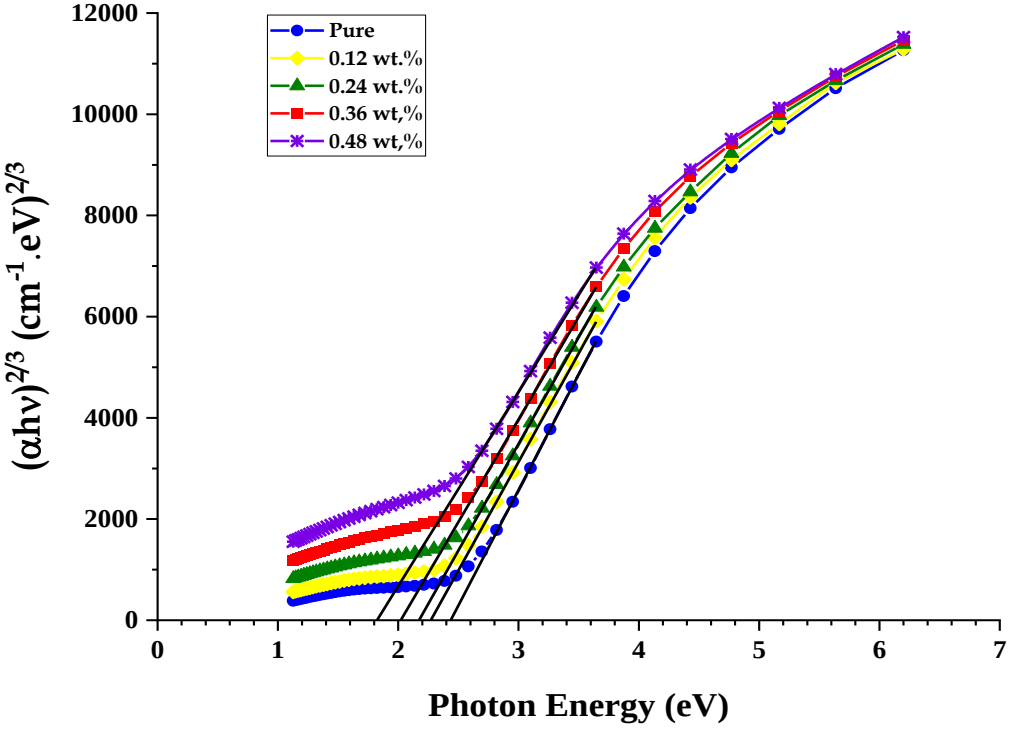

Figure (4.28): Plot of $(ahv)^{2/3}$ of pure Bi_2O_3 sample and doped with ZnO NPs as against photon energy hv at 573 K.

Table (4.6): For (Bi_2O_3:ZnO) thin films, the values of the energy gap for the permissible and banned direct transitions at 473 K.

Zinc Oxide	E_g(eV)	
	Allowed	Forbidden
0	3.347	2.572
0.0012	3.305	2.387
0.0024	3.241	2.291
0.0036	3.156	2.132
0.0048	3.023	1.993

Table (4.7): For (Bi_2O_3:ZnO) thin films, the values of the energy gap for the permissible and banned direct transitions at 573 K.

Zinc Oxide	E_g(eV)	
	Allowed	Forbidden
0	3.3637	2.4405
0.0012	3.2936	2.2763
0.0024	3.2147	2.1786
0.0036	3.0744	2.0267
0.0048	2.9091	1.8286

4.3.6 Refractive index (n)

The refractive index is calculated from equation (2.11). Figures (4.29) and (4.30) show the change of refraction index for (Bi_2O_3:ZnO) thin film as a function of wavelength, respectively. These figures show that the refractive index increases with increasing the weight percentages of the nanoparticles (ZnO). This behavior is attributed to the increasing in the density of thin films. When the incident light interacts with a sample with high refractivity at the UV region, the values of a refractive index will be increasing [160].

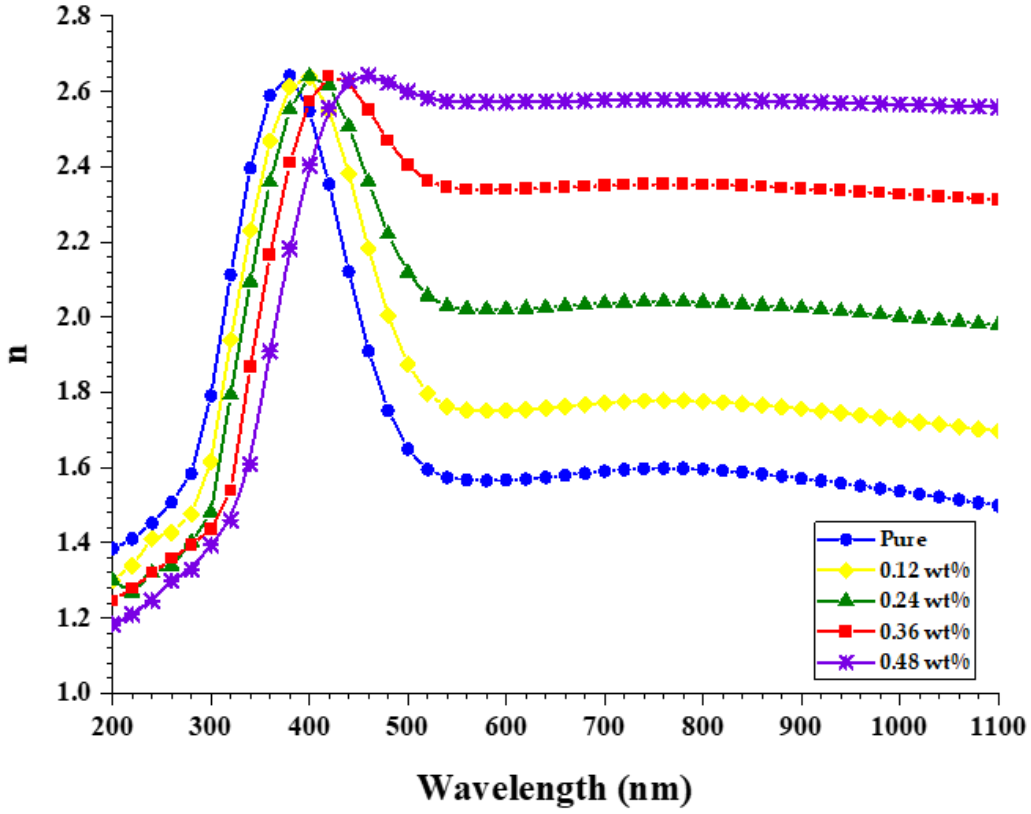

Figure (4.29): The refractive index(n)as a function of wavelength for (Bi_2O_3:ZnO) thin films at 473 K.

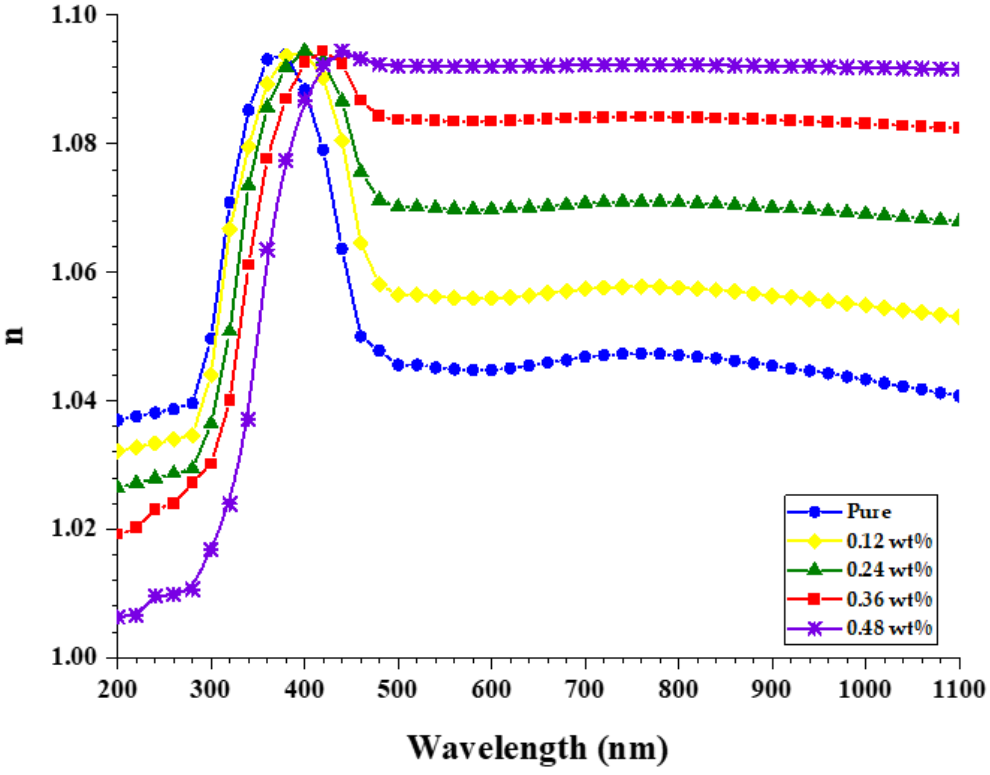

Figure (4.30): The refractive index(n)as a function of wavelength for (Bi_2O_3:ZnO) thin films at 573 K.

4.3.7 Extinction coefficient (k_0)

The Extinction coefficient (k_0) is calculated using equation (2.20). The change of the extinction coefficient, as a function of the wavelength, is shown in Figures (4.31) and (4.32) for (Bi_2O_3:ZnO) thin films. It can be noted that (k_0) has a low value at a low Weight percent, but it increases with the increasing of the Weight percent of nanoparticles for (ZnO). This is attributed to the increases absorption coefficient with the increasing of weight percentages of (ZnO) nanoparticles. The extinction coefficient has high values at in the UV region. This behavior is attributed to the high absorbance of all samples of thin films. Also, the extinction coefficient of thin films increases with the increasing wavelength at visible and near-infrared regions, which is attributed to the absorption coefficient of thin films, which is approximately constant at the visible and near infrared regions. Hence, the extinction coefficient increases with the increasing of the wavelength. These results are similar to the results that are reported by the previous researchers [161].

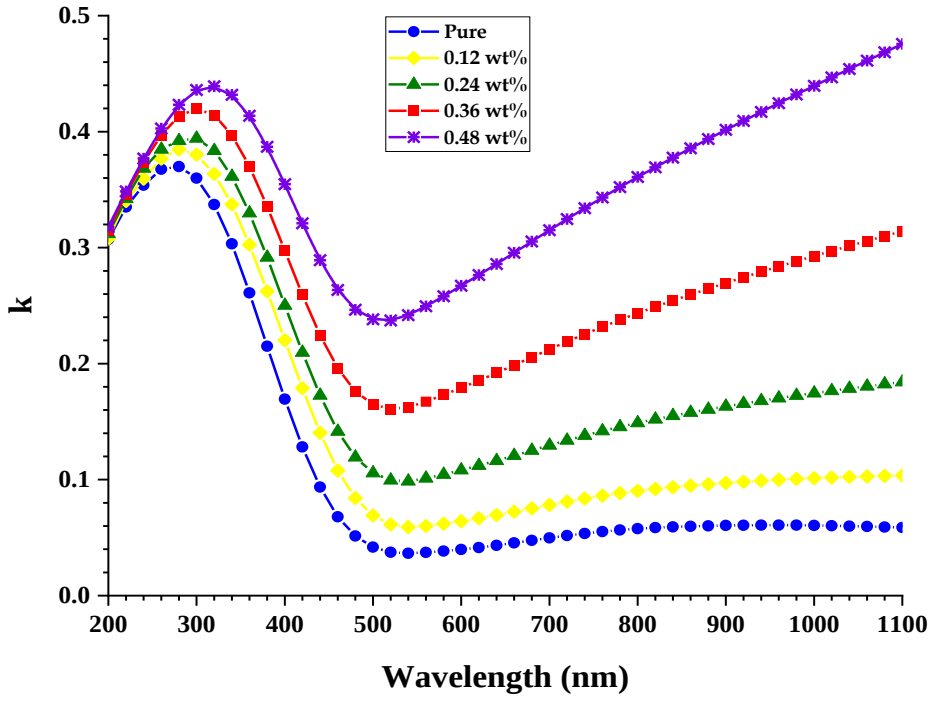

Figure (4.31): The Extinction coefficient as a function of wavelength (Bi_2O_3:ZnO) thin films at 473 K.

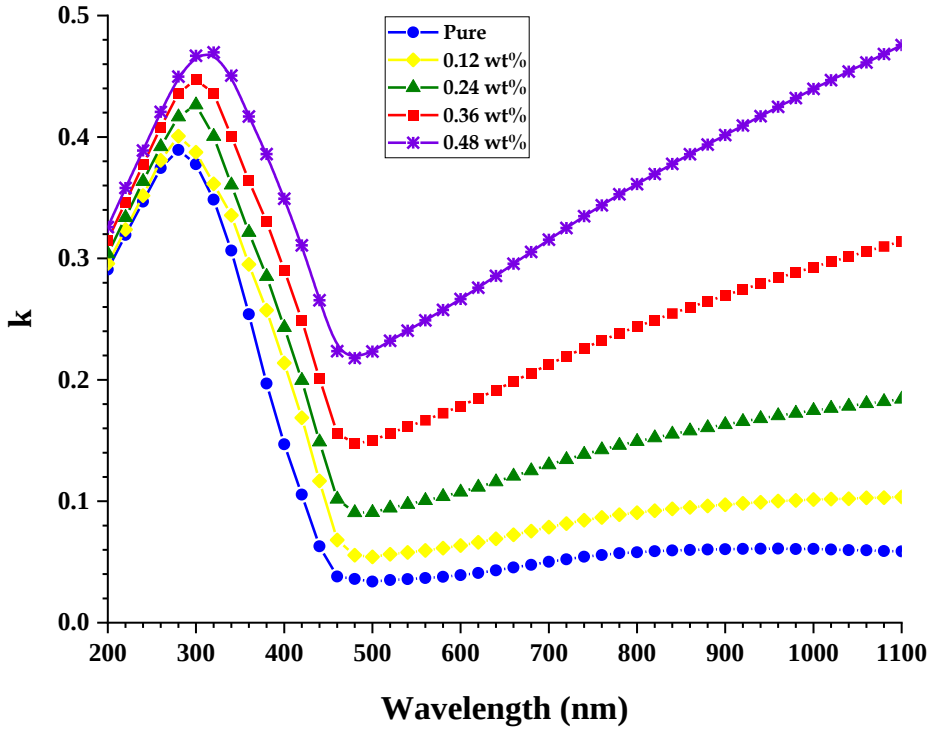

Figure (4.32): The Extinction coefficient as a function of wavelength (Bi_2O_3:ZnO) thin films at 573 K.

4.3.8 Real and imaginary part of dielectric constant

Using equations (2.23) and (2.24), we have determined the real and imaginary components of the dielectric constant for (Bi_2O_3:ZnO) thin films. Figures (4.33), (4.34), (4.35), and (4.36), respectively, display the real and imaginary part dielectric constant variations as a function of wavelength. These numbers demonstrate that raising the weight percent of ZnO nanoparticles raises the dielectric constant for two-part real and imaginary. This behavior can be explained by the fact that nanoparticles contribute a greater degree of electrical polarization to the sample, i.e., the dielectric constant of (Bi_2O_3) increases by a fractional rise in charges within the thin films [160].

The figures show that the real and imaginary parts of the dielectric constant of (Bi_2O_3) are changed with the wavelength. This is due to the real part of the dielectric constant depending on the refractive index because the effect of the extinction coefficient is very small. The imaginary part of the dielectric constant depends on the extinction coefficient, especially in the

visible and near infrared regions of wavelength, where the refractive index is approximately constant. In contrast, the extinction coefficient increases with the increasing of the wavelength. These results are similar to the results of the previous researcher [162,163].

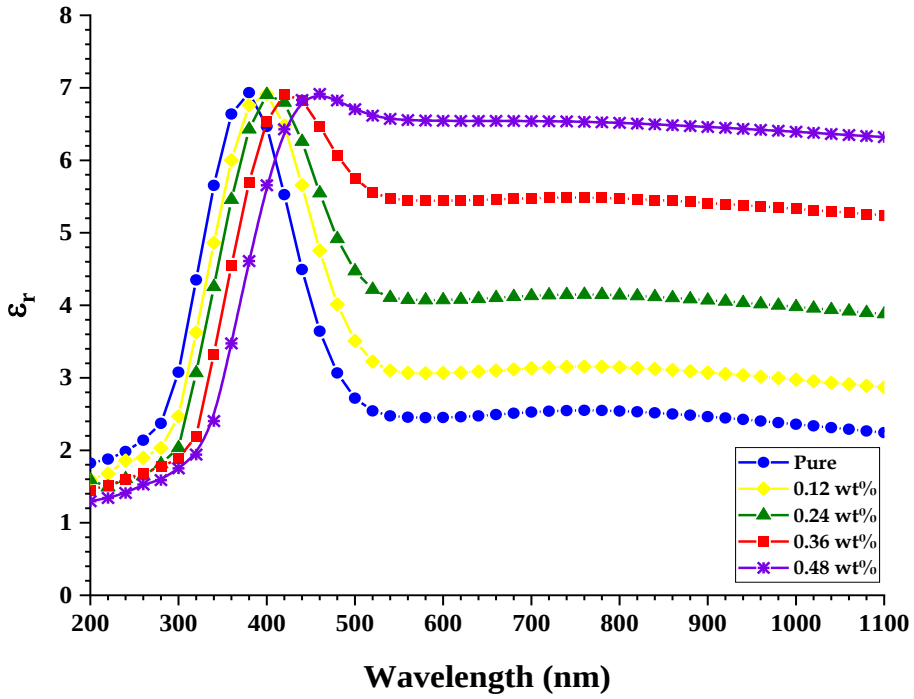

Figure (4.33): The real dielectric constant(ε_r) as a function of incident wavelength for (Bi_2O_3:ZnO) thin films at 473 K.

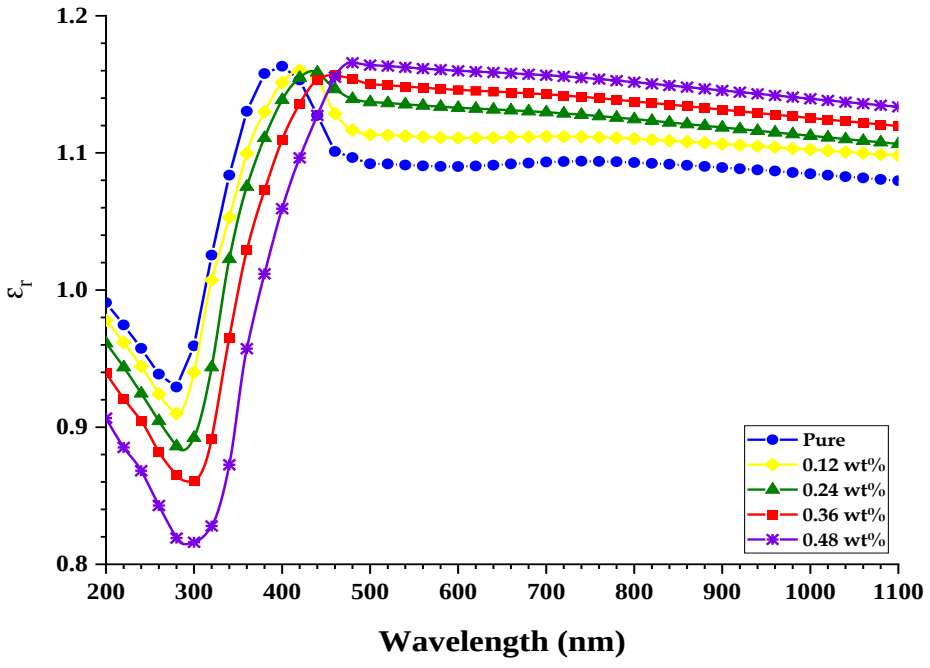

Figure (4.34): The real dielectric constant(ε_r) as a function of incident wavelength for (Bi_2O_3:ZnO) thin films at 573 K.

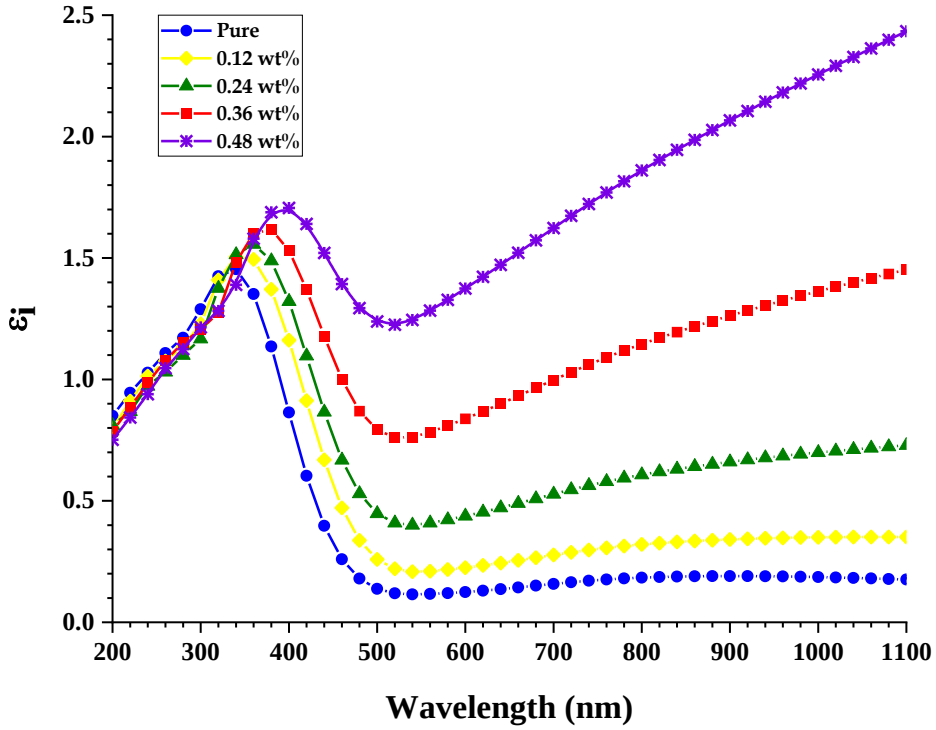

Figure (4.35): The imaginary dielectric constant(ε_i) as a function of wavelength (Bi_2O_3:ZnO) thin films at 473 K.

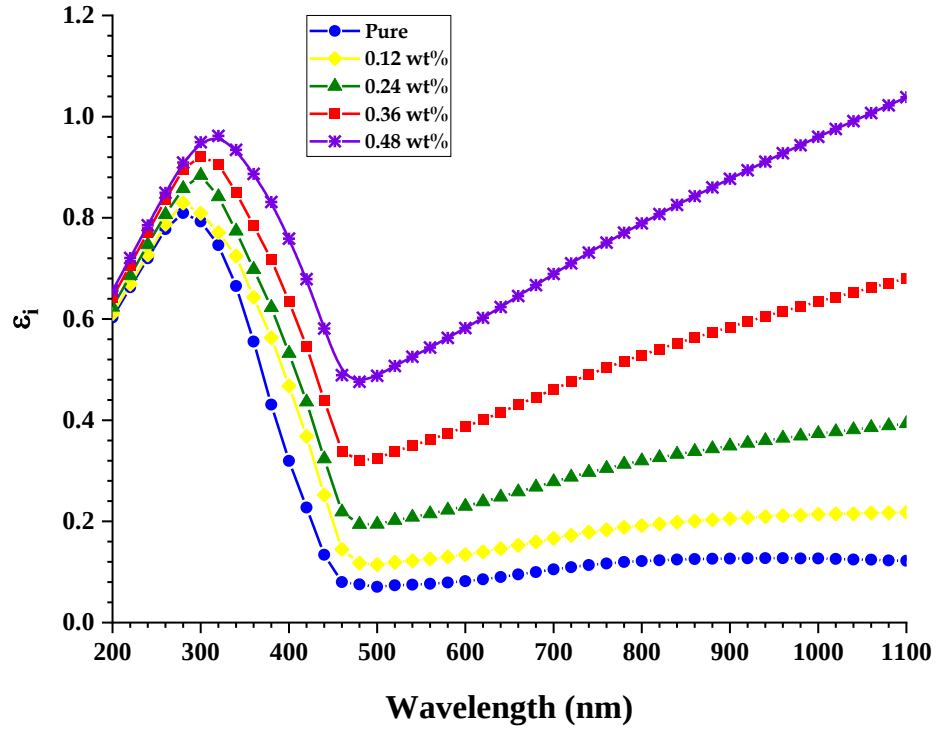

Figure (4.36): The imaginary dielectric constant(ε_i) as a function of wavelength (Bi_2O_3:ZnO) thin films at 573 K.

4.3.9 Optical conductivity (σ_{op})

Figures (4.37) and (4.38) show the variation of optical conductivity as a function of wavelength for (Bi_2O_3:ZnO) thin films. The optical conductivity has been calculated by using equation (2.25). The figure shows that the optical conductivity of all thin film samples decreases with the increasing of the wavelength. This behavior is attributed to the optical conductivity depending on the wavelength of the radiation incident on the samples of thin films; the increasing of optical conductivity at the low wavelength of the photon is due to the high absorbance of all samples of thin films in this region, hence, an increasing of the charge transfer excitations.

The optical conductivity spectra indicated that the samples transmit within the visible and near infrared regions. Also, the optical conductivity of thin films is increases with the increase of ZnO nanoparticle concentrations. This behavior is related to the creation of localized levels in the energy gap; the increasing of ZnO nanoparticles concentrations increases the density of localized stages in the band structure, hence, an increase of the absorption coefficient, consequently increasing the optical conductivity of (Bi_2O_3:ZnO) thin films. These results are similar to the results of the researcher [155,164].

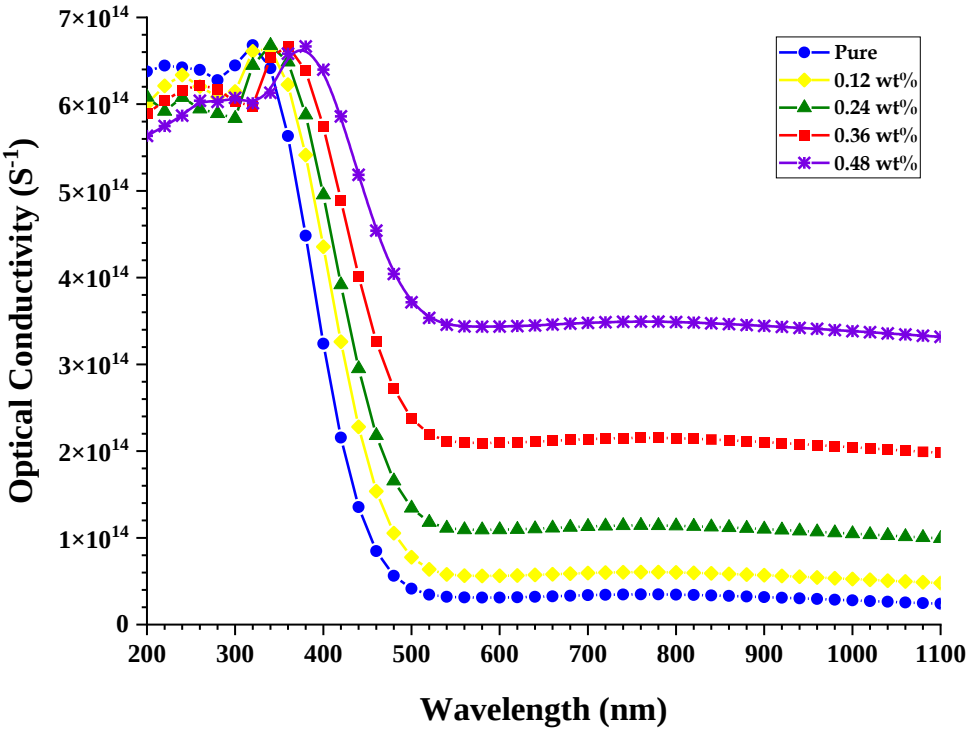

Figure (4.37): Optical conductivity as a function of wavelength for (Bi_2O_3:ZnO) thin films at 473 K.

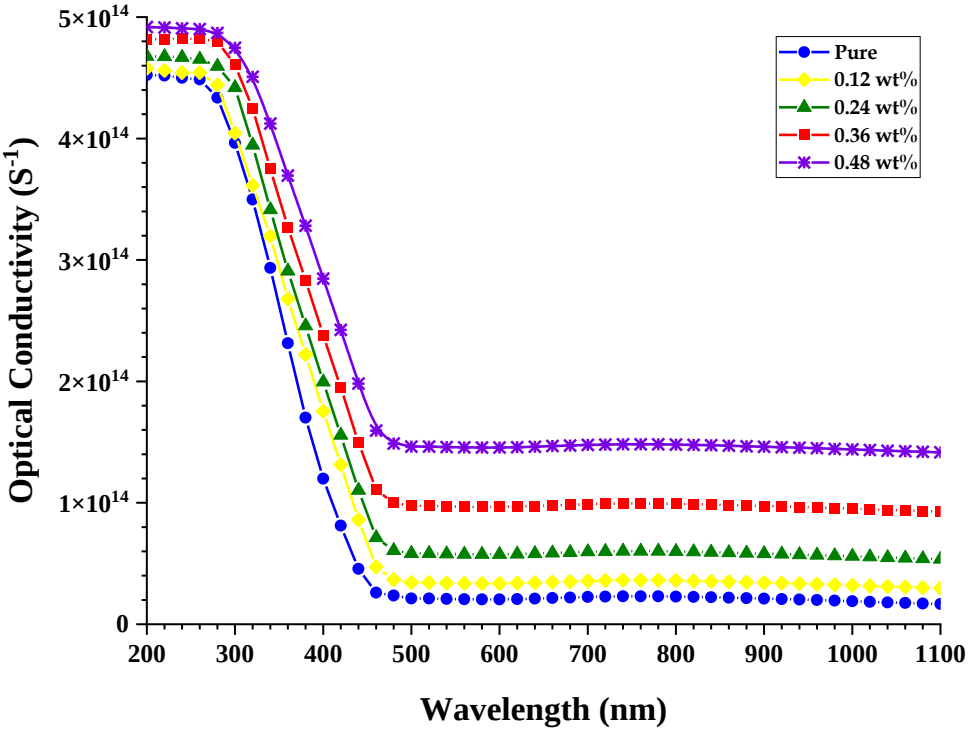

Figure (4.38): Optical conductivity as a function of wavelength for (Bi_2O_3:ZnO) thin films at 573 K.

4.4 The D.C Electrical Properties

The surface electrical conductivity σ_{dc} is calculated for the prepared films by using equation (2.28). The Following are the detailed results of these properties.

4.4.1 The effect of the ZnO additive on the electrical conductivity σ_{dc} of (Bi_2O_3:ZnO) thin films

Figures (4.39) and (4.40) show the D.C surface electrical conductivity as a function of the concentration of (ZnO) nanoparticles samples. From these figures, it can be noticed that the D.C electrical conductivity is increasing with the increasing of concentrations of (ZnO). This is related to the increase in charge carriers which are increased with the increasing filler content, and this is due to the formation of a continuous network of (ZnO) nanoparticles that contain paths inside the thin film and allows charge carriers to pass through. On the contrary, the resistivity decreases with increasing nanoparticle concentration, as shown in the two figures (4.41) and (4.42). These results are similar to the results of other researchers [110,165].

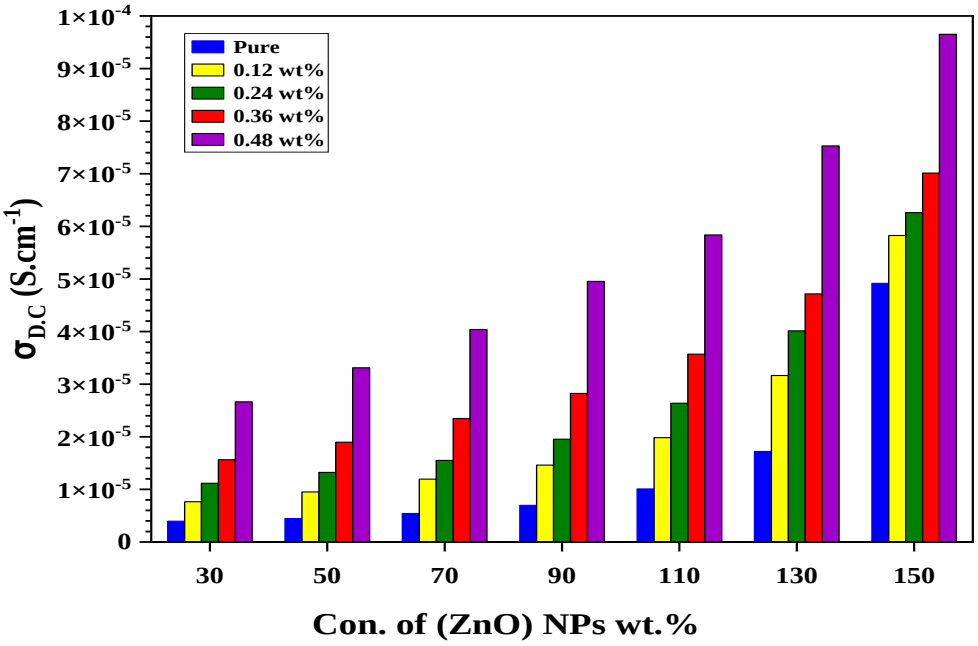

Figure (4.39): plot of D.C electrical conductivity with ZnO nanoparticle wt.% concentration of (Bi_2O_3:ZnO) thin films at 473 K.

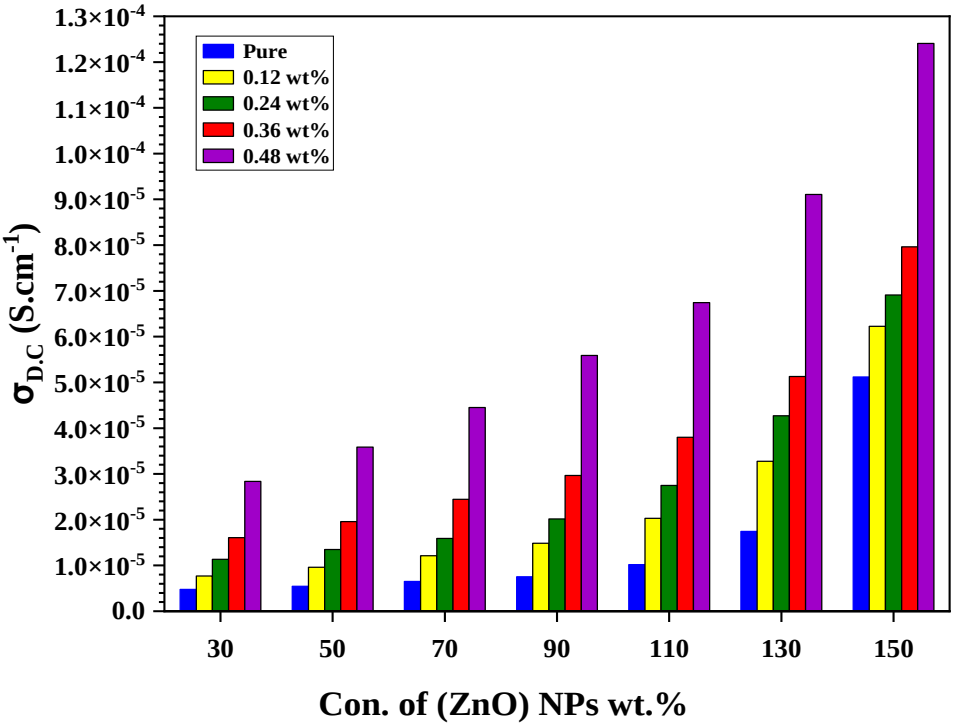

Figure (4.40): plot of D.C electrical conductivity with ZnO nanoparticle wt.% concentration of (Bi_2O_3:ZnO) thin films at 573 K.

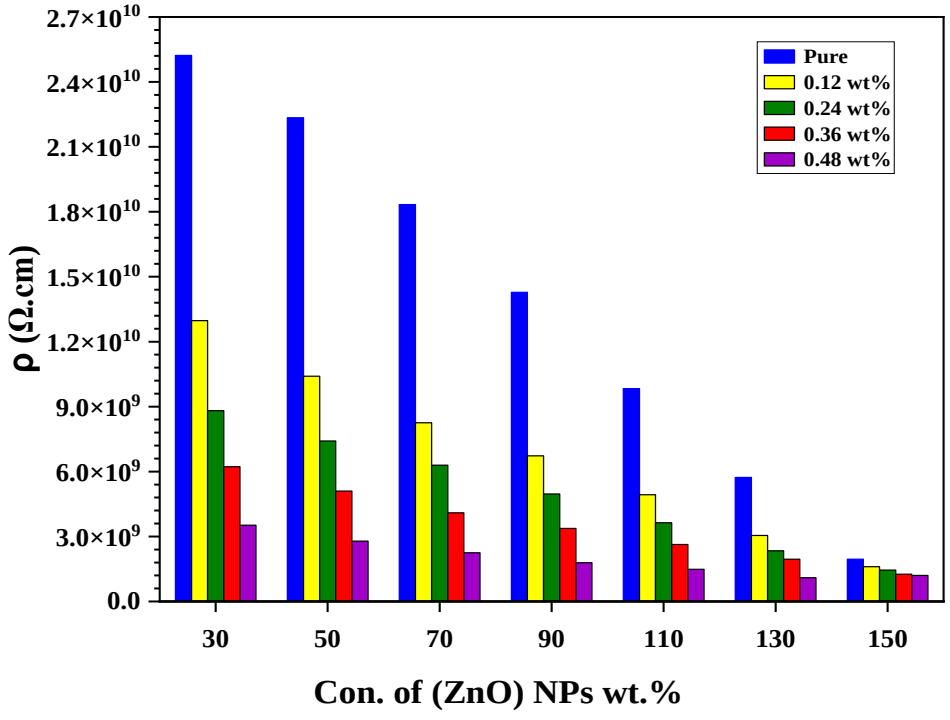

Figure (4.41): plot of D.C resistivity with ZnO nanoparticle wt.% concentration of (Bi_2O_3:ZnO) thin films at 473 K.

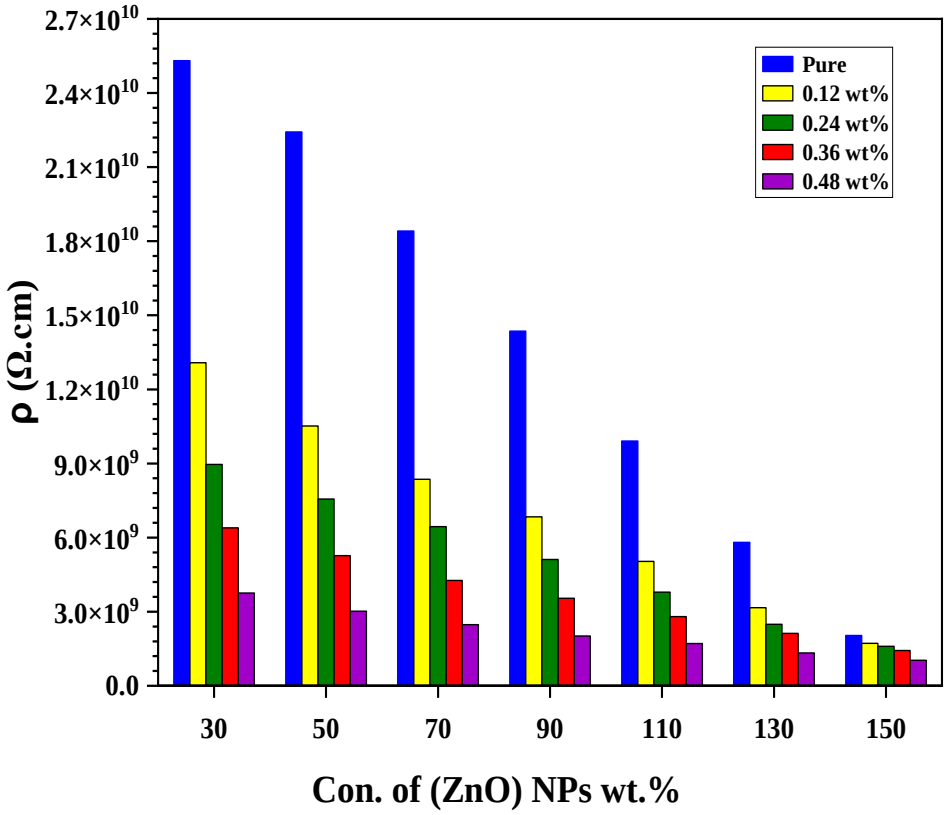

Figure (4.42): plot of D.C resistivity with ZnO nanoparticle wt.% concentration of (Bi_2O_3:ZnO) thin films at 573 K.

4.4.2 The effect of temperature on the electrical conductivity σ_{dc} of (Bi_2O_3:ZnO) thin films

Figures (4.43) and (4.44) show the variation of the electrical conductivity for (Bi_2O_3:ZnO) thin films with temperature. From these figures, it is noted that the conductivity increases with increasing temperature. This indicates that this material has a negative thermal coefficient of resistance; its resistance reduces as the temperature rises because (ZnO) molecules can act as traps for migrating charge carriers via a hopping process. Consequently, the surrounding charge carriers are liberated, and the conductivity of (Bi_2O_3:ZnO) thin films improves due to the increasing charge carriers and the transfer of these charges [149]. On the contrary, the resistivity decreases with increasing temperature, as shown in the figures (4.45) and (4.46). These results are similar to the results of the previous researcher [150].

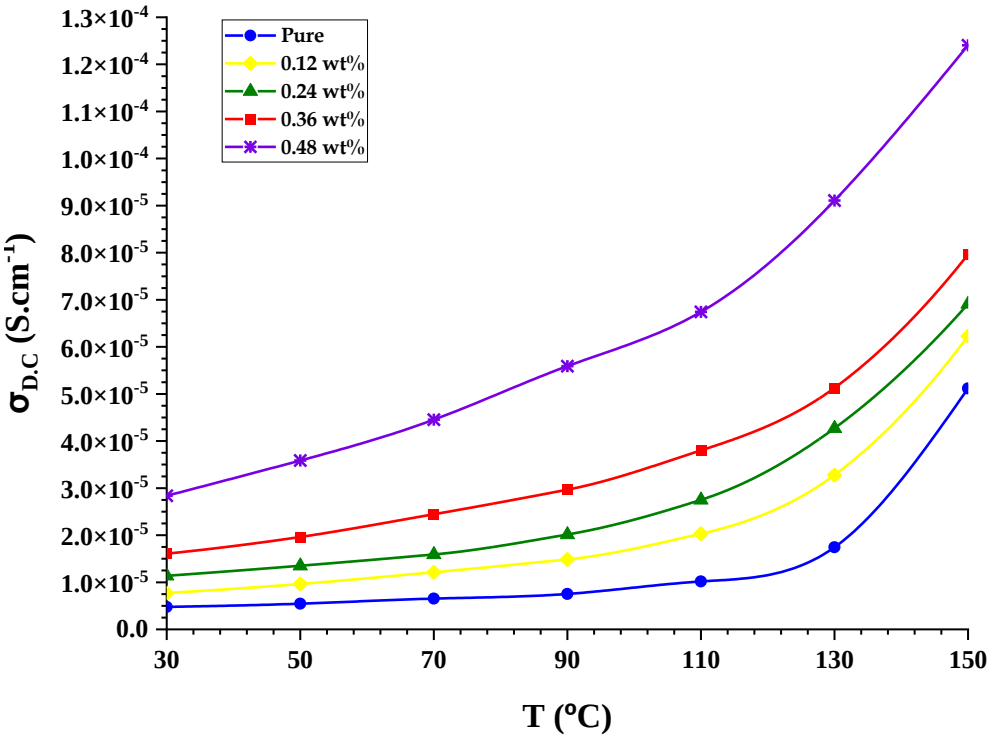

Figure (4.43): Variation of D.C electrical conductivity with temperature of (Bi_2O_3:ZnO) thin films at 473 K.

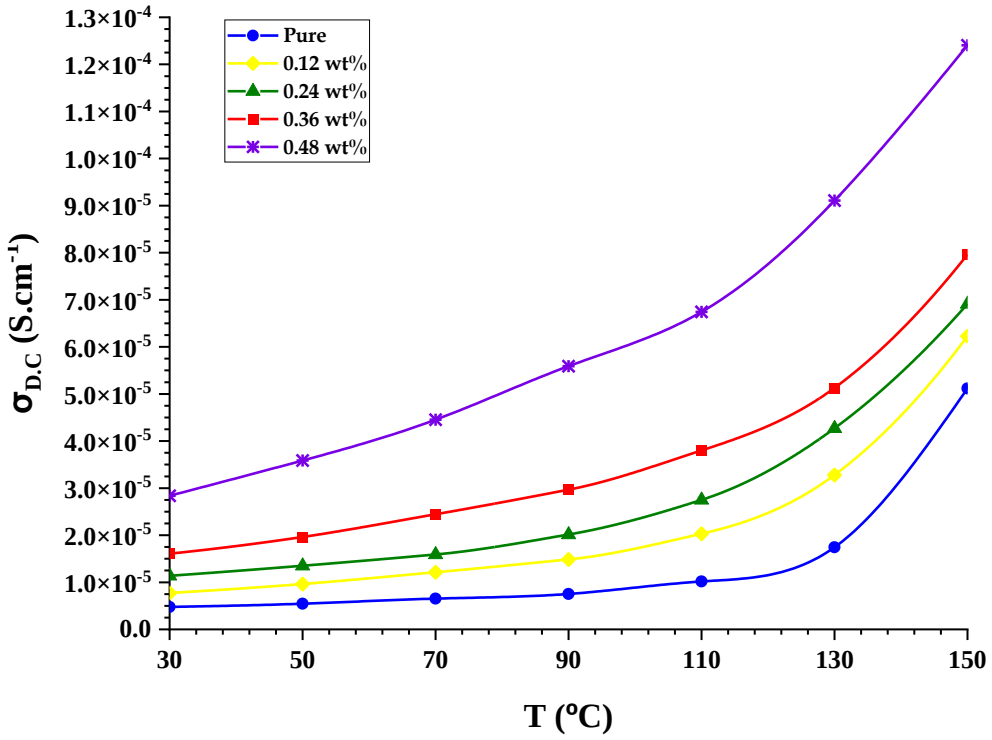

Figure (4.44): Variation of D.C electrical conductivity with temperature of (Bi_2O_3:ZnO) thin films at 573 K.

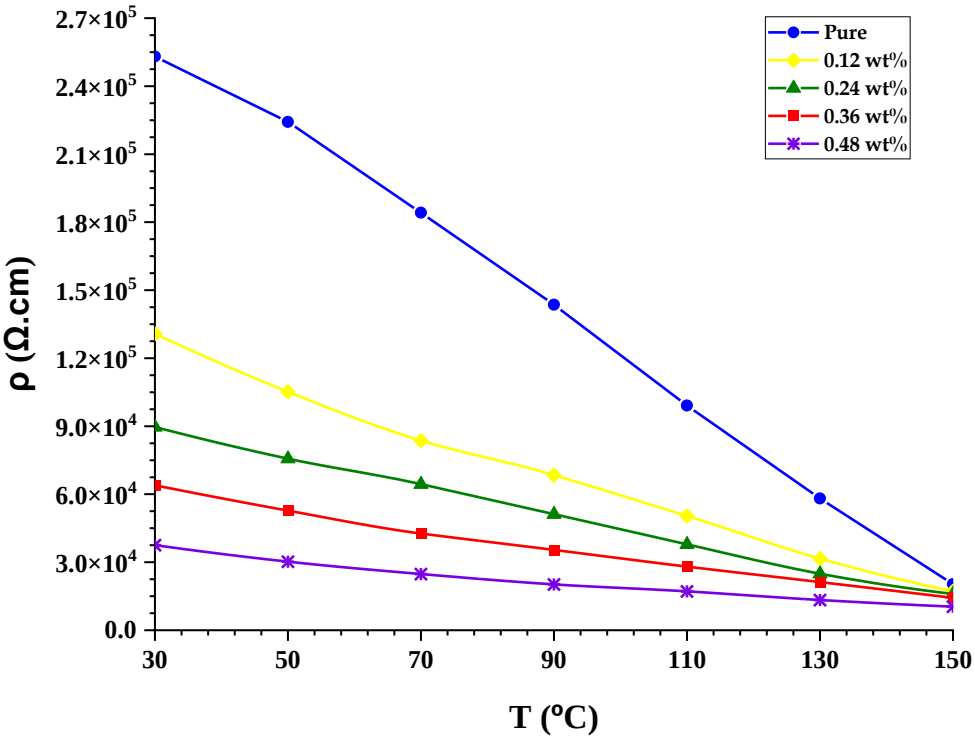

Figure (4.45): Variation of D.C resistivity with temperature of (Bi_2O_3:ZnO) thin films at 473 K.

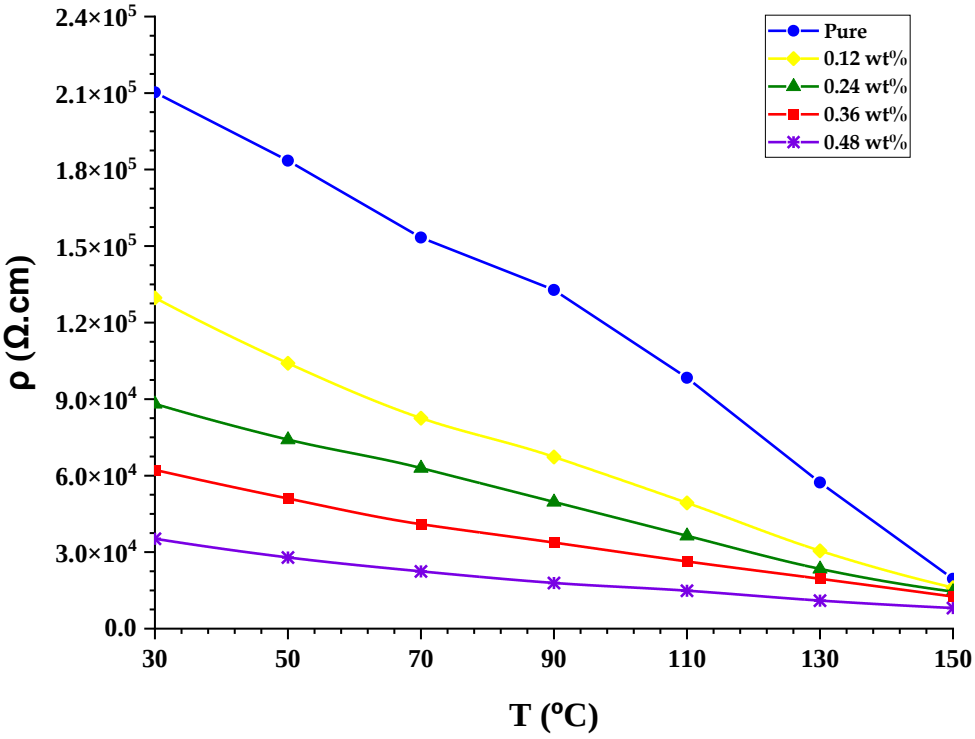

Figure (4.46): Variation of D.C resistivity with temperature of (Bi_2O_3:ZnO) thin films at 573 K.

4.4.3 The activation energy of (Bi_2O_3:ZnO) thin films

Figures (4.47) and (4.48) show the relation between $Ln\sigma_{D.C}$ and the inverse absolute temperature for (Bi_2O_3:ZnO) thin films. The activation energy was calculated by using equation (2.28). The experimental results show that activation energy values ranging from (0.207 eV) to (0.115 eV) for (Bi_2O_3:ZnO) at 473 K and from(0.187 eV) to (0.109 eV) for (Bi_2O_3:ZnO) at 573 K, as shown in tables (4.8), at high value of activation energy for pure thin film (Bi_2O_3) blends attributed to the existence of free ions, and decrease of activation energy with the increasing of the nanoparticles concentrations, the variation of activation energies of (Bi_2O_3:ZnO) thin films with nanoparticles concentrations, as shown in figure (4.49) and (4.50).

These figures show that activation energies decreases with the increasing nanoparticle's concentrations for thin films. This behavior is attributed to creating local energy levels in the energy gap, which act as traps for charge carriers. Current Transmission Mechanism The current is transport in the thin films by tunneling according to the activation energy, where one activation energy appears [166]. These results are similar to the results of the previous researcher [167].

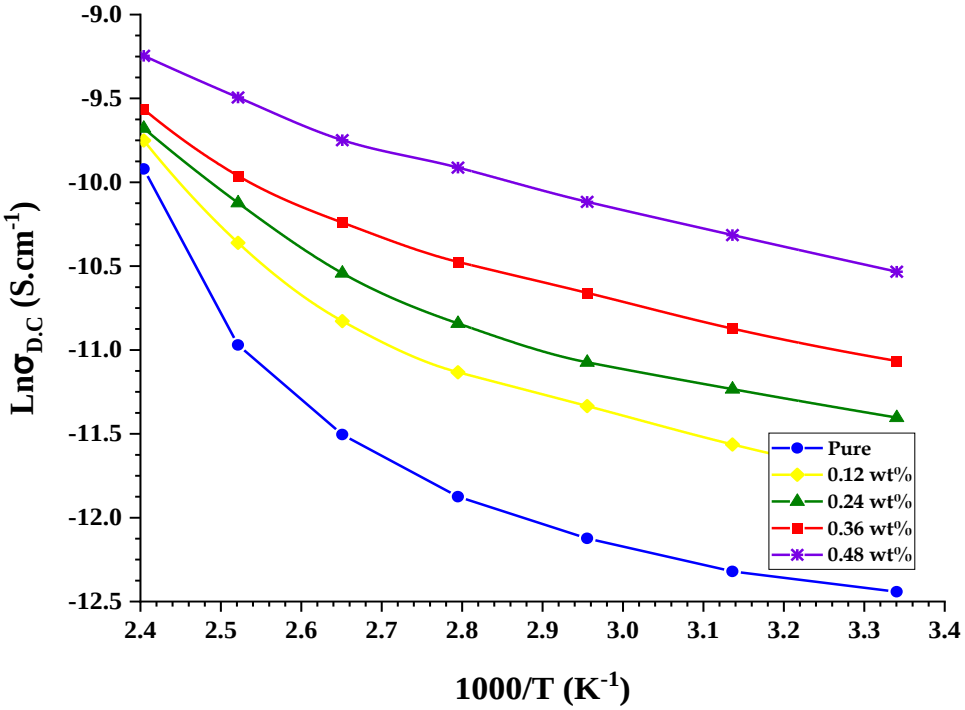

Figure (4.47): Variation of Ln σ electrical conductivity with inverse absolute temperature for (Bi_2O_3:ZnO) thin films at 473 K.

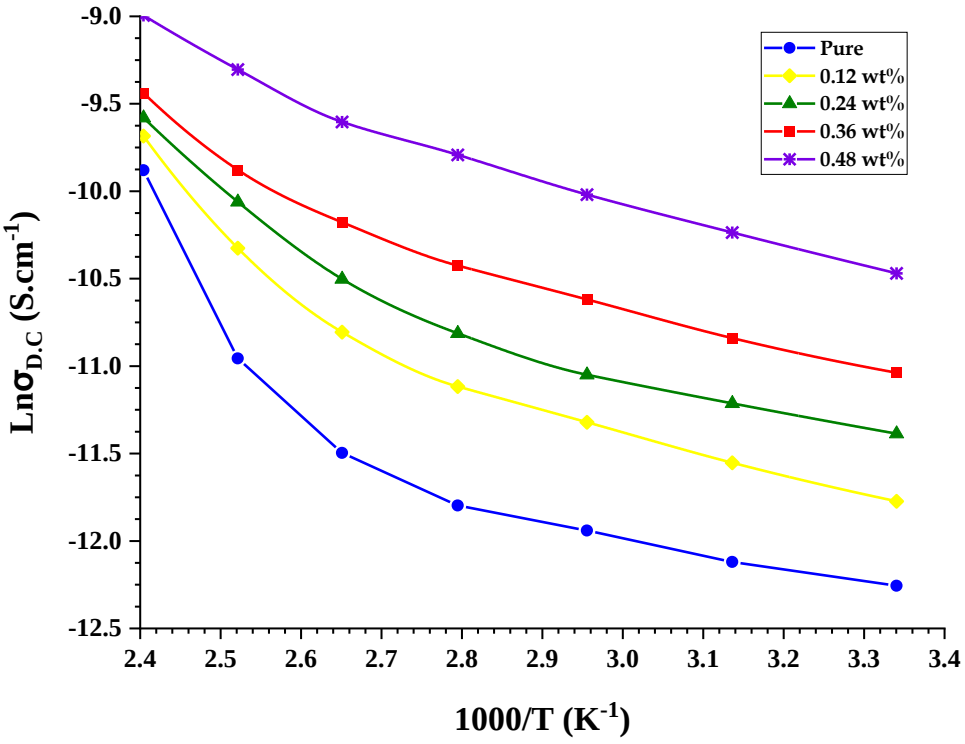

Figure (4.48): Variation of Ln σ electrical conductivity with inverse absolute temperature for (Bi_2O_3:ZnO) thin films at 573 K.

Table (4.8): Values of activation energy for (Bi_2O_3:ZnO) thin films at an annealing temperature of 473K and 573K.

(T) K	Sample No.	Activation Energy Eg (ev)
473 K	**Pure (Bi_2O_3)**	**0.207**
	0.12%(Bi_2O_3:ZnO)	**0.173**
	0.24%(Bi_2O_3:ZnO)	**0.152**
	0.36%(Bi_2O_3:ZnO)	**0.131**
	0.48%(Bi_2O_3:ZnO)	**0.115**
573 K	**Pure (Bi_2O_3)**	**0.187**
	0.12%(Bi_2O_3:ZnO)	**0.177**
	0.24%(Bi_2O_3:ZnO)	**0.159**
	0.36%(Bi_2O_3:ZnO)	**0.139**
	0.48%(Bi_2O_3:ZnO)	**0.109**

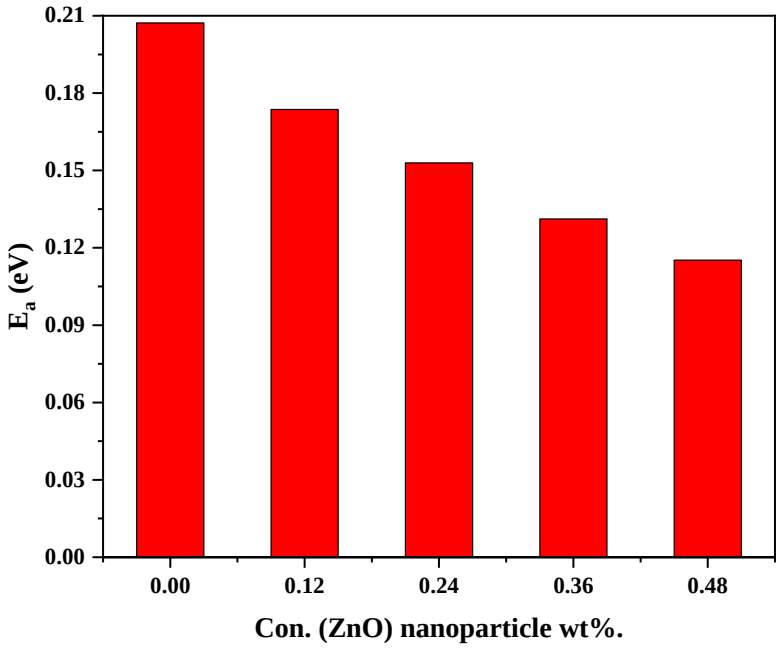

Figure (4.49): Variation of activation energy for D.C electrical conductivity with ZnO wt.% nanoparticles concentration of (Bi_2O_3:ZnO) thin films at 473 K.

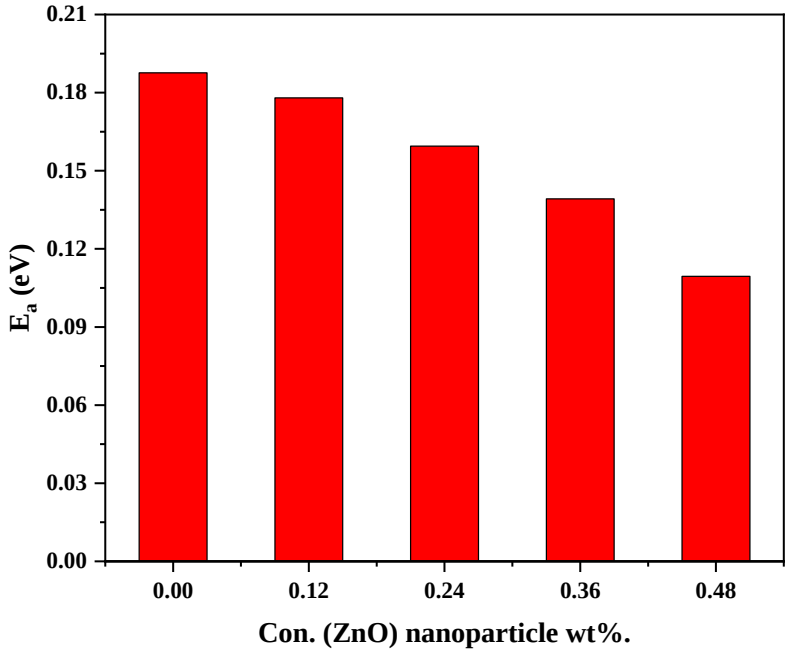

Figure (4.50): Variation of activation energy for D.C electrical conductivity with ZnO wt.% nanoparticles concentration of (Bi_2O_3:ZnO) thin films at 573 K.

4.5 The A.C Electrical Properties

The A.C electrical properties of (Bi_2O_3:ZnO) thin films were studied within frequencies ranging from (100Hz -5MHz). The dielectric constant was calculated by using the equation (2.50) which gives the ratio of the capacitance of a dielectric-filled capacitor (C_p) to a capacitor of free space (C_0). The dielectric loss was calculated by using equation (2.44); using the measured dielectric constant and $tan\delta$, while the A.C electrical conductivity ($\sigma_{A.C}$) was calculated by using equation (2.51) after substituting the measured values of ε'.

4.5.1 The dielectric constant of (Bi_2O_3:ZnO) thin films

Figures (4.51) and (4.52) show the effect of adding the Zinc oxide nanoparticles on the dielectric constant at 100Hz and 35°C. From these figures, we note that the dielectric constant increases with the increasing of the concentration of Zinc oxide nanoparticles.

The reason for this increase in the value of the dielectric constant is the formation of a continuous network of Zinc oxide nanoparticles inside the thin films; at low concentrations, Zinc oxide nanoparticles take the form of clusters or separated groups; hence, the dielectric constant becomes approximately low, and at high concentrations, Zinc oxide nanoparticles form a continuous network inside the thin films and because the increase of (Cp) for the storage charges, and so the value of dielectric constant increases with the volumetric rate of the Zinc oxide nanoparticles. This is similar to the results reached by the researchers[168].

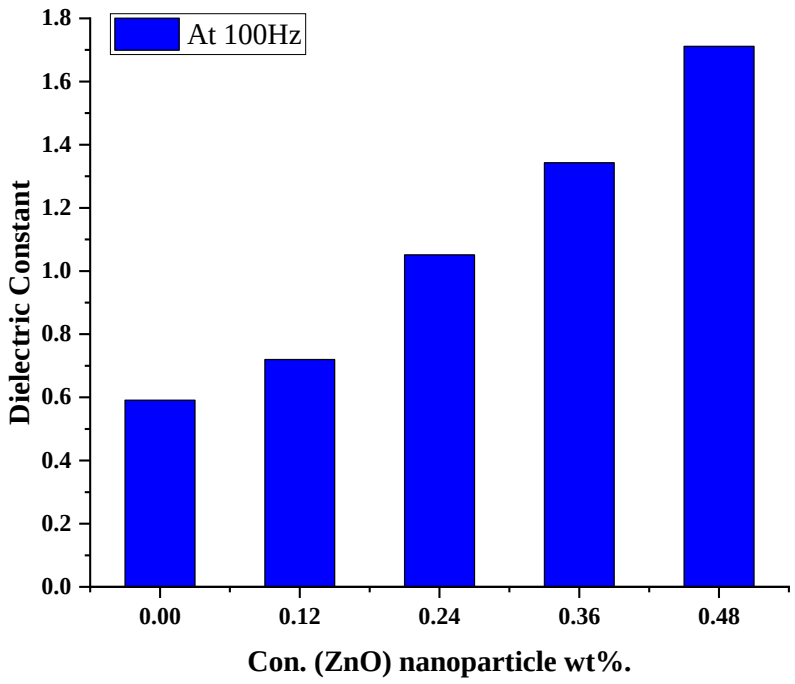

Figure (4.51): Variation of dielectric constant with ZnO at 100 Hz of (Bi_2O_3:ZnO) thin films at 473 K.

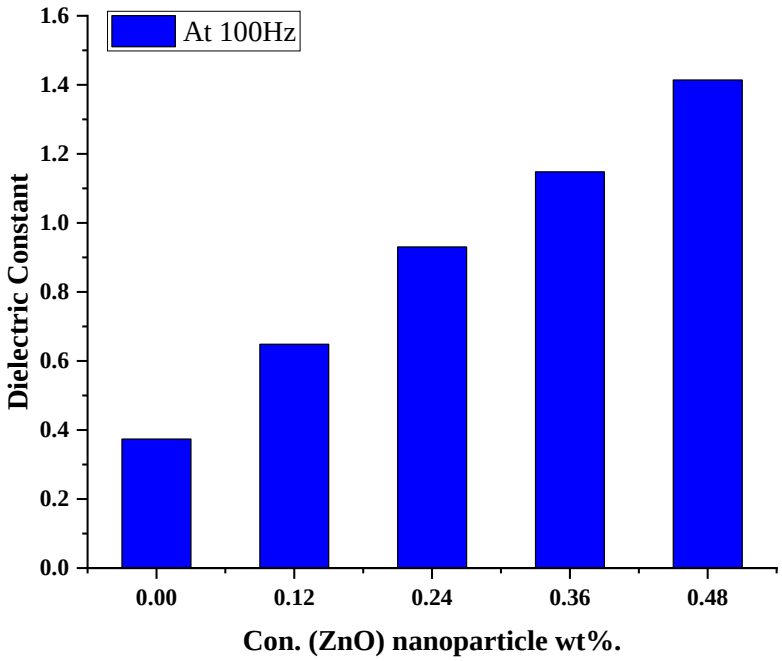

Figure (4.52): Variation of dielectric constant with ZnO at 100 Hz of (Bi_2O_3:ZnO) thin films at 573 K.

Figures (4.53) and (4.54) show the variation of the dielectric constant of (Bi_2O_3:ZnO) thin films with frequency. These figures show that the dielectric constant values decrease when the applied field frequency increases. The increase of frequencies results in the decrease of space charge polarization (interfacial polarization) to the total polarization. The space charge polarization becomes the more contributing type of polarization at low frequencies and less contributing with the increase of frequency. This would result in the decrease of dielectric constant values for all samples of (Bi_2O_3:ZnO) thin films with the increase of the electric field frequency (f).

Other types of polarization appear at high frequencies, such as ion polarization, because the mass of an ion is larger than that of an electron. Electrons even respond to high frequencies of field oscillations. The low mass of electrons makes electronic polarization the only type at higher frequencies. This makes the dielectric constant approximately constant for

all samples at high frequencies. This is similar to the results reached by the researcher [169].

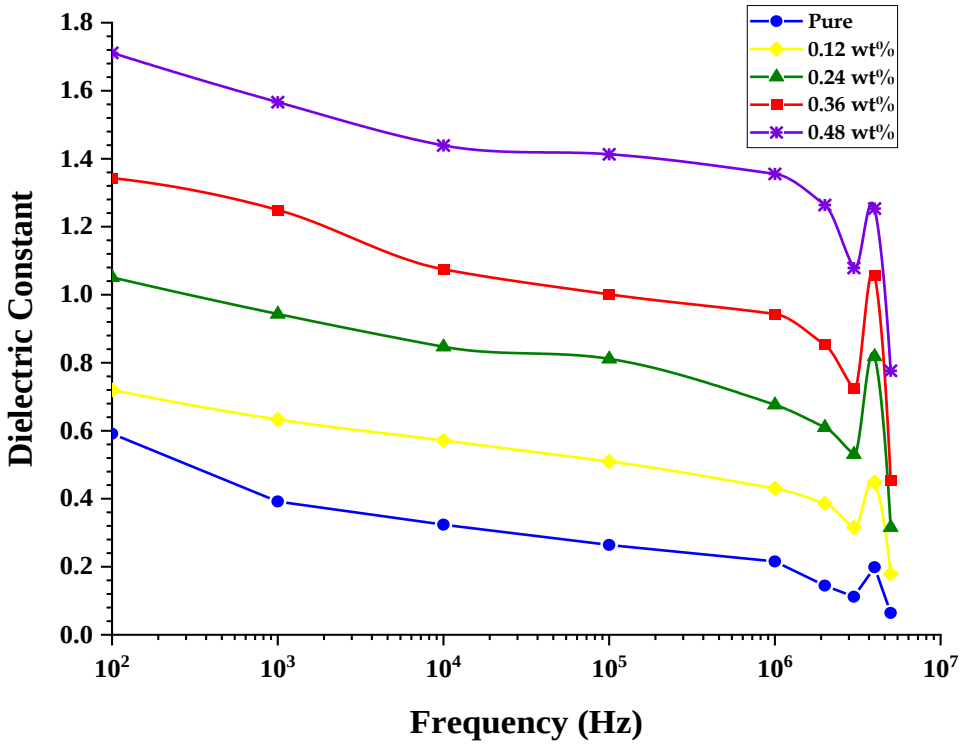

Figure (4.53): Variation of the dielectric constant of (Bi_2O_3:ZnO) thin films with frequency at 473 K.

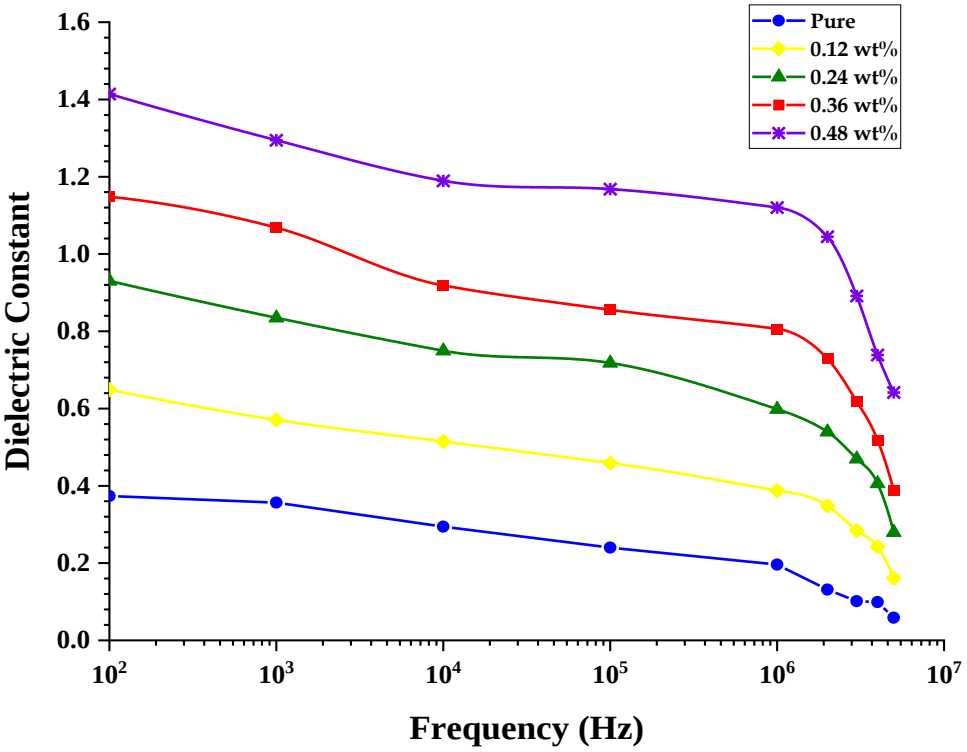

Figure (4.54): Variation of the dielectric constant of (Bi_2O_3:ZnO) thin films with frequency at 473 K.

4.5.2 The dielectric loss of (Bi_2O_3:ZnO) thin films

Figures (4.55) and (4.56) show the dielectric loss as a function of the frequency of (Bi_2O_3:ZnO) thin films. The figures show that the dielectric loss of thin films decreases with increasing the frequency of the applied electric field. This behavior is attributed to the low contribution of space charge polarization. Also, the dielectric loss has a high value for (Bi_2O_3:ZnO) thin films at low frequency and decreases when the frequency increases. Also, the dielectric loss of (Bi_2O_3:ZnO) thin films increases with the increase in the concentration of nanoparticles, as in Figures (4.57) and (4.58), and this is related to the increase in the number of charge carriers. At low concentrations of nanoparticles, they form clusters. When the concentration of nanoparticles reaches high, the nanoparticles form a continuous network in the thin films [170]. These results are similar to the results of the previous researcher [146].

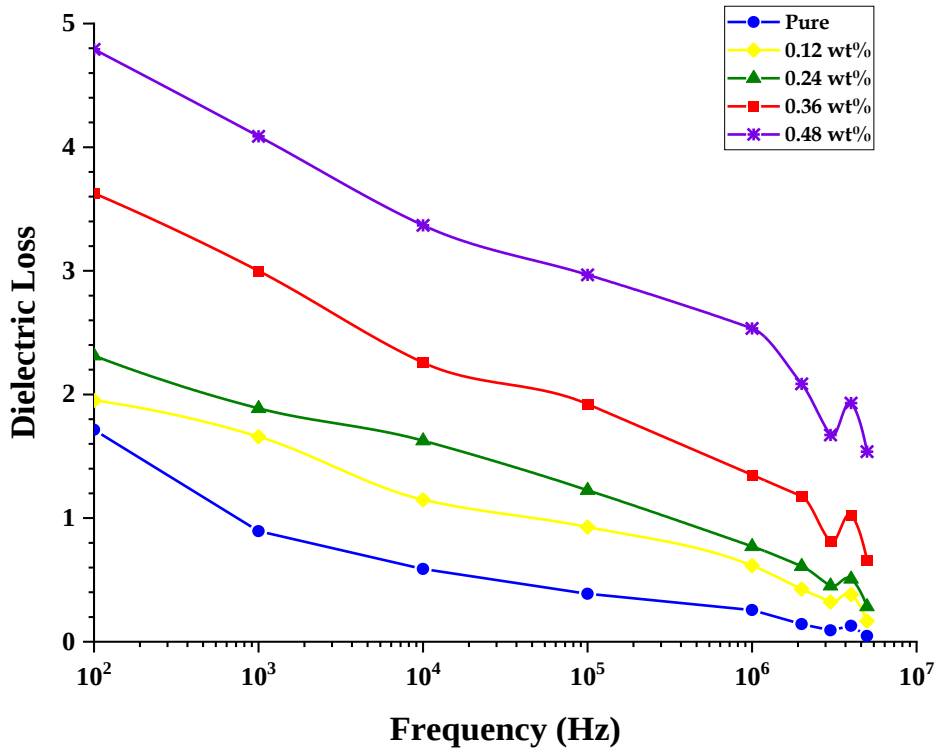

Figure (4.55): Variation of the dielectric loss with frequency of (Bi_2O_3:ZnO) thin films at 473 K.

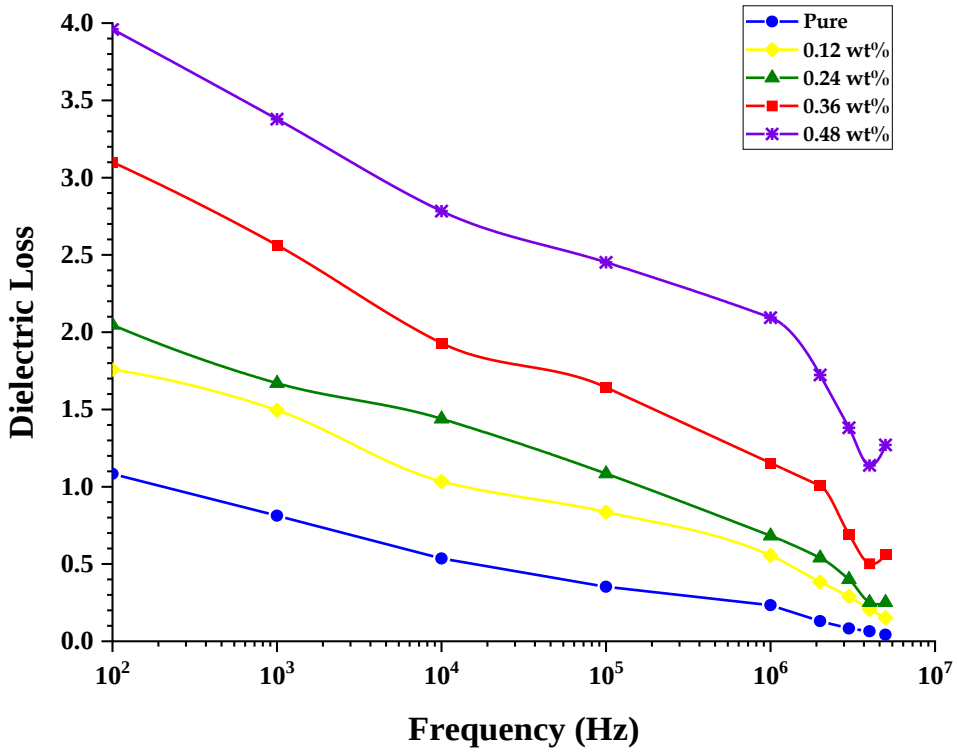

Figure (4.56): Variation of the dielectric loss with frequency of (Bi_2O_3:ZnO) thin films at 573 K.

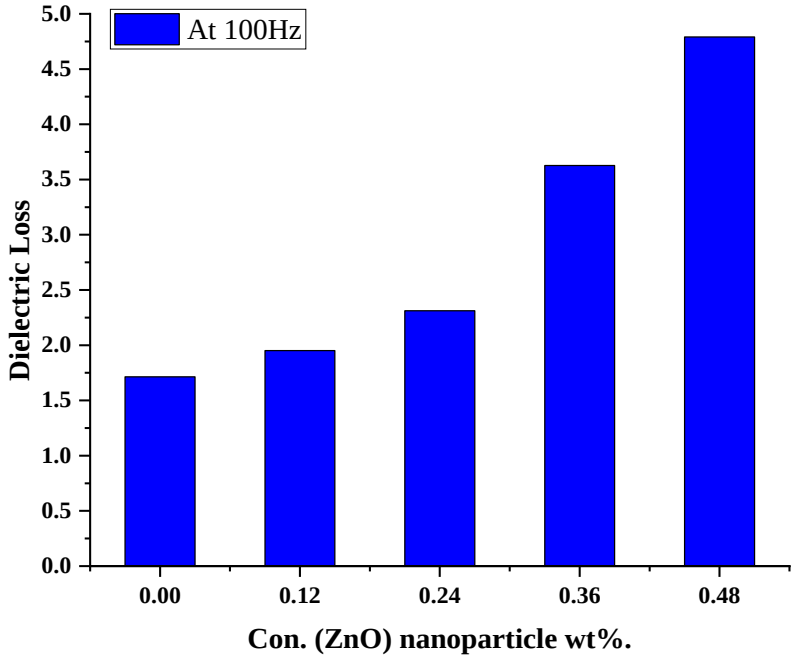

Figure (4.57): plot of the dielectric loss with ZnO of (Bi_2O_3:ZnO) thin films at 473 K.

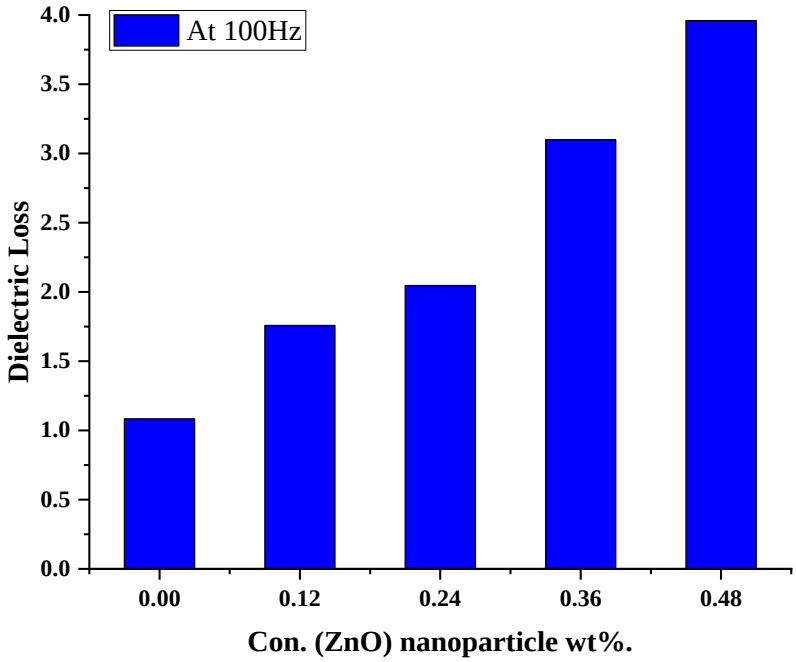

Figure (4.58): plot of the dielectric loss with ZnO of (Bi_2O_3:ZnO) thin films at 573 K.

4.5.3 The A.C electrical conductivity of (Bi_2O_3:ZnO) thin films

The A.C conductivity of (Bi_2O_3:ZnO) thin films at 100 Hz and room temperature (35 ^{0}C) varies as a function of zinc oxide content Figures (4.59) and (4.60). Concentrations of (ZnO) nanoparticles result in higher A.C conductivity. The greater quantity of charge carriers is responsible for the observed conductivity enhancement. These results agree with other researcher result [110].

Figures (4.61) and (4.62) show the variation of the conductivity for (Bi_2O_3:ZnO) thin films with frequency. The figures show that A.C conductivity increases considerably with the increase of frequency (f) from 100 Hz to 5×10^6 Hz. This is attributed to the hopping of charge carriers in the localized state and the excitation of charge carriers to upper states in the conduction band. Consequently, the conductivity increasing when the frequency increases for all different ratio of the zinc oxide nanoparticles for (Bi_2O_3:ZnO) thin films. This is similar to the results reached by the researcher [169,171].

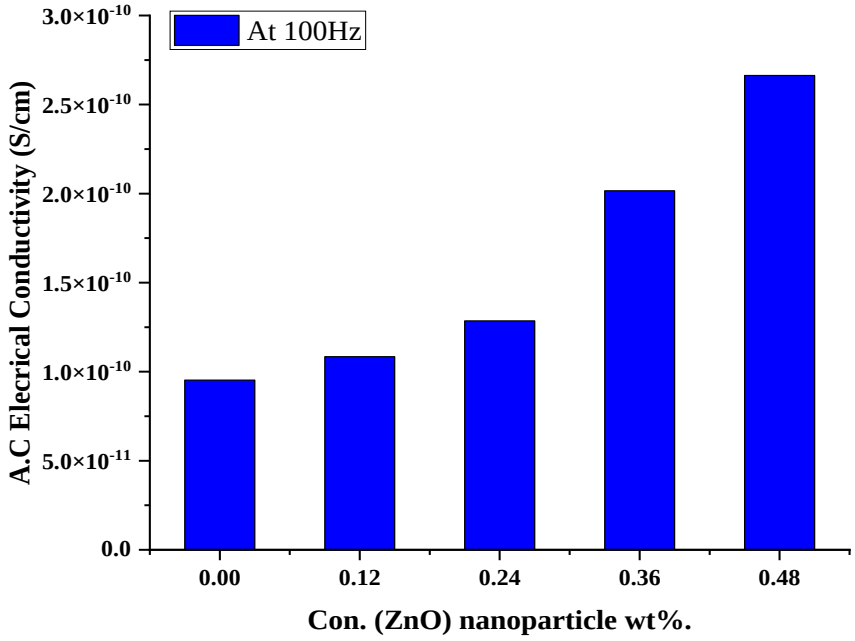

Figure (4.59): plot of A.C electrical conductivity with ZnO nanoparticles wt.% concentration at 100 Hz of (Bi_2O_3:ZnO) thin films at 473 K.

.

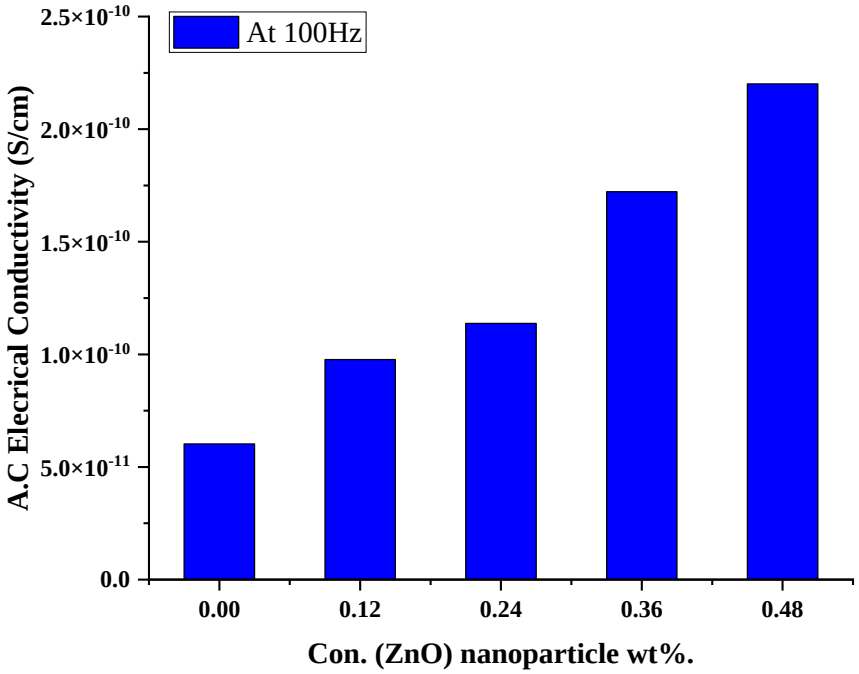

Figure (4.60): plot of A.C electrical conductivity with ZnO nanoparticles wt.% concentration at 100Hz of (Bi_2O_3:ZnO) thin films at 573 K.

.

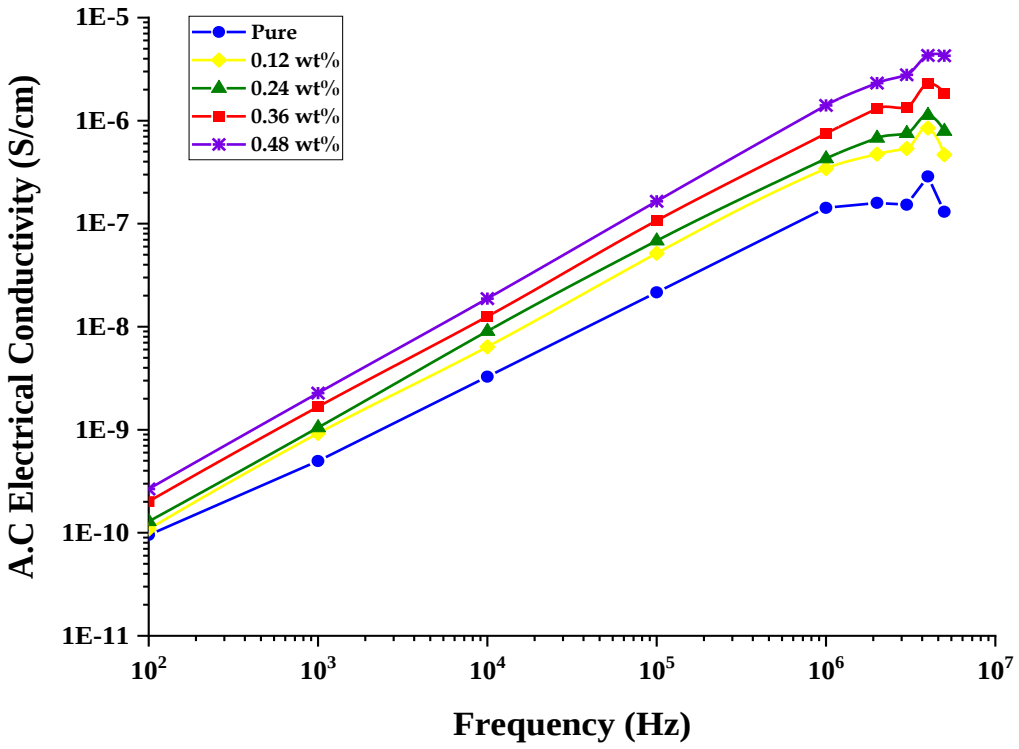

Figure (4.61): Variation of A.C electrical conductivity with frequency of (Bi_2O_3:ZnO) thin films at 473 K.

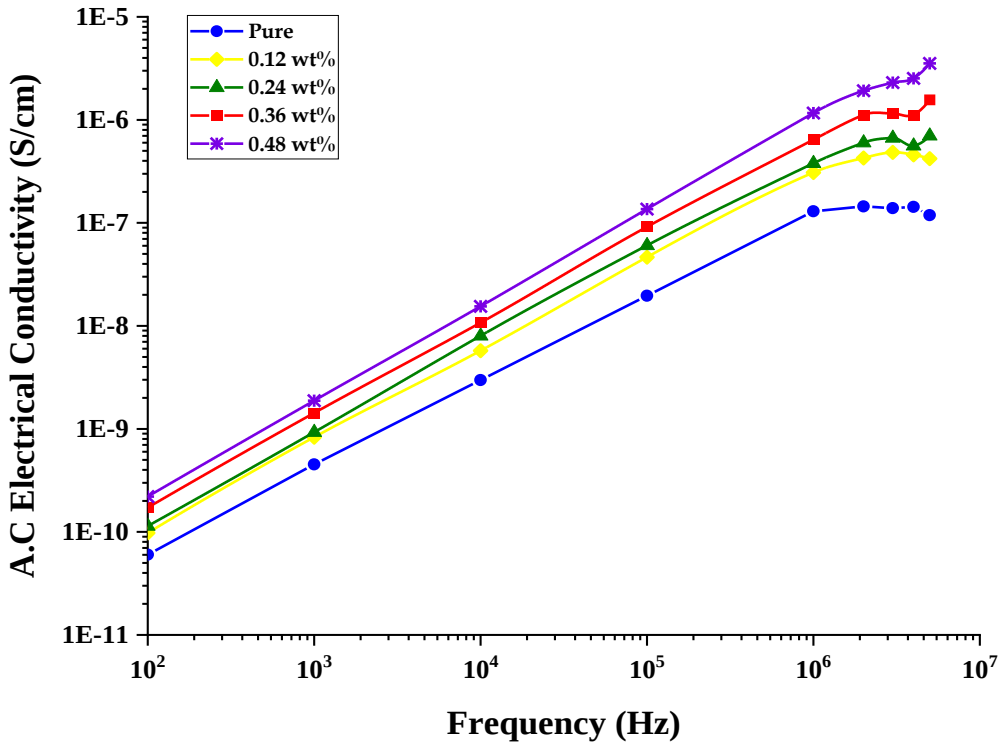

Figure (4.62): Variation of A.C electrical conductivity with frequency of (Bi_2O_3:ZnO) thin films at 573 K.

4.6 Application of (Bi_2O_3:ZnO) Thin Films as Gas Sensors

In this work, the sensing for H_2S and NO_2 gas properties of thin films (Bi_2O_3:ZnO) thin films are investigated as a function of the operating temperature and response and recovery time. In order to understand the temperature dependence on sensitivity to different doping ratios of thin film specimens for chemical sensing H_2S and NO_2 gas with concentrations of about 50.55ppm. The sensing test used a 4% H_2S, NO_2 and 96 % air mixed ratio.

4.6.1 Effect the operation temperature on sensing properties

In general, the surface states play a very important role in the response of solid-state chemical gas sensors. increasing the surface-to-volume ratio or enhancing the surface adsorption which will increase the resistance change and improve the sensitivity, the sensitivity of the sensor is affected by the operating temperature.

The higher temperature enhances the surface interaction of the thin films and results in a higher sensitivity in the temperature range. Figures (4.63) and (4.64) show the variation of the gas sensitivity as a functional operating temperature in the range of (200-300 °C) for (Bi_2O_3:ZnO) thin films deposited on a glass substrate for different doping. It is clear in the Figures that the sensitivity of all samples increases with the increase in the operating temperature, reaching a maximum value corresponding to the optimum operating temperature, which is 250˚C for all samples and reaches the maximum (Bi_2O_3:ZnO) thin films and then decreases with the increase in the operating temperature. The increase in sensitivity with higher operating temperature may be attributed to an increase in the charge carrier density in the active surface and leads to an increase in sensitivity [141].

The change in the temperature reveals resistance of the film decreases as the temperature increases from room temperature to 250˚C showing a typical negative temperature coefficient of resistance, due to

thermal excitation of the charge carriers in semiconductors [172]. Above 250 for all samples, sensor film shows a positive temperature coefficient of film resistance as temperature increases further, which may be due to the saturation of the conduction band with electrons elevated from shallow donor levels caused by oxygen vacancies. Finally, at this point, an increase in temperature leads to a decrease in electron mobility and a subsequent increase in resistance. Similar observations are made by other research groups [173].

The sensitivity factor (S%) at different temperatures is calculated by equation (2.52). The highest average sensitivity of (Bi_2O_3:ZnO) thin films to annealing score 473 K for H_2S gas was found to be 96.47% at 200 ^{0}C at an additional 0.48 wt.% ZnO and the lowest average sensitivity was 68.58% at 200 ^{0}C for at an additional 0.36 wt.% ZnO as in the figure (4.63). (Bi_2O_3:ZnO) thin films are not sensitive to the H2S: air mixture ratio at temperatures less than 200 ^{0}C, as shown in Table (4.9). As for NO_2 gas at an annealing degree of 475 K, the highest average sensitivity of (Bi_2O_3:ZnO) thin films was 88.97% at 300 ^{0}C at an additional 0.48 wt.% ZnO and the lowest average sensitivity was 4.52% at 200 ^{0}C for adding 0.24 wt.% ZnO as in the figure (4.64), as shown in table (4.10).

As for the annealing of 573 K for H_2S gas, the highest average sensitivity of (Bi_2O_3:ZnO) thin films was found to be 69.74% at 200 ^{0}C at an additional 0.48 wt.% ZnO and the lowest average sensitivity was 17.04% at 200 ^{0}C for at an additional 0.12 wt.% ZnO as in figure (4.65), as shown in table (4.11). As for NO_2 gas at an annealing of 573 K, the highest average sensitivity of (Bi_2O_3:ZnO) thin films was 62.5% at 250 ^{0}C at an additional 0.48 wt.% ZnO and the lowest average sensitivity was 4.76% at 200 ^{0}C for adding 0.12 wt.% ZnO as in figure (4.66), as shown in table (4.12).

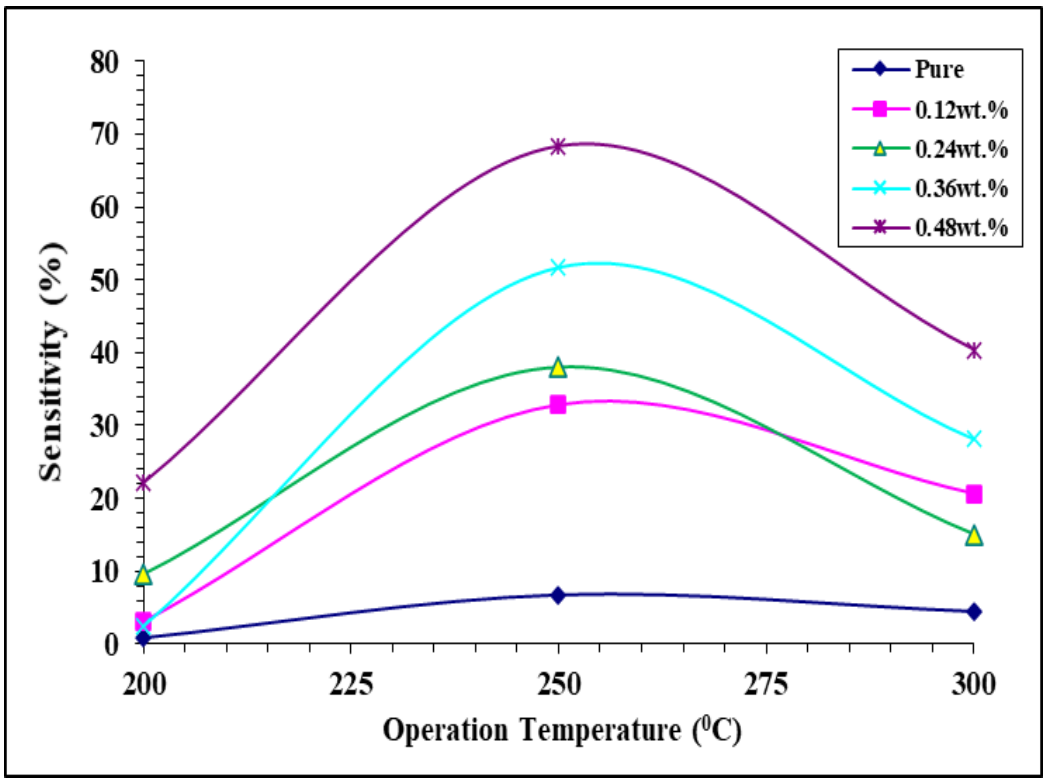

Figure (4.63): The variation of sensitivity with the operating temperature for different doping ZnO of the H_2S gas sensor of (Bi_2O_3:ZnO) thin films at 473 K.

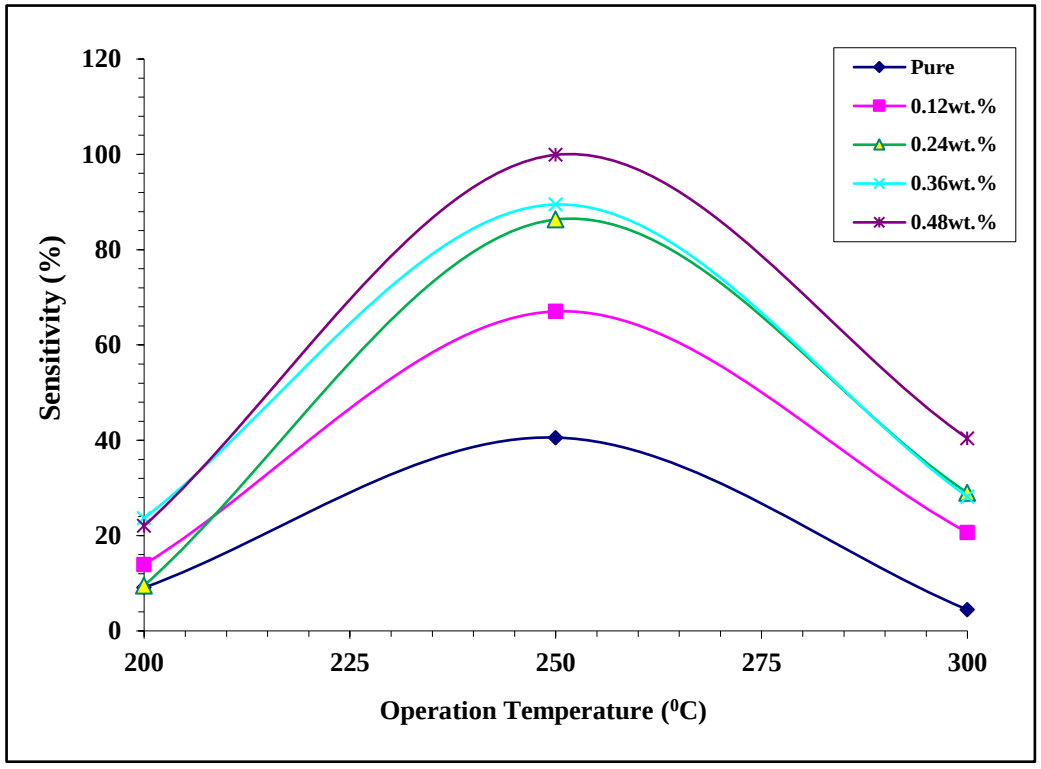

Figure (4.64): The variation of sensitivity with the operating temperature for different doping ZnO of the NO_2 gas sensor of (Bi_2O_3:ZnO) thin films at473 K.

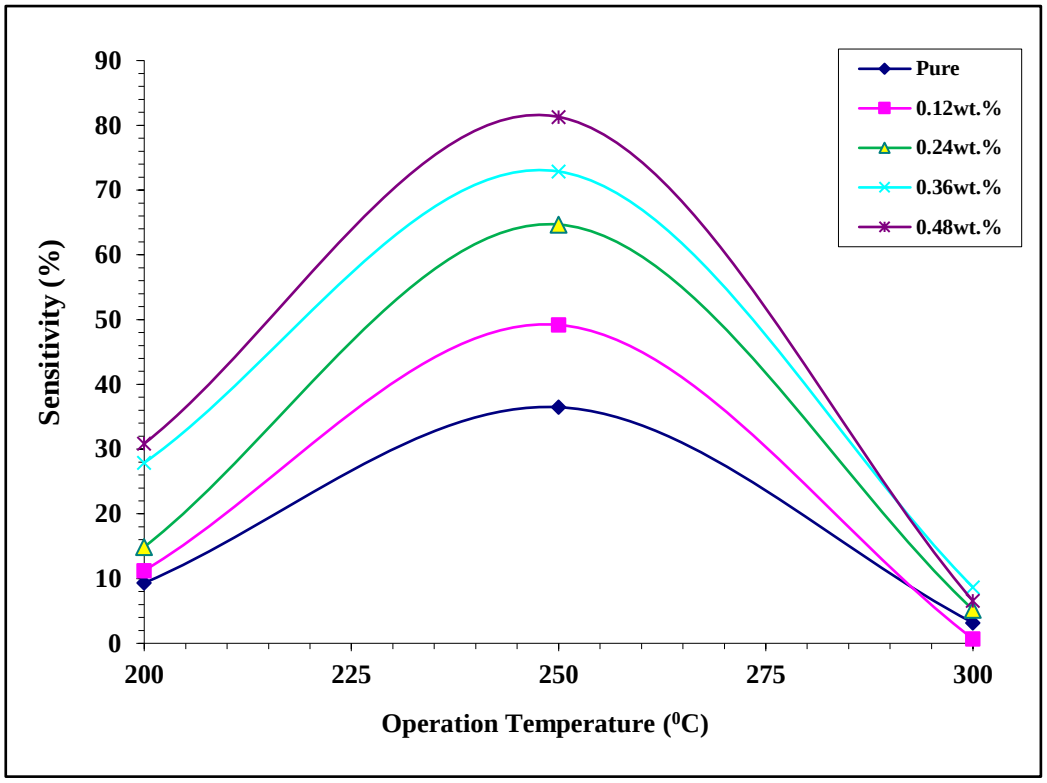

Figure (4.65): The variation of sensitivity with the operating temperature for different doping ZnO of the H_2S gas sensor of (Bi_2O_3:ZnO) thin films at 573 K.

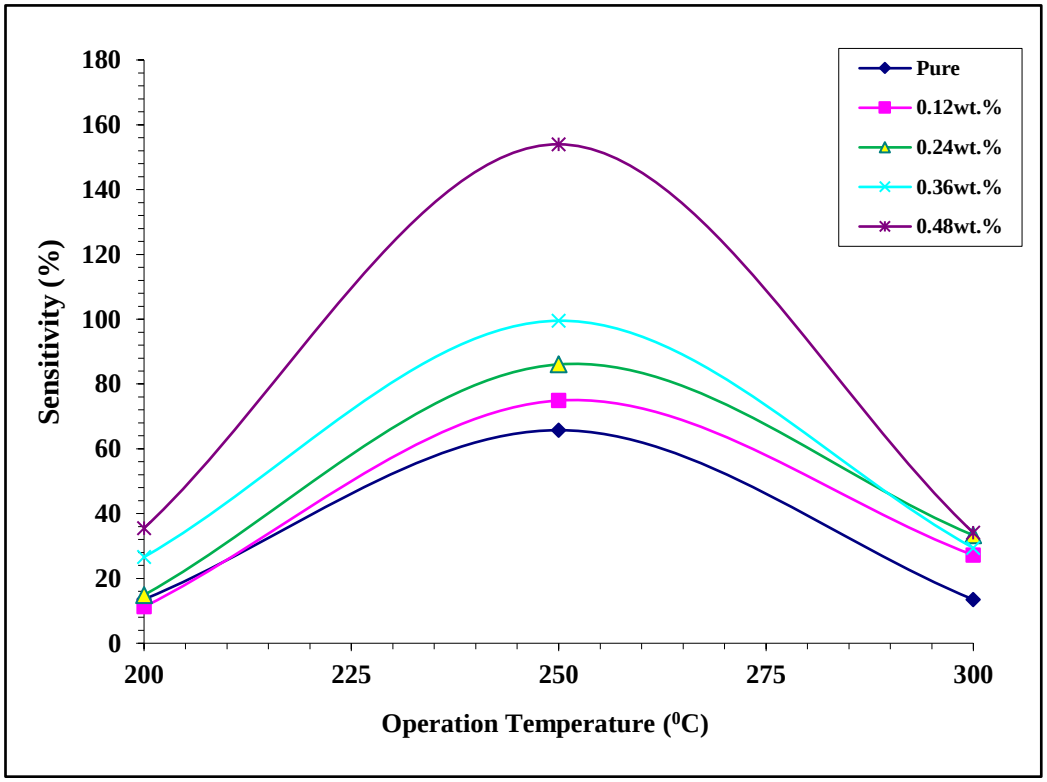

Figure (4.66): The variation of sensitivity with the operating temperature for different doping ZnO of the NO_2 gas sensor of (Bi_2O_3:ZnO) thin films at 573 K.

4.6.2 Response time and recovery time

Response time and recovery time for (Bi_2O_3:ZnO) thin films are about 4% H_2S and NO_2: air. Figures (4.67), (4.68), (4.69), (4.70) and (4.71) show the variation of response and recovery time for H_2S gas as a functional operating temperature in the range (200-300)^{0}C for thin films (Bi_2O_3:ZnO) for annealing temperature 473 K. Figures (4.72), (4.73), (4.74), (4.75) and (4.76) show the variation of the response time and recovery time of NO_2 gas for annealing temperature 473 K.

Figures (4.77), (4.78), (4.79), (4.80), and (4.81) show the variation of response and recovery time for H_2S gas as the functional operating temperature in the range (200–300) ^{0}C for (Bi_2O_3:ZnO) thin films for an annealing temperature of 573 K. Figures (4.82), (4.83), (4.84), (4.85) and (4.86) show the variation of the response and recovery time of NO_2 gas to the annealing temperature of 573 K, deposited on a glass substrate for doping different ZnO doping. It is calculated using equations (2.53) and (2.54).

The responses increase and reach their maximums at a certain temperature and then decrease rapidly with increasing temperature. The shape resulted from the competition between slow kinetics at low temperatures and enhanced desorption at high temperatures. The largest response and recovery time were coming from H_2S at an annealing temperature of 473 K at time 27 sec for response time and 96.3 sec for recovery time when adding 0.24wt.% ZnO, and the least response and recovery time were at 9.9 sec for response time and 39.6 sec for recovery time when adding 0.48wt.% ZnO as shown in Table (4.9). While the largest response and recovery time were coming from NO_2 at an annealing temperature of 473 K at 22.5 sec for response time and 93.6 sec for recovery time when adding 0.24wt.% ZnO and the least response and

recovery time were at 9 sec for response time and 33.3 sec for recovery time when adding 0.48wt.% ZnO as shown in table (4.10).

But at an annealing temperature of 573 K, the largest response and recovery time were coming from H_2S, with 22.5 sec for response time and 90.9 sec for recovery time when adding 0.24wt.% ZnO and the least response and recovery time were at 8.1 sec for response time and 32.4 sec for recovery time when adding 0.48wt.% ZnO, as shown in Table (4.11). While the largest response and recovery time were coming from NO_2 with an annealing temperature of 573 K at 20.7 sec for response time and 81 sec for recovery time when adding 0.24wt.% ZnO and the least response and recovery time were at 7.2 sec for response time and 28.8 sec for recovery time when adding 0.48wt.% ZnO, as shown in table (4.12).

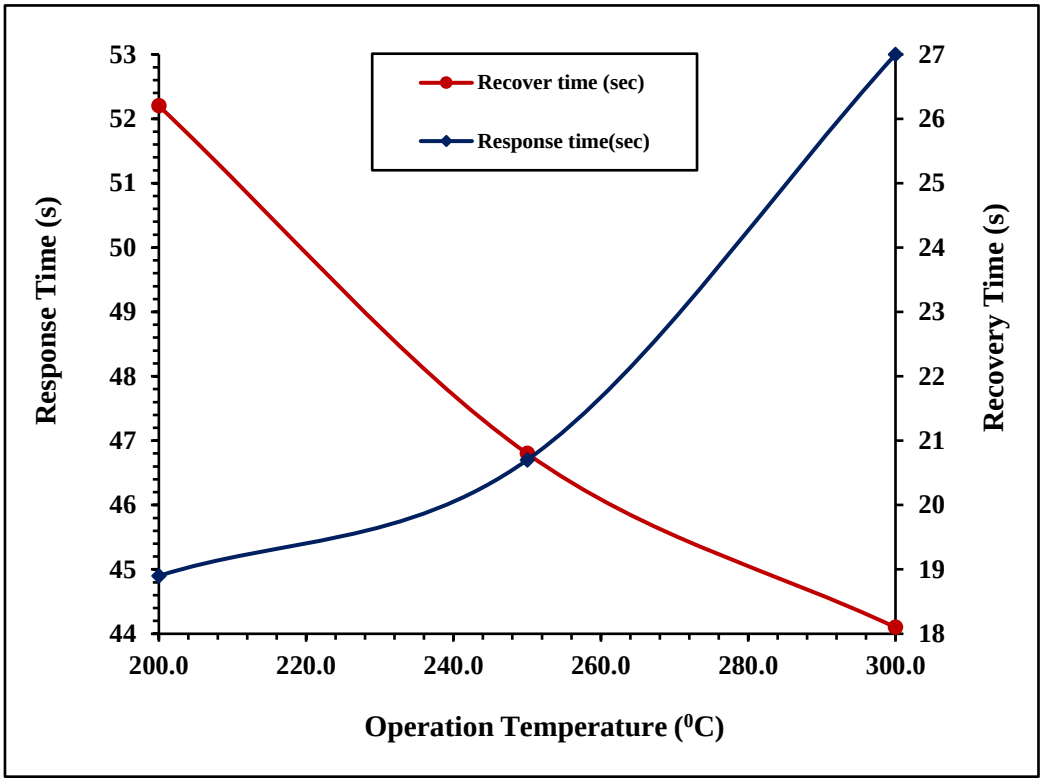

Figure (4.67): The plot of response time and recovery time with the operating temperature for Bi_2O_3 pure for H_2S gas sensor at 473 K.

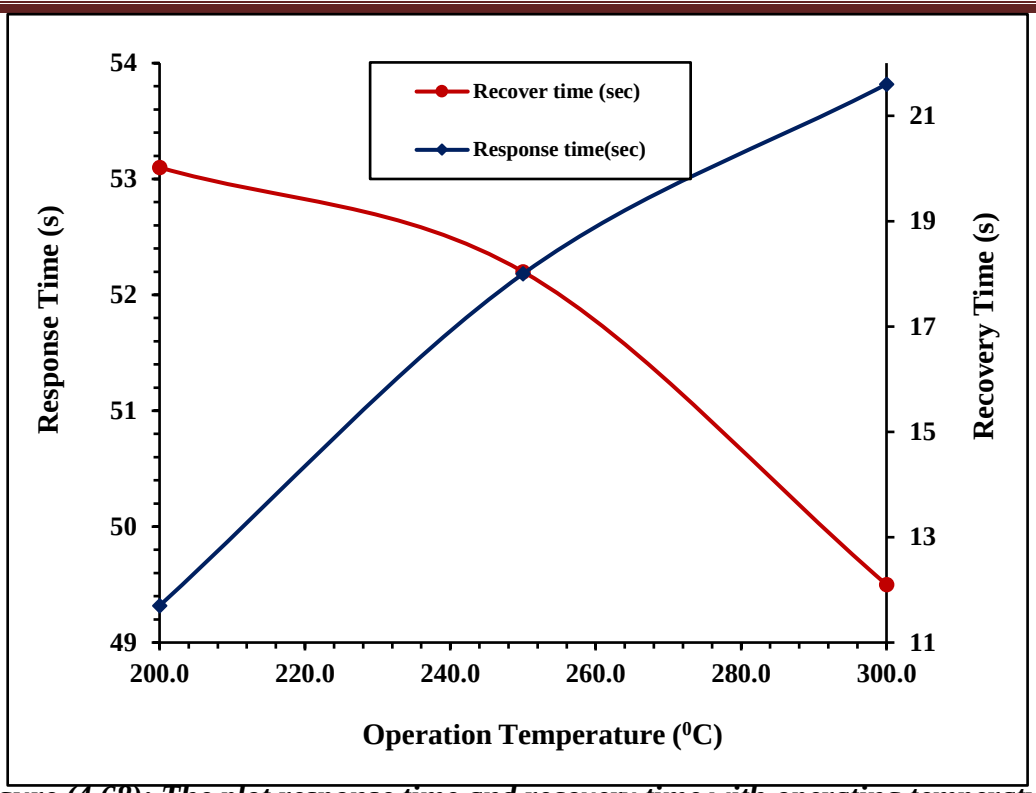

Figure (4.68): The plot response time and recovery time with operating temperature for a concentration of 0.12 wt.% ZnO nanoparticles for (Bi_2O_3:ZnO thin films for an H_2S gas sensor at 473 K.

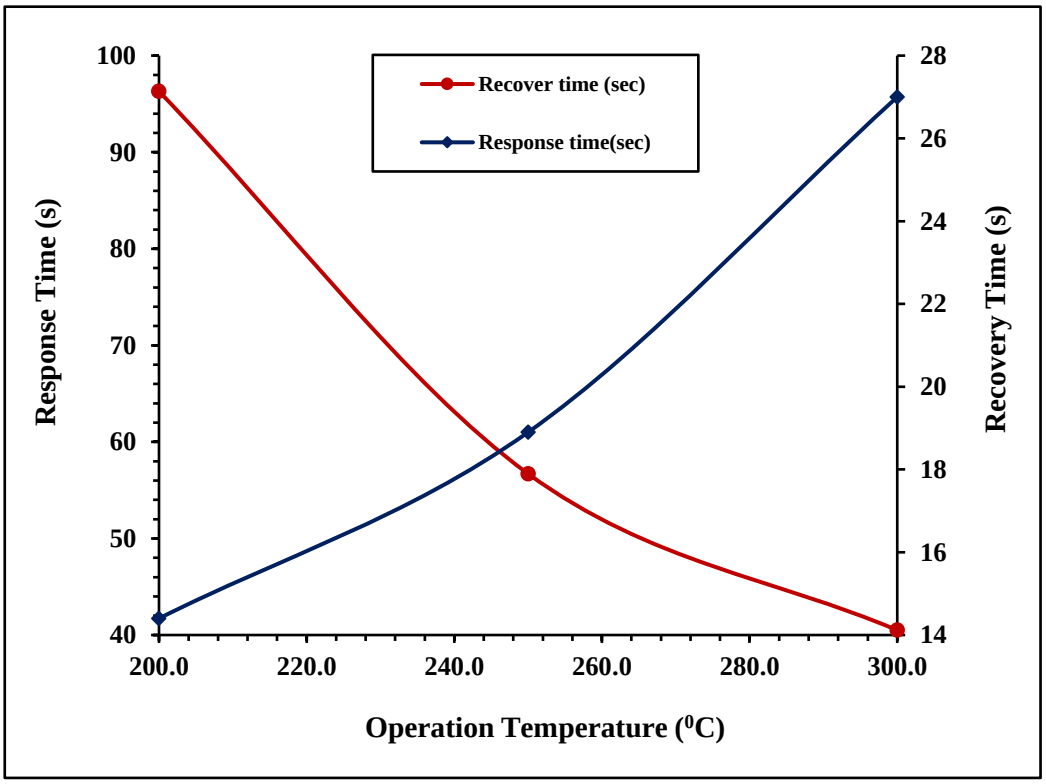

Figure (4.69): The plot response time and recovery time with operating temperature for a concentration of 0.24 wt.% ZnO nanoparticles for (Bi_2O_3:ZnO) thin films for an H_2S gas sensor at 473 K.

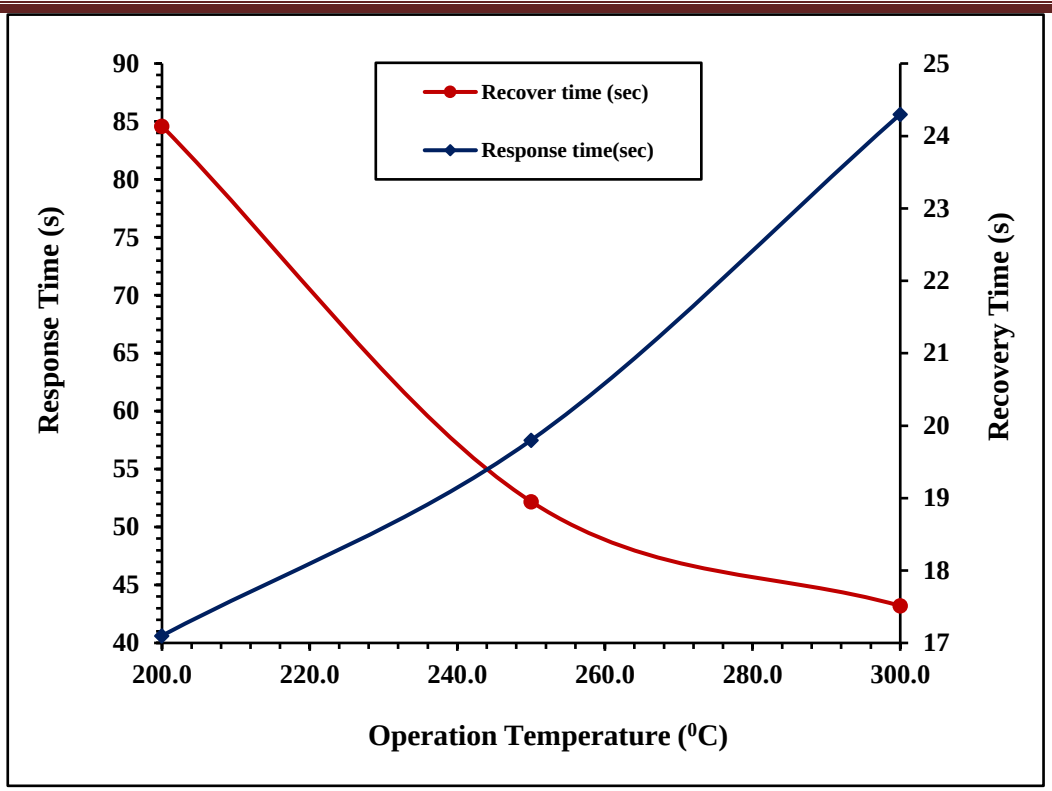

Figure (4.70): The plot response time and recovery time with operating temperature for a concentration of 0.36 wt.% ZnO nanoparticles for (Bi_2O_3:ZnO) thin films for an H_2S gas sensor at 473 K.

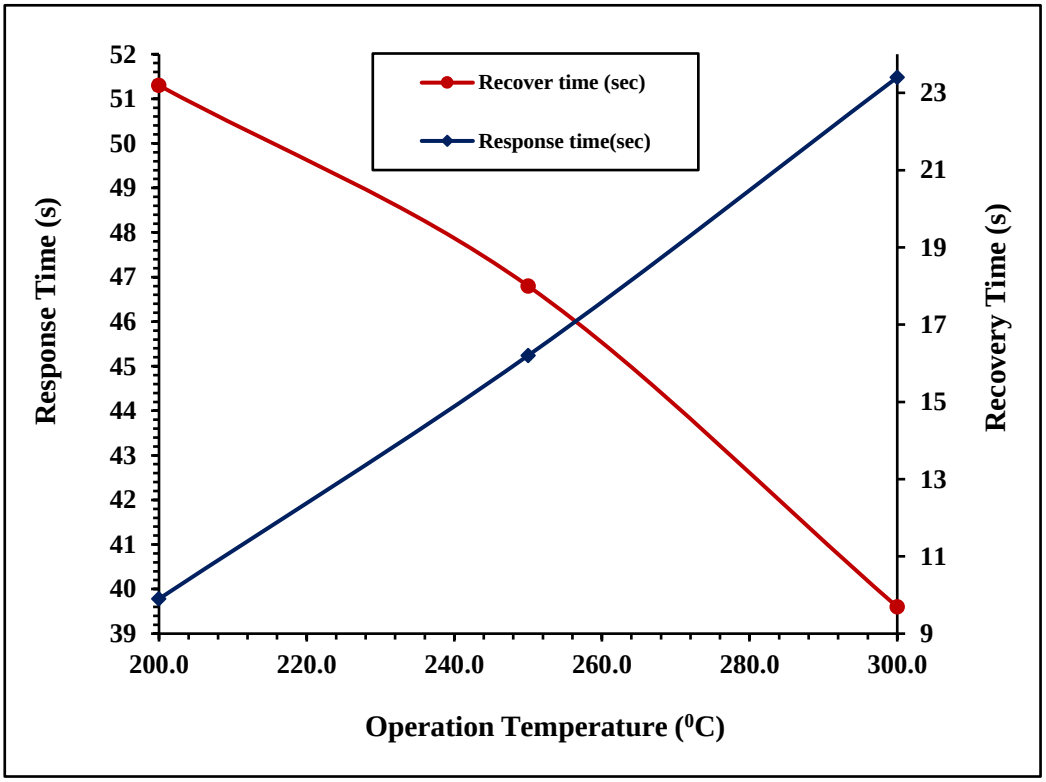

Figure (4.71): The plot response time and recovery time with operating temperature for a concentration of 0.48 wt.% ZnO nanoparticles for (Bi_2O_3:ZnO) thin films for an H_2S gas sensor at 473 K.

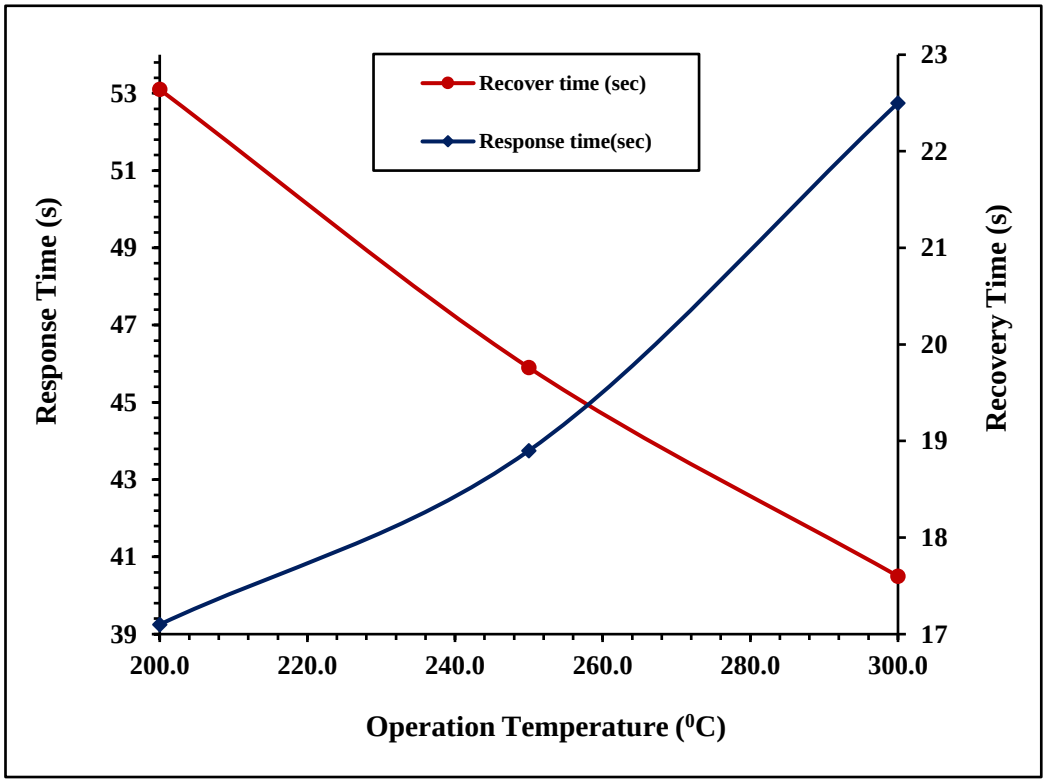

Figure (4.72): The plot of response time and recovery time with the operating temperature for Bi_2O_3 pure for NO_2 gas sensor at 473 K.

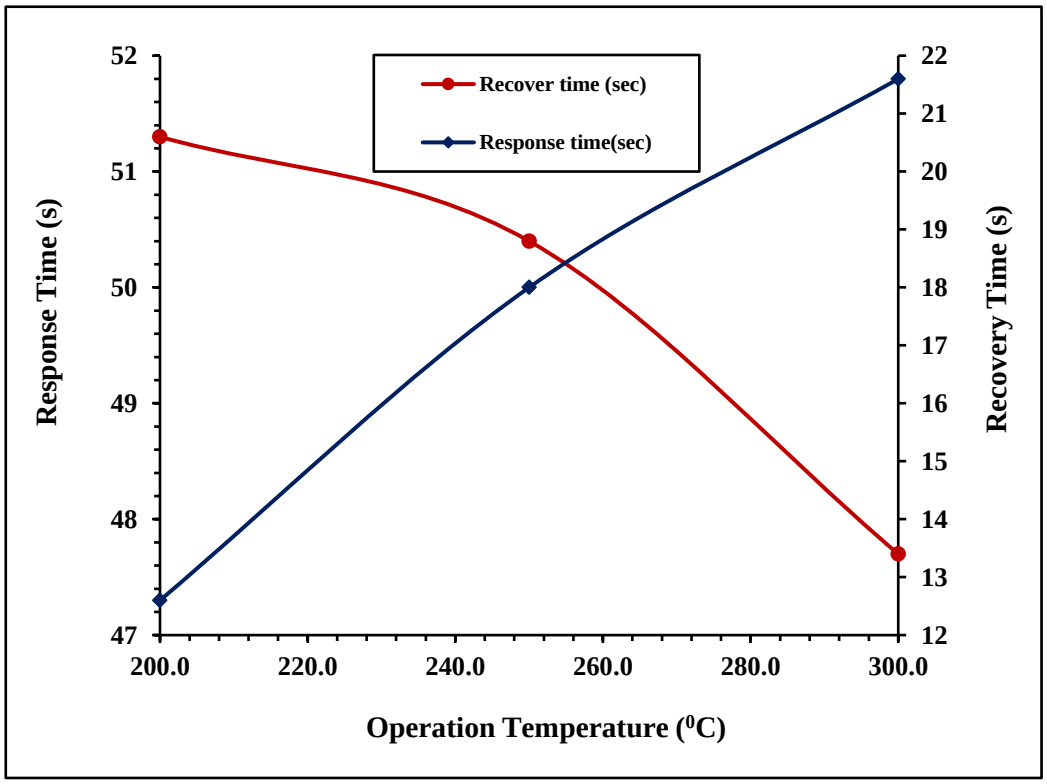

Figure (4.73): The plot response time and recovery time with operating temperature for a concentration of 0.12 wt.% ZnO nanoparticles for (Bi_2O_3:ZnO) thin films for an NO_2 gas sensor at 473 K.

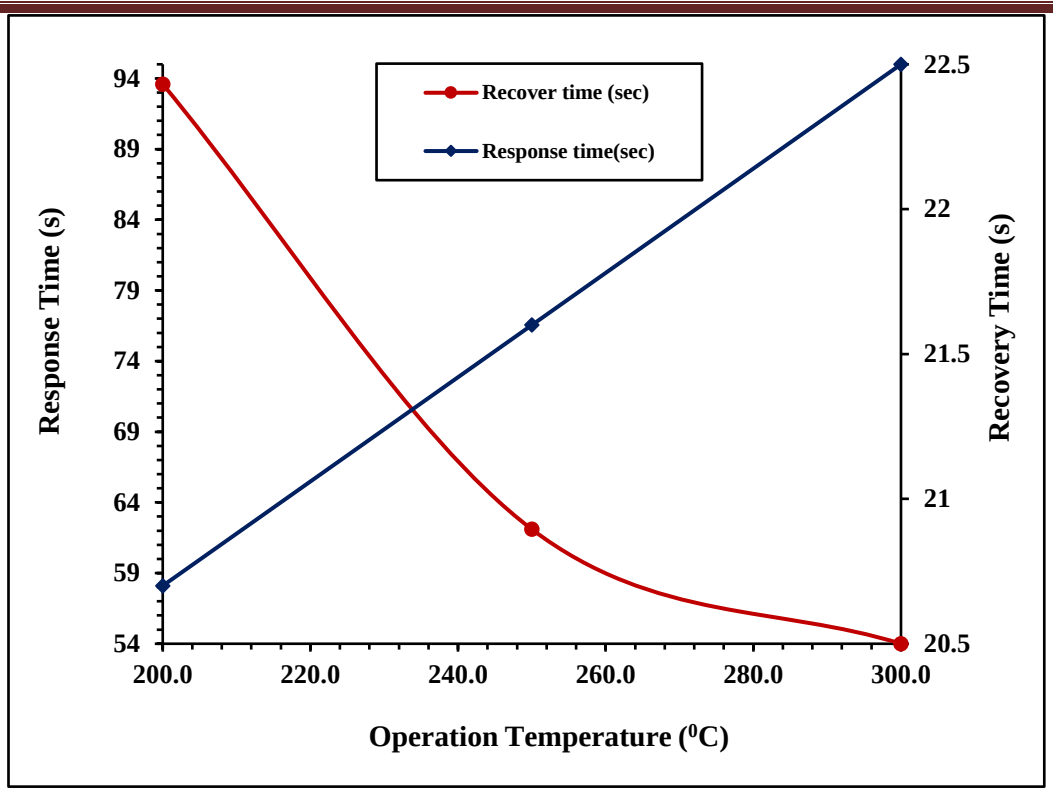

Figure (4.74): The plot response time and recovery time with operating temperature for a concentration of 0.24 wt.% ZnO nanoparticles for (Bi_2O_3:ZnO) thin films for an NO_2 gas sensor at 473 K.

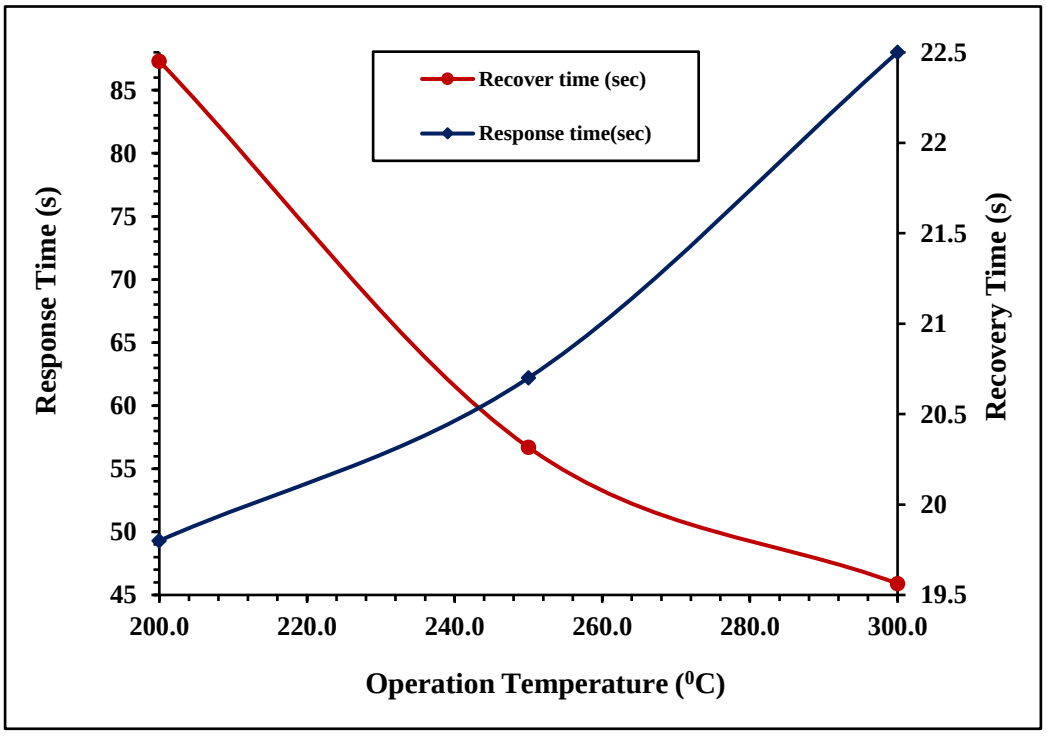

Figure (4.75): The plot response time and recovery time with operating temperature for a concentration of 0.36 wt.% ZnO nanoparticles for (Bi_2O_3:ZnO) thin films for an NO_2 gas sensor at 473 K.

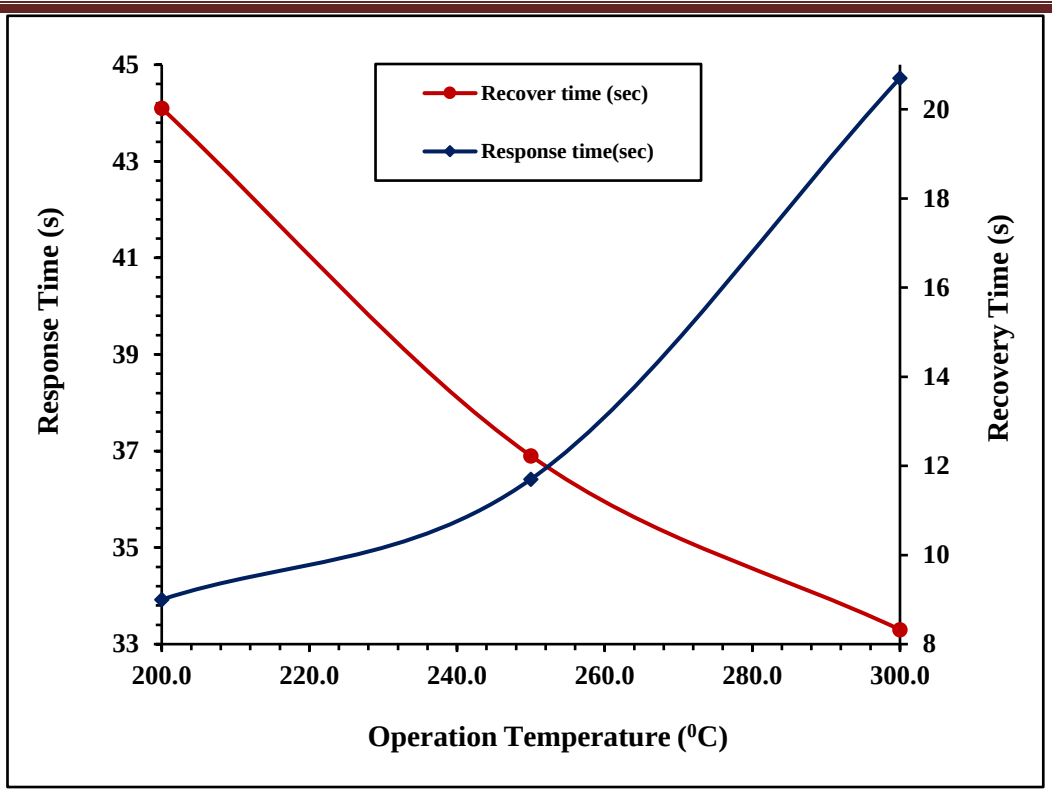

Figure (4.76): The plot response time and recovery time with operating temperature for a concentration of 0.48 wt.% ZnO nanoparticles for (Bi_2O_3:ZnO) thin films for an NO_2 gas sensor at 473 K.

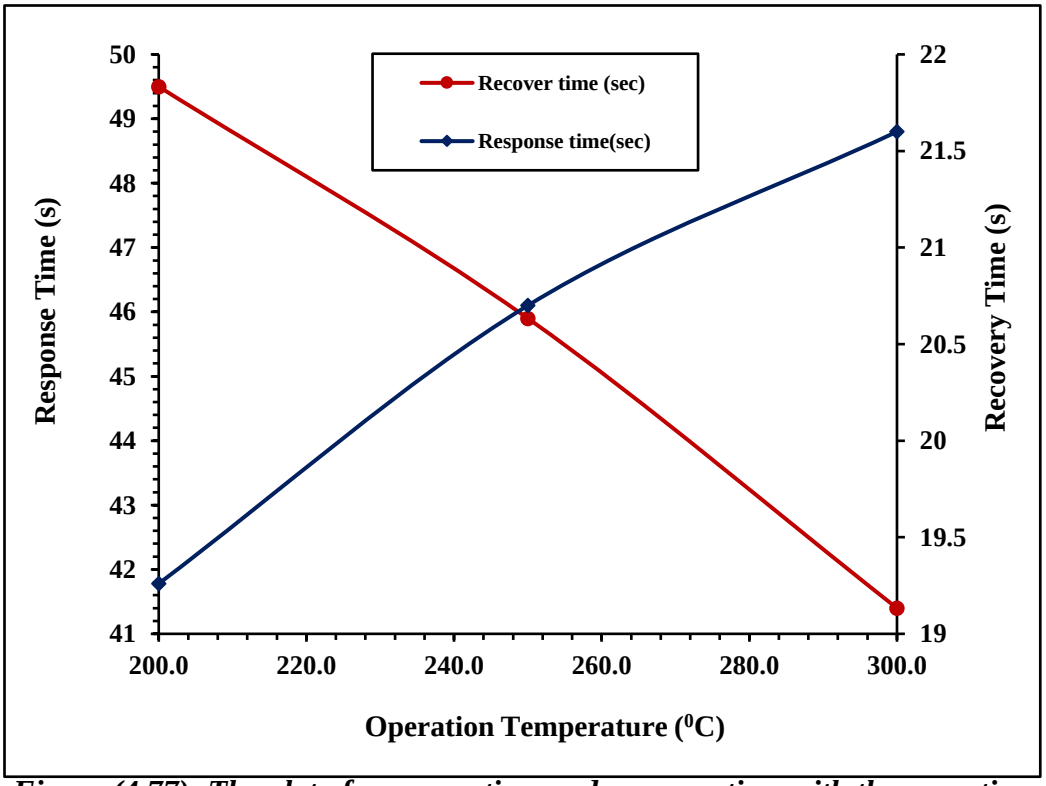

Figure (4.77): The plot of response time and recovery time with the operating temperature for Bi_2O_3 pure for H_2S gas sensor at 573 K.

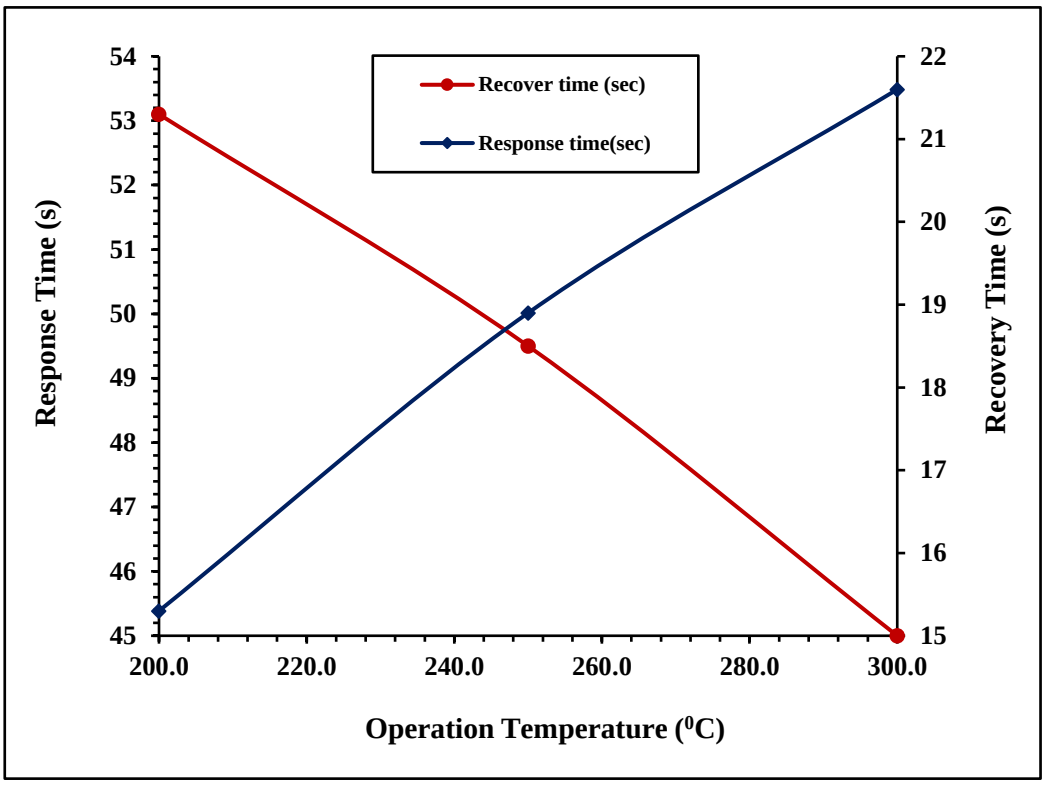

Figure (4.78): The plot response time and recovery time with operating temperature for a concentration of 0.12 wt.% ZnO nanoparticles for (Bi_2O_3:ZnO) thin films for an H_2S gas sensor at 573 K.

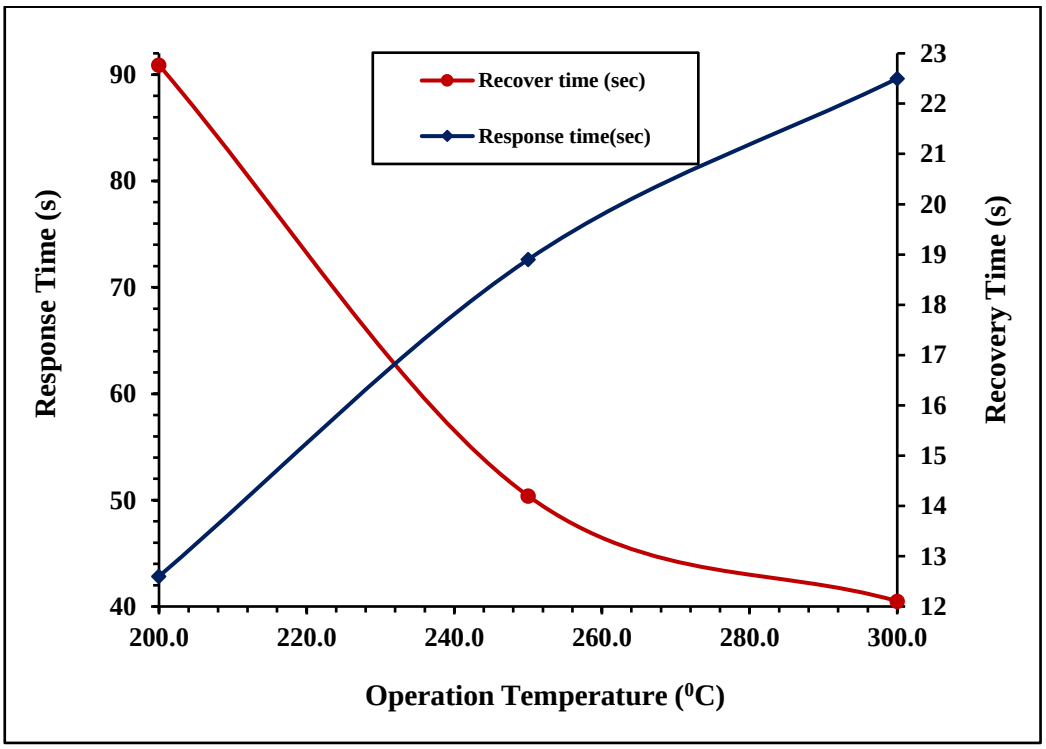

Figure (4.79): The plot response time and recovery time with operating temperature for a concentration of 0.24 wt.% ZnO nanoparticles for (Bi_2O_3:ZnO) thin films for an H_2S gas sensor at 573 K.

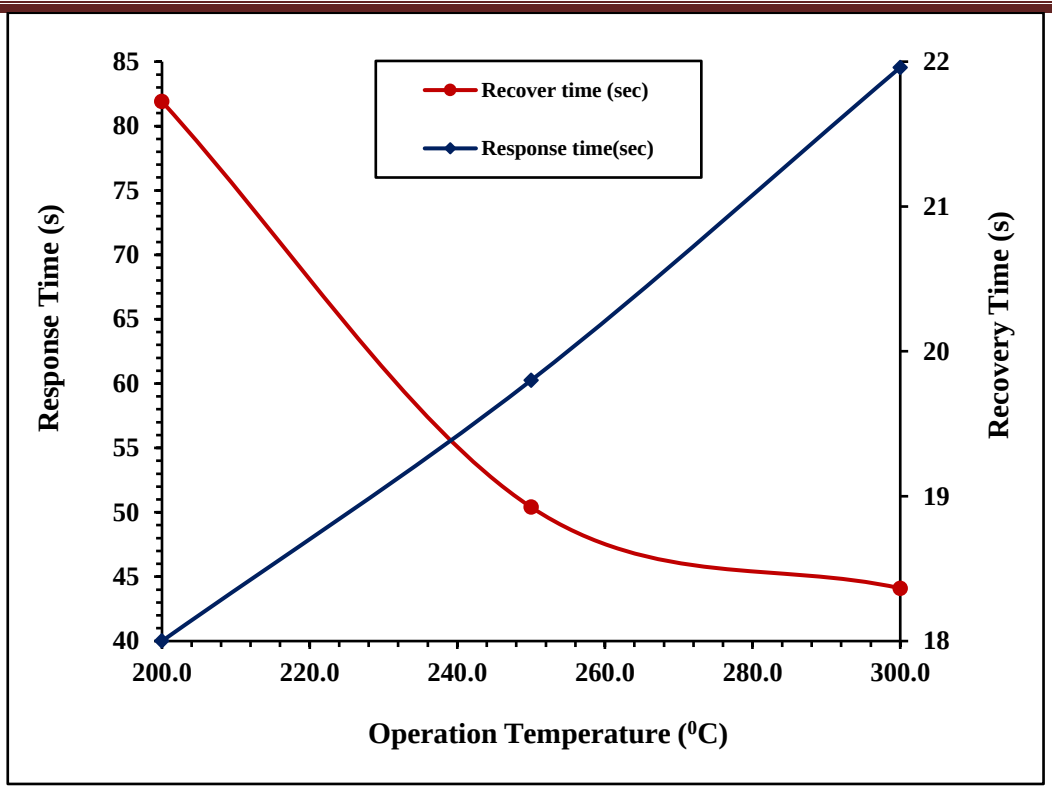

Figure (4.80): The plot response time and recovery time with operating temperature for a concentration of 0.36 wt.% ZnO nanoparticles for (Bi_2O_3:ZnO) thin films for an H_2S gas sensor at 573 K.

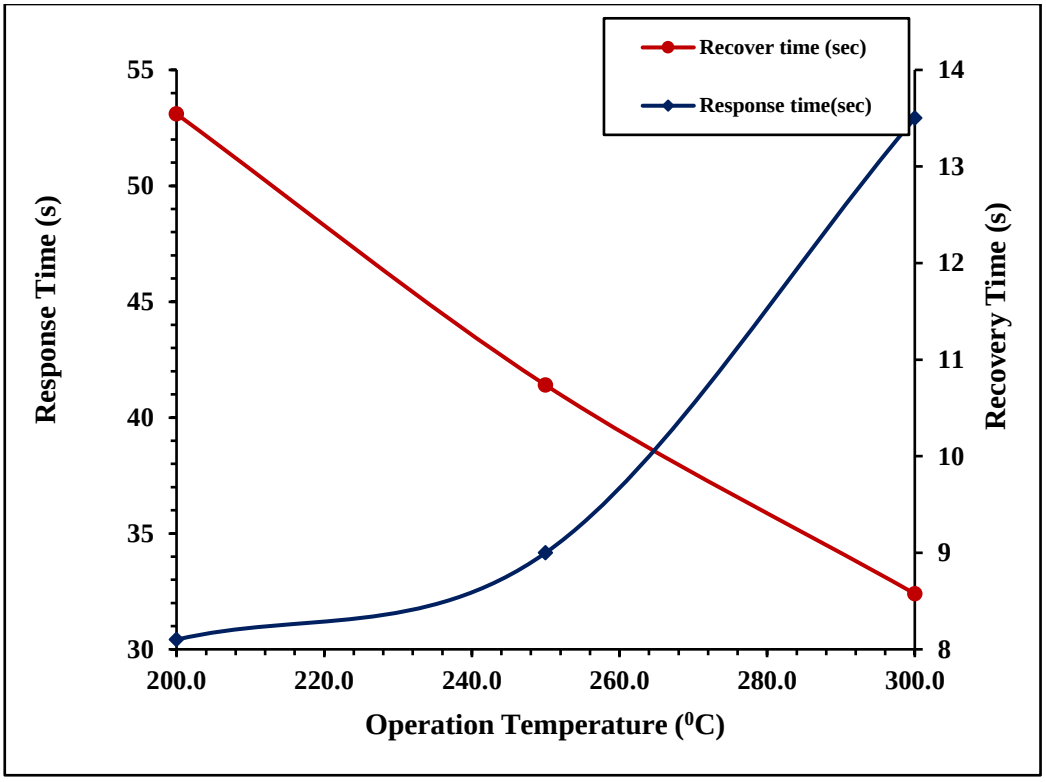

Figure (4.81): The plot response time and recovery time with operating temperature for a concentration of 0.48 wt.% ZnO nanoparticles for (Bi_2O_3 :ZnO) thin films for an H_2S gas sensor at 573 K.

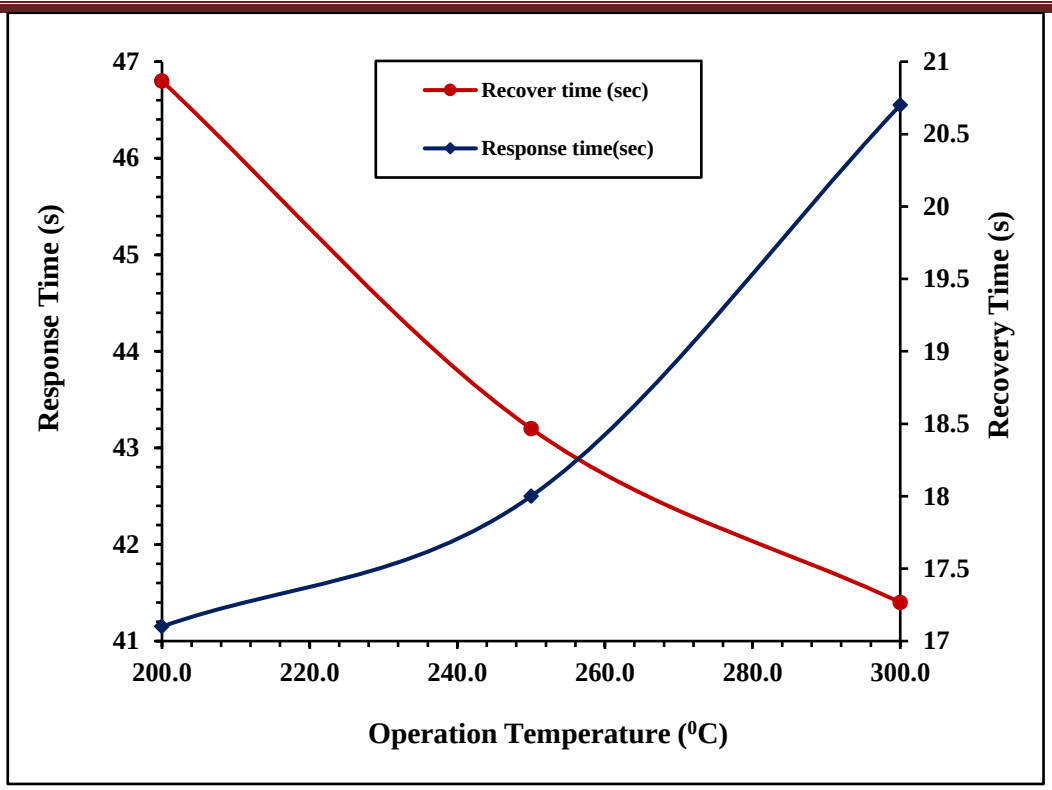

Figure (4.82): The plot of response time and recovery time with the operating temperature for Bi_2O_3 pure for NO_2 gas sensor at 573 K.

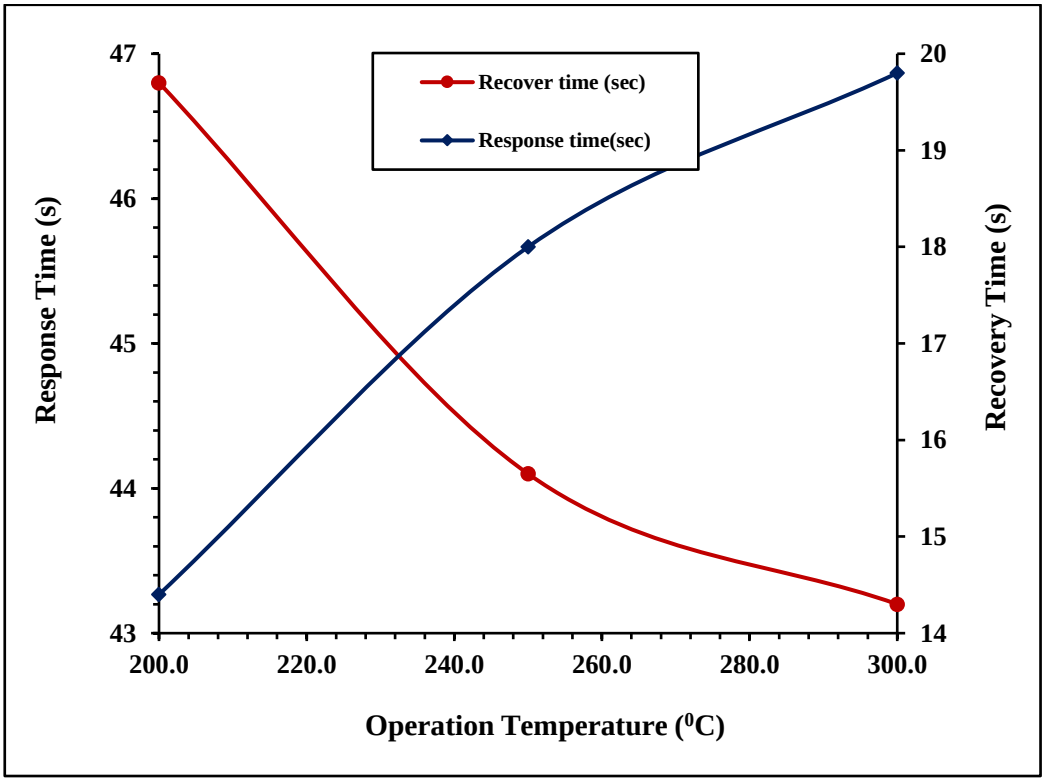

Figure (4.83): The plot response time and recovery time with operating temperature for a concentration of 0.12 wt.% ZnO nanoparticles for (Bi_2O_3:ZnO) thin films for an NO_2 gas sensor at 573 K.

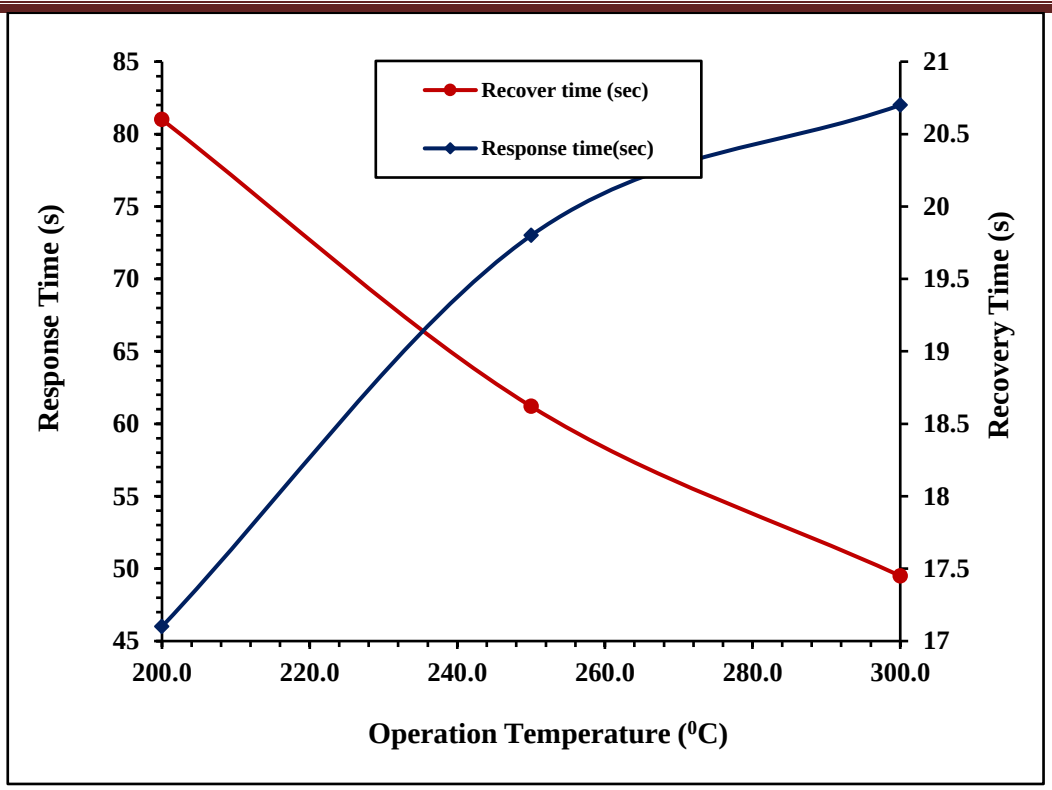

Figure (4.84): The plot response time and recovery time with operating temperature for a concentration of 0.24 wt.% ZnO nanoparticles for (Bi_2O_3:ZnO) thin films for an NO_2 gas sensor at 573 K.

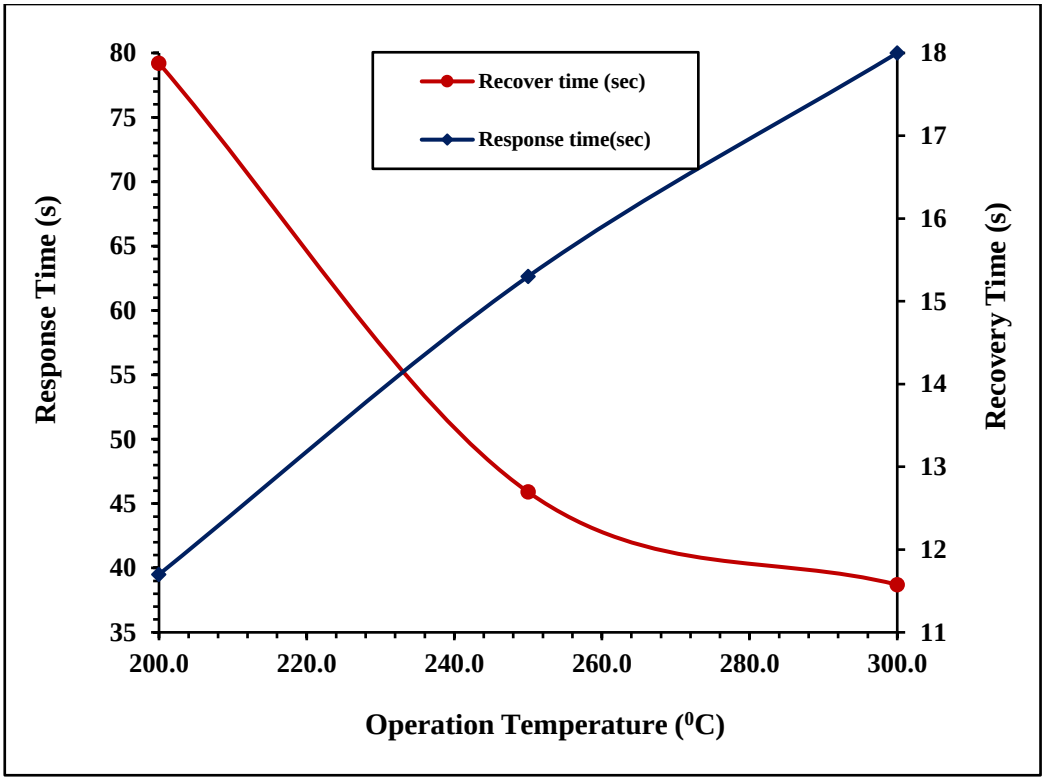

Figure (4.85): The plot response time and recovery time with operating temperature for a concentration of 0.36 wt.% ZnO nanoparticles for (Bi_2O_3:ZnO thin films for an NO_2 gas sensor at 573 K.

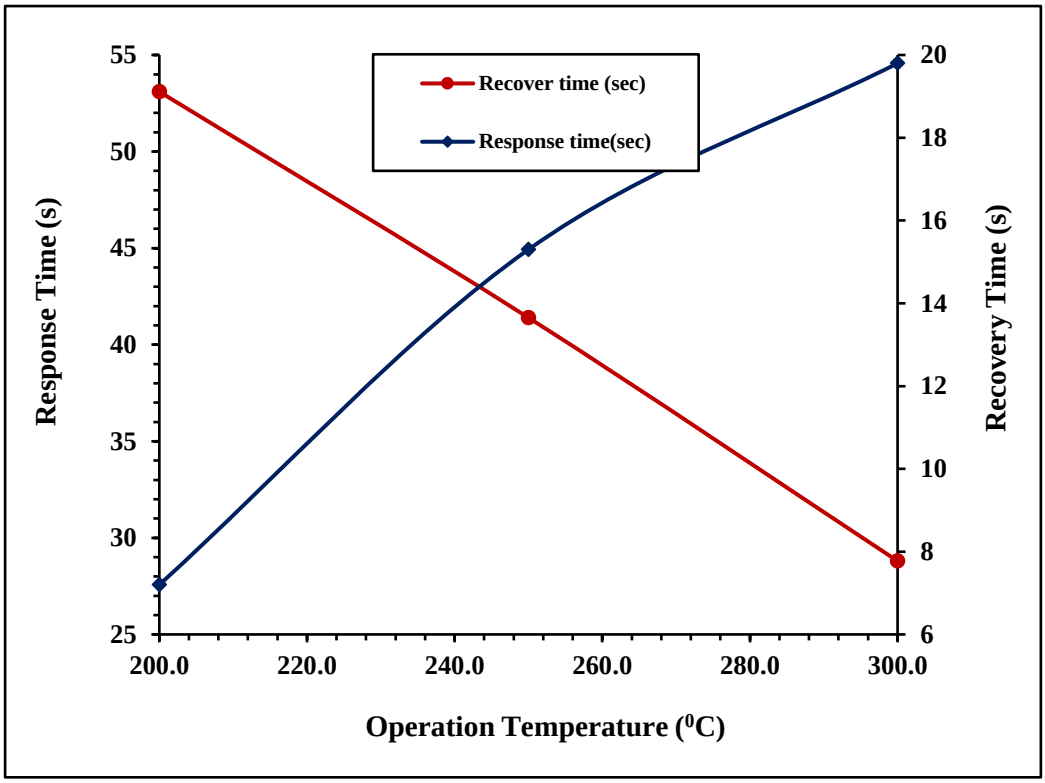

Figure (4.86): The plot response time and recovery time with operating temperature for a concentration of 0.48 wt.% ZnO nanoparticles for (Bi_2O_3:ZnO) thin films for an NO_2 gas sensor at 573 K.

Table (4.9): The gas sensor characteristics results to H_2S gas of (Bi_2O_3:ZnO) thin films at 473 K.

Con. ZnO NPs wt.%	Operation Temperature (^{0}C)	Sensitivity (%)	Response time (sec)	Recover time (sec)
pure	200	0.7769	18.9	52.2
	250	6.7729	20.7	46.8
	300	4.4531	27	44.1
0.12	200	3.0379	11.7	53.1
	250	32.9189	18	52.2
	300	20.6716	21.6	49.5
0.24	200	9.5179	14.4	96.3
	250	38.0110	18.9	56.7
	300	15.0289	27	40.5
0.36	200	2.4729	17.1	84.6
	250	51.7435	19.8	52.2
	300	28.1609	24.3	43.2
0.48	200	22.0588	9.9	51.3
	250	68.4337	16.2	46.8
	300	40.4025	23.4	39.6

Table (4.10): The gas sensor characteristics results to NO_2 gas of (Bi_2O_3:ZnO) thin films at 473 K.

Con. ZnO NPs wt.%	Operation Temperature (^{0}C)	Sensitivity (%)	Response time (sec)	Recover time (sec)
Pure	200	9.0871	17.1	53.1
	250	40.5764	18.9	45.9
	300	4.4531	22.5	40.5
0.12	200	13.9325	12.6	51.3
	250	67.0525	18	50.4
	300	20.6716	21.6	47.7
0.24	200	9.5179	20.7	93.6
	250	86.3337	21.6	62.1
	300	28.9855	22.5	54
0.36	200	23.7001	19.8	87.3
	250	89.4860	20.7	56.6
	300	28.1609	22.5	45.9
0.48	200	22.0588	9	44.1
	250	99.9022	11.7	36.9
	300	41.3015	20.7	33.3

Table (4.11): The gas sensor characteristics results to H_2S gas of (Bi_2O_3:ZnO) thin films at 573 K.

Con. ZnO NPs wt.%	Operation Temperature (^{0}C)	Sensitivity (%)	Response time (sec)	Recover time (sec)
Pure	200	9.3283	19.26	49.5
	250	36.4664	20.7	45.9
	300	3.1822	21.6	41.4
0.12	200	11.2449	15.3	53.1
	250	49.1794	18.9	49.5
	300	0.6944	21.6	45
0.24	200	14.8871	12.6	90.9
	250	64.6743	18.9	50.4
	300	5.2023	22.5	40.5
0.36	200	27.8787	18	81.9
	250	72.8715	19.8	50.4
	300	8.6690	21.96	44.1
0.48	200	30.8343	8.1	53.1
	250	81.2949	9	41.4
	300	6.5510	13.5	32.4

Table (4.12): The gas sensor characteristics results to NO_2 gas of (Bi_2O_3:ZnO) thin films at 573 K.

Con. ZnO NPs wt.%	Operation Temperature (^{0}C)	Sensitivity (%)	Response time (sec)	Recover time (sec)
Pure	200	13.5658	17.1	46.8
	250	56.7510	18	43.2
	300	13.5004	20.7	41.4
0.12	200	14.2449	14.4	46.8
	250	74.9113	18	44.1
	300	27.1929	19.8	43.2
0.24	200	14.8871	17.1	81
	250	86.0514	19.8	61.2
	300	33.3333	20.7	49.5
0.36	200	26.611	11.7	79.2
	250	99.5240	15.3	45.9
	300	29.4158	18	38.7
0.48	200	35.5101	7.2	53.1
	250	153.9753	15.3	41.4
	300	34.1147	19.8	28.8

5.1 Conclusions

According to the results that showed the effect of adding zinc oxide on the synthetic materials, optical and electrical properties, and the gas sensor, the following conclusions were reached:

1- X-ray diffraction showed that the ZnO concentration decreases the average crystal size. Furthermore, the average stress and dislocation values are calculated using the XRD data.

2- The results of the structural properties of the FTIR spectrum of the thin films showed that all the peaks of most of the absorption bonds remain in the same location of the wavelengths, i.e., no chemical reaction occurred.

3- AFM images of thin films appear to be a uniform granular surface. When the ZnO percentage increases, the roughness average and the root mean square (RMS) also increases, where RMS is increases from 1.04 nm to 5.12 nm for annealing temperature 473 K and from 0.571 nm to 2.22 nm for annealing temperature 573 K.

4- SEM images showed that (Bi_2O_3:ZnO) films show uniform density, aggregates, or pieces randomly distributed grains on the top surface morphology of the films, but when the doping ratio of ZnO nanoparticles to compounds is increased, they form a continuous network inside the thin film.

5- The absorbance and absorption coefficient of (Bi2O3:ZnO) thin films increases with the increasing concentrations of (ZnO) nanoparticles. Refractive index, extinction coefficient, and dielectric constant (real, imaginary) are increasing and optical conductivity with the increasing of concentrations nanoparticles. While The energy gap for direct transition (allowed, forbidden) of (Bi2O3:ZnO) thin films decreases with the increasing of the concentrations of (ZnO) nanoparticles. Also, the transmittance decreases with the increase in the additives (ZnO). Since the

transmittance is high in the visible light region, it can be used as a window glass for the solar cell.

6- The increasing in the concentration of (ZnO) nanoparticles and an increasing in temperature leads to an increasing in the DC electrical conductivity of (Bi_2O_3:ZnO) thin films. The activation energy is lower when there is a higher concentration of (ZnO) nanoparticles.

7- The dielectric constant, dielectric loss and A.C electrical conductivity of (Bi_2O_3:ZnO) thin films increase with increasing (ZnO) nanoparticles concentrations. The dielectric constant and dielectric loss of thin films are decreased with increasing frequency. A.C electrical conductivity is increased with the increase of the frequency.

8- The (Bi_2O_3:ZnO) gas sensor was successfully fabricated on a glass substrate and tested for two different gases, H_2S and NO_2. The results show H_2S that annealed 573 K gas sensors have higher sensitivity and higher response time while it has lower recovery time compared to annealed 473 K gas sensors. While the annealed 573 K gas sensor NO_2 has higher sensitivity and response time, while it has a lower recovery time compared to the annealed 473 K gas sensor.

9- When comparing the deposited films from (Bi_2O_3:ZnO) for Gases H_2S and NO_2, it was found that the best results can be obtained at an annealing temperature of 573 K and for gas NO_2.

5.2 Future Works

1 -Prepare a thin film of Bi_2O_3 with different impurities such as (AL, Cu, and In) on a glass substrate and study the effect of doping on the physical and sensor properties of the prepared films.

2 -Study the effect of the substrate type on the sensor properties of the thin film.

3 -Studying thin films (Bi_2O_3:ZnO) as a photodetector application.

4 - Study of (Bi_2O_3:ZnO) thin films as a UV detector.

5- Studying different annealing temperatures for those used in this study and their effect on structural, optical and gas sensing properties.

6- Study different thicknesses of the prepared films and their effect on gas sensing.

7- A study of the effect of humidity on the gas sensitivity of thin films.

[1] L.A. Kolahalam, I. V. Kasi Viswanath, B.S. Diwakar, B. Govindh, V. Reddy, Y.L.N. Murthy, "Review on nanomaterials: Synthesis and applications", Mater. Today Proc. **18** (2019) 2182–2190. https://doi.org/10.1016/j.matpr.2019.07.371.

[2] P.R. Robinson, C.S. Hsu, "Introduction to petroleum technology", Springer Handbooks. PartF**1** (2017) 1–83. https://doi.org/10.1007/978-3-319-49347-3_1.

[3] H.S. Nalwa, "Handbook of nanostructured materials and nanotechnology", five-volume set, Academic Press, 1999.

[4] S. Logothetidis, "Nanostructured materials and their applications", Springer Science & Business Media, (2012).

[5] K.M.M. Abou El-Nour, A. Eftaiha, A. Al-Warthan, R.A.A. Ammar, "Synthesis and applications of silver nanoparticles", Arab. J. Chem. **3** (2010) 135–140. https://doi.org/10.1016/j.arabjc.2010.04.008.

[6] T. Braun, A. Schubert, S. Zsindely, "Nanoscience and nanotechnology on the balance", Scientometrics. **38** (1997) 321–325. https://doi.org/10.1007/BF02457417.

[7] J.M. Köhler, L. Abahmane, J. Wagner, J. Albert, G. Mayer, "Preparation of metal nanoparticles with varied composition for catalytical applications in microreactors", Chem. Eng. Sci. **63** (2008) 5048–5055.

[8] T.Y. Poh, N.A.T.B.M. Ali, M. Mac Aogáin, M.H. Kathawala, M.I. Setyawati, K.W. Ng, S.H. Chotirmall, "Inhaled nanomaterials and the respiratory microbiome: Clinical, immunological and toxicological perspectives", Part. Fibre Toxicol. **15** (2018) 1–16. https://doi.org/10.1186/s12989-018-0282-0.

[9] R. Kumar, W. Zheng, X. Liu, J. Zhang, M. Kumar, "MoS2-Based Nanomaterials for Room-Temperature Gas Sensors", Adv. Mater. Technol. **5** (2020) 1–28. https://doi.org/10.1002/admt.201901062.

[10] X. Liu, T. Ma, N. Pinna, J. Zhang, "Two-Dimensional Nanostructured Materials for Gas Sensing", Adv. Funct. Mater. **27** (2017) 1–30. https://doi.org/10.1002/adfm.201702168.

[11] C. Dong, R. Zhao, L. Yao, Y. Ran, X. Zhang, Y. Wang, "A review on WO3 based gas sensors: Morphology control and enhanced sensing properties", Elsevier B.V., (2020). https://doi.org/10.1016/j.jallcom.2019.153194.

[12] A. Dey, "Semiconductor metal oxide gas sensors: A review", Mater. Sci. Eng. B Solid-State Mater. Adv. Technol. **229** (2018) 206–217. https://doi.org/10.1016/j.mseb.2017.12.036.

[13] N. Yamazoe, G. Sakai, K. Shimanoe, "Oxide semiconductor gas sensors", Catal. Surv. from Asia. **7** (2003) 63–75. https://doi.org/10.1023/A:1023436725457.

[14] S. Poongodi, P.S. Kumar, D. Mangalaraj, N. Ponpandian, P. Meena, Y. Masuda, C. Lee, "Electrodeposition of WO3 nanostructured thin films for electrochromic and H_2S gas sensor applications", J. Alloys Compd. **719** (2017) 71–81. https://doi.org/10.1016/j.jallcom.2017.05.122.

[15] H.J. Nam, T. Sasaki, N. Koshizaki, "Optical CO gas sensor using a cobalt oxide thin film prepared by pulsed laser deposition under various argon pressures", J. Phys. Chem. B. **110** (2006) 23081–23084. https://doi.org/10.1021/jp063484f.

[16] T. Anukunprasert, C. Saiwan, E. Traversa, "The development of gas sensor for carbon monoxide monitoring using nanostructure of Nb-TiO_2", Sci. Technol. Adv. Mater. **6** (2005) 359–363. https://doi.org/10.1016/j.stam.2005.02.020.

[17] N.A. Ibrahim, "Nanomaterials for Antibacterial Textiles", Elsevier Inc., (2015)191-216.https://doi.org/10.1016/B978-0-12-801317-5.00012-8.

[18] Z. Yang, H. Peng, W. Wang, T. Liu, "Crystallization behavior of

poly(ε-caprolactone)/layered double hydroxide nanocomposites", J. Appl. Polym. Sci. **116** (2010) 2658–2667. https://doi.org/10.1002/app.

[19] S. Murthy, P. Effiong, C.C. Fei, "Metal oxide nanoparticles in biomedical applications", INC, (2020) 233-251. https://doi.org/10.1016/b978-0-12-817505-7.00011-7.

[20] G.A. Kontos, A.L. Soulintzis, P.K. Karahaliou, G.C. Psarras, S.N. Georga, C.A. Krontiras, M.N. Pisanias, "Electrical relaxation dynamics in TiO_2-polymer matrix composites", Express Polym Lett. **1** (2007) 781–789.

[21] S. Laurent, S. Boutry, R.N. Muller, "Metal Oxide Particles and Their Prospects for Applications", Elsevier Ltd., (2018) 3-42. https://doi.org/10.1016/b978-0-08-101925-2.00001-2.

[22] Y. Liu, D. Tu, H. Zhu, X. Chen, "Lanthanide-doped luminescent nanoprobes: Controlled synthesis, optical spectroscopy, and bioapplications", Chem. Soc. Rev. **42** (2013) 6924–6958. https://doi.org/10.1039/c3cs60060b.

[23] S. Chaisitsak, "Nanocrystalline SnO_2: F thin films for liquid petroleum gas sensors", Sensors. **11** (2011) 7127–7140. https://doi.org/10.3390/s110707127.

[24] G. Hoogers, "Development of a Protected Gas Sensor for Exhaust Automotive Applications", Fuel Cell Technol. Handb. **2** (2002) 342-348. https://doi.org/10.31399/asm.hb.v21.a0003474.

[25] K. Song, Q. Wang, Q. Liu, H. Zhang, Y. Cheng, "A wireless electronic nose system using a Fe2O3 gas sensing array and least squares support vector regression", Sensors. **11** (2011) 485–505. https://doi.org/10.3390/s110100485.

[26] G.G. Xiao, Z. Zhang, J. Weber, H. Ding, H. Mcintosh, D. Desrosiers, G. Nong, D. Won, J. Dunford, J. Tunney, K. Darcovich, G. Diaz-quijada, "Trace Amount Formaldehyde Gas Detection for Indoor Air

Quality Monitoring", (2011) 1–4. https://doi.org/ 10.1109/IMTC.2011.5944050.

[27] I. Chen, "The Assessment for Sensitivity of a NO_2 Gas Sensor with ZnGa2O4/ZnO Core-Shell Nanowires—a Novel Approach", **10** (2010) 3057-3072. https://doi.org/10.3390/s100403057.

[28] G. Korotcenkov, "Handbook of Gas Sensor Materials", (ANASYS), n.d. **1** (2013). https://doi.org/10.1007/978-1-4614-7165-3

[29] I.C. Communication, M. Ghobadifard, Q. Maleki, M. Khelghati, E. Zamani, S. Farhadi, A. Aslani, "Zinc oxide nano-crystals assisted for carbon dioxide gas sensing prepared by solvothermal and sonochemical methods", **3** (2015) 26–40.

[30] M. Tadic, D. Nikolic, M. Panjan, G.R. Blake, "Magnetic properties of NiO (nickel oxide) nanoparticles: blocking temperature and Neel temperature Marin", J. Alloys Compd. **647** (2015) 1061-1068. https://doi.org/10.1016/j.jallcom.2015.06.027.

[31] N. Barsan, U. Weimar, T. Chemistry, "Fundamentals of Metal Oxide Gas Sensors. Tagungsband", (2012) 618–621. https://doi.org/10.5162/IMCS2012/7.3.3.

[32] L. Leontie, M. Caraman, M. Delibaş, G.I. Rusu, "Optical properties of bismuth trioxide thin films", Mater. Res. Bull. **36** (2001) 1629–1637. https://doi.org/10.1016/S0025-5408(01)00641-9.

[33] L. Zhang, Y. Hashimoto, T. Taishi, I. Nakamura, Q.Q. Ni, "Fabrication of flower-shaped Bi 2 O 3 superstructure by a facile template-free process", Appl. Surf. Sci. **257** (2011) 6577–6582. https://doi.org/10.1016/j.apsusc.2011.02.081.

[34] M.M. Patil, V. V. Deshpande, S.R. Dhage, V. Ravi, "Synthesis of bismuth oxide nanoparticles at 100 °c", Mater. Lett. **59** (2005) 2523–2525. https://doi.org/10.1016/j.matlet.2005.03.037.

[35] M.G. Ma, J.F. Zhu, R.C. Sun, Y.J. Zhu, "Microwave-assisted synthesis

of hierarchical Bi_2O_3 spheres assembled from nanosheets with pore structure", Mater. Lett. **64** (2010) 1524–1527. https://doi.org/10.1016/j.matlet.2010.04.010.

[36] H. Oudghiri-Hassani, S. Rakass, F.T. Al Wadaani, K.J. Al-ghamdi, A. Omer, M. Messali, M. Abboudi, "Synthesis, characterization and photocatalytic activity of α-Bi 2 O 3 nanoparticles" , J. Taibah Univ. Sci. **9** (2015) 508–512. https://doi.org/10.1016/j.jtusci.2015.01.009.

[37] V. Fruth, A. Ianculescu, D. Berger, S. Preda, G. Voicu, E. Tenea, M. Popa, "Synthesis, structure and properties of doped Bi_2O_3", J. Eur. Ceram. Soc. **26** (2006) 3011–3016. https://doi.org/10.1016/j.jeurceramsoc.2006.02.019.

[38] R. Grazziotin-Soares, M.H. Nekoofar, T.E. Davies, A. Bafail, E. Alhaddar, R. Hübler, A.L.S. Busato, P.M.H. Dummer, "Effect of bismuth oxide on white mineral trioxide aggregate: Chemical characterization and physical properties", Int. Endod. J. **47** (2014) 520–533. https://doi.org/10.1111/iej.12181.

[39] A. Moezzi, A.M. McDonagh, M.B. Cortie, "Zinc oxide particles: Synthesis, properties and applications", Chem. Eng. J. **185–186** (2012) 1–22. https://doi.org/10.1016/j.cej.2012.01.076.

[40] W. Gao, Z. Li, "ZnO thin films produced by magnetron sputtering", Ceram. Int. **30** (2004) 1155–1159. https://doi.org/10.1016/j.ceramint.2003.12.197.

[41] M.K. Khalaf, B.T. Chiad, A.F. Ahmed, F.A.H. Mutlak, "Thin film technique for preparing nano-ZnO gas sensing (O_2, NO_2) using Plasma Deposition", Int. J. Appl. Innov. Eng. Manag. **2** (2013) 178–184.

[42] Ü. Özgür, Y.I. Alivov, C. Liu, A. Teke, M.A. Reshchikov, S. Doğan, V. Avrutin, S.J. Cho, H. Morkọ, "A comprehensive review of ZnO materials and devices", J. Appl. Phys. **98** (2005) 1–103. https://doi.org/10.1063/1.1992666.

[43] L. Cong, X. Zheng, P. Hu, S. Dan-Feng, " Bi_2O_3 vaporization in microwave-sintered ZnO varistors", J. Am. Ceram. Soc. **90** (2007) 2791–2794. https://doi.org/10.1111/j.1551-2916.2007.01848.x.

[44] V.S. Kalyamwar, F.C. Raghuwanshi, N.L. Jadhao, A.J. Gadewar,"Zinc Oxide Nanostructure Thick Films as H 2 S Gas Sensors at Room Temperature", **3** (2013) 31–35.

[45] X. Liu, W. Bian, C. Tian, "Morphology, structure and optical properties of 3D Bi_2O_3 hierarchical architectures", Mater. Lett. **112** (2013) 1–4. https://doi.org/10.1016/j.matlet.2013.08.107.

[46] W. Mielcarek, A. Gubański, G. Paściak, K. Prociów, J. Warycha, J.M. Wrobel, "The effect of bismuth oxide polymorph forms on degradation processes in ZnO varistors", Ceram. Int. **39** (2013) 8219–8226. https://doi.org/10.1016/j.ceramint.2013.04.006.

[47] J. Li, S. Li, P. Cheng, M.A. Alim, "Advances in ZnO – Bi 2 O 3 based varistors", J. Mater. Sci. Mater. Electron. **26** (2015) 4782–4809. https://doi.org/10.1007/s10854-015-3093-1.

[48] F. Teimoori, K. Khojier, N.Z. Dehnavi, "On the Dependence of H 2 Gas Sensitivity of ZnO Thin Films on Film Thickness, Procedia Mater. Sci. **11** (2015) 474–479. https://doi.org/10.1016/j.mspro.2015.11.061.

[49] T. Liu, M. Wang, H. Zhang, "Synthesis and Characterization of ZnO / Bi 2 O 3 Core / Shell Nanoparticles by the Sol – Gel Method", **45** (2016) 4412–4417. https://doi.org/10.1007/s11664-016-4568-4.

[50] M. Ahila, M. Malligavathy, E. Subramanian, D.P. Padiyan, "Controllable synthesis of α and β- Bi_2O_3 through anodization of thermally evaporated bismuth and its characterization", Solid State Ionics. **298** (2016) 23–34. https://doi.org/10.1016/j.ssi.2016.10.017.

[51] M. Sajjad, I. Ullah, M.I. Khan, J. Khan, M.Y. Khan, M.T. Qureshi, "Structural and optical properties of pure and copper doped zinc oxide nanoparticles", Results Phys. **9** (2018) 1301–1309.

https://doi.org/10.1016/j.rinp.2018.04.010.

[52] S.R. Alharbi, A.F. Qasrawi, "Effects of Ge substrate on the structural and optical conductivity parameters of Bi_2O_3 thin films", Optik (Stuttg). **181** (2019) 714–720. https://doi.org/10.1016/j.ijleo.2018.12.133.

[53] S. Kumari, D. Mohan, S. Yadav, "Effect of Bi 2 O 3 content on non linear optical properties and of TeO 2 .Bi 2 O 3 .B 2 O 3 .ZnO glass system, AIP Conf. Proc. **2093** (2019) 2–5. https://doi.org/10.1063/1.5097118.

[54] L. Meng, W. Xu, Q. Zhang, T. Yang, S. Shi, "Study of nanostructural bismuth oxide films prepared by radio frequency reactive magnetron sputtering", Appl. Surf. Sci. **472** (2019) 165–171. https://doi.org/10.1016/j.apsusc.2018.02.017.

[55] U.M. Nayef, R.I. Kamel, " Bi_2O_3 nanoparticles ablated on porous silicon for sensing NO_2 gas", Optik (Stuttg). **208** (2020) 164146. https://doi.org/10.1016/j.ijleo.2019.164146.

[56] A.A. Najim, "Synthesis and characterization of bismite nano-island thin films for optoelectronic applications", Mater. Sci. Semicond. Process. **121** (2021) 105334. https://doi.org/10.1016/j.mssp.2020.105334.

[57] P. Wang, S.Z. Wang, Y.R. Kang, Z. Sen Sun, X.D. Wang, Y. Meng, M.H. Hong, W.F. Xie, "Cauliflower-shaped Bi_2O_3–ZnO heterojunction with superior sensing performance towards ethanol", J. Alloys Compd. **854** (2021) 157152. https://doi.org/10.1016/j.jallcom.2020.157152.

[58] Ahmed, G., Mahmoud, T., Mohammed, H., & Hussein, "A. Fabrication and Study of ZnO thin Films using Thermal Evaporation Technique", Egyptian Journal of Chemistry **64** (2021) 5183-5191. https://doi.org/10.21608/ejchem.2021.71184.3563.

[59] I. Dhahri, M. Ellouze, S. Labidi, Q.M. Al-Bataineh, J. Etzkorn, H. Guermazi, A. Telfah, C.J. Tavares, R. Hergenröder, T. Appel, "Optical and structural properties of ZnO NPs and ZnO– Bi_2O_3 nanocomposites", Ceram. Int. **48** (2022) 266–277.

[60] J.L. Vossen, W. Kern, W. Kern, "Thin film processes II", Gulf Professional Publishing, **2** (1991).

[61] R.W. Berry, P.M. Hall, M.T. Harris, "Thin film technology", D. VAN NOSTRAND CO., INC., PRINCETON, N. J. (1968) 706 P.

[62] J. Sólyom, "The Structure of Noncrystalline Solids", Fundam. Phys. Solids. **1** (2007) 303–330. https://doi.org/10.1007/978-3-540-72600-5_10.

[63] M. Rudan, "Physics of semiconductor devices: Second edition", 2017. https://doi.org/10.1007/978-3-319-63154-7.

[64] B.L. Theraja, "Modern physics", S. Chand Publishing, 2008.

[65] S. Kumari, D. Suthar, G. Chasta, Himanshu, N. Kumari, M.S. Dhaka, "An approach towards CdI2 treatment on CdSe absorber layer for solar cells", Chem. Phys. Lett. **803** (2022) 139868. https://doi.org/10.1016/j.cplett.2022.139868.

[66] S.L. Patel, S. Chander, A. Purohit, M.D. Kannan, M.S. Dhaka, "Influence of NH4Cl treatment on physical properties of CdTe thin films for absorber layer applications", J. Phys. Chem. Solids. **123** (2018) 216–222. https://doi.org/10.1016/j.jpcs.2018.07.021.

[67] S. Kumari, D. Suthar, Himanshu, M.D. Kannan, N. Kumari, M.S. Dhaka, "Grain growth in thermally evaporated CdS thin films: An approach to MgF2 activation for window layer applications", Inorg. Chem. Commun. **144** (2022) 109893. https://doi.org/10.1016/j.inoche.2022.109893.

[68] K. Venkateswarlu, A. Chandra Bose, N. Rameshbabu, "X-ray peak broadening studies of nanocrystalline hydroxyapatite by

WilliamsonHall analysis", Phys. B Condens. Matter. **405** (2010) 4256–4261. https://doi.org/10.1016/j.physb.2010.07.020.

[69] H. Khan, A.S. Yerramilli, A. D'Oliveira, T.L. Alford, D.C. Boffito, G.S. Patience, "Experimental methods in chemical engineering: X-ray diffraction spectroscopy—XRD", Can. J. Chem. Eng. **98** (2020) 1255–1266. https://doi.org/10.1002/cjce.23747.

[70] S.K. Sen, T.C. Paul, S. Dutta, M.N. Hossain, M.N.H. Mia, "XRD peak profile and optical properties analysis of Ag-doped h-MoO3 nanorods synthesized via hydrothermal method", J. Mater. Sci. Mater. Electron. **31** (2020) 1768–1786. https://doi.org/10.1007/s10854-019-02694-y.

[71] V. Mote, Y. Purushotham, B. Dole, "Williamson-Hall analysis in estimation of lattice strain in nanometer-sized ZnO particles", J. Theor. Appl. Phys. **6** (2012) 2–9. https://doi.org/10.1186/2251-7235-6-6.

[72] S. Mustapha, M.M. Ndamitso, A.S. Abdulkareem, J.O. Tijani, D.T. Shuaib, A.K. Mohammed, "A. Sumaila, Comparative study of crystallite size using Williamson-Hall and Debye-Scherrer plots for ZnO nanoparticles", Adv. Nat. Sci. Nanosci. Nanotechnol. **10** (2019). https://doi.org/10.1088/2043-6254/ab52f7.

[73] P. Nwaokafor, K.B. Okeoma, O.K. Echendu, A.C. Ohajianya, K.O. Egbo, "X-ray Diffraction Analysis of a Class of AlMgCu Alloy Using Williamson–Hall and Scherrer Methods", Metallogr. Microstruct. Anal. **10** (2021) 727–735. https://doi.org/10.1007/s13632-021-00792-0.

[74] Â. Pe, R. Garcõ, "Dynamic atomic force microscopy methods", **47** (2002) 197-301. https://doi.org/10.1016/S0167-5729(02)00077-8

[75] J.H. Hafner, C. Cheung, A.T. Woolley, C.M. Lieber, "Structural and functional imaging with carbon nanotube AFM probes", **77** (2001) 73–110.

[76] R. Splinter, "Action potential transmission and volume conduction",

Handb. Phys. Med. Biol. **56** (2010) 5-1. https://doi.org/10.1201/9781420075250.

[77] W. Zhou, R. Apkarian, Z.L. Wang, D. Joy, "Fundamentals of scanning electron microscopy (SEM)", Scanning Microsc. Nanotechnol. Tech. Appl. (2007) 1–40. https://doi.org/10.1007/978-0-387-39620-0_1.

[78] J.A. Kubby, J.J. Boland, "Scanning tunneling microscopy of semiconductor surfaces", Surf. Sci. Rep. **26** (1996) 61–204. https://doi.org/10.1016/S0167-5729(97)80001-5.

[79] B.J. Inkson, "Scanning Electron Microscopy (SEM) and Transmission Electron Microscopy (TEM) for Materials Characterization", Elsevier Ltd, (2016) 17-43. https://doi.org/10.1016/B978-0-08-100040-3.00002-X.

[80] A. Bogner, P.H. Jouneau, G. Thollet, D. Basset, C. Gauthier, "A history of scanning electron microscopy developments: Towards “wet-STEM” imaging", Micron. **38** (2007) 390–401. https://doi.org/10.1016/j.micron.2006.06.008.

[81] A. Bogner, G. Thollet, D. Basset, P.H. Jouneau, C. Gauthier, Wet STEM: "A new development in environmental SEM for imaging nano-objects included in a liquid phase", Ultramicroscopy. **104** (2005) 290–301. https://doi.org/10.1016/j.ultramic.2005.05.005.

[82] A. Ul-Hamid, "A Beginners Guide to Scanning Electron Microscopy", **1** (2018). https://doi.org/10.1007/978-3-319-98482-7.

[83] C.J. Brinker, G. Cao, "Annual Review of Nano Research", (2006).

[84] M.L. Cohen, J.R. Chelikowsky, "Electronic structure and optical properties of semiconductors", Springer Science & Business Media, **75** (2012).

[85] R.T. Kivaisi, "Optical properties of obliquely evaporated aluminium films", Thin Solid Films. **97** (1982) 153–163. https://doi.org/10.1016/0040-6090(82)90224-3.

[86] M. Gerard, A. Chaubey, B.D. Malhotra, "Application of conducting polymers to biosensors", Biosens. Bioelectron. **17** (2002) 345–359. https://doi.org/10.1016/S0956-5663(01)00312-8

[87] D.R. Tobergte, S. Curtis, "The Physics of Thin Film Optical Spectra: An Introduction", Springer. 2013.

[88] N.A. Hassan, I.H. Khudayer, "Study of the structural and optical properties of CuAlxIn1-xTe2 thin film", AIP Conf. Proc. **2190** (2019) 20050. https://doi.org/10.1063/1.5138536.

[89] PanelA.M.TalebA.J.H.Al-Wattar, "Design of windows to reduce solar radiation transmittance into buildings", Sol. Wind Technol. **5** (1988) 503-515. https://doi.org/10.1016/0741-983X(88)90041-0

[90] A.S. Hassanien, I. Sharma, "Band-gap engineering, conduction and valence band positions of thermally evaporated amorphous Ge15-x Sbx Se50 Te35 thin films: Influences of Sb upon some optical characterizations and physical parameters", J. Alloys Compd. **798** (2019) 750–763. https://doi.org/10.1016/j.jallcom.2019.05.252.

[91] C. Kittel, P. McEuen, P. McEuen, "Introduction to solid state physics", Wiley New York, **2** (1978).

[92] J.I. Pankove, "Optical processes in semiconductors", Courier Corporation, 1975.

[93] Z. Sen, "Solar energy fundamentals and modeling techniques: atmosphere, environment, climate change and renewable energy", Springer Science & Business Media, 2008.

[94] R. Enderlein, N.J.M. Horing, "Fundamentals of semiconductor physics and devices", World Scientific, 1997.

[95] O.S. Heavens, "Optical properties of thin solid films", Courier Corporation, 1991.

[96] J. Tauc, "Amorphous and liquid semiconductors", Springer Science & Business Media, 2012.

[97] V.N. Suryawanshi, A.S. Varpe, M.D. Deshpande, "Band gap engineering in PbO nanostructured thin films by Mn dopin", Thin Solid Films. **645** (2018) 87-92. https://doi.org/10.1016/j.tsf.2017.10.016.

[98] R.G. Kadhim, M.H. Shinen, M.S. Abdali, "Study the Optical Properties of Polyaniline- Multiwelled Carbon Nanotubes Nano", **25** (2017) 1031-1042.

[99] J.H. Nahida, "Introduction : Experimental part", (2012) 58–67.

[100] N.D. Alharbi, O.W. Guirguis, "Macrostructure and Optical studies of Hydroxypropyl Cellulose in Pure and Nano-composites Forms Article ' s reference number RINP 102637 Article title . Aut", Results Phys. **15** (2019) 102637. https://doi.org/10.1016/j.rinp.2019.102637.

[101] B. Gündüz, "Optical properties of poly[2-methoxy-5-(3′,7′-dimethyloctyloxy)-1,4-phenylenevinylene] lightemitting polymer solutions: effects of molarities and solvents", Polym. Bull. **72** (2015) 3241-3267. https://doi.org/10.1007/s00289-015-1464-7.

[102] O.G. Abdullah, B.K. Aziz, S.A. Hussen, "Optical Characterization of Polyvinyl alcohol-Ammonium Nitrate Polymer Electrolytes Films", Chem. Mater. Res. **3** (2013) 84–90.

[103] H. Meixner, U. Lampe, "Metal oxide sensors", Sensors Actuators, B Chem. **33** (1996) 198–202. https://doi.org/10.1016/0925-4005(96)80098-0.

[104] R.E. Hummel, "Electronic Properties of Materials", Electron. Prop. Mater. **1** (2011) 419–429. https://doi.org/10.1007/978-1-4419-8164-6.

[105] A.R. Blythe, T. Blythe, D. Bloor, "Electrical properties of polymers", Cambridge university press, 2005.

[106] R. Bel Hadj Tahar, T. Ban, Y. Ohya, Y. Takahashi, "Tin doped indium oxide thin films: Electrical properties", J. Appl. Phys. **83** (1998) 2631–2645. https://doi.org/10.1063/1.367025.

[107] D.R. Rolison, B. Dunn, "Electrically conductive oxide aerogels: New

materials in electrochemistry", J. Mater. Chem. **11** (2001) 963–980. https://doi.org/10.1039/b007591o.

[108] A. El-ghandour, N.A. El-Ghamaz, M.M. El-Nahass, H.M. Zeyada, "Temperature and frequency dependence outline of DC electrical conductivity, dielectric constants, and AC electrical conductivity in nanostructured TlInS2 thin films", Phys. E Low-Dimensional Syst. Nanostructures. **105** (2019) 13–18. https://doi.org/10.1016/j.physe.2018.08.024.

[109] D.A. Neamen, "Semiconductor Physics and Devices", University of New Mexico, Richard D. Irwin, (1992) 746.

[110] S. Indris, P. Heitjans, M. Ulrich, A. Bunde, "AC and DC Conductivity in Nano- and Microcrystalline Li2O : B2O3 Composites: Experimental Results and Theoretical Models", Zeitschrift Fur Phys. Chemie. **219** (2005) 89–103. https://doi.org/10.1524/zpch.219.1.89.55015.

[111] R.M. Levy, "Principles of solid state physics", Elsevier, (2012).

[112] R.I. Khaleel, "Electrical and Optical properties modification of Poly (Vinyl Chloride) by Zinc, Copper and Nickel Ethyl Xanthate chelate Complexes", M. Sc., Coll. Sci., Mustansiryah. (2004).

[113] A. Schönhals, F. Kremer, "Theory of Dielectric Relaxation", Broadband Dielectr. Spectrosc. (2003) 1–33. https://doi.org/10.1007/978-3-642-56120-7_1.

[114] W.D. Kingery, "Introduction to Ceramics 2nd ed.", John Wiley Sons. (1976) 449–468.

[115] H. Rishbeth, "Polarization fields produced by winds in the equatorial F-region", Planet. Space Sci. **19** (1971) 357–369. https://doi.org/10.1016/0032-0633(71)90098-5.

[116] X. An, G. Meng, Q. Wei, X. Zhang, Y. Hao, L. D. Zhang, "Synthesis and photoluminescence of SnO_2/SiO_2 microrings", Adv. Mater. **17** (2005) 1781–1784.

[117] N.E. Hill, "Dielectric properties and molecular behaviour", Van Nostrand Reinhold, (1969) 282.

[118] C.T. O'Konski, "Electric properties of macromolecules. V. Theory of ionic polarization in polyelectrolytes", J. Phys. Chem. **64** (1960) 605–619. https://doi.org/10.1021/j100834a023.

[119] C.J.F. Böttcher, O.C. van Belle, P. Bordewijk, A. Rip, "Theory of electric polarization", Elsevier Science Ltd, **121** (1978) 211. https://doi.org/10.1149/1.2402382.

[120] B.M. Tareev, "Physics of dielectric materials", Mir publishers, 1975.

[121] J.J. O'Dwyer, "The theory of electrical conduction and breakdown in solid dielectrics", Clarendon Press, 1973.

[122] E. Doktorgrades, "Manipulating the Structural and Electronic Properties of Epitaxial NaNbO 3 Films via Strain and Stoichiometry Biya Cai", (2016).

[123] B.K. Kuanr, G.P. Srivastava, B.K. Kuanr, "Dispersion observed in electrical properties of titaniumsubstituted lithium ferrites Dispersion observed in electrical lithium ferrites properties of titanium-substituted", **6115** (2013) 21–24. https://doi.org/10.1063/1.355478.

[124] S.A. Mazen, A. Elfalaky, "Effect of Ti4 + substitution in copper ferrite : an analogous study", **44** (2000) 293–297.

[125] S. Nasri, M. Megdiche, M. Gargouri, "DC conductivity and study of AC electrical conduction mechanisms by non-overlapping small polaron tunneling model in LiFeP2O7 ceramic", Ceram. Int. 42 (2015) 943-951. https://doi.org/10.1016/j.ceramint.2015.09.023.

[126] A. Muheisin, "Study of Electrical Conductivity for Amorphous and Semi Crystalline Polymers Filled with Lithium Fluoride Additive", (2009).

[127] B.H. Rabee, R. Hader, "The effect of adding Ag nanoparticles on the electrical properties (A . C) of the PMMA-SPO-PS blend", 1973

(2021) 12102. https://doi.org/10.1088/1742-6596/1973/1/012102.

[128] C.D. Richard, "The electrical engineering handbook", (1997).

[129] R.S. Al-Khafaji, "Study the Effect of Iraqi Bentonite Clay addition on the Properties of Porcelain Body Prepared from Local Clays", PhD. Thesis, College of Education/Ibn Al-Haithem, University of Baghdad,Iraq, (2009).

[130] X. Zhang, X. Chen, X. Zhang, "The impact of exposure to air pollution on cognitive performance", **115** (2018) 9193-9197. https://doi.org/10.1073/pnas.1809474115.

[131] M. Zhang, Z. Yuan, J. Song, C. Zheng, "Sensors and Actuators B : Chemical Improvement and mechanism for the fast response of a Pt / TiO 2 gas sensor", Sensors Actuators B. Chem. **148** (2010) 87–92. https://doi.org/10.1016/j.snb.2010.05.001.

[132] G. Korotcenkov, "Metal oxides for solid-state gas sensors" , **139** (2007) 1–23. https://doi.org/10.1016/j.mseb.2007.01.044.

[133] C. Wang, L. Yin, L. Zhang, D. Xiang, R. Gao, "Metal Oxide Gas Sensors: Sensitivity and Influencing Factors", **10** (2010) 2088–2106. https://doi.org/10.3390/s100302088.

[134] T. Hübert, L. Boon-brett, G. Black, U. Banach, "Sensors and Actuators B", Chemical Hydrogen sensors – A review, **157** (2011) 329–352. https://doi.org/10.1016/j.snb.2011.04.070.

[135] N. Yamazoe, "Toward innovations of gas sensor technology", **108** (2005) 2–14. https://doi.org/10.1016/j.snb.2004.12.075.

[136] V. Balouria, S. Samanta, A. Singh, A.K. Debnath, A. Mahajan, R.K. Bedi, D.K. Aswal, S.K. Gupta, "Chemiresistive gas sensing properties of nanocrystalline Co3O4 thin films", Sensors Actuators B. Chem. **176** (2012) 38-45. https://doi.org/10.1016/j.snb.2012.08.064.

[137] H. Liu, S. Xu, M. Li, G. Shao, H. Song, W. Zhang, W. Wei, M. He, H. Song, J. Tang, "Chemiresistive gas sensors employing solution-

processed metal oxide quantum dot Chemiresistive gas sensors employing solution-processed metal oxide quantum dot films", Applied Physics Letters, **163104** (2014) 1–6. https://doi.org/10.1063/1.4900405.

[138] F.S. Freitas, A.S. Gonçalves, A. De Morais, J.E. Benedetti, A.F. Nogueira, "Graphene-like MoS2 as a low-cost counter electrode material for dye-sensitized solar cells", This J. Is © NanoGe J. Energy Sustain. **1** (2012) 11002–11003. https://doi.org/10.1039/c0xx00000x.

[139] L.A. Patil, A.R. Bari, M.D. Shinde, V. V. Deo, D.P. Amalnerkar, "Synthesis of ZnO nanocrystalline powder from ultrasonic atomization technique, characterization, and its application in gas sensing", IEEE Sens. J. **11** (2011) 939–946. https://doi.org/10.1109/JSEN.2010.2066265.

[140] M.H. Sarfi, M. Ghadimi, A. Babaee, "H 2 S Gas Sensor Based on SnO 2 and CuO Nanoparticles" , STEM Fellowsh. J. **1** (2015) 21–26. https://doi.org/10.17975/sfj-2015-012.

[141] N.H. Harb, F.A.H. Mutlak, "Gas sensing characteristics of WO3NPs sensors fabricated by pulsed laser deposition on PS n-type", J. Opt. **52** (2022) 323-331. https://doi.org/10.1007/s12596-022-00877-1.

[142] K.L. Chopra, "Thickness measurement and analytical techniques", Thin Film. Phenomena. New York McGraw-Hill. (1969) 346.

[143] P.D. File, "Joint committee on powder diffraction standards", ASTM, Philadelphia, (1967) 9–185.

[144] C. Indium, "Crystallographic parameters Subfiles and Quality Comments References Peak list", (2010) 1–2.

[145] G.A. Kumar, M.V.R. Reddy, K.N. Reddy, "Structural and optical properties of ZnO thin films grown on various substrates by RF magnetron sputtering", IOP Conf. Ser. Mater. Sci. Eng. **73** (2015) 3–7. https://doi.org/10.1088/1757-899X/73/1/012133.

[146] L.X. Li, Y.X. Jin, H.L. Dong, S.H. Yu, D. Xu, "Effect of Sn4+ substitution on the dielectric properties of Bi_2O_3-ZnO-Nb2O5 pyrochlores", Ceram. Int. **40** (2014) 16133–16139. https://doi.org/10.1016/j.ceramint.2014.07.044.

[147] A.K. Sahoo, M.R. Panigrahi, "A study on strain and density in graphene-induced Bi_2O_3 thin film", Bull. Mater. Sci. **44** (2021) 1–9. https://doi.org/10.1007/s12034-021-02515-1.

[148] M.K. Halimah, A. Azuraida, M. Ishak, L. Hasnimulyati, "Influence of bismuth oxide on gamma radiation shielding properties of boro-tellurite glass", J. Non. Cryst. Solids. **512** (2019) 140–147. https://doi.org/10.1016/j.jnoncrysol.2019.03.004.

[149] S.M. Lam, J.C. Sin, A.Z. Abdullah, A.R. Mohamed, "Efficient photodegradation of endocrine-disrupting chemicals with Bi 2O3-ZnO nanorods under a compact fluorescent lamp", Water. Air. Soil Pollut. **224** (2013). https://doi.org/10.1007/s11270-013-1565-6.

[150] A.A.P. Frit, K. Deepalakshmi, N. Prithivikumaran, N. Jeyakumaran, "The effect of annealing time on lead oxide thin films coated on indium tin oxide substrate", Int. J. ChemTech Res. **6** (2014) 5347–5352.

[151] A.-L. Barabási, H.E. Stanley, "Fractal concepts in surface growth", Cambridge university press, 1995.

[152] M. Yasin, M. Saeed, M. Muneer, M. Usman, A. ul Haq, M. Sadia, M. Altaf, "Development of Bi_2O_3-ZnO heterostructure for enhanced photodegradation of rhodamine B and reactive yellow dyes", Surfaces and Interfaces. **30** (2022) 101846. https://doi.org/10.1016/j.surfin.2022.101846.

[153] R.I. Kamel, D.S. Ahmed, U.M. Nayef, "Synthesis of Bi_2O_3 nanoparticles by laser ablation on porous silicon for photoconversion application", Optik (Stuttg). **193** (2019) 163013. https://doi.org/10.1016/j.ijleo.2019.163013.

[154] S. Sharma, R. Vyas, Y.K. Vijay, "A study on luminescence enhancement in ion irradiated TiO_2/poly (methyl methacrylate) nanocomposites", in: Adv. Mater. Res., Trans Tech Publ, 585 (2012) 139–143.

[155] B. Rabee, M. Habeeb, A. Hashim, "Preparation of (PS-PMMA-ZnCl2) Composites and Study their Electrical and Optical Properties", Int. J. Sci. Res. **3** (2014) 2319–7064.

[156] A.D. Ghaleb Abdul Wahab, N.N. Hussein, B. Ahmed, T. Rafia, "The Effect of Bismuth Oxide Bi_2O_3 on Some Optical Properties of Poly-Vinyl Alcohol", Br. J. Sci. **4** (2012) 117–124.

[157] D.K. Eric, "Engines of Creation. The Coming Era of Nanotechnology", Anchor B. (1986).

[158] H.S. Suhail, B.H. Rabee, "New nanocomposites (PMMA-SPO-SiC) fabrication and of their structural and electrical properties for pressure sensors", AIP Conf. Proc. **2213** (2020). https://doi.org/10.1063/5.0000093.

[159] Y. Al-Hadeethi, M.I. Sayyed, Y.S. Rammah, "Investigations of the physical, structural, optical and gamma-rays shielding features of Bi_2O_3 – Bi_2O_3 – ZnO – CaO glasses", Ceram. Int. **45** (2019) 20724–20732. https://doi.org/10.1016/j.ceramint.2019.07.056.

[160] H. Hakim, N. Al-Garah, A. Hashim, "The Effect of Aluminum Oxide Nanoparticles on Optical Properties of (Polyvinyl Alcohol-Polyethylene Glycol) Blend", **1** (2015) 94-98.

[161] A. Hashim, Q. Hadi, "Structural , electrical and optical properties of (biopolymer blend / titanium carbide) nanocomposites for low cost humidity sensors", J. Mater. Sci. Mater. Electron. **29** (2018) 11598-11604. https://doi.org/10.1007/s10854-018-9257-z.

[162] A. Razzaq, A. Ridha, N.A. Al-isawi, "Studying the effect of annealing temperatures on the optical properties of CdS : 1 % Cu nanoparticles

thin films prepared by thermal evaporation technique", In Journal of Physics: Conference Series, **1234** (2019) 12029. https://doi.org/10.1088/1742-6596/1234/1/012029.

[163] N.H.A.- Garah, A. Hashim, "The Effect of Aluminum Oxide Nanoparticles on Optical Properties of (Polyvinyl alcohol-polyethylene glycol) Blend", Polymer-Plastics Technology and Engineering, **1** (2015) 94–98.

[164] H.N.Najeeb, H.N.Najeeb, "Study of Some Electrical and Optical Properties for Thin Films Prepared from Polymeric Composites", M.Sc. thesis ,College of sciences, University of Babylon , 2011.

[165] A. Hashim, M.A. Habeeb, A. Hadi, "Synthesis of novel polyvinyl alcohol–starch-copper oxide nanocomposites for humidity sensors applications with different temperatures", Sens. Lett. **15** (2017) 758–761.

[166] M.S. Ahmad, A.M. Zihilif, E. Martuscelli, G. Ragosta, E. Scafora, "The electrical conductivity of polypropylene and nickel-coated carbon fiber composite", Polym. Compos. **13** (1992) 53–57.

[167] A. Sawalha, A.Ã. Sedky, "Electrical conductivity study in pure and doped ZnO ceramic system", **404** (2009) 1316–1320. https://doi.org/10.1016/j.physb.2008.12.017.

[168] H.J. Youn, T. Sogabe, C.A. Randall, T.R. Shrout, M.T. Lanagan, "Phase Relations and Dielectric Properties in the Bi_2O_3-ZnO-Ta2O5 System", J. Am. Ceram. Soc. **84** (2001) 2557–2562. https://doi.org/10.1111/j.1151-2916.2001.tb01053.x.

[169] B.H. Rabee, "Effect addition Al2O3 on the (AC, DC) Electrical Properties of Ethylene-Alpha Olefin Copolymer", Int. J. Sci. Res. **6** (2017) 2319–7064.

[170] S. Satapathy, P.K. Gupta, K.B.R. Varma, P. Tiwari, V. Ganeshan, "Study on dielectric behavior of Lithium Tantalate (LT) nano particle

filled poly (vinylidene fluoride)(PVDF) nano composite", ArXiv Prepr. ArXiv0808. **420** (2008).

[171] I.H. Hilal, H.L. Abdullah, K.J. Kadhim, "Investigation of structural electrical properties of nanocomposite (Ag-PMMA) thin films synthesis via photo polymerization", Adv. Environ. Biol. **10** (2016) 58–66.

[172] N.H. Al-Hardan, M.J. Abdullah, A.A. Aziz, "Sensing mechanism of hydrogen gas sensor based on RF-sputtered ZnO thin films", Int. J. Hydrogen Energy. **35** (2010) 4428–4434. https://doi.org/10.1016/j.ijhydene.2010.02.006.

[173] A.O. Mousa, S.H. Trier, "Effect of Doping and Temperature Operating on (NO 2) Gas Sensing Properties for Mg x ZnO 1-x / n-Si Heterojunction", Al-Qadisiyah Journal of Pure Science, **22** (2017) 87-95.

List of Symbols

Symbol	Physical Meanings	Unites
n^*	Complex Refractive Index	-
$\mathbf{E}_\mathbf{i}^-$	Internal Field of a Molecule	eV
α	Absorption Coefficient	nm^{-1}
μ_i	Electrical Dipole Moment	$C \cdot m^2 \cdot V^{-1}$
A	Absorption	%
c	Velocity of Light	m/s
C	Capacitance	F
D	Electrical Displacement Vector	C/m^2
d	Thickness	nm
E	Energy	eV
E_g	Energy Gap	eV
E_i	Electrical Field Intensity	V/m
E_{ph}	Energy of Phonon	eV
ε	Complex Dielectric Constant	-
ε_o	Vacuum Permittivity	F/cm
f	Photon Frequency	Hz
h	Planck Constant	J. s
i	Imaginary Number	-
I	Electrical Current	A
I_A	Absorbed light intensity	eV/m^2. s
I_E	Incoming Light Intensity	eV/m^2. s
I_o	Incident Intensity of Light	Lumen
I_p	Conduction Current	A
I_q	Capacitate Current	A
I_R	Intensity of Reflected Rays	eV/m^2. s
I_S	Scattered Light Intensity	eV/m^2. s
I_T	Intensity of the transmitted light	eV/m^2. s
K	Wave Vector	-
K_B	Boltzmann Constant	JK^{-1}
k_o	Extinction coefficient	m^2/mol
M	Electrical Dipole Moment	C.m
N	Number of layers	-
n	Refractive index	-
N_O	Number of Molecules Per a Unit of Volume	-
P	Polarization	C/m^2

P_0	Space or Interfacial Polarization	C/m^2
P_i	Ionic Polarization	C/m^2
R	Value Determines the Type of Electronic Transitions	-
R_P	Parallel Resistance	Ω
R_r	Reflectance	%
R_v	Volume Electrical Resistance	$Ω/m^2$
S_A	Area	m^2
S	sensitivity	%
T	Transmittance	%
υ	Frequency	Hz
V_m	Maximum Voltage	V
w	Angular Frequency	rad s^{-1}
λ	Wavelength of Light	nm
ρ_v	Resistivity	Ω .cm
σ	Electrical Conductivity	$(Ω.cm)^{-1}$
σ_{op}	Optical Conductivity	s^{-1}
τ_{rec}	Recovery time	sec
τ_{res}	Response time	sec
θ	the Incidence Angle	Degree

List of Abbreviations

Abbreviations	**Physical Meanings**
MOS	metal oxide semiconductors
Bi_2O_3	Bismuth Oxide
ZnO	Zinc Oxide
H_2S	Hydrogen sulfide
NO_2	Nitrogen dioxide
fcc	Face center cubic
CVD	Chemical vapor deposition
XRD	X-ray diffraction
FTIR	Fourier Transformation Infrared Ray
AFM	Atomic Force Microscope
RMS	Root mean square
SEM	Scanning Electron Microscopy
UV	Ultra Violet
Vis	Visible Light
IR	Infrared
T_m	Melting Temperature

C.B	Conduction Band
V.B	Valence Band
NPs	Nanoparticles

List of Figures

List of Tables